IRAQI JOURNAL OF APPLIED PHYSICS

The *Iraqi Journal of Applied Physics (IJAP)* is a peer reviewed journal of high quality devoted to the publication of original research papers from applied physics and their broad range of applications. IJAP publishes quality original research papers, comprehensive review articles, survey articles, book reviews, dissertation abstracts in physics and its applications in the broadest sense. It is intended that the journal may act as an interdisciplinary forum for Physics and its applications. Innovative applications and material that brings together diverse areas of Physics are particularly welcome. Review articles in selected areas are published from time to time. It aims to disseminate knowledge; provide a learned reference in the field; and establish channels of communication between academic and research experts, policy makers and executives in industry, commerce and investment institutions. IJAP is a quarterly specialized periodical dedicated to publishing original papers, letters and reviews in: Applied & Nonlinear Optics, Applied Mechanics & Thermodynamics, Digital & Optical Communications, Electronic Materials & Devices, Laser Physics & Applications, Plasma Physics & Applications, Quantum Physics & Spectroscopy, Semiconductors & Optoelectronics, Solid State Physics & Applications, Alternative & Renewable Energy, and Environmental Science & Technology.

ISSN (Print): 1813-2065, ISSN (Online): 2309-1673

EDITORIAL BOARD

Oday A. HAMMADI	Asst. Professor	Editor-in-Chief	Molecular Physics	IRAQ
Walid K. HAMOUDI	Professor	Member	Laser Physics	IRAQ
Dayah N. RAOUF	Asst. Professor	Member	Laser and Optics	IRAQ
Raad A. KHAMIS	Asst. Professor	Member	Plasma Physics	IRAQ
Raid A. ISMAIL	Professor	Member	Semiconductor Physics	IRAQ
Kais A. AL-NAIMEE	Professor	Member	Quantum Physics	IRAQ
Haitham M. MIKHLIF	Lecturer	Managing Editor	Molecular Physics	IRAQ

Editorial Office:
P. O. Box 88052, Baghdad 12631, IRAQ
Mobile: +964 7832 360 114 (Telegram, Viber, WhatsApp)
Website: www.iraqiphysicsjournal.com
Emails: info@iraqiphysicsjournal.com, editor_ijap@yahoo.co.uk, ijap.editor@gmail.com,

ADVISORY BOARD

Andrei KASIMOV, Professor, Institute of Material Science, National Academy of Science, Kiev,	UKRAINE
Ashok KUMAR, Professor, Harcourt Butler Technological Institute, Kanpur, Uttar Pradesh 208 002,	INDIA
Chang Hee NAM, Professor, Korean Advanced Institute of Science and Technology, Daehak-ro, Daejeon,	KOREA
Claudia GAULTIERRE, Professor, Faculty of Sciences and Techniques, University of Rouen, Rouen,	FRANCE
El-Sayed M. FARAG, Professor, Department of Sciences, College of Engineering, AlMinofiya University,	EGYPT
Gang XU, Assistant Professor, Department of Engineering and Physics, University of Central Oklahoma,	U.S.A
Heidi ABRAHAMSE, Professor, Faculty of Health Sciences, University of Johannesburg,	S. AFRICA
Madis-Lipp KROKALMA, Professor, School of Science, Tallinn University of Technology, 19086 Tallinn,	ESTONIA
Mansoor SHEIK-BAHAE, Associate Professor, Department of Physics, University of New Mexico,	U.S.A
Mohammad Robi HOSSAN, Assistant Professor, Dept. of Eng. and Physics, Univ. of Central Oklahoma,	U.S.A
Morshed KHANDAKER, Associate Professor, Dept. of Engineering and Physics, Univ. of Central Oklahoma,	U.S.A
Qian Wei Chang, Professor, Faculty of Science and Engineering, University of Alberta, Edmonton, Alberta,	CANADA
Sebastian ARAUJO, Professor, School of Applied Sciences, National University of Lujan, Buenos Aires,	ARGENTINA
Shivaji H. PAWAR, Professor, D.Y. Patil University, Kasaba Bawada, Kolhapur-416 006, Maharashtra,	INDIA
Xueming LIU, Professor, Department of Electronic Eng., Tsinghua University, Shuang Qing Lu, Beijing,	CHINA
Yanko SAROV, Assistant Professor, Micro- and Nanoelectronic Systems, Technical University Ilmenau,	GERMANY
Yushihiro TAGUCHI, Professor, Dept. of Physics, Chuo University, Higashinakano Hachioji-shi, Tokyo,	JAPAN

SPONSORED AND PUBLISHED BY
AMERICAN QUALITY FOR SCIENTIFIC PUBLISHING INC.
1479 South De Gaulle Ct, Aurora, CO 80018, United States

IRAQI JOURNAL OF APPLIED PHYSICS

Iraqi Journal of Applied Physics
Q4 Electronic, Optical and Magnetic Materials
best quartile
SJR 2022
0.19
powered by scimagojr.com

INSTRUCTIONS TO AUTHORS

CONTRIBUTIONS

Contributions to be published in this journal should be original research works, i.e., those not already published or submitted for publication elsewhere, individual papers or letters to editor.
Manuscripts should be submitted to the editor at the mailing address:

Iraqi Journal of Applied Physics, Editorial Board, P. O. Box 88052, Baghdad 12631, IRAQ
Mobile: +964 7832 360 114 (Telegram, Viber, WhatsApp)
Website: www.iraqiphysicsjournal.com
Email: info@iraqiphysicsjournal.com, editor_ijap@yahoo.co.uk, ijap.editor@gmail.com

MANUSCRIPTS

Two hard copies or a soft Word copy on a CD or DVD should be submitted to the Editor in the following configuration:

- **One-column** Double-spaced one-side A4 size with 2.5 cm margins of all sides
- Times New Roman font (16pt bold for title, 14pt bold for names, 12pt bold for headings, 12pt regular for text)
- Manuscripts presented in English only are accepted.
- English abstract not exceed 150 words
- 4 keywords (at least) should be maintained on (PACS preferred)
- Author(s) should express all quantities in SI units
- Equations should be written in equation form (*italic* and symbolic) NOT in plain text
- Tables and Figures should be separated from text and placed in new pages after the references
- Charts should be indicated by the software used for generating them (e.g., Excel, MATLAB, Grapher, etc.)
- Figures and diagrams can be submitted in original colored forms for assessment and they will be returned to authors after provide printable copies
- Only original or high-resolution scanner photos are accepted
- For electronic submission, articles should be formatted with MS-Word software
- Figures, charts, photos, images or pictures **SHOULD NOT** be grouped in Word file
- Figure caption should be written as plan text **NOT** inside a text box

AUTHOR NAMES AND AFFILIATIONS

It is IJAP policy that all those who have participated significantly in the technical aspects of a paper be recognized as co-authors or cited in the acknowledgments. In the case of a paper with more than one author, correspondence concerning the paper will be sent to the first author unless staff is advised otherwise.
Author name should consist of first name, middle initial, last name. The author affiliation should consist of the following, as applicable, in the order noted:
- Company or college (with department name or company division), Postal address, City, Governorate or State, zip code, Country name, contacting telephone number, and e-mail

REFERENCES

The references should be brought at the end of the article, and numbered in the order of their appearance in the paper. The reference list should be cited in accordance with the following examples:
[1] F.H. Al-Berkdar, D.N. Raouf and F.H. Hamza, "A Line Tuned TEM_{00} Mode CW CO_2 Laser", *Iraqi J. Appl. Phys.*, 1(1) (20025) 8-10.
[2] W. Demtröder, **"Atoms, Molecules, and Photons"**, Springer-Verlag (Berlin, 2006), Ch. 4, p. 130.
[3] Y. Lee, S.A. Korpela and R. Horne, "Structure of Multi-Cellular Natural Convection in a Tall Vertical Annulus", Proceedings of 7th International Heat Transfer Conference, U. Grigul et al., eds., Hemisphere (NY), 2 (1982) 221–226.
[5] M. Hashish, "Waterjet Technology Development", High Pressure Technology, PVP-Vol. 406 (2000) 135-140.
[6] D.W. Watson, "Thermodynamic Analysis", ASME Paper No. 97-GT-288 (1997).
[7] Z. Cheng, "Vibrational Discrete Action Theory", Ph.D. thesis, Columbia University, USA (2021).

PROOFS

Authors will receive proofs of papers and are requested to return one corrected copy as a WORD file on a compact disc (CD) or by email. New materials inserted in the original text without Editor's permission may cause rejection of paper unless the handling editor is informed.

COPYRIGHT FORM

Author(s) will be asked to sign the IJAP Copyright Form and hence transfer copyrights of the article to the Journal soon after acceptance of it. This will ensure the widest possible dissemination of information.

OFFPRINTS

Authors will receive electronic offprint free of charge and any additional reprints can be ordered.

SUBSCRIPTION AND ORDERS

Annual fees (4 issues per year) of subscription are:
50 US$ for individuals inside Iraq; **200** US$ for institutions inside Iraq; **100** US$ for individuals abroad; **300** US$ for institutions abroad.

IRAQI JOURNAL OF APPLIED PHYSICS
Vol. 19, No. 4B, November 2023, pp. 83-92

Meriem Andam [1]
Jamila El Alami [1]
Younes Louartassi [1]
Rabie Zine [2]

[1] *Laboratory for System Analysis, Information Processing, and Integrated Management (LASTIMI), High School of Technology-Salé, Mohammed V University in Rabat, MOROCCO*
[2] *School of Science and Engineering, Al Akhawayn University in Ifrane, MOROCCO*

Technical and Economic Analysis Criteria for Optimal Configurations in PV Battery Systems

Nowadays, the use of renewable energies has become a priority in order to meet the growing energy needs and protect the environment with clean and natural resources. Nevertheless, this type of energy faces a number of challenges related to fluctuation, intermittency, high price, design complexity and storage difficulty. We will consider the last two challenges by proposing the optimal configuration for a grid-connected photovoltaic system while analyzing the need and added value of a storage system. Therefore, a grid-connected photovoltaic system located in Marrakech, Morocco has been studied with a photovoltaic field of about 5.3 KWp and a storage of about 1407 Ah. The aim is to analyze three factors based on two different configurations of the photovoltaic (PV) grid connected with and without the battery. These factors are maximum independence of the system, interaction with external factors, and economic gain.

Keywords: Optimization criteria; Grid connected; Photovoltaic system; Economic gain
Received: 17 August 2023; **Accepted:** 02 September 2023

1. Introduction

1.1. General context

Morocco is characterized by its geographical position and its advantageous climate facilitating and encouraging the integration of renewable energies. The average incident solar radiation varies between 4.7 and 5.6 kWh/m^2/day with a total number of sunshine hours varying from 2700 h/year in the North of Morocco to more than 3500 h/year in the South [1]. In this regard, the country is committed to several projects based on solar energy with the various existing technologies, namely photovoltaic (PV) and concentrated solar power (CSP). Morocco encourages and promotes access to clean electrical energy at the level of large power plants, at the industrial level and in rural areas. Nevertheless, this type of energy suffers from different challenges that all actors in the field are trying to overcome.

Several advanced researches have been carried out in order to find solutions to the different challenges presented in Fig. (1), in our case we focus on analyzing the reaction of a photovoltaic system regarding three main aspects: independence, interaction with other external parameters and cost.

1.1.1. Technical independence

When investing in a renewable energy system, the first objective is to meet the desired energy demand and ensure maximum energy independence from conventional sources. If independence is established for one's own system, the benefits can also reach the different operators involved. Through the simulation and optimization of photovoltaic systems used for household power supply in Iraq, it has been demonstrated that this type of systems not only meets the energy needs of households but also allows to supply the national electrical grid [2,3]. The maximum technical independence of photovoltaic systems is increasingly associated to optimized systems. The various components of the photovoltaic system remain critical elements whose operation should be optimized to ensure maximum production and minimum energy losses. The article [4] for exemple demonstrated the importance of developing more suitable energy conversion tools, a set of guidelines for installation and maintenance with minimum intervention required.

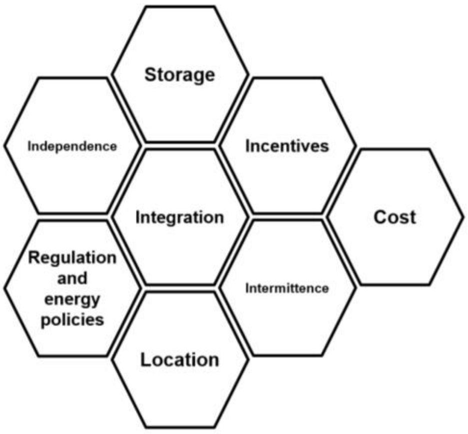

Fig. (1) Renewable energies challenges

1.1.2. Impact of external parameters

The photovoltaic system with its different components is exposed to a set of parameters that can impact and reduce the whole performance of the system as external factors [5]. Extern factors may include climate, location, maintenance tools, interest, policies and consumer awareness. As an illustration, the article [6] presents the effects of environmental factors on the operation of the photovoltaic system including dust accumulation on the panels, water droplet distribution, bird droppings and partial shading conditions. Bird fouling and dust have a negative effect on the photovoltaic current and voltage, which in addition influences the photovoltaic energy collected. The presence of one quarter more shading can lead to a reduction in power output of up to 33.7%. On the other hand, water contributes to the reduction of temperature and consequently to the improvement of the output power. The external parameters can be divided into technical and non-technical parts such as the implication of the consumer. Before investing in renewable energy systems, consumers must be able to live with the presence of PV Systems. The first consumer must be directly involved, and his interest should not be restricted to technical or economic gain, but must extend to a more crucial aspect, which is environmental preservation. A study in the article [5] has shown that the use of renewable energy, especially solar energy, is not related to the consumer's awareness of environmental protection. Thus, it proposes to further develop the solar market by introducing programs and strategies to protect the environment against the harmful effects of conventional energy sources.

1.1.3. Optimisation cost

As mentioned previously, the investment in renewable energies is always beneficial in environmental terms, however it is also necessary to meet the desired technical requirements with appropriated lower costs. In this sense, the economic optimization is one of the priorities and can concern many internal and external parameters. It can involve all the elements, for example, the article [6] presented a methodology for an adequate sizing of the inverter aiming at the reduction of the losses and the generated electricity cost. In our article, we will analyse two possible configurations and the costs involved in the implementation and the costs generated during operation.

It is true that there is a great interest in optimizing photovoltaic systems, but to achieve maximum optimization, a combination between technical and economic gains is required. Balancing economic and technical gains is one of the major current interests for a number of researchers. The article [9] presented energy, economic and environmental analyses for three technologies for grid-connected systems (2.04 kWp of polycrystalline (p-Si), 2.04 kWp of monocrystalline (m-Si) and 1.86 kWp of amorphous) installed in institutional buildings at the level of Moroccan cities with different climate conditions. The results of the energy analysis showed that the poly-Si modules exceeded the other two technologies in terms of conversion efficiency and performance. The economic analysis also demonstrated the advantages of the polycrystalline technology in terms of payback period and LCOE). The environmental impact is also important for the same technology. In addition to the technology, the type of location can influence the economic gain. A study was established in the article [8] to determine the appropriate sites for economically beneficial investments in Texas based on economic parameters such as payback period which is between 2-20 years and incentives.

In some countries, the technology itself is not really beneficial and requires framing. Taking the case of a rural area in Nigeria [11], PV technologies are not attractive for a set of factors especially in terms of profitability and capital dependency. The corresponding paper proposed a model to evaluate the benefits of a stand-alone PV system in this area. The results showed that the PV technology remains advantageous because the investments involved can be recovered in the appropriate time frame. In this sense, two main parameters were taken into account: infrastructure and energy policies.

1.2. Objectives

In this article, we have examined three types of factors mentioned above. When setting up a photovoltaic system, there are several factors to consider, which have been divided into three parts. As an ordinary consumer, the photovoltaic system must first meet the majority of existing energy needs, so optimal sizing is recommended. Secondly, the solar system is integrated into a continuous process, and must therefore interact with a range of disturbing parameters. This interaction must also be prevented and studied. Finally, we have chosen to analyze the economic impact of the system: the more we invest in energy independence and consumer comfort, the more money is needed. Consequently, the economic impact must be moderated and the costs generated fairly reasonable.

In the next part, we will start with a description of the technical and economic criteria considered for the optimization of PV Battery Systems. Then a case study will be analyzed according to three different criteria mentioned considering the absence of storage in the first configuration and presence of the battery in the second configuration. We are going to study the system's reaction and its characteristics in order to define the most suitable configuration in technical and economic terms, and demonstrate the type of configuration most affected by external factors such as temperature and consumer involvement. The region considered is Marrakech which is characterized by an important solar radiation. PV Syst software will be used for analysis and study.

2. Optimization criteria in pv battery systems

Before investing in a renewable energy system, it is important to identify its purpose and mission, analyze the existing system , study the feasibility and predict the technical, economic and environmental gain. The nature of the system, its components, the target groupe, integration and other parameters must be considered before each renewable energy project (Fig. 2).

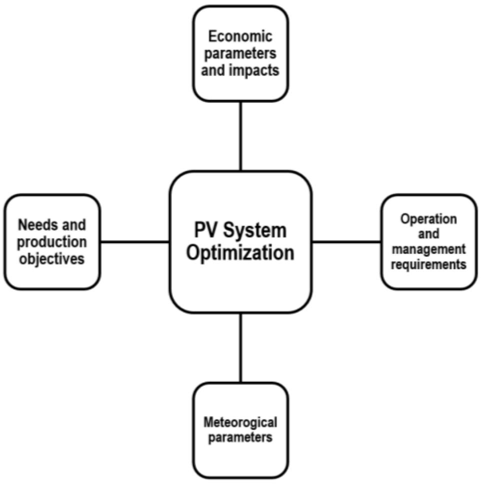

Fig. (2) Optimization criteria for PV Systems

In our article, we will focus on three criteria to determine the profitability and necessity of the system with or without battery using simulation with PV System Software. When it comes to optimization, set of parameters or just one can be considered, and the impact would still be significant. Nevertheless, the novelty of this article is the identification of three different criteria to guide the user on which type of photovoltaic system should be invested in, how to adapt certain external parameters to optimize the system and then demonstrate that surplus energy always represents an economic gain that should not be lost or neglected, especially if the opportunity for surplus resale is not available, which is the current case in Morocco. Depending on the consumer's priority interest, he or she would be able to define in advance the added value of having a storage system and the degree of adaptation with this type of system. The final goal is to achieve optimal operation of the photovoltaic system.

2.1. Maximum independence of the system

The main purpose of the integration of renewable energies is to ensure a certain autonomy and energy independence that guarantees the maximum continuous response to needs. This independence must be achieved by avoiding energy and economic losses. To optimize a power generation system based on clean energies, particularly in the presence of storage, the demandshould be met, the battery should be charged and the surplus avoided. For example, and in order to optimize an autonomous photovoltaic system with hydrogen storage [12], it was necessary to meet the consumption needs while avoiding the production surplus that can neither be stored nor converted into hydrogen. Homer software was used in this sense.

In another research paper and to ensure that the energy needs of a stand-alone photovoltaic system are met, it was first necessary to identify the most appropriate sizing, in particular the most suitable number of days of autonomy for the required battery capacity. The right capacity guarantees maximum energy for the consumer and less energy loss. In combination with a generator and an economic analysis, the technical configuration identified was both technically and economically approved [13].

In some critical cases, energy independence is an obligation. In the article [14], the importance of certain measures and criteria to achieve the performance of a stand-alone photovoltaic system for primary health Centres in Nigeria was studied based on the following parameters: PV battery, inverter, lack and surplus, load growth, availability and yield. In this article, we will demonstrate how the presence of the battery is a crucial element in ensuring technical independence but have other limitations also that should be considered. Taking into account the presence of the network and also the presence of the battery, the goal is to use one or the other based on an optimal method minimizing the energy loss.

2.2. Interaction with external factors

Several factors contribute in the degradation of the solar plant and affect the performance of the system directly or through time. Two parameters are analyzed in our case, the temperature and hours energy use managed by the consumer which can be considered as variables.

Indeed, there are several factors that can influence the performance of photovoltaic systems, including weather conditions, shading, dust, orientation, type of material, location, temperature and others. Temperature is one of the main external factors that can influence the system. Certainly, with a high temperature, we can have more photovoltaic production. Nevertheless, the consequent losses are more important. When the temperature increases, for instance the conversion efficiency also decreases with an average value of 0.5%/°C [15].

Therefore, it is always important to adopt protective measures. In order to protect against and prevent the negative effects of temperature increase on the operation of photovoltaic modules, the article [16] proposes the following measures in Fig. (3).

When you have renewable energy system that is fluctuating and non-programmable, it is essential as a consumer to know how to deal with it and integrate it into your daily life. The paper [17] studied the possibility of synchronizing consumption with existing production. Surveys were conducted with households in Wallonia. The results showed that women and older people are more willing to adapt their loads. Also people interested in environmental protection are willing to synchronize their consumption. Other prosumers are able to get more involved with the availability of more attractive financing and support measures, with the accessibility of existing consumption and production informations and the adoption of smart devices for load shifting. Consumers need to know the real situation of their consumption in order to be able to adapt and improve it according to the production. As a solution and following the article [18], the use of smart meters should be promoted in order to make electricity visible and allow consumers adaption.

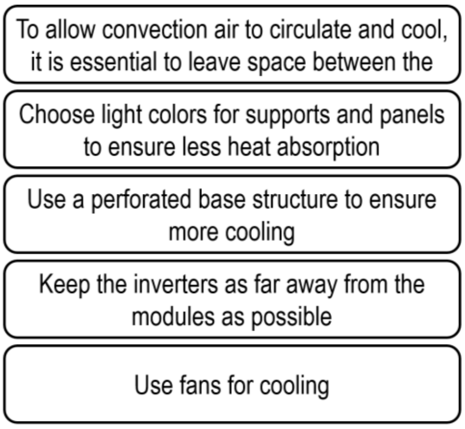

Fig. (3) Protective measures against the effects of temperature on PV systems

2.3. Economic gain

Any energy savings generated through the optimization of the two previous criteria will contribute to the generation of a cost gain which is estimated. The optimization of technical parameters influences the economic gain and can generate cost benefits. The alternative situation is also possible, and economic parameters can be first identified in order to determine the nature of the appropriate system in terms of size and appropriate technologies.

This is the case proposed by several researchers in the field. As presented in the article [19], the optimal sizing of the battery PV System especially for irrigation and pumping was chosen depending on two important parameters: the net present cost (NPC) which represents the life cycle cost of the whole system including investment, replacement, operation and maintenance costs as well as recovery and the energy cost (EC) which represents the average cost per kWh of electrical energy produced in the case studied by the battery PV system.

In the same context, the article [20] aims to define the optimal configuration of a PV System in Poland for which corresponds a high Net Present Value (NPV) for two scenarios of electricity regulation feed in tariff and net metring. The results demonstrated that the Net Metring offers more advantageous NPV (70%) with larger installation sizes comparing to the Feed in Tariffs (FITs).

Moreover, and in order to ensure an economic gain, it is essential to include the previous criteria namely consumers' attitudes, particularly their capacity to integrate such a renewable enrgy system. Based on Australian survey data, the article [21] studied the impact of FITs on electricity consumption at the household level. The results showed that FIT schemes increase the amount of electricity purchased by generating companies. In fact, consumers mainly consider the overall amount to pay for electricity. Nevertheless, a separation must be considered between the FIT's income and the electricity payment.

A major parameter that should also be highlighted is renewable energy policies, a well-adapted regulation can contribute to the reduction of the LCOEs [22]. LCOE represents the price of the Kwh produced. It is used to measure the feasibility and competitiveness of a system compared to other technologies [23]. It can be calculated as follows:

$$LCOE=\frac{\sum_{t=1}^{n}\frac{I_t+M_t}{(1+r)^t}}{\frac{E_t}{(1+R)^t}} \qquad (1)$$

I_t = Investment and expenditures for the year (t),
M_t = Operational and maintenance expenditures for the year (t),
E_t = Electricity production for the year (t),
r = Discount rate that could be earned in alternative investments, and
n = Lifetime of the system

3. Application to grid connected pv systems without storage

In this section, we will analyze the different three parameters mentioned above in order to study the reaction and interaction of our grid-connected PV system without the presence of storage. The aim is to define the system's technical independence, its interaction with two priority parameters and the costs involved. The software used will be PV Syst.

3.1. Maximum independence of the system

In this case, we are talking about a system connected to the grid but without battery, during the day the need is ensured through the photovoltaic production of the panels and the rest is generated to the grid but without gain compared to the case with the presence of the battery. The technical gain is less important especially in our case when the consumer is a simple user. In Fig. (4) below, we present the energy supplied to the consumer, the energy supplied by the grid and the energy supplied by the solar photovoltaic. It can be noticed that the grid provides the most important energy rate, which is justified by the important energy consumption during the night and with the absence of storage, it is only the grid that is dominant.

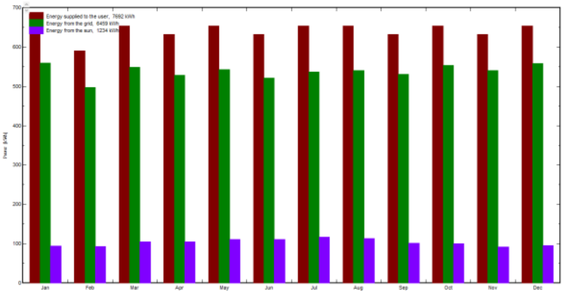

Fig. (4) Energy supplied to the user, from the grid and the solar production (PVsyst)

3.2. Interaction with external factors

In this section, two parameters have been prioritized for the analysis because of their importance and impact. The first one is related to the temperature and the second one is related to the consumption hours. In this case, the consumer's consumption cannot be freely adjusted. However, it can be adapted according to the time of day, particularly during periods of high photovoltaic production.

3.2.1. Impact of the temperature

A high temperature certainly generates a very important solar photovoltaic production but also a certain loss of energy that cannot be ignored. In this sense, in addition to the region of Marrakech, we have chosen a less hot region like Tetouan to make a comparison. The results are described in figures (5) and (6).

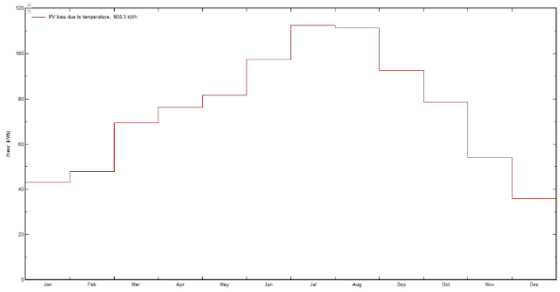

Fig. (5) PV Loss due to temperature in Marrakech (PVsyst)

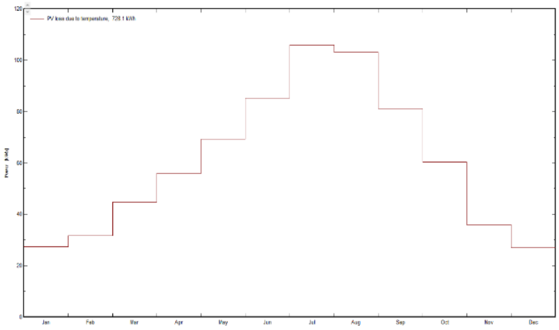

Fig. (6) PV loss due to temperature in Tétouan (PVsyst)

3.2.2. Impact of use hours

The standard energy requirements of the household studied are higher in the evening, although they can be adjusted in particular for the use of certain electrical appliances such as washing machines and dishwashers during the day. A new alternative and estimative scenario can be proposed instead of the reference scenario. Both are presented below in figures (7) and (8).

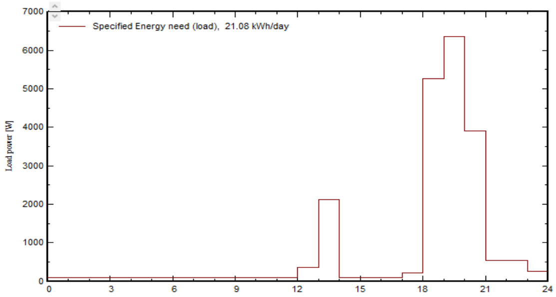

Fig. (7) Reference consumption allocation scenario (PVsyst)

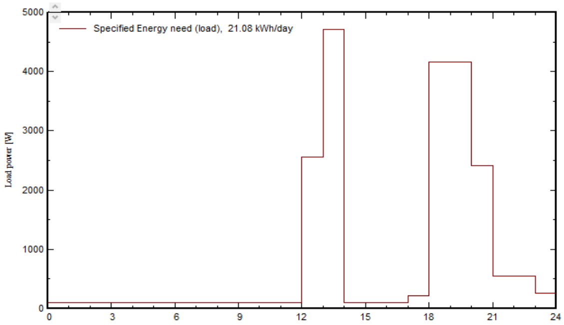

Fig. (8) Alternative consumption distribution scenario (PVsyst)

We have suggested an alternative scenario in order to analyze the behavior of our photovoltaic system and therefore compare the energy provided by the grid and the solar photovoltaic system (Fig. 9).

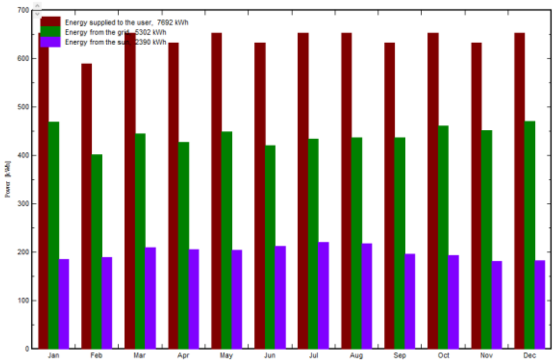

Fig. (9) Energy supplied to the user, from the grid and the solar production in alternatif scenario (PVsyst)

3.3. Economic gain

In the first configuration, our PV System consists of 11 PV modules and an inverter that are connected to the grid. An economic evaluation has been established based on the PV Syst software. The consumption fee per kWh is considered according to the tariffs of the National Office of Electricity and

Potable Water which is the Moroccan operator of electricity supply in the country. An economic evaluation has been established and the peak - tariffs and Off-peak tariffs have been considered. The results are represented as follows (table 1).

Table (1) Overview of the technical and economic characteristics of the configuration 1

LCOE	0,053 Euro/kWh
Installation Cost	5255 Euro
Self-Consumption	1234 kWh/year
Surplus of Solar energy	7374 kWh/year

Actually and as residential, the electricity resale to the operator in not yet possibl, the real economic gain E_g is then estimated between the following two values:

$$83 \text{ Eur/ year} \leq E_g \leq 160 \text{ Eur/ year}$$

Supposing the surplus is sold or even compensated during the year, the economic gain generated will vary as follows:

$$577 \text{ Eur/ year} \leq E_g \leq 1119 \text{ Eur/ year}$$

This last estimation must be less in reality because the resale price is generally less than the electricity purchase price.

4. Application to grid connected pv battery systems

In recent years and considering the important energy crisis that a set of countries are experiencing, several researches, models, software and configurations have been provided to model photovoltaic systems. The article [24] presented several guidelines and criteria for the implementation of such a system, especially with the presence of storage:

- In order to achieve system reliability with low cost, the choice of photovoltaic technology and the configuration of the whole system must be considered;
- Choosing a suitable battery with adequate capacity to have a high lifetime;
- In order to guarantee the durability of the system, the problem of the high cost of the battery and its short life span must be addressed;

4.1. Maximum Independence of the system

When we talk about a photovoltaic system connected to the grid but with the presence of a battery, we are referring to a system whose aim is to meet the maximum of its energy needs through photovoltaic energy. It is a system whose aim is both to meet energy needs with photovoltaic energy and avoid an energy shortage by using the grid. With the presence of the grid, the battery remains an additional tool requiring highly efficient management. In this case, it is advisable to exploit the energy stored in the battery to the optimum, especially since grid feed-in is not profitable in our case. Figure (10) presents energy supplied to the user, from the grid and the solar production.

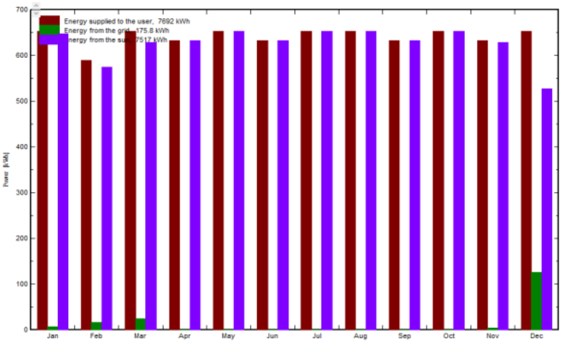

Fig. (10) Energy supplied to the user, from the grid and the solar production (PVsyst)

4.2. Interaction with external factors

Given that the orientation of the panels and their angle of inclination are fixed parameters for our case. In this second part, we will study the impact of two parameters: temperature (PV loss, overall battery loss, etc.) and consumer management with the presence of the battery.

4.2.1. Impact of temperature

In the previous section, we have already presented the impact of temperature on the PV modules which remains unchanged. In this part, we also present its impact on the inverter (Fig. 11) and the battery (Fig. 12).

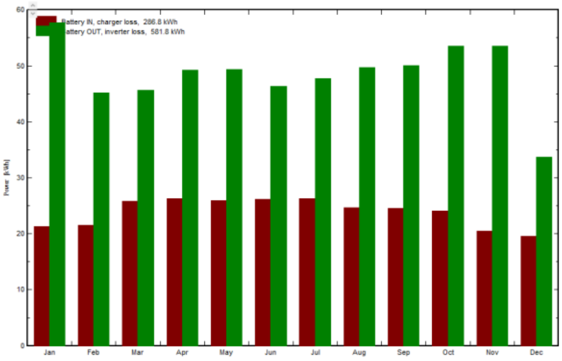

Fig. (11) Losses present at the level of the battery and the inverter in Marrakech (PVsyst)

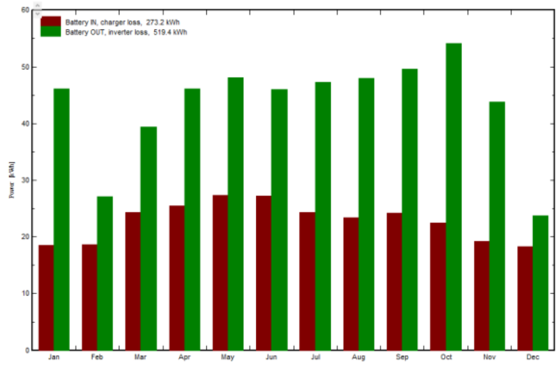

Fig. (12) Losses present at the battery and inverter in Tetouan (PVsyst)

4.2.2. Impact of hours' use

It is more beneficial for the consumer to adapt his needs to maximum use of the PV system during peak hours. The graphs of the battery, the grid and the PV system are shown in Fig. (13). The same alternative scenario has been considered.

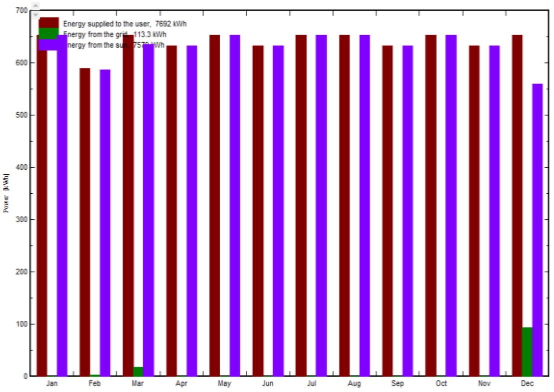

Fig. (13) Energy supplied to the user, from the grid and the solar production in alternatif scenario (PVsyst)

4.3. Economic Gain

In the second configuration, the system consists of 11 photovoltaic modules, an inverter and a 1407 Ah battery. An economic evaluation has been established using the PV Syst software. The results are represented as follows in table (2).

Table (2) Overview of the technical and economic characteristics of the configuration 2

LCOE	0,15 Euro/kWh
Installation Cost	9834,4 Euro
Self-Consumption	5677 kWh/year
Surplus of Solar energy	2274 kWh/year

While the resale of electricity as residential to the operator is not yet possible, the real economic gain E_g is estimated between the following two values:

$$\mathbf{380\ Eur/year \leq E_g \leq 738\ Eur/\ year}$$

Supposing the surplus is sold or even compensated during the year, the economic gain generated will vary as follows:

$$\mathbf{533\ Eur/year \leq E_g \leq 1034\ Eur\ /year}$$

5. Results and Discussion

5.1. Description

Following the different results above relative to the three chosen criteria, we can notice that each configuration is advantageous either on a technical or economic level.

- **Maximum Independence of the system:** On this aspect, the configuration 2 is more advantageous because the battery allows to meet more the needs of energy even during the night allowing less reliance on the grid (Fig. 14) and (Fig. 15).
- **Interaction with external factors:** Temperature has the same impact on both configurations: losses are generated compared to a cooler region. This influences the whole system. On the other hand, the adjustment of the hour's use remains beneficial for the first configuration and the results show an increase of the energy supplied by the solar system. Moreover, configuration 2 is not influenced by this change and then gives the consumer more freedom to act with his system.
- **Economic Gain:** In this part and certainly with the presence of the battery, configuration 1 remains cheaper in terms of installation cost and LCOE (Fig. 16 and Fig. 17). Nevertheless, the economic gain in terms of grid dependency and especially taking into account the absence of the FIT is more important for configuration 2.

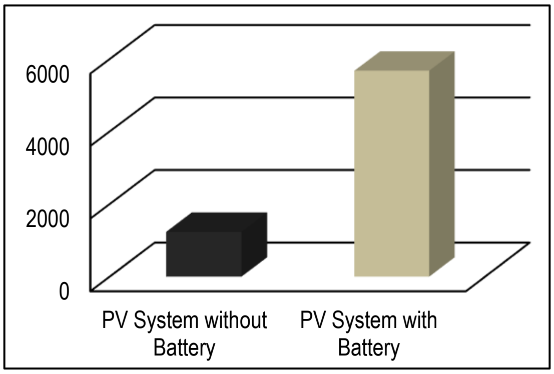

Fig. (14) Self-Consumption (kWh/year)

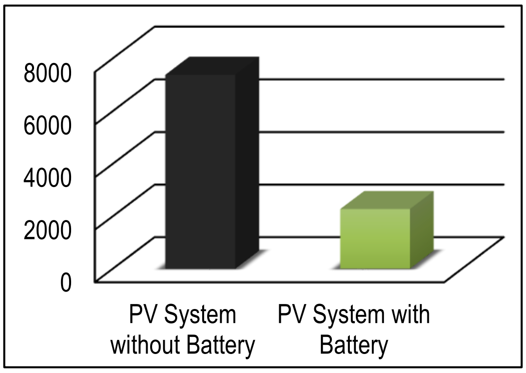

Fig. (15) Solar energy provided to the grid (kWh/year)

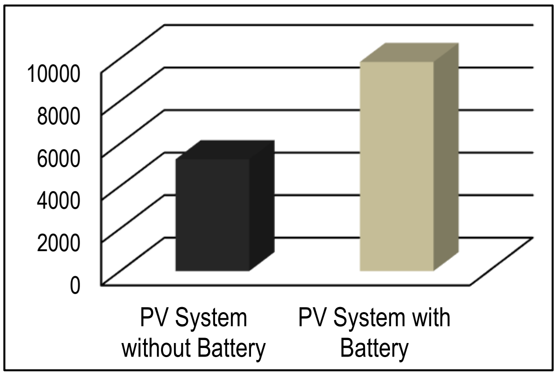

Fig. (16) Installation cost (Euro)

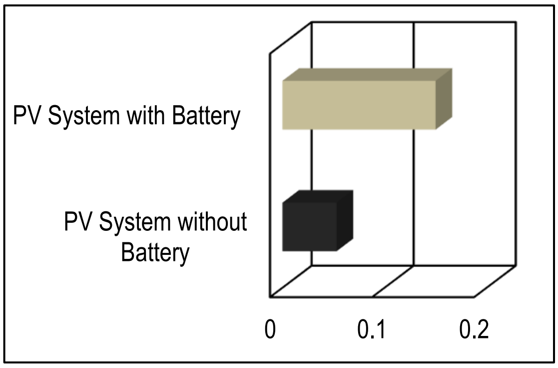

Fig. (17) LCOE (Euro/kWh)

5.2. Discussion

In this section, we will review the contribution of the present paper. The objective is a comparative study between two configurations with the presence and absence of the battery for a grid-connected photovoltaic system. We propose three priority factors to be studied before investing in a PV system and determining the usefulness of storage. Firstly, in the second configuration, the system is more autonomous and guarantees greater energy independence, which also generates fewer CO_2 emissions. The article [25], for example, presented a new method for sizing photovoltaic storage systems for different types of household, such as ordinary households, shared apartments and pensioner households. An important factor considered is the degree of self-sufficiency (DSS) and the aim is to identify the most ideal sizing to maximize this factor. However, increasing this parameter with the use of batteries is not cost-effective, so other parameters need to be addressed, particularly economic ones, such as reducing investment costs.

In many cases and due to the diversity of parameters influencing renewable energy systems, it is necessary to identify and analyze several configurations in order to choose the optimal configuration that meets the economic and technical needs. According to the article [26], grid-connected photovoltaic systems have been assessed economically and environmentally in order to define the most suitable configuration for a photovoltaic panel-based roof intended for a 14-family building in China set up in different climate zones. In this sense, the grid only; the grid PV and the grid PV battery were considered. The first one was the least expensive but the most polluting. The other two produce much less CO_2 emissions but the grid PV is the cheapest. Thus, it was more appropriate for this type of installation. Considering the technical and environmental factors, and according to other research, the battery is still advantageous, but the economic factor completely reverses these results.

The article [27] presented the different energy storage applications with their characteristics, challenges and prospects. Solutions were also proposed to overcome the various challenges and achieve some improved performance. Nevertheless, research is still underway to overcome the first drawback, namely the high price, which will encourage commercialization.

Similarly, the comparison between PV alone and PV-battery continues to interest a number of researchers. A comparative technical and economic study was carried out in three different regions for a 20 MW solar photovoltaic plant with FITs. Among the results obtained, PV battery systems generated a slightly higher LCOE than PV systems alone, due to their higher costs. All the sites studied recorded a negative NPV rate. This shows that this type of configuration is not economically satisfying [28].

For the first parameter "maximum independence of the system" is guaranteed by the battery but unfortunately and economically speaking, the presence of battery generates additional costs influencing the whole system. This disadvantage can be overcome with a set of solutions, namely by adapting the systeme to the existing electricity tariffs. The technical-economic and even environmental analysis can be influenced by energy policies that are more global like the case of the feed in tariff and as a consumer, it is sometimes more suitable to act on its own system and adapt it to the existing electricity tariff. A model has been proposed to define the optimal PV size and profitability for the new feed in tariff in Indonesia considering its rules and limits. Oversized PV systems can cause financial losses especially with the limitation of calculation for the energy fed into the grid [29]. Moreover, an economic analysis has been elaborated for 5 kW rooftop PVs through Homer simulation at the level of 9 Provinces within Turkey. Among the results, it was shown that the FIT and incentives should be determined according to the solar radiation at the country level. The Fits rates should also be adapted according to the nature of each consumer (residential, industrial and consumer). The residential and especially the small scale systems remain the least profitable, which requires more appropriate Fit rates and incentives [30].

The particularity of our work comparing to other advancements is that we have considered the reduced surplus as an economic gain that generates costs not really considered by the simple consumer. This gain is extremely important given that, in our case, the buy-back of electricity is not functional. Therefore, it is necessary to identify other sources of economic efficiency. To support the system's performance, it is also essential to ensure its self-sufficiency by adapting the times of electricity use and protecting the system against high temperature damage.

6. Conclusion

In this article we have analyzed two possible configurations of a grid-connected PV system according to three priority criteria (maximum independence, interaction with external factors, economic gain). The only difference between the two is the presence of a storage system in the second configuration. The battery guarantees more technical independence, more comfort and freedom for the consumer in terms of distribution of consumption hours. On the other hand, in economic terms, the first configuration is more beneficial in terms of LCOE and installation cost but in terms of real economic gain the second configuration is more advantageous as less energy is supplied by the grid and less surplus is generated. The economic profitability of one or the other can only be effective by integrating the resale rates of electricity and also see the possibility of subsidies or incentives that makes the system more favorable not only in technical terms but also economically.

It should be mentioned at the end that the constraints and challenges of renewable energy can be overcome by adapting the policies acting on this energy source. Despite the advances in net metering at the Asian level, there is still a need for a more synthetic analysis of this policy which is well detailed in article [31].

References

[1] M. Meliani et al., “Smart grid implementation in Morocco: Case study”, *Mater. Today: Proc.*, 45(8) (2021) 7675-7679.

[2] Q. Hassan, “Evaluation and optimization of OFF-GRID and on-grid photovoltaic power system for typical household electrification”, *Renew. Ener.*, (2020), doi: 10.1016/j.renene.2020.09.008.

[3] O.A. Hammadi and N.I. Naji, “Effect of Acidic Environment on the Spectral Properties of Hibiscus sabdariffa Organic Dye used in Dye-Sensitized Solar Cells“, *Iraqi J. Appl. Phys.*, 10(2) (2014) 27-31.

[4] L. Hernández-Callejo, S. Gallardo-Saavedra and V. Alonso-Gómez, “A review of photovoltaic systems: Design, operation and maintenance”, *Sol. Ener.*, 188 (2019) 426-440.

[5] O.A. Hamadi, B.A.M. Bader and A.K. Yousif, “Electrical Characteristics of Silicon p-n Junction Solar Cells Produced by Plasma-Assisted Matrix Etching Technique”, *Eng. Technol. J.*, 26(8) (2008) 995-1001.

[6] R.J. Mustafa et al., “Environmental Impacts on the Performance of Solar Photovoltaic Systems”, *Sustainability*,12 (2020) 608.

[7] B. Kesari, S. Atulkar and S. Pandey, “Consumer Purchasing Behaviour towards Eco-Environment Residential Photovoltaic Solar Lighting Systems”, *Glob. Busin. Rev.*, 22(1) (2021) 236–254.

[8] E. Martins Deschamps and R. Rüther, “Optimization of inverter loading ratio for grid connected photovoltaic systems”, *Sol. Ener.*, 179 (2019) 106-118.

[9] A. Allouhi et al., “Energetic, economic and environmental (3E) analyses and LCOE estimation of three technologies of PV grid-connected systems under different climates”, *Sol. Ener.*, 178 (2019) 25-36.

[10] B. Chang and K. Starcher, “Evaluation of wind and solar energy investments in Texas”, *Renew. Ener.*, 132 (2019) 1348-1359.

[11] C. Onyeka Okoye and B. Chioma Oranekwu-Okoye, “Economic feasibility of solar PV system for rural electrification in Sub-Sahara Africa”, *Renew. Sustain. Ener. Rev.*, 82(3) (2018) 2537-2547.

[12] C. Marino et al., “Energetic and economic analysis of a stand-alone photovoltaic system with hydrogen storage”, *Renew. Ener.*, 142 (2019) 316-329.

[13] M. Andam et al., “Days of autonomy for optimal Battery Sizing in Stand-alone Photovoltaic Systems”, *Indonesian J. Electr. Eng. Inform.*, 11(1) (2023) 300-317.

[14] O. Babatunde et al., “Evaluation of a grid-independent solar photovoltaic system for primary health centres (PHCs) in developing countries”, *Renew. Ener. Focus*, 24 (2018) 16-27.

[15] M. Libra et al., “Changes in the Efficiency of Photovoltaic Energy Conversion in Temperature Range With Extreme Limits”, *IEEE J. Photovolt.*, 11(6) (2021) 1479-1484.

[16] K.V. Vidyanandan, “An Overview of Factors Affecting the Performance of Solar PV Systems”, *Energy Scan*, 27 (2017) 2-8.

[17] A. Gautier et al., “Self-consumption choice of residential PV owners under net-metering”, *Energy Policy*, 128 (2019) 648-653.

[18] A. Kendel, N. Lazaric and K. Maréchal, “What do people ‘learn by looking’ at direct feedback on their energy consumption? Results of a field study in Southern France”, *Energy Policy*, 108 (2017) 593-605.

[19] H. Rezk, M.A. Abdelkareem and C. Ghenai, “Performance evaluation and optimal design of stand-alone solar PV-battery system for irrigation in isolated regions: A case study in Al Minya (Egypt)”, *Sustain. Ener. Technol. Assess.*, 36 (2019) 100556.

[20] R. Górnowicz and R. Castro, “Optimal design and economic analysis of a PV system operating under Net Metering or Feed-In-Tariff support mechanisms: A case study in Poland”, *Sustain. Ener. Technol. Assess.*, 42 (2020) 100863.

[21] K. Tanaka, C. Wilson and S. Managi, “Impact of feed-in tariffs on electricity consumption”, *Env. Econom. Policy Stud.*, 24 (2022) 49-72.

[22] W. Shen et al., "A comprehensive review of variable renewable energy levelized cost of electricity”, *Renew. Sustain. Ener. Rev.*, 133 (2020) 110301.

[23] J. Aldersey-Williams and T. Rubert, “Levelised cost of energy – A theoretical justification and critical assessment”, *Energy Policy*, 124 (2019) 169-179.

[24] H.M. Ridha et al., “Multi-objective optimization and multi-criteria decision-making methods for optimal design of standalone photovoltaic system: A comprehensive review”, *Renew. Sustain. Ener. Rev.*, 135 (2021) 110202.

[25] B. Boeckl and T. Kienberger, “Sizing of PV storage systems for different household types”, *J. Energy Storage*, 24 (2019) 100763.

[26] C. Li, D. Zhou and Y. Zheng, “Techno-economic comparative study of grid-connected PV power systems in five climate zones, China”, *Energy*, 165(Pt. B) (2018) 1352-1369.

[27] A.G. Olabi et al., “Critical review of energy storage systems”, *Energy*, 214 (2021) 118987.

[28] E.B. Agyekum, “Techno-economic comparative analysis of solar photovoltaic power systems with and without storage systems in three different climatic regions, Ghana”, *Sustain. Ener. Technol. Assess.*, 43 (2021) 100906.

[29] K.B. Adam and H. Miyauchi, “Optimal Planning of Solar PV Using Simple Model for New Feed-in Tariff in Indonesia”, *Int. Sem. on Intel. Technol. and Its Appl. (ISITIA)*, Surabaya, Indonesia (2019) pp. 171-176.

[30] A. Can Duman and Ö. Güler, “Economic analysis of grid-connected residential rooftop PV systems in Turkey”, *Renew. Energy*, 148 (2020) 697-711.

[31] W.U. Rehman et al., “The Penetration of Renewable and Sustainable Energy in Asia: A State-of-the-Art Review on Net-Metering”, *IEEE Access*, 8 (2020) 170364-170388.

IRAQI JOURNAL OF APPLIED PHYSICS
Vol. 19, No. 4B, November 2023, pp. 93-102

Adsorption, Kinetics, Thermodynamics, and Isothermal Studies of Phenol Red Dye Adsorption Using Activated Charcoal Prepared from Iraqi Local Dates

Luma A. Jassim
Layla A. Jabor

Department of Chemistry,
College of Science,
Tikrit University,
Tikrit, IRAQ

Current study presents the preparation of activated charcoal from Khestawi dates and dye (phenol red 50 mg/L). The effects of some factors on the adsorption process, such as the amount of adsorbent, the optimum concentration, the ideal weight, optimum time to reach equilibrium, optimum pH value, optimum particle size of the adsorbent material, and the highest value of adsorption, were studied at temperature of 25°C. Optimum values of these factors were determined to be 0.013 g/L, 50 ppm, 40-35 minutes, pH=3; 7; 11, 750 μm, respectively. These values mean that the system's behavior is endothermic. In addition, the Langmuir equation, the Temkin equation, the second-order equation, the second Freundlich equation, the isotherm, and thermodynamics were considered to investigate the adsorption kinetics.

Keywords: Thermodynamics; Nanoparticles; Activated carbon; Phenol red
Received: 09 June 2023; **Revised:** 23 August 2023; **Accepted:** 30 August 2023

1. Introduction

The interior surface area and pore volume of activated carbon are enormous for a mostly amorphous material [1]. Its adsorptive capabilities, which are used in several liquids- and gas-phase applications, are caused by these distinctive qualities [2]. The adsorptive qualities of goods are adjusted for applications as varied as the filtration of drinkable water and the regulation of gasoline emissions from motor vehicles via the selection of precursor, the technique of activation, and the management of processing conditions [3]. The consensus is that activated carbon has a low affinity for water, which is a crucial characteristic for the adsorption of gases in the presence of moisture. Products made of commercial activated carbon are made from carbon-rich organic sources, mainly coal, lignite, wood, nut shells, peat, pitches, and cokes [4]. Thermal and chemical activation are the two types of manufacturing processes. Activated carbons are made and categorized as granular, powdered, or shaped materials to fulfil the technical specifications of certain applications. Activated carbon is a substance that may be recycled and renewed [5]. Thus, industrial regeneration capacity impacts the economics of activated carbon, particularly market expansion. Environmental and financial restrictions on landfill disposal are increasing. Therefore, regeneration is a desirable choice for big users of carbon powder [6]. Activated carbon is a bother and a moderate irritant regarding inhalation, skin contact, eye exposure, and ingestion [7]. Conversely, hazardous substances could be concentrated in wasted carbon [8]. Activated carbon is used in liquid phases for manufacturing food, drinks, cooking oil, medicines, and sweeteners, as well as potable water treatment, groundwater remediation, industrial and municipal wastewater treatment, sweetener decolorization, and chemical processing [9]. Catalysis, separation, and gas storage are uses for activated carbon in the gas phase [10]. Granular or shaped activated carbon is most commonly employed in gas-phase applications. Other applications include industrial off-gas management, solvent recovery, and catalysis [11]. Dyes are often utilized, and dyestuff pollution is one of the biggest environmental issues. The first pollutant found in wastewater is color [12]. The dyes are visible and unwanted in water at low concentrations [13] and may be hazardous to aquatic life [14]. As a result, dyes in waterways must be removed. But since dyes are refractory organic molecules, resistant to aerobic digestion, and stable to light, heat, and oxidizing agents, it is exceedingly challenging to treat wastewaters containing dyes [15]. One of its primary industrial applications is utilizing activated carbon in metal finishing to purify electroplating solutions. For instance, the direct purification technique removes organic impurities from solutions for brilliant nickel plating [16]. Various organic compounds are added to improve qualities like brightness, smoothness, flexibility, etc. and the deposit properties of plating solutions [17]. Because of the direct current flow and the electrolytic processes of anodic oxidation and cathodic reduction, organic additions cause undesired breakdown products to form in the solution [18]. The deposited metal's plating quality and physical features may suffer from its excessive buildup [19]. By treating with activated carbon, these impurities are removed, and the plating performance is restored to the necessary level [20]. Activated carbon is used to treat overdoses and poisonings when taken orally. To treat diarrhea, indigestion, and gas, activated carbon pills or capsules are used in several countries [21]. However, activated charcoal has little effect on intestinal gas or diarrhea [22]. Medical treatment is sometimes futile if poisoning is caused by ingesting caustic chemicals, boric acid, or petroleum compounds. It is vulnerable to poisoning from solid acids and bases that include cyanide, iron, lithium, arsenic, methanol, ethanol, and ethylene glycol [23]. Activated carbon is listed as one of the essential drugs by the WHO [24].

The aim of the study is to remove pollutants by using materials that are not harmful to the environment, where activated carbon prepared from plant sources is considered harmless to the environment, and this is considered within green chemistry.

2. Experimental Part

The chemicals and raw materials used in this work include phenol red, hydrochloric acid (HCl), sodium chloride (NaCl), sodium carbonate (Na_2CO_3), sodium hydroxide (NaOH), adsorbent surface (activated charcoal), and adsorbent surface (phenol red) supplied by Fluka and BDH companies.

The prepared samples were characterized and investigated using a Shimadzu 800 UV-visible spectrophotometer, a HACH T875/0752 pH meter, Shimadzu 6000 x-ray diffractometer (XRD), and ZEISS Sigma 300 scanning electron microscope (SEM).

A dye (phenol red) was prepared at a concentration of 80 mg/L by dissolving 0.08 g in 1000 mL of distilled water, and a series of dilute solutions were prepared [25,26].

The activated charcoal was prepared according to the route described by [27,28]. A solution of 20 g $ZnCl_2$ in 100 mL distilled water was prepared, then a 50 g of date stones (Khestawi dates from the Hawija region) was soaked for three days at a temperature of 80-90 °C with a boiling stone added to distribute the heat. After soaking, the material is burned at a temperature of 550 °C for three hours. After burning, the material was washed with 1 M HCl acid. The material is soaked in 10 M HCl acid solution for 24 hours, then filtered and washed until the pH value becomes 7. It is dried in the oven for 4 hours at a temperature of 100 °C, then the material is ground until it becomes a powder.

3. Results and Discussion

The XRD pattern of activated charcoal nanoparticles was recorded and the particle size, according to the Scherrer's formula [29], was calculated to be 1.05 nm, as shown in table (1) and Fig. (1).

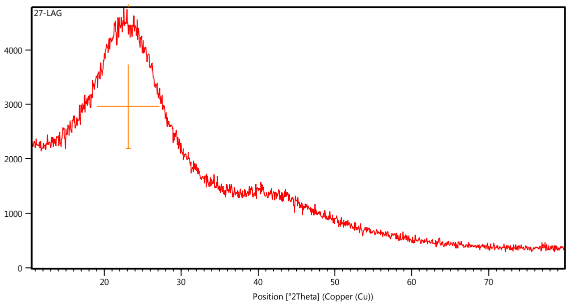

Fig. (1) XRD pattern of activated charcoal nanoparticles prepared in this work

Table (1) XRD parameters of activated charcoal prepared from date stones

Position (deg)	Height (cps)	FWHM Left (deg)	d-spacing (Å)	Rel. Int. (%)	Tip Width
23.10(1)	1540(12)	8.06(5)	3.84697	100.00	9.6683

As confirmed by the FE-SEM measurements, the best sample prepared in this work contain nano-channels and nano-slits and is characterized by periodic nanostructures and sizes, as shown in Fig. (2), which provides a very high surface area. In addition, the material has micro-spacing between particles, so we can predict that the adsorption on the surface will be very effective [30].

A 1 g of activated charcoal was weighed before and after exposure to humidity for 24 hours. The weight after exposure was 1.3 g. Then the humidity percentage of the prepared charcoal was determined to be 0.%, which is very low.

The density of activated charcoal prepared from date stones was measured by the ratio between mass and volume, as the results showed that the prepared charcoal had a high density of 0.74 g/cm^3. This high density indicates that the prepared charcoal has very high efficiency and adsorption capacity compared to other prepared types in previous studies [31].

The acidity function of the prepared charcoal from date stones was measured for the solution using the pH meter and the value of pH was 6.5. This indicates that the prepared charcoal is neutral and it is one of the good characteristics of the readily activated charcoal.

After burning 1.0 g of the powder at a temperature of 1000 °C, the produced ash was weighed to be 8 mg. The percentage of ash content was calculated to be 0.8%, which is within the permitted rates of the international and commercial activated charcoal specifications [32].

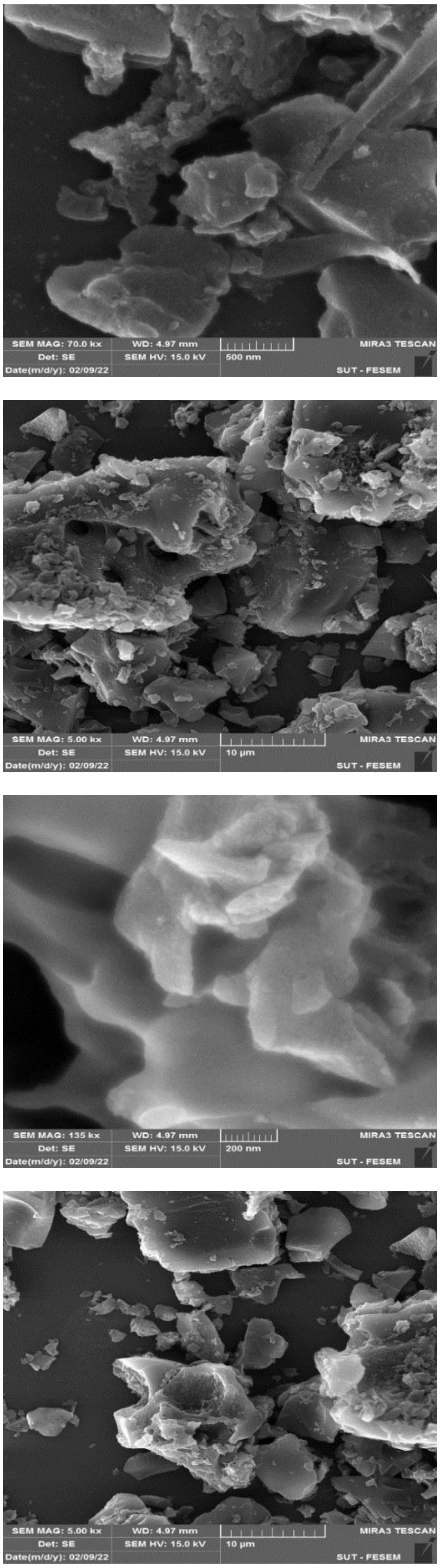

Fig. (2) FE-SEM images of activated charcoal nanoparticles prepared in this work

The effect of the adsorbent weight on the adsorption process was studied as the adsorption reaches a state of equilibrium. Therefore, experiments were conducted on the surface of activated charcoal prepared in this study for the phenol red dye of the mentioned materials in experimental conditions at 50.80 ppm concentration of the dye phenol red, pH value of 7 (neutral pH) at temperature of 25 °C, where five different weights of the prepared activated charcoal were taken (0.004, 0.007, 0.01, 0.013, and 0.02g). The results shown in table (٢) show that increasing the weight of activated charcoal (adsorbent) leads to an increase in the speed of the adsorption process and thus to reach equilibrium during shorter time due to the rise in the surface area of adsorption. This leads to a significant decrease in the absorbance and the reason for this decrease is the low concentrations after the occurrence of the adsorption process. So, it was found that the optimum weight of the adsorbent material, which is suitable to accomplish this study, is 0.013 g. After reaching the state of equilibrium, there is an increase in the absorbance, and the adsorption rate decreases due to the occurrence of adsorption and the saturation of all active sites (pores) of the prepared activated charcoal [33].

Table (٢) Effect of adsorbent weight on adsorption of Ph.R dye from aqueous solutions

% Adsorption	q_e (mg/g)	Dose (mg/L)	C_e (mg/L)
77.0	68.50	0.010	11.50
82.1	44.05	0.013	15.95
91.0	31.75	0.020	28.25
93.5	26.40	0.025	13.60
95.0	21.30	0.040	29.80
96.7	13.75	0.070	16.25

The effect of the prepared activated charcoal volume was studied to find the appropriate measure for the granules suitable for the readily activated charcoal. Five different volumes were used for the prepared charcoal (1500, 250, 500, 750, and 1000 ppm), where the experimental conditions are 80.50 ppm concentration of red phenol propanol, and pH value of 7 at temperature of 25 °C. The results shown in table (٣) show that the optimum volume of the granules of the adsorbent (prepared activated charcoal) is 750 μm. After reaching the state of equilibrium, there is an increase in the absorbance, and the adsorption rate decreases due to the occurrence of the adsorption process and the saturation of all the active sites (pores) in the prepared activated charcoal.

Table (٣) Effect of particle size of activated charcoal on phenol red dye (Ph.R)

Volume (ppm)	250	500	750	1000	1500
Absorbance	0.372	0.268	0.261	0.257	0.249

It was noted that the prepared activated charcoal had high adsorption efficiency for the materials under study, and to know the effect of changing the concentration, the adsorption process was performed on a group of different concentrations of the materials used. This study examined the concentrations of 80, 70, 60, 50, 40, 30, 20, and 10 ppm, and the optimum value was 50 ppm for the red phenol dye.

The adsorption efficiency of compounds is affected by the nature of the medium in which they adsorb. The pollutants used in the research were studied in different acidic media. In this research, the adsorption efficiency of the contaminants was analyzed using the same conditions (25°C temperature, 50 ppm concentration of phenol red dye, and 0.01 g of adsorbent). The study was carried out within the range of pH 3-11. It was found that the adsorption efficiency percentage of the prepared activated charcoal increased in the acidic medium and then gradually decreased in the neutral medium and then the basic medium. The reason for the initial increase in the acidic medium is the increase in the number of positive ions, thus the electrostatic attraction with the activated charcoal surface increases, then gradually decreases in the basic medium. The decrease is due to the molecular interferences in the adsorption medium for these pollutants, thus weakening the adsorption efficiency [34]. It is noted from table (4) that the percentage adsorption efficiency of the materials studied here follows the following order: pH=3 → pH=7 → pH=11, respectively.

Table (٤) Effect of pH value on the adsorption efficiency using activated charcoal prepared on phenol red dye (Ph. R)

pH	3	5	7	9	11
Absorbance	89.7	92.2	80.5	69.9	71.1

The changes of concentration with time until reaching the equilibrium state was observed. The adsorption process for all studied materials reaches equilibrium within a period of 40-35 min. This study was conducted at the most excellent wavelength and the natural pH value. When comparing the values of the concentration of materials before and after adding activated charcoal, a significant decrease was noted in the concentration values within the first 10 minutes. It was noted that the adsorption efficiency is very high due to the great affinity between these materials and the prepared adsorbent surface. This decrease in the concentration values for each material after adding the readily activated charcoal within the first 10 minutes is consistent with the kinetic adsorption theory, as the adsorption is very fast at its beginning. A gradual slowdown in adsorption occurs due to the saturation of the active sites on the surface of the prepared activated charcoal, and this slowdown continues until the adsorption reaches equilibrium. After that, the contact time can affect the amount of adsorbent, and after the state of balance, concentration increases. The adsorption rate decreases due to the adsorption and saturation of all active sites (pores) of the prepared activated charcoal. Figure (3) and table (٥) show these results.

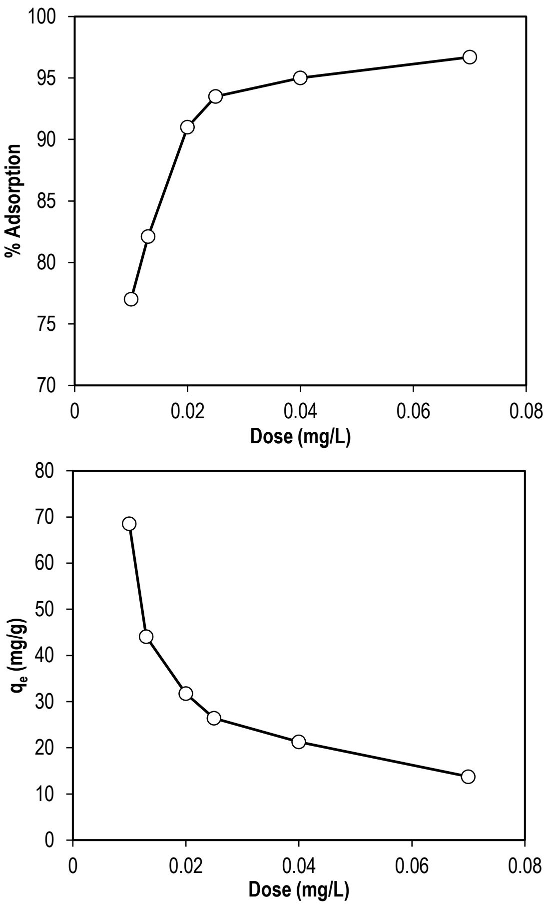

Fig. (٣) The change in the percentage adsorption and the percentage against the amount of charcoal used in the adsorption process of the dye phenol red

Table (٥) The change in percentage adsorption efficiency of the dye with time

Time (min)	C_t (mg/L)	q_e (mg/g)	Adsorption (%)
5	24.95	207.24	80.30
10	21.15	234.00	82.78
15	19.08	267.80	89.30
20	16.99	289.00	90.41
25	15.04	307.90	92.40
30	14.87	322.80	93.12
45	14.23	345.50	93.43
60	13.89	355.00	94.10
90	13.74	367.80	94.56
120	13.66	372.30	94.78
150	13.66	372.30	94.78
180	13.54	373.60	94.88

A study of the effect of temperature on the adsorption of the pollutants above from their aqueous solutions was conducted on the surface of activated charcoal prepared at different temperatures (٢٠-٣٥°C) with an increase of 5°C for each time at the neutral acidity function of each dye pollutant with the proof of other conditions of concentration and amount of adsorbent. The results shown in table (5) show that the adsorption efficiency of all used solutions decreases gradually with increasing temperature due to the fact that the rise in temperature leads to an increase in the tendency of molecules to leave the adsorbent surface to the adsorption solution because the bonding forces between them are broken. This process is called desorption. As well, increasing the temperature works to improve the swelling of the surface, and the percentage adsorption decreases with increasing the temperature due to this swelling and the occurrence of the desorption process. It was found that the amount of adsorption at a temperature of 25°C is the highest, and this means that the behavior of the system was absorbent endothermic. After the formation of the dimer, there is a decrease in the adsorption with increasing temperature. This means that the adsorbed molecules before the construction of the dimer have a more remarkable ability to penetrate into the pores of the prepared activated charcoal, and after the formation of the dimer, as a result of the increase in the size of the molecule, there is a decrease in the adsorption (penetration within the surface), and thus a reduction in the adsorption occurs.

In general, when comparing the results in table (٦), it can be seen that the change in the percentage of adsorption efficiency in the mentioned thermal range is limited and irregular, and that the adsorption process on the surface of activated charcoal is the endothermic type, as the positive (ΔH) indicates the possibility of absorbance, as the adsorbed molecules spread inside the pores and the speed of their diffusion increases with the increase in temperature. It is likely that the absorbance will be accompanied by an adsorption process. As the conditions were proven, this study proved that the adsorption process is consistent with what has been reached in other studies.

Table (٦) Effect of temperature on the adsorption percentage of the Ph.R dye

Temperature (°C)	C_e (mg/L)	q_e (mg/g)	% Adsorption
٢٠	29.88	220.60	91.6
٢٥	29.48	242.80	94.5
٣٠	21.38	255.15	85.9
٣٥	14.04	275.75	82.7

The fundamental thermodynamic functions for the adsorption of dyes on the surface of the prepared activated charcoal are estimated by calculating the values of K_e (the thermodynamic equilibrium constant of the adsorption process) at different temperatures through the importance of q_e (the maximum amount of adsorption) and C_e (the maximum equilibrium concentration) at the neutral acidity of each dye using the same conditions and the amount of activated charcoal prepared from date stones. From the graph of lnK against the reciprocal of temperature, we get a straight line as shown in Fig. (٤) and table (٧).

From the slope of this straight line, we can calculate the change in enthalpy (ΔH), and the values of adsorption heat (H) are calculated as we get a straight line [35]. From the slope of this line, we can extract the value of the heat of adsorption based on the Vant Hoff equation and other equations to calculate the values of thermodynamic functions as follows:

$$\text{Log } K_{eq} = (-\Delta H / 2.303\, RT) + C \qquad (1)$$

$$-\Delta H = \text{Slope} \times R \qquad (2)$$

$$K_{eq} = q_e / C_e \qquad (3)$$

$$q_e = (C_0 - C_e).V_{sol} / M \qquad (4)$$

We notice from the values in the table below that there is a fluctuation in the thermodynamic equilibrium constant for the adsorption process at low temperatures, followed by an increase up to the temperature of 308 K in case of using prepared activated charcoal.

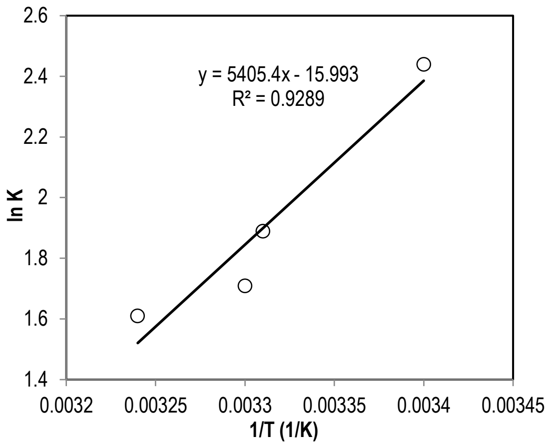

Fig. (٤) Vant Hoff curve for adsorption of phenol red dye on the surface of activated charcoal prepared at a concentration of 50 ppm

Table (٧) Effect of temperature on the thermodynamic equilibrium constant in the adsorption of phenol red dye on the surface of the prepared activated charcoal

T(K)	1/T (K^{-1})	Ce (mg/L)	qe (mg/g)	K	ln K	
٢٩٣,٠٠	0.00340	29.88	220.60	8.38	2.44	
٢٩٨,٠٠	0.00331	29.48	242.80	8.82	2.17	
٣٠٣,٠٠	0.00330	21.38	255.15	5.57	1.71	
٣٠٨,٠٠	0.00324	14.04	275.75	5.03	1.61	

The values of the change in ΔG° and ΔS° were calculated based on the pressure relationship of the equilibrium as shown in table (٨).

Table (٨) The values of the thermodynamic functions for the adsorption of phenol red dye on the surface of activated charcoal prepared at different temperatures

T (K)	ΔG° (J.mole^{-1})	ΔH° (J.mole^{-1})	ΔS° (J.mole^{-1}.K^{-1})
293	-0.15	-44940.49	-153.38
٢٩٨	-2.09		-150.80
٣٠٣	-2.56		-148.31
٣٠٨	-0.21		-145.91

According to the values given in previous tables, it is noticed that the value of the heat of adsorption (ΔH°) for the ions under study on the surface of the prepared activated charcoal, is measured at the concentration of 80.50 ppm and other previously mentioned conditions. The value of ΔH° is negative in the adsorption of the red phenol dye, and this indicates that the adsorption process is endothermic. This suggests the possibility of an adsorption process that may accompany the adsorption process. This process is called sorption, meaning that adsorption and adsorption occur together, where the adsorbed molecules diffuse within the pores of the solid phase [36]. The speed of their diffusion increases with the increasing temperature. It is known that the dependency of the adsorption heat measurement at the most significant concentration includes the bonding energies of the particles adsorbed on the various effective sites on the surface with all possibilities. In addition to being negative (ΔH) is that during the initial adsorption stage and the growth stage of adsorption, the percentage of the adsorbent material penetrating the surface pores of the prepared activated charcoal is high, which causes the endothermic nature of the adsorption process. The previous tables also show that the values of change in free energy (ΔG) are negative, and this indicates that the adsorption process is an automatic process within the experimental conditions and decreases with an increase in temperature. This is consistent with most of the results that were reached in the fact that the reaction is endothermic. The change in entropy (ΔS) is negative at the concentration of 80 ppm due to the possibility of forming van der Waals forces [37]. Also, ΔS is negative for the adsorption of the red phenol dye on the surface of the prepared coal due to the adsorbed and interfering particles that are less regular when the double process occurs. For adsorption and absorbance together in the solution, in addition to the fact that the particles are still in a state of continuous movement, this explains that ΔS is negative.

There are many models of adsorption isotherms that help to explain the obtained results. In this study, we will address three types of these models:

The Freundlich isotherm differs in its interpretation of the obtained results, as it gives the Freundlich constants (k_f), which are related to the adsorption capacity, and *n* reflects the intensity of adsorption and its preference when its value is confined within 1-10 and is not preferred when it is less than one. The Freundlich constants were obtained from the slope and intersection of linear relations, and the results were included in table (8). The Freundlich isotherm equation was applied to the adsorption of the materials under study on the surface of activated charcoal prepared at different concentrations (6, 12, 18, 24, 30, 36, 42, 46, and 50 ppm) for the phenol red dye, as shown in table (٩) and Fig. (5).

From the preceding results mentioned in table (١٠), it can be concluded that there is a decrease in the value of k_f for dyes in varying proportions, and this means that the adsorption process is endothermic [38]. We also notice a fluctuation in the value of *n* at different concentrations, and this is due to the adsorption efficiency on the solid surface. When the value of *n* is confined between 1 and 10, this indicates that the adsorption efficiency is good, so we note that all materials have a value of n in this range. This indicates that all the materials under study have good adsorption efficiency, and the application of this isotherm to all studied materials showed good linear relationships, which are indicated by the values of the correlation coefficient, as shown in Fig. (5). This suggests that the prepared activated charcoal is in good agreement with the Freundlich model.

Table (٩) Values of ln(C_e) and ln(q_e) for the adsorption of the phenol red dye on the surface of activated charcoal at different concentrations according to the Freundlich equation

Concentration (ppm)	lnC_e (mg/L)	lnq_e (mg/g)
6	1.37	5.43
12	2.17	5.32
18	2.63	5.19
24	3.06	4.96
30	3.31	4.71
36	3.41	4.59
42	3.64	4.08
46	3.82	5.54
50	3.89	1.64

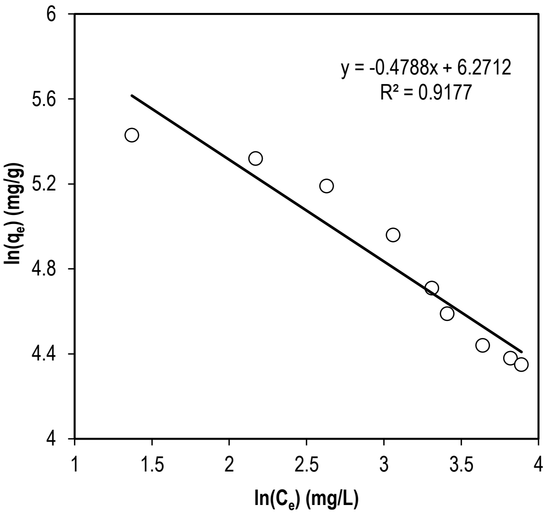

Fig. (5) The Freundlich isotherm for adsorption of phenol red dye on the surface of the prepared activated charcoal

Table (١٠) Empirical Freundlich constants and root values of the correlation coefficient for the adsorption of the dye under study at different concentrations

Dyes	k_f (L/mg)	n	R
Ph.R	-0.4788	6.2712	0.91

The Langmuir isotherm model was applied for the adsorption of the materials under study on the surface of activated charcoal prepared at different concentrations (6, 12, 18, 24, 30, 36, 42, 46, and 50ppm) for the red phenol dye as in the results shown in table (١١) and the Fig. (6).

Throughout the results above, including table (١٢), we notice that the values of the maximum amount of adsorbent material is calculated according to the Langmuir model on the surface of the prepared activated charcoal and is fluctuated at different concentrations [39]. As for the values of the root correlation coefficient R2 of the Langmuir isotherm model for the materials under study, we note that they could be better, indicating that this equation is not suitable for the adsorption results of materials on the surface of the prepared coal [40]. It turns out that there is no specific pattern or relationship with particular features that describe a change in the values of ***b*** on the one hand and the percentage values on the other hand and that the adsorption capacity ***q*** in all materials under study is different due to the existence of obstacles to adsorption such as steric obstruction, molecular interferences, or dimer formation and its effect on the adsorption process.

Table (١١) Values of C_e and C_e/q_e for adsorption of phenol red on the surface of activated charcoal at different concentrations according to the Langmuir equation

Concentration (ppm)	C_e (mg/L)	C_e/q_e (g/L)
6	3.966	0.017
12	8.844	0.042
18	13.896	0.076
24	21.384	0.149
30	27.570	0.245
36	30.276	0.306
42	38.136	0.642
46	45.770	0.786
50	47..650	0.877

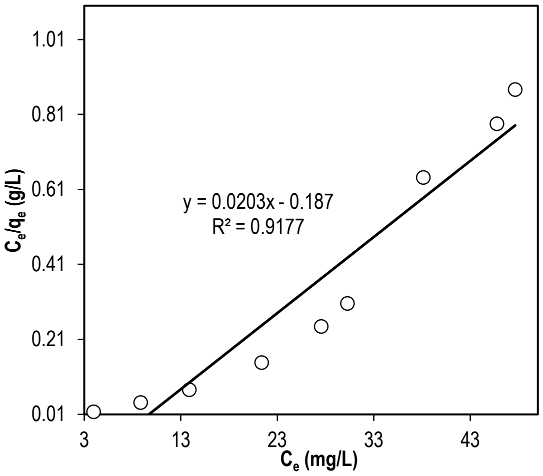

Fig. (6) Langmuir isotherm for adsorption of phenol red dye on the surface of the prepared activated charcoal

Table (١٢) Experimental Langmuir constants and root values of the correlation coefficient for adsorption of the materials under study at different concentrations

Dye	B	K_L	R
Ph.R	0.187	0.187	0.917

The Temkin isotherm model was applied for the adsorption of the materials under study on the surface of activated charcoal prepared at different concentrations (6, 12, 18, 24, 30, 36, 42, 46, and 50 ppm) for the red phenol dye as in the results shown in table (١٣) and Fig. (7).

Table (١٣) ln(C_e) and q_e values for the adsorption of the materials on the surface of activated charcoal at different concentrations according to the Langmeyer equation

Concentration (ppm)	q_e (mg/g)	Ln(C_e) (mg/L)
6	230.17	1.37
12	205.78	2.17
18	180.52	2.63
24	143.08	3.06
30	112.15	3.31
36	98.62	3.41
42	59.32	3.64
46	25.15	3.82
50	5.175	3.89

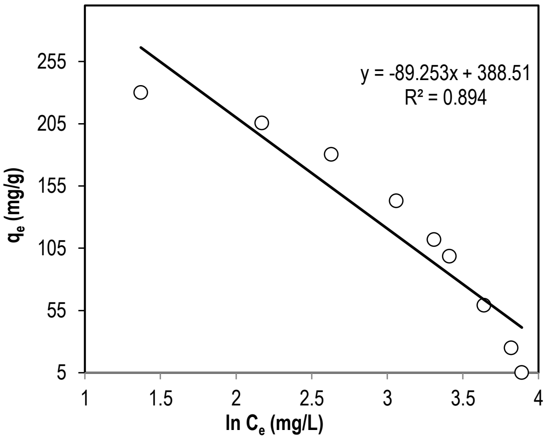

Fig. (٧) Isotherm for adsorption of phenol red dye on the surface of the prepared activated charcoal

According to the results above, including table (١٤), we notice that the values of the maximum amount of the adsorbent material calculated according to the Temkin model on the surface of the prepared activated charcoal is fluctuated at different concentrations [39]. As for the values of the root correlation coefficient R^2 of the Temkin isotherm model for the materials under study, we note that they are few, which indicates that they are not. The suitability of this equation for the results of material adsorption on the surface of the prepared coal. There is no specific pattern or relationship with apparent features describing a change in ***b_T*** values on the one hand and percentage values on the other hand [39].

Table (١٤) Experimental Langmuir constants and root values of the correlation coefficient for adsorption of the materials under study at different concentrations

Dye	K_T	bT (L/mg)	R
Ph.R	-89.253	388.51	0.89

The adsorption kinetics of the dyes on the surface of activated charcoal was studied based on the effect of time on the adsorption capacity. The kinetics of the studied system goes through several stages to reach the state of equilibrium, whereby running balance and time does not affect concentration.

The first-order reaction equation was applied to the dye adsorption process data by drawing the relationship between ln(q_e-q_t) against time t. The obtained graphics are included in Fig. (8). From the slope of the straight line of the drawing, the reaction rate constant k was obtained for the false first order, and from the straight-line section, the theoretical value of the adsorption capacity was found, as the results listed in the table (١٥) were obtained.

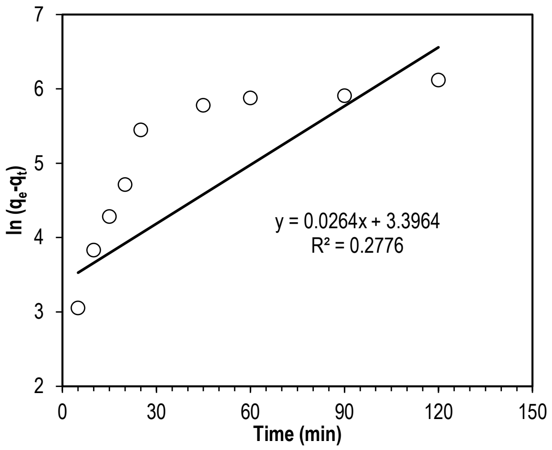

Fig. (8) The first order equation and its application to dye adsorption in the presence of combed charcoal

Table (١٥) The results of the kinetic study when applying the false first-order equation for the dye at temperature of 298 K absolute using activated charcoal as an adsorbent

Dye	$q_{e\,(exp)}$ (mg/g)	k_1 (min^{-1})	$q_{e\,(calc)}$ (mg/g)	R^2
Ph.R	٣,٣٩	0.026	2.47	0.277

By observing the results from table (14), we find a significant difference between the practical adsorption capacity values of the dyes and the theoretical values obtained by drawing the false first-order relationship, which indicates that this equation does not apply to the adsorption system. The other evidence is that the values of the correlation coefficient R^2 are not close to one, which indicates that the linear relations are weak for straight lines, leading to the application of the second-order equation on the systems under study.

The false second-order equation was applied by drawing t/qt against t, where the graphs were obtained in Fig. (٩). Results obtained from applying this motor model are listed in table (16).

Table (16) The kinetic study when applying the pseudo second-order equation for the dye at temperature of 298 °C using activated charcoal as an adsorbent surface

Dye	$q_{e\,(exp)}$ (mg/g)	k_2 (min^{-1})	$q_{e\,(calc)}$ (mg/g)	R^2
Ph.R	0.308	0.0255		0.903

According to the values observed in the table, the value of the correlation coefficient R^2 is very close to one. Also, the value of the theoretical adsorption capacity obtained from the drawing is identical to the value of the practical adsorption capacity [40], and this means that the false second-order equation applies to the dye adsorption process by the surface of activated charcoal, and this means that the effect is not only the concentration of the adsorbent (dye) but also the concentration of the adsorbent affects the rate of adsorption.

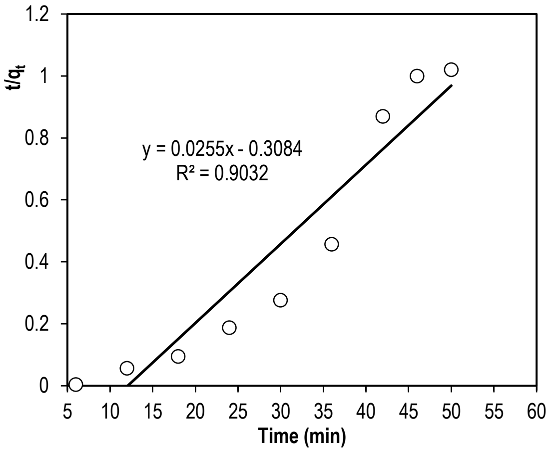

Fig. (9) The pseudo-second-order equation and its application to the adsorption of phenol red dye in the presence of activated charcoal

4. Conclusions

Activated charcoal exhibits notable adsorption capacity. The observed negative value of ΔH° signifies an endothermic nature of the adsorption process. Additionally, negative ΔG and ΔS values suggest a spontaneous adsorption process that diminishes with escalating temperature and reduction in randomness. On the other hand, the Temkin isotherm aligns well with the findings of this study. A substantial discrepancy arises between the practical adsorption capacity values of the dyes and the theoretical values derived from the erroneous first-order relationship. Additionally, the relatively low values of the correlation coefficient R^2 suggest weak linear associations, prompting the utilization of the second-order equation for the studied systems.

References

[1] Z. Heidarinejad et al., “Methods for preparation and activation of activated carbon: a review”, *Env. Chem. Lett.*, 2 (2020) 393-415.

[2] A. Bhatnagar et al., “An overview of the modification methods of activated carbon for its water treatment applications”, *Chem. Eng. J.*, 219 (2013) 499-511.

[3] M.S. Shafeeyan et al., “A review on surface modification of activated carbon for carbon dioxide adsorption”, *J. Anal. Appl. Pyrol.*, 89(2) (2010) 143-151.

[4] M. Suzuki, “Activated carbon fiber: fundamentals and applications”, *Carbon*, 32(4) (1994) 577-586.

[5] M.J.B. Evans, E. Halliop and J.A.F. MacDonald, “The production of chemically-activated carbon”, *Carbon*, 37(2) (1999) 269-274.

[6] B. Guo, L. Chang and K. Xie, “Adsorption of carbon dioxide on activated carbon”, *J. Nat. Gas Chem.*, 15(3) (2006) 223-229.

[7] J. Gamby et al., “Studies and characterisations of various activated carbons used for carbon/carbon supercapacitors”, *J. Power Sour.*, 101(1) (2001) 109-116.

[8] O. Ioannidou and A. Zabaniotou, “Agricultural residues as precursors for activated carbon production - A review”, *Renew. Sustain. Ener. Rev.*, 11(9) (2007) 1966-2005.

[9] T. Lee et al., “Activated carbon fiber-the hybrid of carbon fiber and activated carbon”, *Rev. Adv. Mater. Sci.*, 36(2) (2014) 118-136.

[10] G.J. McDougall, “The physical nature and manufacture of activated carbon”, *J. South. African Inst. Mining Metall.*, 91(4) (1991) 109-120.

[11] I.N. Najm et al., “Using powdered activated carbon: a critical review”, *J. Amer. Water Works Assoc.*, 83(1) (1991) 65-76.

[12] H. Marsh and F. Rodriguez-Reinonso, **“Activated Carbon”**, Elsevier Science & Technology Books (Amsterdam, 2006), 89-100.

[13] R.C. Bansal and M. Goyal, **“Activated Carbon Adsorption”,** CRC Press (NY, 2005).

[14] T.J. Bandosz and C.O. Ania, “Surface chemistry of activated carbons and its characterization”, In Interface Science and Technology, Elsevier, Vol. 7 (2006) 159-229.

[15] H. Sontheimer, J.C. Crittenden and R.S. Summers, “Activated Carbon for Water Treatment”, Univ. of Karlsruhe, Germany (1988).

[16] A. Dąbrowski, “Adsorption—from theory to practice”, in “Advances in Colloid and Interface Science”, 93(1-3) (2001) 135-224.

[17] G. Crini, “Non-Conventional Low Cost Adsorbents for Dye Removal: A Review”, *Biores. Technol.*, 97 (2006) 1061-1085.

[18] P. Nigam et al., “Physical removal of textile dyes from effluents and solid-state fermentation of dye-adsorbed agricultural residues”, *Biores. Technol.*, 72(3) (2000) 219-226.

[19] R. Beiras, “Towards standard methods for the classification of aquatic toxicity for biologically active household chemicals (BAHC) present in plastics, pharmaceuticals, and cosmetic products”, *Env. Monitor. Assess.*, 193 (2021) 1-10.

[20] Q. Sun and L. Yang, “The adsorption of basic dyes from aqueous solution on modified peat-resin particle”, *Water Res.*, 37 (2003) 1535-1544.

[21] P.J. Paul, “Value Added Products from Gasification–Activated Carbon”, *Bangalore: The Combustion" Gasification and Propulsion Laboratory (CGPL) at the Indian Institute of Science (IISc)*, (2002).

[22] J. Lehmann and S. Joseph, “Biochar for environmental management: an introduction”, in Biochar for environmental management, Routledge (2002) pp. 1-13.

[23] J. Xia et al., “A review on adsorption mechanism of gold cyanide complex onto activation carbon”, *J. Ind. Eng. Chem.*, 111 (2022) 35-42.

[24] G. Oliveira et al., “Paper pulp-based adsorbents for the removal of pharmaceuticals from wastewater: a novel approach towards diversification”, *Sci. Total Env.*, 631 (2018) 1018-1028.

[25] P. Cataldi et al., “An electrically conductive oleogel paste for edible electronics”, *Adv. Func. Mater.*, 32(23) (2022) 2113417.

[26] World Health Organization, World Health Organization model list of essential medicines: 21st list, No. WHO/MVP/EMP/IAU/2019.06).

[27] K.A. Adegoke et al., “Modification of cellulosic material for rapid dyeability with malachite green dye”, *Sci. African*, (2022) e01138.

[28] M. Rajabi, K. Mahanpoor and O. Moradi, “Preparation of PMMA/GO and PMMA/GO-Fe_3O_4 nanocomposites for malachite green dye adsorption: kinetic and thermodynamic studies”, *Compos. B: Eng.*, 167 (2019) 544-555.

[29] A.S. Vorokh, “Scherrer formula: estimation of error in determining small nanoparticle size”, *Nanosys.: Phys. Chem. Math.*, 9(3) (2018) 364-369.

[30] A.H. Dalaf et al., “Synthesis, Characterization, Biological Evaluation, and Assessment Laser Efficacy for New Derivatives of Tetrazole”, in *Key Eng. Mater.*, Trans Tech Publications Ltd., 911 (2022) 33-39.

[31] S.D. Khalaf, N.A.A.S. Ahmed and A.H. Dalaf, “Synthesis, characterization and biological evaluation (antifungal and antibacterial) of new derivatives of indole, benzotriazole and thioacetyl chloride”, *Mater. Today: Proc.*, 47(17) (2021) 6201-6210.

[32] C. Yanan et al., “Adsorption of paracetamol and ketoprofenon activated charcoal prepared from the residue of the fruit of Butiacapitate: Experiments and theoretical interpretations”, *Chem. Eng. J.*, 454 (2023) 139943.

[33] P.T. Yeung et al., “Preparation and characterization of bio-safe activated charcoal derived from coffee waste residue and its application for removal of lead and copper ions”, *RSC Adv.*, 4(73) (2014) 38839-38847.

[34] J.N. Dann et al., “A New XRD tool for Metallurgical Research: ICDD's Metals & Alloys Indexes”, *Adv. X-Ray Anal.*, 37 (1993) 109-115.

[35] Y.K. Alasadi, F.H. Jumaa and A.H. Dalaf, “Synthesis, identification, antibacterial activity and laser effect of new derivatives of bis-1, 3-oxazepene-4, 7-dione and 1, 3-diazepine-4, 7-

dione", in *AIP Conf. Proc.*, 2394(1) (2022) 040019.

[36] M.D. LeVan, G. Carta and C.M. Yon, "Adsorption and ion exchange", *Energy*, 16 (1997) 17.

[37] E.C. Albuquerque Jr. et al., "Specifications of the Quality of Granulated Activated Charcoal Used in Water Systems Treatment in Hemodialysis Centers in Brazil", Technical Problems in Patients on Hemodialysis, InTech, Dec. 07 (2011) doi: 10.5772/23898.

[38] J.M. Thoma, "The existence of endothermic adsorption", *J. Chem. Edu.*, 38(3) (1961) 138.

[39] M. Negarestani et al., "Facile preparation of sisal–Fe/Zn layered double hydroxide bio-nanocomposites for the efficient removal of rifampin from aqueous solution: kinetic, equilibrium, and thermodynamic studies", *Int. J. Phytorem.*, 25(5) (2023) 586-597.

[40] M.C. Nayak et al., "Preparation and characterization of PPSU membranes with BiOCl nanowafers loaded on activated charcoal for oil in water separation", *J. Taiwan Inst. Chem. Eng.*, 77 (2017) 293-301.

IRAQI JOURNAL OF APPLIED PHYSICS
Vol. 19, No. 4B, November 2023, pp. 103-112

Fouzi Bouanaka
Amira Boudjadar
Saida Rebiai

Laboratoire de Microsystèmes et Instrumentation (LMI),
Faculté des Sciences de la Technologie,
Université Frères Mentouri Constantine 1,
Constantine 25000, ALEGRIA

Effect of Polyimide Layer on Surface Dielectric Barrier Discharge Characteristics Studied for Air Flow Improvement

Experimental measurements and a numerical analysis of a surface dielectric barrier discharge (SDBD) have been investigated in this work. At first, we focused our study on the electrical characterization of the discharge in a plane–parallel SDBD cell generated in air at atmospheric pressure using a sinusoidal voltage of 7kV peak value and a frequency of 6 kHz. The measurements of the electrical plasma parameters such as the voltage across the air, the discharge current and the consumed discharge power in the plasma have been also carried out. The second part of this work consists of exploring the numerical model developed under COMSOL@ software in case of plane-parallel configuration SDBD in air to investigate the effect of adding polyimide layer in the SDBD structure. The calculated current discharge shows several current pulses indicating the presence of micro-discharges in the plasma. The power consumption and the morphology of the plasma filaments are affected by the actuator structure and the presence of the polyimide layer.

Keywords: Plasma actuator; Flow control; Electrohydrodynamic force; SDBD cell
Received: 20 July 2023; **Revised:** 26 August 2023**; Accepted:** 02 September 2023

1. Introduction

Surface dielectric barrier discharge (SDBD) plasma is a non-equilibrium low temperature plasma source. It usually consists of a set of asymmetrically arranged electrodes and a dielectric material. At sufficiently high voltages, the air near the exposed electrodes will be ionized; such a way the formed plasma is visible to the naked eye [1]. Plasma actuators convert electrical energy into mechanical energy making the control of the fluid flow very quick and easy. Their principle of operation is based on the generation of hydrostatic force by a dielectric barrier discharge on the surface, which influences the gas flow rate [1]. This new generation of actuator improves airflow and reduces fuel consumption. The latter has the advantage of real-time control of airflow without moving mechanical parts. A plasma actuator generates an electrical discharge in this zone of fluid flow [2]. A dielectric barrier discharge is obtained by applying a differential potential to a gas between two electrodes in the presence of a dielectric. There are different types of barrier discharge; among them we find [3,4]:

- Volume dielectric barrier discharge which occurs in the volume between two electrodes, separated by a gas layer. In some cases, a dielectric barrier is used to prevent switching to the arc regime.
- Surface discharge which includes corona discharge and surface dielectric barrier discharge.

Dielectric barrier discharge (DBD) is one of the most important techniques for generating uniform low temperature plasmas [5-7]. Due to its ease of use, DBD has been the subject of extensive research [2]. Atmospheric pressure cold plasma (APLTP) is used in many industrial applications, such as, environment, biomedical, sterilization processes [8-15], thin film deposition [16,17], airflow control [18], ozone generation [19], surface treatment [9,20] and plasma display panel (PDP) [21].

The purpose of the present paper is mainly experimental and numerical modeling. In order to establish the effect of using polyimide layers as the dielectric material, visual and electrical characterization of the discharge generated in plane–parallel SDBD cells with air gas (using sinusoidal voltage of 7 kV at frequency of 6 kHz) have been carried out for two different structures. The first structure is made of two plane metallic electrodes deposited by physical vapor deposition on a 1mm thick glass used as a dielectric barrier in the plasma reactor. The grounded electrode is coated with a thin layer of polyimide to prevent the creation of plasma discharge around it. The second structure is similar to the first one, but in this case the dielectric layer is constituted of two extra layers of polyimide separating each electrode from the glass substrate (Fig. 1). Electrical parameters measurements including the voltage across the air, the discharge current and the discharge power consumed in the plasma have been evaluated. In addition, a numerical model for a plane–parallel configuration SDBD, under sinusoidal form of applied voltage has been investigated under the COMSOL$^{@}$ software. The dynamic behavior of the discharge parameters such as electron, positive and negative ions densities, electron temperature, voltage and discharge current have been studied with the proposed numerical model. The voltage–current curves obtained from the simulation have been used to analyze and to find the optimal electrical parameters to create the plasma discharge in an SDBD structure for a given application.

2. Experimental setup details

The most common form of a plasma SDBD actuator consists essentially of two axially electrodes, one exposed to air and the second hidden in a dielectric layer [1]. The studied actuator shown in Fig. (1) consists of 2 cm × 10 cm sized structure containing multilayers. A standard glass substrate serving as a good dielectric material with a thickness of about 1mm and a relative permittivity of 5 and two Aluminum electrodes (6mm wide and 0.05mm thick) deposed by metallization technique. The glass substrate is surrounded by two polyimide layers with a thickness of 0.05 mm (Fig. 1a). For both structures, the upper electrode is placed on the dielectric surface and the grounded one (separated with a gap of 3mm) is encapsulated to avoid the creation of a lower side discharge.

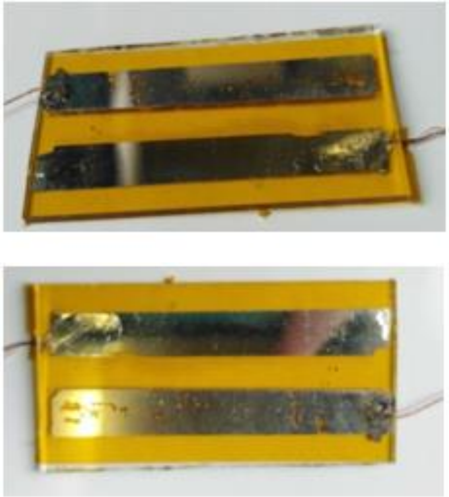

Fig. (1) Structure of the study SDBD: (a) with and (b) Without the polyimide layer

In the experimental setup (shown in Fig. 2), the upper electrode is connected to the high voltage (6 kHz, 14 kV peak-to peak) and the bottom electrode is connected to a single pole double throw (a switch connected to a 47 Ω resistor in parallel with 1μF capacitor).

The discharge current is monitored across the resistor R, in order to measure the dissipated power. The capacitor C is used instead to monitor charges transfer. Both voltages across R and C are recorded simultaneously by a digital oscilloscope. The output voltage and current waveforms and the Lissajous figures are also recorded.

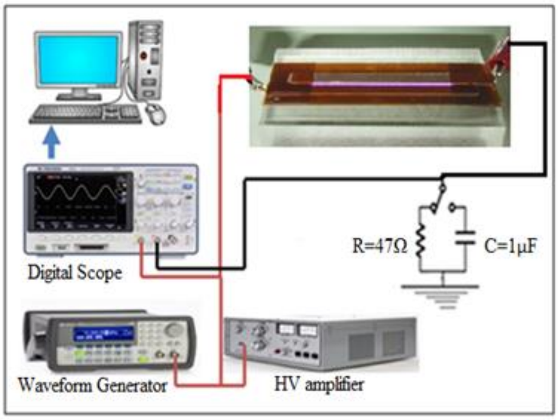

Fig. (2) Schematic diagram of the experimental setup

3. Experimental results and discussions

An image of the ignited SDBD in air is shown in Fig. (3) and the current–voltage characteristics of the discharge for the two studied structures are shown in figures (4a) and (4b).

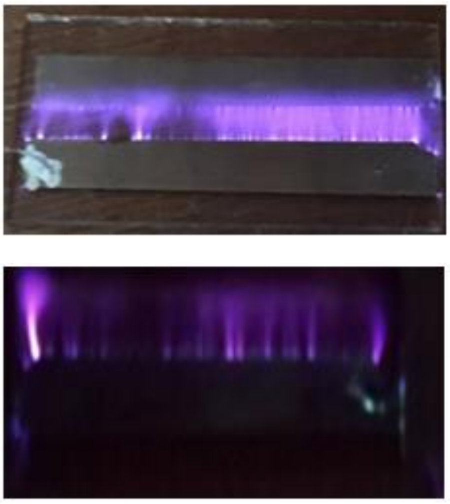

Fig. (3) Photograph of the ignited SDBD plasma: (a) with and (b) Without the polyimide layer

In the ignited plasma image (Fig. 3), a large numbers of distributed filaments, perpendicular to the electrodes, are clearly visible, usually called micro-discharges. The plasma is generated in the micro-discharges channels and the charges are mainly transported in these filamentary channels. As the voltage increases, plasma forms on the surface of the dielectric. This plasma is not maintained continuously during this phase: it actually develops a succession of micro discharges corresponding to rapid current pulses (Fig. 4). Each measured current peak then corresponds to the creation of plasma on the actuator surface [22,23].

During the positive alternation, plasma is ignited when the upper electrode serves as an anode and the electrons deposited on the surface of the dielectric (during the previous negative half-wave) are set in motion towards the upper electrode. Then, they have collisions with the neutral species of the air causing ionization processes. Positive charge species are then created. For example, figure (4a) shows that the discharge current is characterized by two distinct periods, corresponding to the discharges occurred during both cycles in the two cases. The positive-going cycle is characterized by high current pulses up to 1A corresponding to streamer propagation. The negative half-cycle corresponds to a glow regime, characterized by small current pulses up to several tens of 0.75A.

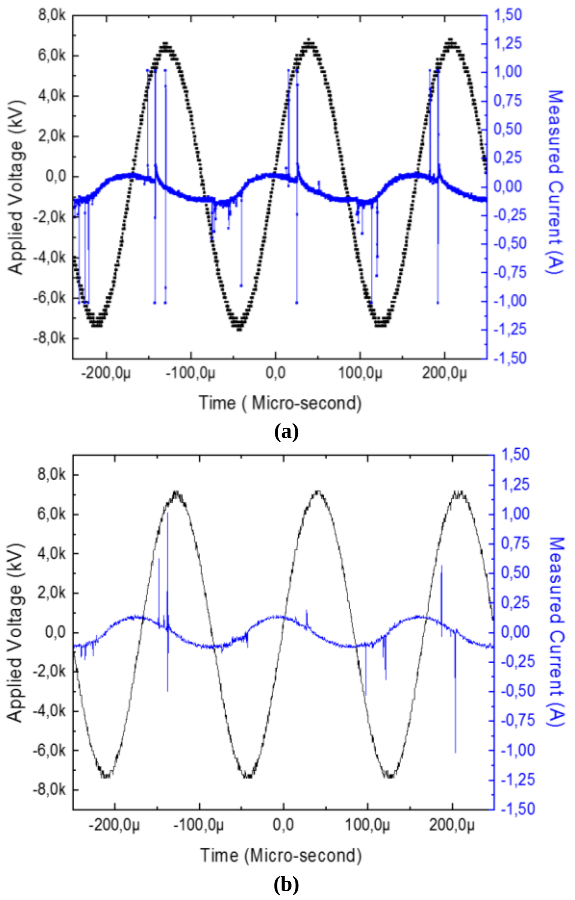

Fig. (4) The SDBD discharge current and applied voltage: (a) With and (b) Without the polyimide layer

Moreover, the comparison of the current waveforms with and without the polyimide layers (Fig. 4) indicates that the amplitude of the discharge current and the density of current picks are smaller in the case of structure without the polyimide layer:

- With the polyimide layer; the electrons located on the dielectric recombine with the positive nitrogen ions and a filamentary regime occurs (Fig. 4a).
- Without the polyimide layer; the observed discharge regime is luminescent (Fig. 4b). Because the accumulated electrons do not recombine, the surface of the dielectric acts as a cathode.

3.1. Power consumption

The consumed electrical power for an applied high voltage is an established way to describe the electrical characteristics of the plasma SDBD. In this work, measured Lissajous figures are used in order to compute the energy dissipated in the SDBD discharge in each voltage cycle [24,25] and to deduce the consumed SDBD actuator power (*Pw*) by its multiplication by the plasma frequency *f*.

Figure (5a and b) show V-Q Lissajous curves of the studied structures. In this study Matlab software has been used for the numerical calculation of the energy and the power dissipated for the two SDBD configurations.

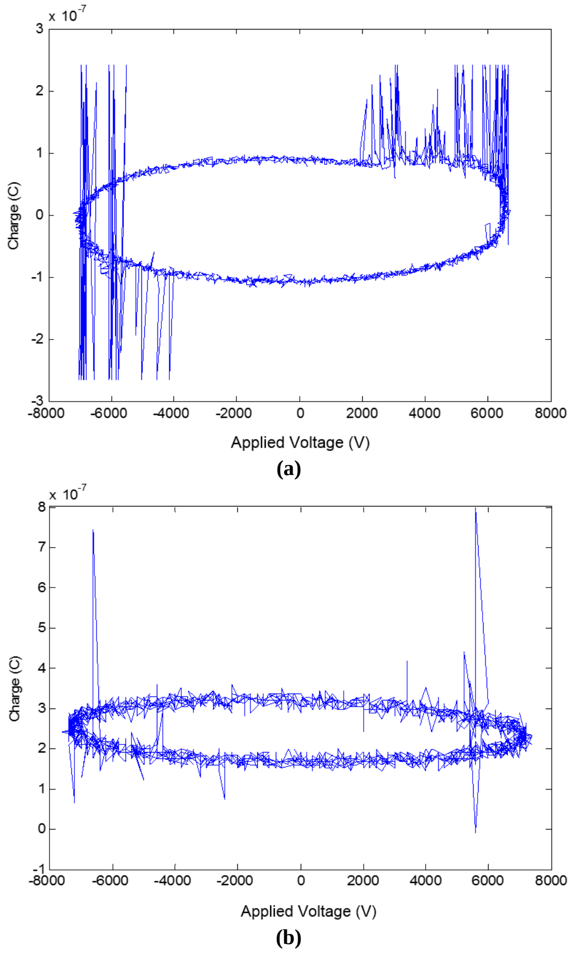

Fig. (5) V-Q Lissajous figures of the two different structures: (a) with and (b) without polyimide layer

The measured values of energies were in the order of 0.0069 and 0.009 J for the structure with polyimide layer and without, respectively and the corresponding dissipated power values were about 41.4 and 54.6 W, respectively. This significant difference in dissipation power values is mostly due to the geometrical difference between the two structures. In fact, the additional layer of polyimide reduces the secondary electron emission which is found to be higher when the electrodes are only separated with one substrate of glass. Because the structure with the polyimide layer offers a better power optimization compared to the other structure, it will be considered in our numerical modeling of the SDBD structure in atmospheric air.

4. Numerical modeling of the SDBD discharge plasma in Air

The presence of charged particles created by collisions in the plasma discharge has been considered in the simulation process of the dielectric barrier discharge. The transport of charged particles present in the plasma discharge and their interactions with the electric field have been described to evaluate the energy distribution functions (EEFD), the densities of charged species, the electric field profile, the electric potential as well as the electronic temperature. When the plasma is weakly ionized, the numerical model consists of resolving the Boltzmann equation. The approach of a self-consistent fluid model [26-29] can be used in case of modeling a continuous medium. In this study, a theoretical model of the discharge plasma in air has been investigated for the SDBD structure with polyimide film. The model is based on the resolution of transport equations deduced from the Boltzmann equation, coupled with Poisson's equation to determine the electric field values [30]. The system of partial differential equations has been solved numerically in a two-dimensional geometry containing an asymmetrical SDBD actuator (Fig. 6), using the finite volume method under COMSOL® Multiphysics software. The discretization process of Scharfetter–Gummel [28,31] has been used.

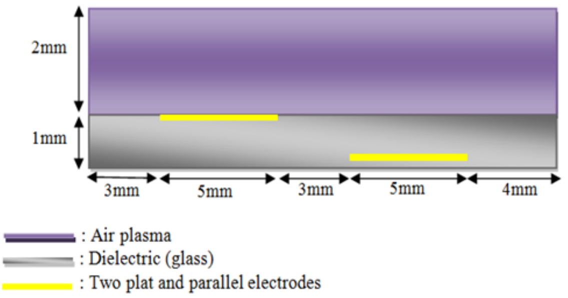

Fig. (6) The simulated SDBD area

To simulate the gas (air) ionization process and the flux of charged particles at an applied electric potential, the numerical model presented in the following section has been used. The high electric field generated by the applied high potential causes the electron drift and gas (air) ionization close to the exposed electrode. The resulting positive ions generate more electrons through secondary emission. This process is responsible for sustaining the plasma discharge.

4.1. Domain equations

In the simulation process, we have considered positive and negative ions and electrons as plasma species. For all type of particles, the transport equations describing the plasma discharge are given by [32]:

$$\frac{\partial}{\partial t}(n_i) + \nabla[-n_i(\mu_i . E) - D_i . \nabla n_i] = R_i \qquad (1)$$

where *i* can indicate electrons "*e*", positive ions "*p*" or negative ions "*n*". *n* is the density of the indicated particles and R_i is the source term of reactions in the plasma.

The electron energy density n_ε is calculated from their respective drift-diffusion equations by:

$$\frac{\partial}{\partial t}(n_\varepsilon) + \nabla[-n_\varepsilon(\mu_\varepsilon . E) - D_\varepsilon . \nabla n_\varepsilon] + E . \Gamma_e = R_\varepsilon \quad (2)$$

Where *E* is the electric field and Γ_e is the electron flux. R_ε is the energy loss caused by inelastic collisions.

The source coefficients in equations (2) are determined by the plasma chemistry using rate coefficients.

The electron diffusivity (D_e), the energy mobility (μ_ε) and the energy diffusivity (D_ε) are obtained from Einstein relations:

$$D_e = \mu_e T_e \, , \mu_\varepsilon = \frac{5}{3}\mu_e \, , D_\varepsilon = \mu_e . T_e \qquad (3)$$

With T_e is the electron temperature

The mean electron energy ε_e is calculated by the Einstein relation:

$$\varepsilon_e = \frac{3}{2} k_B T_e \qquad (4)$$

The electrostatic field is directly subtracted using Poisson's equation:

$$-\nabla \epsilon_0 \epsilon_r \nabla V = \rho \qquad (5)$$

Here *V* is the electrical potential, ϵ_0 is free space permittivity and ϵ_r is the relative permittivity of considered dielectric material. The space charge density ρ is deduced from the plasma chemistry specified in the model.

In the fluid equations and for a mixture of 80% nitrogen and 20% oxygen, nitrogen and oxygen are not treated separately as in a detailed chemistry. Instead, a general species *A* is used for the background gas. The ionization of species *A* forms a positive ions *p* and negative ions *n* if attached to an electron. The creation and loss of electrons in the discharge is governed by ionization and attachment (Townsend coefficients) and by the rate constants of a three-body attachment and electron-ion recombination. The Townsend coefficients which are a function of the mean electron energy are deduced by the suitable averaging of the electron energy distribution obtained using a Boltzmann solver with a consistent set of electron scattering collisions cross sections of nitrogen and oxygen [33].

The electrostatic or electro-hydrodynamic force (FEHD) is the result of the transfer of momentum from charged particles to neutral species. For the determination and the evaluation of this force, the densities of different types of charged particles should be taken into consideration [31,32].

$$\overrightarrow{F_{EHD}} = e(n_p - n_n - n_e)\vec{E} - [k.T_p \nabla n_p + k.T_n \nabla n_n + k.T_e \nabla n_e] \qquad (6)$$

Where T_p, T_n and T_e are the positive ions, negative ions and electrons temperatures, respectively. *K* is Boltzmann constant and *e* is the electron charge

In Eq. (6), we find a drift term in the electric field and a diffusion term associated with the density gradient. In case of the atmospheric pressure discharges, the force is mainly due to the drift term [32], it simplifies to:

$$\overrightarrow{F_{EHD}} = e(n_p - n_n - n_e)\vec{E} \qquad (7)$$

The plasma chemistry sustained in air is very complex process and a full study of the main excited states requires a lot of reactions. The main objective of this modeling is to investigate the charge particle density profiles and currents. To do so, a simplified set of reactions that precisely explain the creation and the loss of the charged species in dry air have been used. The different chemical reactions considered in this model are: ionization, attachment and surface reactions [34]. During the simulation process, the considered reactions of nitrogen and oxygen are associated with the mentioned plasma reactions. The creation and recombination of electrons in the volume are described by ionization and attachment, Townsend coefficients, rate constants for a three-body attachment and electron-ion recombination [35].

4.2. Boundary and initial conditions

The above equations (Eqs. 1, 2, 5 and 7) should be solved and each one has different boundary conditions that should be imported in the computational domain. The discharge is driven by the electric potential applied to the upper electrode [36].

$$V_{app}=V_0.\sin(2.\pi.f) \qquad (8)$$

The dielectric layer limits the charge current transported by the discharges through the surface. The surface charge accumulation is added to the dielectric surfaces by means of the following boundary condition [29,31]:

$$n.(D_d - D_p) = \rho_s \qquad (9)$$

Where $(D_d - D_p)$ is the difference in electric displacement between the plasma (D_p) and the dielectric material (D_d), ρ_s is the surface charge density, which is computed by solving the following distributed ordinary differential equations (ODE) on the surfaces [29,31]:

$$\frac{d\rho_s}{dt} = n.J_i + n.J_e \qquad (10)$$

Where $n{\cdot}J_i$ and $n{\cdot}J_e$ are the total current density normal component at the wall for ion and electron, respectively.

Ions are assumed to change back to neutral atoms when reaching the wall. The secondary emission coefficient is set to 0.05 and 0 for positive ions on the metallic electrode boundary and at the grounded electrode, respectively. The secondary electron mean electron energy is set to 4 eV.

When the plasma is initially ignited, the main charged species present in the discharge are ions. For this reason, both positive and negative ions densities have the same initial conditions and electrons have a relatively small density. These later assumptions maintain charge neutrality which is important for the numerical calculations.

4.3. Mesh

Generally, the selection of mesh is based on a compromise between the calculation precision and the computation time, meaning that the use of a fine mesh results in very long time of computation with more precise simulation results. In this study, a finer free triangular mesh calibrate for plasma type, illustrated in Fig. (7) has been considered to get a good result in a reasonable time.

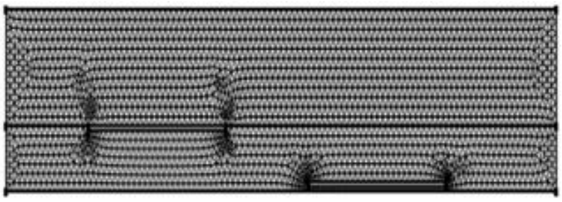

Fig. (7) An overview of the applied mesh. The areas with the finest mesh are over the surface area and the two electrodes

The parameters of this mesh are 15315 elements with a maximum element size of 0.2 nm and a minimum one of 0.05nm, a maximum growth rate of the elements of 1.2, a curvature resolution of 0.2 and a narrow regions resolution of 1.

5. Numerical results and discussions

The simulation is carried out with a sinusoidal waveform applied voltage, with amplitude of 7kV and a frequency of 6 kHz for two periods. The discharge gap is fixed to 3mm, the gas temperature is set to 300 K while the initial electron temperature is set to 4eV and the initial electron density is fixed to 10^{10} m^{-3}. The observation of the SDBD actuators discharges current can be a great source of information about the properties of the generated plasma. This current is usually the product of several components of different origins. The first component is a capacitive reactive current due to the dielectric layer separating the electrodes.

In this model we calculate the discharge current in the SDBD structure. Figure (8) shows the simulation result for two periods. We noticed that the current response has a many peaks. As explained above section, these pulses are due to the creation of micro discharges like those occurring in case of filamentary regime. The picks are more intense in the positive half-wave (about 0.87 A) than in the negative one (about 0.25 A).These current values have been compared with the experimental ones reported by P. Boeuf et al [37], Wu et al [38] and Sun et al [39].

The comparison between our calculated discharge current (deduced by COMSOL$^{@}$ model) and the reported experimental values indicates that the results illustrated in figures (4) and (8) are in good agreement. This validation gives our theoretical model the possibility of using the electrical characteristics of the SDBD reactor simulation results to optimize the design of its structure for particular applications.

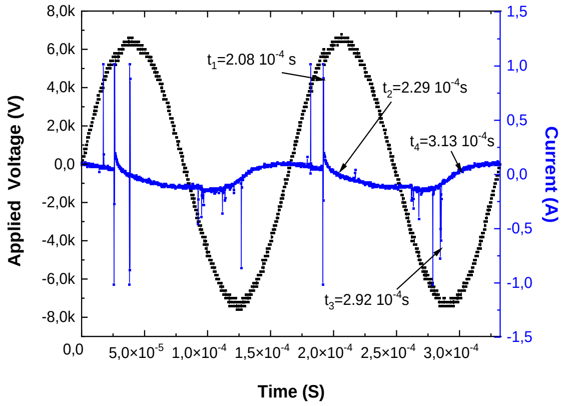

Fig. (8) Evolution of the discharge current for two periods

The two-dimensional spatiotemporal variation of charged spaces densities, electron temperature (Te), electric potential and electrical force are presented in figures (9-12), respectively. Solving the transport equation of charged particles, coupled with all other equations system gives the distribution of charged species and neutrals. To represent this result, four instants of the time simulation at the second period of the applied voltage have been selected. The chosen instants during the discharge phase are t_1=2.08 10^{-4} s, t_2=2.29 10^{-4} s, t_3=2.92 10^{-4} s and t_4=3.13$10^{-4}$ s representing the apparition time of the current peaks as shown in Fig. (8), where t_1 and t_2 are from the positive alternation, while t_3 and t_4 belong to the negative one. Moreover, t_1 and t_3 correspond to instants of the discharge current peaks unlike the instants t_2 and t_4. The densities of electrons, negative and positive ions are shown in Fig. (9a, b and c), respectively.

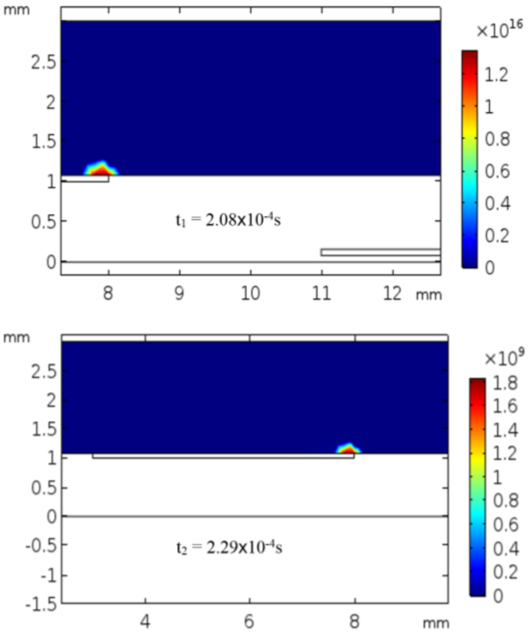

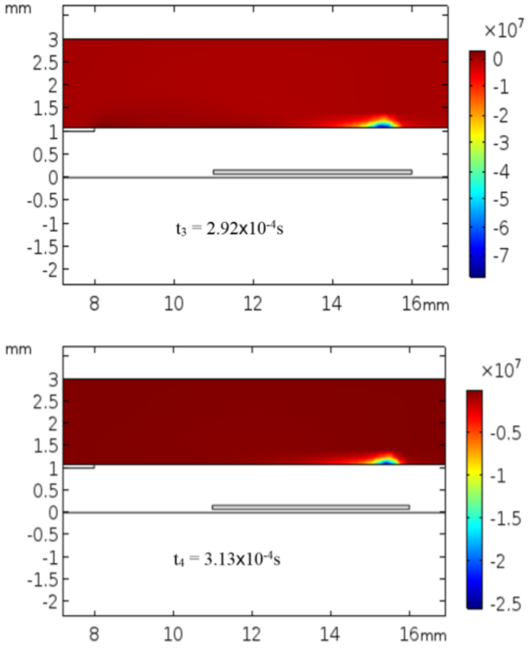

(a)

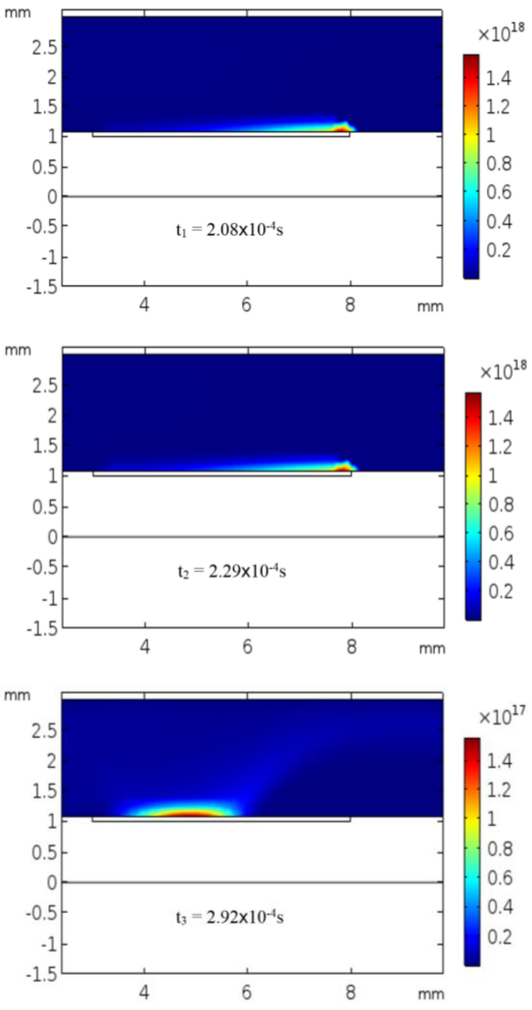

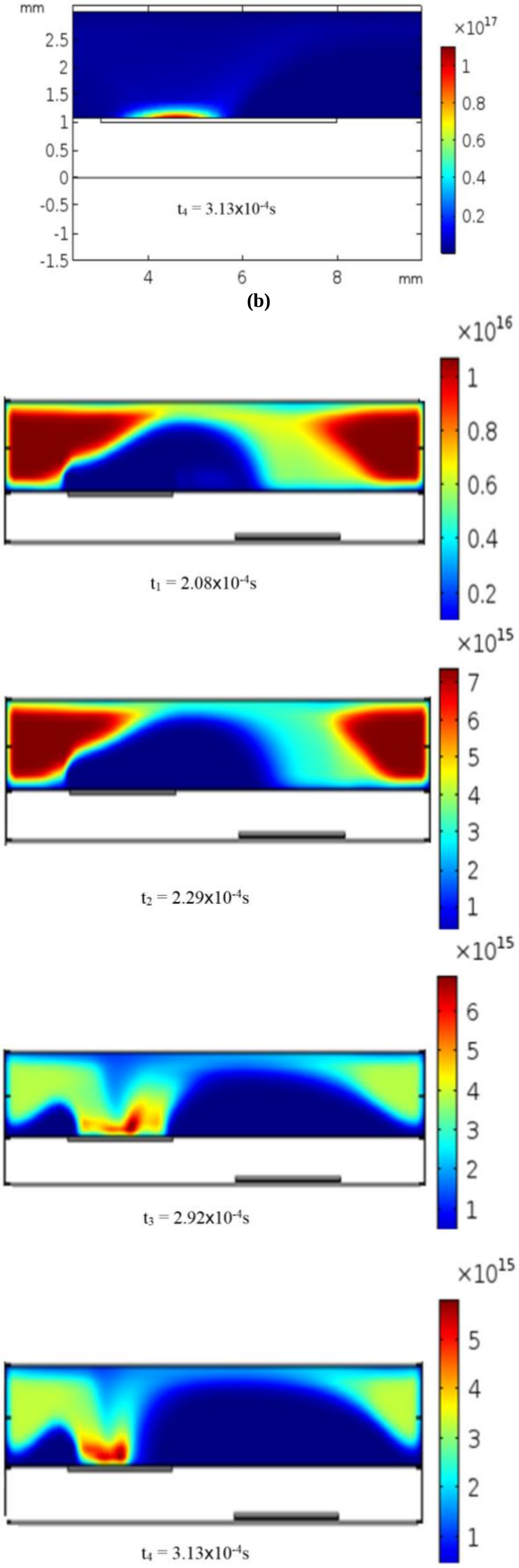

(b)

(c)

Fig. (9) (a) Spatial distribution of electron density for various time values (T=period=1.66 10-4 s), (b) Spatial distribution of negative ion density, and (c) Spatial distribution of positive ion density

The spatial distribution of both electrons and negative ions is similar at the first chosen instants t_1 and t_2; they only differ in the density values where the electron density is lower. At the instants t_3 and t_4, the electrodes polarization becomes inversed, therefore electrons change their position to the opposite side of the reactor while negative ions stay spread on the upper electrode as they cannot follow the frequency of the polarization due to their heavier mass. It's important to note the high concentration of negative oxygen ions in the air ($1.5x10^{18}$ m^{-3}). We observe a uniform distribution in the centre of the plasma with an axial extension with a low peak density. The peak of electron density is observed around the exposed electrode between the gas and the dielectric region, along the centre line of the discharge with a maximum peak value of 1.2 10^{16} m^{-3}. At this point, we can also notice that the filamentary plasma discharge has developed and progressed to the end of the simulation domain in a thin layer near the electrode surface. In contrast, the positive ions are repulsed from the high voltage electrode in the positive alternation at the instants t_1 and t_2 with a high value of density of about 10^{16} m^{-3}, then, at the negative alternation (t_3 and t_4) they are attracted towards the electrode and accumulated on the surface keeping the same density. The determination of the electronic temperature by the presented model is obtained by solving the electron energy equation. The simulation result is shown in Fig. (10a,b), for both periods.

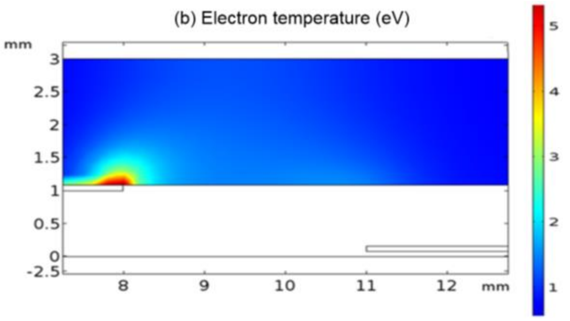

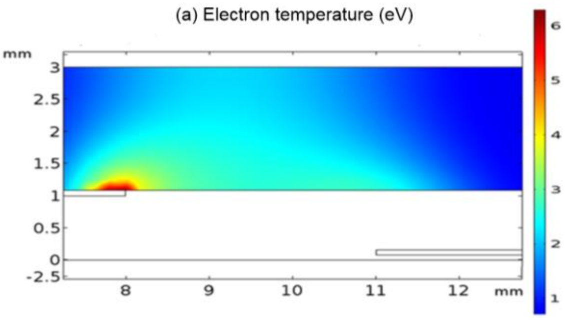

Fig. (10) Spatial distribution of electronic temperature

From these curves, we find that electron temperature, for both periods is very high near the polarized electrode and at the surface of the glass. Their values are about 5 eV at t'_1= 4.1 10^{-5} s (max of the first period) and 6 eV at $t_2=2.29\ 10^{-4}$ s (max of the second period). In these areas, thermal agitation and collisions occur due to the presence of a strong electric field leading to a large electronic temperature values. However, this temperature decreases in the zone of the neutral plasma where the electric field is zero and electrons become less energetic. Different types of plasmas can be determined according to their electronic temperatures and the densities of charged particles. For cold plasma at high pressure out of equilibrium, the electron density is between 10^{10} and 10^{15} cm^{-3} and the temperature is between 1eV and 10eV [40-42]. These reported values are in accord with the results obtained by the presented simulation.

Solving the Poisson's equation gives the spatial distribution of the electric potential and the electric field shown in Fig. (11a,b), respectively for the time t_2. At this time of the first alternation of the applied sin-wave, the electric potential is located at the proximity of the high voltage electrode while near the grounded one the electric potential is very low (Fig. 11a).

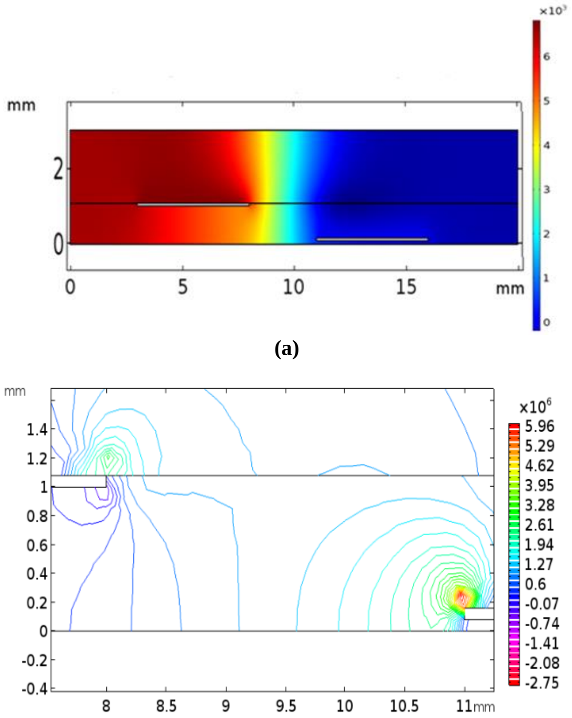

(a)

(b)

Fig. (11) Spatial distribution at t2 of: (a) Electric potential (surface plot) and (b) Electric field (contour plot)

Moreover, figure (11a) confirms that the electric potential is high near the exposed electrode edge and decreases as we move longitudinally along the exposed dielectric surface. The movement of the charged species behaves as expected, when the exposed electrode has a positive voltage (the ions move away and the electrons move towards, from the electrode). The behavior of the electric field and the charged species changes during the simulation due to the surface charge accumulation on the dielectric material. As we notice in Fig. (11b), the electric field strength is larger on the upper electrode than inside the dielectric material. It intends to decrease in the longitudinal and lateral directions. The unsymmetrical geometry and the difference of relative permittivity together with the surface charge contribute to the electric field changes behavior with time.

The FEHD force in the case of an applied sinusoidal voltage is also considered in this study. The result of simulation, under the previous conditions is illustrated in Fig. (12) as a distribution of this force per unit of length over the time.

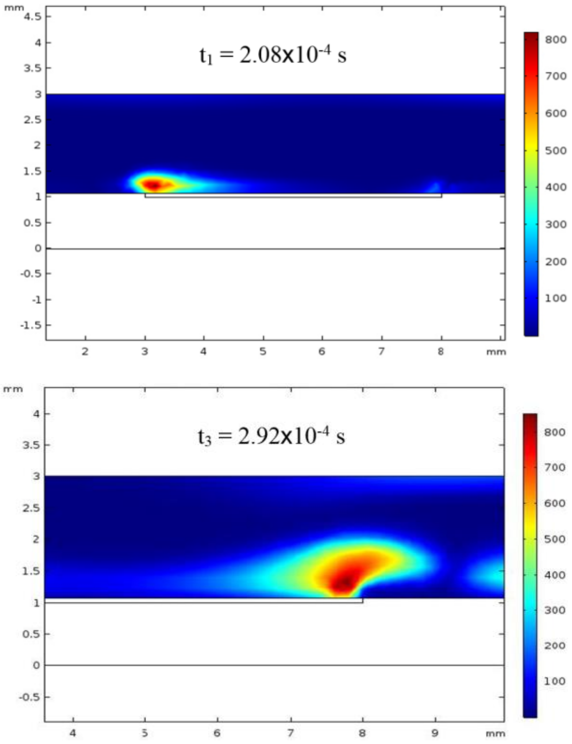

Fig. (12) Spatial distribution of force FEHD (N/m^3)

We observe in Fig. (12) that the force is distributed over a region greater for t_3 than for t_1. This means the extension of the positive ion cloud at the moment without a breakdown for both half waves**.** The area where the force occurs, the densities of electrons and negative ions are almost zero, where we practically find only positive charges. These regions are the sheaths or space charges where the field is different from zero and the electrostatic force takes a maximum value of 894.65 and 932.84 N/m^3 for t_1 and t_3, respectively. On the other hand, the simulation result shows that in the breakdown moment, this force reaches its maximum value. This increase is due to the presence of some intense currents peaks at the break down moment.

6. Conclusion

In this paper experimental and numerical investigations of SDBD plasma actuator operating in a controlled air atmosphere have been investigated.

The experimental measurements revealed that the discharge current-voltage waveforms, the power consumption and the plasma filaments morphology are influenced by the actuator structure and the presence of the polyimide layer. In case of structure without the polyimide layer, the consumed electrical power was greater, the plasma extension is longer and the number of filaments is higher. The SDBD actuator simulation revealed that the plasma is out of equilibrium, the electrons have high energy around the exposed electrode and the electrostatic force is almost zero in the neutral zone of the plasma and takes a maximum value in electrostatic sheaths. The calculated electrical current discharge presents some current pulses explaining the presence of micro discharges in the plasma. The qualitative and quantitative agreement of our developed model with the experimental ones gives the simulation process the ability of describing the discharge process accurately, which allows the use of the simulation process as an effective method to find the optimal electrical parameters to create the plasma discharge in an SDBD structure for a given application.

References

[1] P. Audier et al., “Experimental investigation of a surface DBD plasma actuator at atmospheric pressure in different N_2/O_2 gas mixtures”, *Plasma Sour. Sci. Technol.*, 23 (2014) 065045.

[2] R. Brandenburg, “Dielectric barrier discharges: progress on plasma sources and on the understanding of regimes and single filaments”, *Plasma Sour. Sci. Technol*, 26 (2017) 053001.

[3] R. Brandenburg, “Corrigendum: Dielectric barrier discharges: progress on plasma sources and on the understanding of regimes and single filaments”, *Plasma Sour. Sci. Technol.*, 27 (2018) 079501.

[4] M.K. Khalaf, O.A. Hammadi and F.J. Kadhim, “Current-Voltage Characteristics of DC Plasma Discharges Employed in Sputtering Techniques”, *Iraqi J. Appl. Phys.*, 12(3) (2016) 11-16.

[5] R. Krumpolec et al., “Multi-hollow surface dielectric barrier discharge for plasma treatment of patterned silicon surfaces”, *Surf. Interfaces*, 16 (2019) 181-187.

[6] B.T Chiad et al., “Characteristics and operation conditions of a closed-field unbalanced dual magnetrons plasma sputtering system”, *Open Access Library J.*, 1(6) (2014) 1-7

[7] W.A. Altun et al., “Magnetic Field Distribution of Closed-Field Unbalanced Dual Magnetrons Employed in Plasma Sputtering Systems”, *Iraqi J. Appl. Phys.*, 12(3) (2016) 35-42.

[8] M. Domonkos et al., “Applications of Cold Atmospheric Pressure Plasma Technology in Medicine, Agriculture and Food Industry”, *Appl. Sci.*, 11 (2021) 4809.

[9] M. Kogoma and K. Tanaka, “Low temperature atmospheric discharge plasma and its applications for the surface treatment”, *Rev. Mod. Plasma Phys.*, 5 (2021) 3.

[10] X. Min et al., “Surface modification of aramid fiber by air DBD plasma at atmospheric pressure with continuous on-line processing”, *Surf. Coat. Technol.*, 202 (2008) 6029–6033.

[11] M. Kuchenbecker et al., “Characterization of DBD plasma source for biomedical applications”, *J. Phys. D: Appl. Phys.*, 42 (2009) 045212.

[12] K.G. Kostov et al., “Bacterial sterilization by a dielectric barrier discharge (DBD) in air”, *Surf. Coat. Technol.*, 204(18-19) (2010) 2954-2959.

[13] D. Kuvshinov et al., “Efficient Compact Micro DBD Plasma Reactor for Ozone Generation for Industrial Application in Liquid and Gas Phase Systems”, *Int. J. Chem. Mole. Nucl. Mater. Metall. Eng.*, 8(1) (2014) 80-83.

[14] R.P. Guragain et al., “Characterization of Dielectric Barrier Discharge (DBD) Produced In Air at Atmospheric Pressure and Its Application in Surface Modification of High-Density Polyethylene (HDPE)”, *J. Technol. Space Plasmas*, 1(1) (2020) 27-35.

[15] J.R. Roth and X. Dai, “Optimization of the Aerodynamic Plasma Actuator as an Electrohydrodynamic (EHD) Electrical Device”, *44th AIAA Aerospace Sciences Meeting and Exhibit AIAA*, Reno, Nevada (2006).

[16] M. Gao et al., “Deposition of thin films on glass fiber fabrics by atmospheric pressure plasma jet”, *Surf. Coat. Technol.*, 404 (2020) 126498.

[17] O.A. Hammadi et al., “Employment of Magnetron to Enhance Langmuir Probe Characteristics of Argon Glow Discharge Plasma in Sputtering System”, *Iraqi J. Appl. Phys.*, 12(4) (2016) 19-28.

[18] R. Abidat, F. Bouanaka and S. Rebiai, “Computational Study of Surface Dielectric Barrier Discharge Plasma Actuator for Flow Control Using Comsol Multiphysics”, *CISTEM’18 - Algiers, Algeria, c2018 IEEE* (2018).

[19] T. Homola et al., “Efficiency of Ozone Production in Coplanar Dielectric Barrier Discharge”, *Plasma Chem. Plasma Process.*, 39(5) (2019) 1227-1242.

[20] H.W. Lee et al., “Modelling of atmospheric pressure plasmas for biomedical applications”, *J. Phys. D: Appl. Phys.*, 44 (2011) 053001.

[21] F. Larry, “History of the Plasma Display Panel”, *IEEE Trans. Plasma Sci.*, 34(2) (2006) 268-278.

[22] B. Dong et al., “Experimental study of a DBD surface discharge for the active control of subsonic airflow”, *J. Phys. D : Appl. Phys.*, 41 (2008) 155201.

[23] J.C. Laurentie, J. Jolibois and E. Moreau, “Surface dielectric barrier discharge: Effect of encapsulation of the grounded electrode on the electromechanical characteristics of the plasma actuator”, *J. Electrostat.*, 67 (2009) 93-98.

[24] M. Tanski et al., “Ozone Generation by Surface Dielectric Barrier Discharge”, *Appl. Sci.*, 13 (2023)

7001.

[25] J. Kriegseis et al., “Capacitance and power consumption quantification of dielectric barrier discharge (DBD) plasma actuators”, *J. Electrostat.*, 69 (2011) 302-312.

[26] J.P. Boeuf and L.C. Pitchford, “Electrohydrodynamic force and aerodynamic flow acceleration in surface dielectric barrier discharge”, *J. Appl. Phys.*, 97 (2005) 103307.

[27] J.T. Holgate and M. Coppins, “Numerical implementation of a cold-ion, Boltzmann-electron model for no planar plasma-surface interactions”, *Phys. Plasmas*, 25 (2018) 043514.

[28] G. Colonna and A. D’Angola, **“Plasma Modeling Methods and Applications”**, IOP Pub., (Bristol, 2016) Ch. 8, p. 13.

[29] F. Bouanaka, A. Boudjadar and S. Rebiai, “Modeling and electrical characterization of atmospheric-pressure surface dielectric barrier discharge (SDBD) in Argon”, *ICAEE 2019, IEEE* (2019).

[30] A. Saridj and A. W. Belarbi, “Numerical modeling of a DBD in glow mode at atmospheric pressure”, *J. Theor. Appl. Phys.*, 13 (2019) 179-190.

[31] A.V. Likhanskii et al., “Modeling of dielectric barrier discharge plasma actuator in air”, *J. Appl. Phys.*, 103 (2008) 053305.

[32] M. Abdollahzadeh et al., “Two-dimensional numerical modeling of interaction of micro-shock wave generated by nanosecond plasma actuators and transonic flow”, *J. Comput. Appl. Math.*, 270 (2014) 401-416.

[33] M.A. Lieberman and A.J. Lichtenberg, **“Principles of Plasma Discharges and Materials Processing”**, 2nd ed., John Wiley & Sons (NJ, 2005) Ch. 10, p. 345.

[34] A.A. Kulikovsky, “Positive streamer between parallel plate electrodes in atmospheric pressure air”, *J. Phys. D: Appl. Phys.*, 30 (1997) 441-450.

[35] W. Yang et al., “Boltzmann equation studies on electron swarm parameters in Townsend breakdown of copper vapor plasma using independently assessed electron-collision cross sections”, *AIP Adv.*, 9 (2019) 035041.

[36] H. Abdelraouf, A.M.N. Elmekawy and S.Z. Kassab, “Simulations of flow separation control numerically using different plasma actuator models”, *Alexandria Eng. J.*, 59 (2020) 3881-3896.

[37] J.P. Boeuf, Y. Lagmich, and L. C. Pitchford, “Contribution of positive and negative ions to the electrohydrodynamic force in a dielectric barrier discharge plasma actuator operating in air”, *J. Appl. Phys.*, 106 (2009) 023115.

[38] K. Wu et al., “Atmospheric pressure self-organized filaments in dielectric barrier discharge excited by a modulated sinusoidal voltage”, *Phys. Plasmas*, 27(8) (2020) 082308.

[39] Q. Sun et al., “Study on Characteristics of an AC Sliding Discharge Plasma Actuator Operating at Different Pressures”, *Actuators*, 12(1) (2023) 34.

[40] M Bouzidi, “Étude d’une Décharge à Barrière Diélectrique (DBD) homogène dans l’azote à pression atmosphérique: Effet mémoire et Optimisation du transfert de Puissance”, *PhD thesis, Institut National Polytechnique de Toulouse (INPT)*, (2014).

[41] F.L. Tabares and I. Junkar, “Cold Plasma Systems and their Application in Surface Treatments for Medicine”, *Molecules*, 26(7) (2021) 1903.

[42] V. Kolobov and V. Godyak, “Electron kinetics in low-temperature plasmas”, *Phys. Plasmas*, 26 (2019) 060601.

IRAQI JOURNAL OF APPLIED PHYSICS
Vol. 19, No. 4B, November 2023, pp. 113-120

Characterization and Antibacterial Activity of Copper Oxide Nanoparticles Prepared Using Nd:YAG Pulsed-Laser Ablation

Mays W. Skakir
Awatif S. Jasim

Department of Physics,
College of Science,
University of Tikrit,
Tikrit, IRAQ

In this work, a pulsed Nd:YAG laser with 1064nm wavelength and100mJ energy was used to irradiate copper plate placed in ethanol with different number of pulses (200, 250, 300, 350, and 400). The structural characterizations showed that the nanoparticle sizes were identical, averaged at 44.66 nm for low concentration and 27.91 nm for high concentration of nanoparticles in the solution. As well, only copper and oxygen elements were detected in the final samples, which indicates exceptional purity of the colloidal nanoparticles. The surface plasmon resonance (SPR) was observed in the absorption spectra ranging in 590-615 nm for the prepared samples with different number of pulses. When the prepared nanoparticles were employed as an antibacterial agent for positive (Streptococcus mutans) and negative bacteria (Escherichia coli) and Candida albicans that were isolated from the oral cavity, the higher the concentration of nanoparticles, the greater the ability to degrade bacteria and discourage them.

Keywords: Laser ablation; nanoparticles; Nd:YAG laser; Antibacterial activity
Received: 04 August 2023; **Revised:** 30 August 2023; **Accepted:** 06 September 2023

1. Introduction

Recently noble metal nanoparticles have received a lot of research attention due to their applications in catalysis, biology, electronics, and information technology [1-4]. In general, nanoparticles have several advantages as they have unique optical, magnetic, electronic, biological, and chemical properties compared to bulk materials due to their increased reaction surface area [5-7]. More specifically, copper nanoparticles are used in flexible electronics and nano-circuits because of their superior electrical conductivity [8-11].

Due to its simplicity, size content, and shape of the synthesized nanomaterials, the pulsed laser ablation (PLA) approach was recently used to synthesize copper nanoparticles in a liquid as one of the key techniques. The most reliable, practical, and ecologically friendly method for synthesizing pure and stable nanoparticles is known as pulsed laser ablation of a target in liquid (PLAL). This method has the advantage of being straightforward and not requiring chemical reagents like stabilizers or surfactants [12]. However, the laser parameters may be altered and managed, including medium, repetition rate, wavelength, and pulse width [13].

Recently, numerous studies on copper/copper oxide nanocomposites have been conducted [14-22], encompassing a variety of topics such as production techniques, optical characteristics, and analysis of structures. Moreover, it is a global concern that antibiotics and other antimicrobial medicines are becoming less effective. Due to their exceptional antibacterial qualities, copper nanoparticles are receiving a great attention [23-25]. Copper nanoparticles are usually prepared by laser ablation in aqueous solutions of ligands using nanosecond laser pulses [26]. However, metal-based nanoparticles have been included in biomaterials crucial to human health care due to their potential antioxidant and antibacterial characteristics [27,28].

In this work, PLAL technique was used to synthesize nanoparticles by irradiating copper plate in ethanol. The optical and structural characteristics of these nanoparticles were introduced, and their antibacterial activity against some common types of bacteria and fungi was determined.

2. Experimental Setup

Utilizing a pure copper plate with a diameter of 1 cm and the PLAL process using a Q-switched nanosecond Nd:YAG laser with a pulse duration of 9 ns, the nanoparticles were produced. A 3 ml of 99.99% pure ethanol was put in a beaker and placed 15 cm away from the laser source. The repetition rate of the Nd:YAG laser pulses was 5 Hz. Also, the number of pulses was varied during the irradiation time (200, 250, 300, 350, and 400 pulses). Figure (1) shows schematically the PLAL setup.

Thin films of the prepared nanomaterials were deposited on glass substrates by drop casting method for the characterization and measurement tests such as x-ray diffraction (XRD) filed-emission scanning electron microscopy (FE-SEM), UV-visible spectrophotometry, while other tests such as energy-dispersive x-ray spectroscopy (EDX), transmission electron microscopy (TEM), and Fourier-transform infrared (FTIR) spectroscopy. The antibacterial activity of the prepared samples was then tested against a strain of gram-positive bacteria (*Streptococcus mutans*) and a strain of gram-negative bacteria (*Escherichia coli*), as well as *Candida albicaus* obtained from the oral cavity. The results were analyzed and charted using Origin 2018 software.

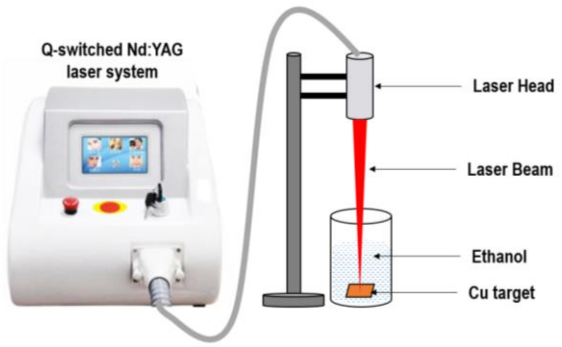

Fig. (1) Schematic diagram of PLAL setup used in this work

3. Results and Discussion

By using UV-visible spectrophotometry, the prepared nanoparticles were first characterized. Figure (2) shows the absorption spectra of the nanoparticles prepared using the 1064 nm laser pulses with an energy of 100 mJ. It can be seen that the SPR for the various samples was ranging between 590 and 615nm, and the peaks were higher (except for some peaks) and wider when the number of pulses is increased up to the absorption peaks of all spectra (580 nm). The figure shows that the larger number of laser pulses resulted in a high absorbance, indicating that the solutions contain high concentration of copper nanoparticles. By increasing the number of pulses, the optical absorption intensity of the liquid medium increases, which indicates that the number of pulses has an effect on the density of nanoparticles in the liquid [29]. When light irradiates the nanoparticles, their free electrons move together, inducing the SPR property.

Figure (3) displays the XRD patterns of the synthesized nanoparticles, with one pattern representing a sample produced using the wavelength 1064 nm. The JCPDS card 04-0836 of copper was used to compare the three peaks at 2θ values of 37.43°, 41.28°, 57.03°, and 62.53° those are correspond respectively to (002), (200), (020), and (113) crystalline planes of copper oxide (CuO). This figure also demonstrates that the final patterns exhibit a variety of intensities and peaks related to these nanoparticles with a face-centered cubic (FCC) crystalline structure [30].

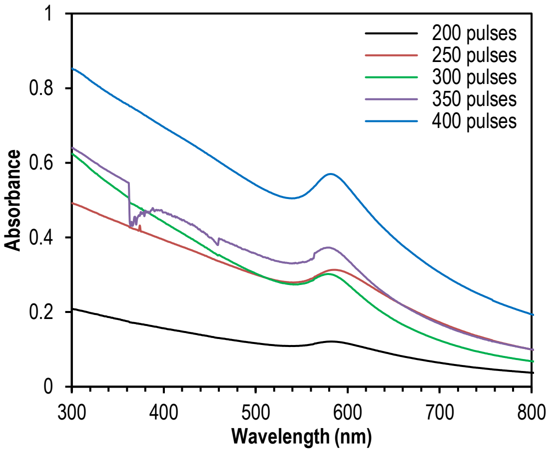

Fig. (2) UV-visible spectra of the nanoparticles prepared using different number of pulses

Using 1064nm laser pulses, the peaks belonging to the cubic phase of the nanoparticles were observed in addition to peaks belonging to various phases of copper oxides, including CuO (tenorite) and Cu_2O (cuprite) in the monoclinic phase, where the peaks at 42.43°, 51.08°, and 74.93° those correspond respectively to (111), (200), and (220) crystalline planes of Cu_2O in the orthorhombic phase [31].

The fitted XRD pattern stands out in particular when compared to the unfit pattern (JCPDS Card 04-0836). The average crystallite size (D) could be calculated using Debye-Scherrer formula:

$$D = \frac{0.9\lambda}{\beta \cos\theta} \qquad (1)$$

where λ is the wavelength of x-ray beam (0.1541nm), β is the full-width at half maximum (FWHM), and θ is the diffraction angle [32]

The crystallite size for the sample prepared with 200 laser pulses was ranging in 59.3-35.5nm, while for the sample prepared with 400 laser pulses was ranging in 23.3-31.0nm.

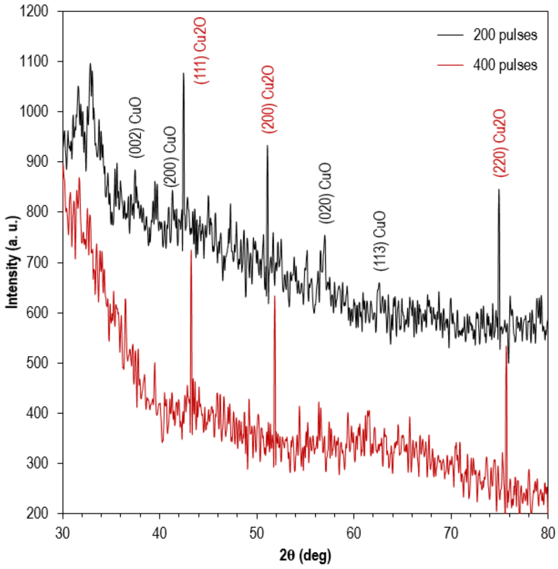

Fig. (3) XRD patterns of the nanoparticles prepared with two different number of pulses (200 and 400)

All samples contain metal nanoparticles and their oxides, which supports the assumption of the formation of nanoparticles with a core-shell structure. Although there was a slight displacement of some diffraction peaks, this can be attributed to mechanical stress from various sources, such as impurities, defects, and voids inherent in the film.

A research work has claimed that the interaction between metal atoms and oxygen leads to the production of radicals or atoms of metal oxide, as the synthesized nanoparticles break down in liquids. Additionally, they noted that the temperatures and oxygen partial pressure affect the type of formed oxide [33].

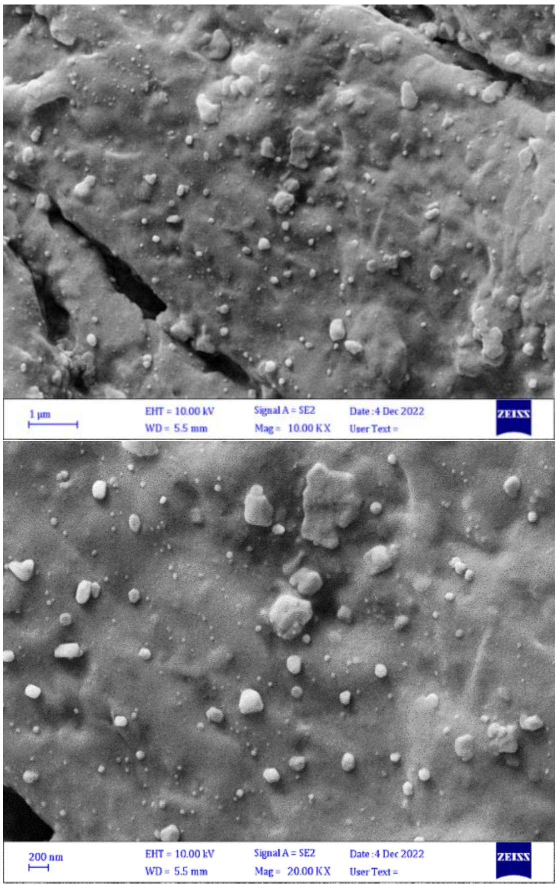

Fig. (4) FE-SEM images of the synthesized nanoparticles using 1064nm laser pulses with scale of (a) 200nm, (b) 1µm, for low concentration of nanoparticles in ethanol

The shape of the synthesized nanoparticles was examined using the FE-SEM images. Figures (4) and (5) demonstrate that the produced nanoparticles and nanospheres are ethanol-ablated. According to the particle size distribution, nanoparticle sizes typically range between 44.66 nm for low concentration and 27.91 nm for high concentration of nanoparticles in the ethanol. This difference in size and shape reveals the mechanisms involved in the nanoparticle formation process. The incident radiation from the laser beam that hits the copper plate is absorbed, raising the temperature of the copper above its melting point. This heating leads to the formation of the plasma plume, which is entirely contained within the liquid layer. In this process, the material on the surface of the plate is pulled out and condensed by the surrounding liquid to nucleate and grow by coalescence [34]. Nucleation and growth of particles are governed by the cooling rate and the reaction between the species in the surrounding medium and the target. In this sense, although ethanol has a higher heat transfer coefficient at room temperature, the remarkable effects of the solvent molecules decomposition at high temperatures in the ablation process in ethanol, carbon species (C^*) cover the surface of the initial particles, stopping the growth of nuclei [34,35].

On the other hand, the nanoparticle formation process is influenced by the duration of laser pulses. When nanosecond laser pulses impact the material, there is a temporal overlap between the pulses and the ablation event. Therefore, in the presence of a long laser pulse, the plasma plume can absorb part of the incoming laser energy, increasing the plasma temperature and boosting the atomization of the material, as reported in previous works, which evidences that the ablation process starts a few tens of picoseconds after the laser irradiation and the plasma lasts for tens of nanoseconds [36]. This process results in nanoparticles with small average diameters.

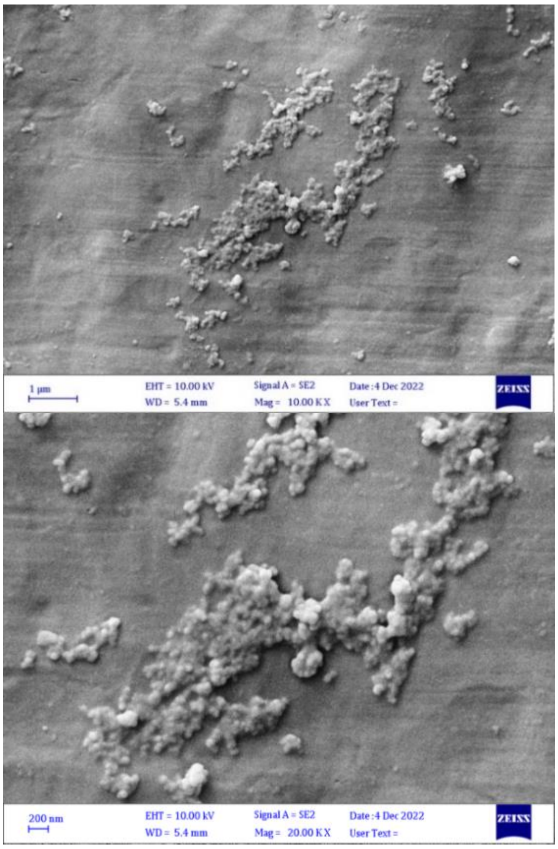

Fig. (5) FE-SEM images of the synthesized nanoparticles using 1064nm laser pulses with scale of (a) 200nm, (b) 1µm, for high concentration of nanoparticles in ethanol

Figure (6) displays the elemental compositions of the nanoparticles obtained by the EDX test with peaks indicating the presence of copper in the final sample. These EDX results revealed a relatively continuous fluctuation of the elemental atomic percentage [37] since the values determined by the EDX analysis are relative measures of the elemental atomic percent content rather than absolute measures of element mass. The high pace of counting during the analysis is what causes the appearance of high and narrow peaks [38]. The increase in oxygen percentage causes the percentages of produced metal nanoparticles to drop.

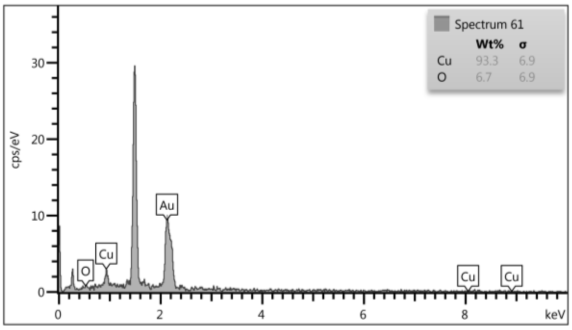

Fig. (6) EDX analyze of nanoparticles synthesized in this work

The biologically active chemical component compounds found in the nanoparticles' solution were identified using FTIR spectroscopy. The absorption peaks are seen at 3358.18, 2974.33, 2879.81, 1923.09, 1656.90, 1379.14, 1273.06, 1089.81, 1047.38, 879.59, 501.50 and 432.06 cm^{-1} on the FTIR spectra in Fig. (7). Peaks at 2974.33, 2879.81, 1923, and 1656.90 cm^{-1} represent the C-H asymmetric stretching, the C=O aromatic vibrations, and the C=C stretching, respectively [39]. The peaks positioned at 1379.14, 1089.81, and 1047.38 cm^{-1} correlate to the organic and aromatic molecule derivatives, including phenolics, alkaloids, tannins, flavonoids, aldehydes, and ketones, that are present in the plant extract. The peaks at 879.59, 630.90 and 432.06 cm^{-1} are recognized as the aromatic rings of amino acids. For derivatives of organic and aromatic molecules such as phenols, alkaloids, tannins, flavonoids, and ketones, the peaks located at 1394 and 1258 cm^{-1} are assigned. It's possible that phenolic compounds stretching under OH or NH conditions caused the peak at 3427 cm^{-1}. The FTIR investigation lends credence to the idea that phytochemicals play a role in the synthesis of Cu NPs. Thus, it follows that these phytochemicals are essential for the production of nanoparticles [40].

The FTIR spectra of nanoparticles shown in Fig. (7) are useful for describing the chemistry of surfaces of these nanoparticles. In addition to the apparent C=O carboxylic acid stretching group, these FTIR spectra demonstrated absorption peaks corresponding to the groups of hydroxyl (O-H), alkane (C-H), and aliphatic amine (C-O) stretching vibrations [41]. The reason for the blue shift at the Cu-O vibrational mode may be related to the impact of small particle size, which says that the Cu-O-H bonds cause bending absorptions in the range 866 cm^{-1}, and the shift in the location of the bond depends on how strong the hydrogen bonding is. The synthesis of copper oxide nanoparticles is a result of the band above 650 cm^{-1}. The figure shows that, because the number of pulses influences the concentration of nanoparticles in ethanol, it also affects the value of the absorbance peaks as well as the emergence and disappearance of certain of them [42].

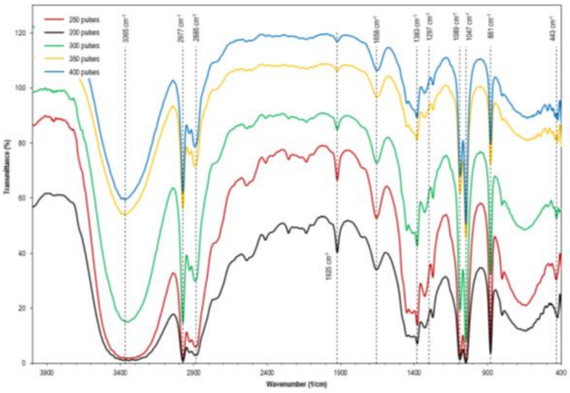

Fig. (7) FTIR spectra of the nanoparticles prepared with different number of pulses

According to TEM results shown in Fig. (8), the synthesized nanoparticles are mostly spherical, and since the removal process was carried out in a free medium without the use of any capping agent, some particles overlapped with each other. The investigation of a particle's crystalline or flawed structure can be done via TEM analysis, which provides a reliable assessment of particle average size [43]. Throughout TEM investigation, the average particle size, size distribution, and shape of specific nanoparticles produced by the laser ablation approach are verified [44].

This morphology is probably the product of nanosecond pulses that produce particles during thermal processes (rapid solidification, melting, and superheating), which cause the nanoparticles to be formed by explosive ejection [45].

The antibacterial activity of the synthesized nanoparticles was analyzed using the disc diffusion method. The bacterial inoculums were first grown in LB broth for 24 hours at 28°C and 200 rpm. It was then re-suspended in LB medium until the optical density (OD) was adjusted to 0.1 at 600nm, which corresponds to 10^8 colony-forming units (CFU)/mL. The spread plate technique was used, in which 100μL of each bacterial suspension was spread over nutrient agar medium. A set of four concentrations (50, 100, 150, and 200 μL) of the nanoparticle colloidal solutions in the disc were prepared and used in the study. The four different concentrations of nanoparticles in the respective discs were placed over the bacterial culture and standard. All the agar plates were incubated in the bacteriological incubator for 24 hours at 37°C. A measuring scale (mm) was used to calculate the zone of inhibition (ZOI) surrounding the discs.

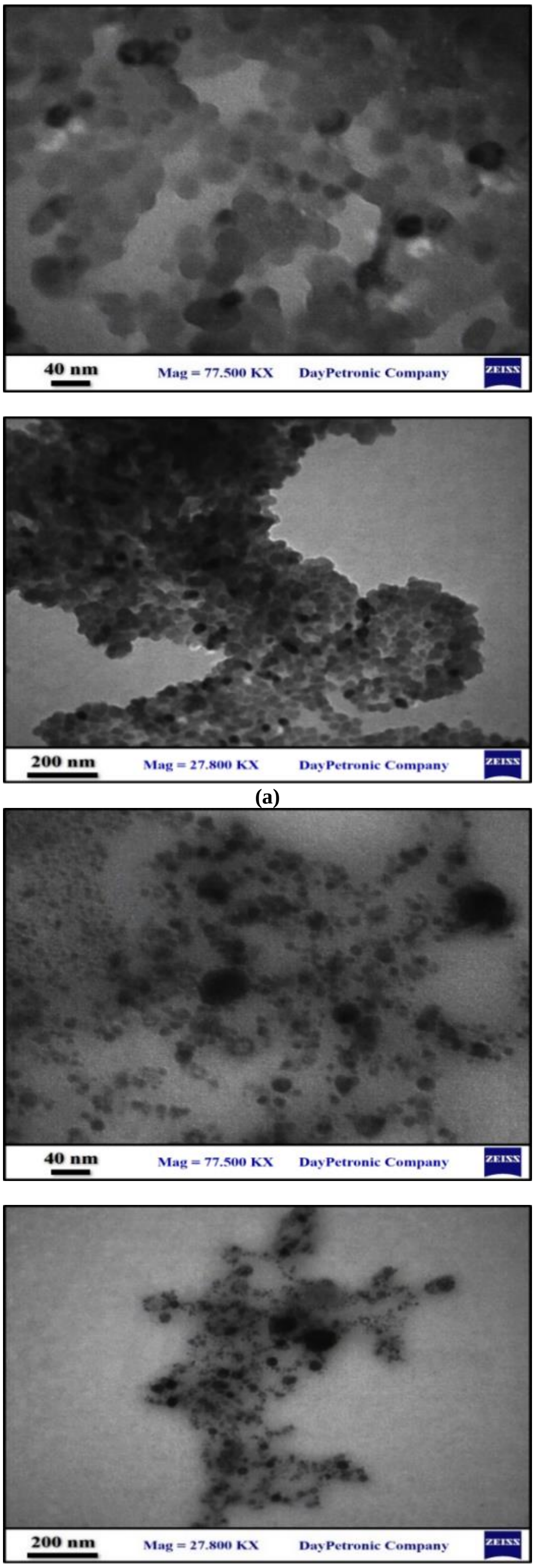

(a)

(b)

Fig. (8) TEM images of nanoparticles at different scales (40 and 200 nm) in (a) low concentration, and (b) high concentration of nanoparticles in ethanol

By measuring the diameter of the inhibition zone, as was done in other research [46,47], it was possible to determine how well the produced nanoparticles worked at preventing the growth of a few different species of bacteria. Their antibacterial activity was then compared with that of traditional antibiotics. The findings of our investigation indicated that some of the two bacteria mentioned (*Streptococcus mutans and Escherichia coli*) and *Candida albicans* fungus respond significantly to the nanoparticles, which may be a result of bacterial resistance to antibiotics as demonstrated. Figure (9) shows the inhibitory zones of the bacterial samples treated with nanoparticles synthesized by laser ablation.

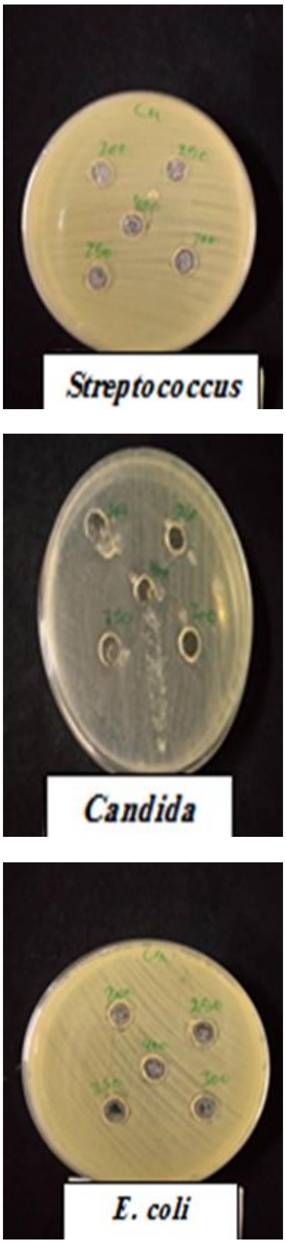

Fig. (9) Antibacterial activity of the synthesized nanoparticles against (a) *Streptococcus mutans*, (b) *Candida albicans*, (c) *Escherichia coli*

Good results in the inhibition zone were observed as the number of pulses increases, and hence the concentration of nanoparticles increases, and thus the inhibition zone increases, as shown in Fig. (10).

There are different accepted mechanisms for the antibacterial activity of metal nanoparticles [48,49]. The most-reported mechanism is based on the reactive oxygen species generation (ROS). The nanoparticles also dramatically enhance the cellular ROS level that influences lipid peroxidation, protein oxidation, and DNA destruction and finally inhibition the microorganism cells [50]. The ROS contain radical compounds such as hydroxyl (OH^-), superoxide radical (O_2^-), singlet oxygen ($^1O_2$), and hydrogen peroxide (H_2O_2), which destroy the bacteria. To conclude, the synthesized nanoparticles demonstrated significant antibacterial activity against various organisms.

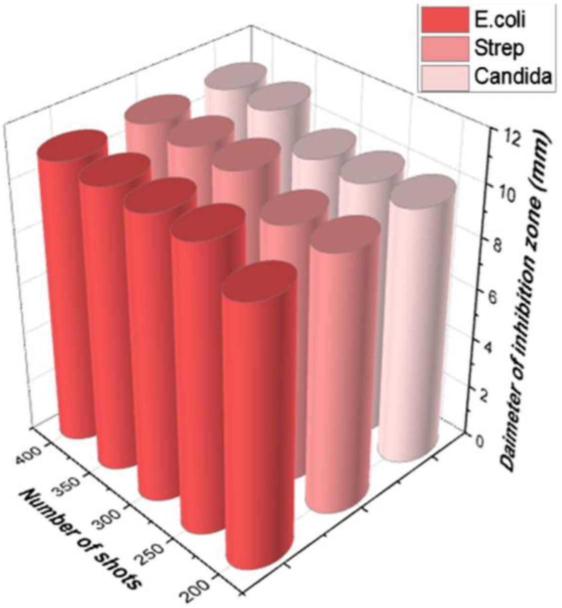

Fig. (10) Histogram of antibacterial activity of the synthesized nanoparticles against the bacteria and fungus

1. Conclusions

In concluding remarks, ethanol, as an optimum liquid medium to synthesize nanoparticles by PLAL, preserves the nanomaterial and does not lead to its aggregation over time. Copper oxide nanoparticles can be used as an alternative to antibiotics since these nanoparticles have an apparent effect on both Gram-positive, Gram-negative bacteria and fungi.

References

[1] G. Bagherzade, M.M. Tavakoli and M.H. Namaei, “Green synthesis of silver nanoparticles using aqueous extract of saffron (Crocus sativus L.) wastages and its antibacterial activity against six bacteria”, *Asian Pacific J. Tropic. Biomed.*, 7(3) (2017) 227-233.

[2] S. Agrawal et al., “Silver nanoparticles and its potential applications: A review”, *J. Pharmacog. Phytochem.*, 7(2) (2018) 930-937.

[3] M.A. Hameed, S.H. Faisal, R.H. Turki, “Characterization of Multilayer Highly-Pure Metal Oxide Structures Prepared by DC Reactive Magnetron Sputtering Technique”, *Iraqi J. Appl. Phys.*, 16(4) (2020) 25-30

[4] Asraa M. Hameed and Mohammed A. Hameed, “Highly-Pure Nanostructured Metal Oxide Multilayer Structure Prepared by DC Reactive Magnetron Sputtering Technique”, *Iraqi J. Appl. Phys.*, 18(4) (2022) 9-14.

[5] K.S. Khashan, G.M. Sulaiman and F.A. Abdulameer, “Synthesis and Antibacterial Activity of CuO Nanoparticles Suspension Induced by Laser Ablation in Liquid”, *Arab. J. Sci. Eng.*, 41(1) (2016) 301-310.

[6] S.H. Faisal and M.A. Hameed, “Heterojunction Solar Cell Based on Highly-Pure Nanopowders Prepared by DC Reactive Magnetron Sputtering”, *Iraqi J. Appl. Phys.*, 16(3) (2020) 27-32.

[7] Asraa M. Hameed and Mohammed A. Hameed, “Optical Microscopy of Highly-Pure Metal Oxide Nanoparticles Irradiated with Electromagnetic Radiation in Nonmetallic Hosts”, *Iraqi J. Appl. Phys. Lett.*, 6(1) (2023) 7-10.

[8] B.K. Park et al., “Direct writing of copper conductive patterns by ink-jet printing”, *Thin Solid Films*, 515(19) (2007) 7706-7711.

[9] K. Woo et al., “Ink-Jet printing of Cu− Ag-based highly conductive tracks on a transparent substrate”, *Langmuir*, 25(1) (2009) 429-433.

[10] Y. Lee et al., “Large-scale synthesis of copper nanoparticles by chemically controlled reduction for applications of inkjet-printed electronics”, *Nanotechnol.*, 19(41) (2008) 415604.

[11] S. Jang et al., “Sintering of inkjet printed copper nanoparticles for flexible electronics”, *Scripta Materialia*, 62(5) (2010) 258-261.

[12] R. Rawat et al., “Effects on surface-enhanced Raman scattering from copper nanoparticles synthesized by laser ablation”, *Rad Effects Defects in Solids*, 175(3-4) (2020) 332-341.

[13] A.M. Mostafa, E.A. Mwafy and M.S. Hasanin, “One-pot synthesis of nanostructured CdS, CuS, and SnS by pulsed laser ablation in liquid environment and their antimicrobial activity”, *Opt. Laser Technol.*, 121(9) (2019) 105824.

[14] M. Yin et al., “Copper oxide nanocrystals”, *J. Am. Chem. Soc.*, 127 (2005) 9506-9511.

[15] J. Pike et al., “Formation of stable Cu_2O from reduction of CuO nanoparticles”, *Appl. Catal. A*, 303 (2006) 273-277.

[16] R.M. Tilaki, A. Iraji Zad and S.M. Mahdavi, “Size, composition and optical properties of copper nanoparticles prepared by laser ablation in liquids”, *Appl. Phys. A*, 88 (2007) 415-419.

[17] K. Amikura et al., “Copper oxide particles produced by laser ablation in water”, *Appl. Surf. Sci.*, 254 (2008) 6976-6982.

[18] D.B. Pedersen, S. Wang and S.H. Liang, “Charge-transfer-driven diffusion processes in Cu@Cu-oxide core-shell nanoparticles: oxidation of 3.060.3 nm diameter copper nanoparticles”, *J. Phys. Chem. C*, 112 (2008) 8819-8826.

[19] A. Nath and A. Khare, “Size induced structural modifications in copper oxide nanoparticles synthesized via laser ablation in liquids”, *J. Appl. Phys.*, 110 (2011) 043111.

[20] P. Liu et al., “Fabrication of cuprous oxide nanoparticles by laser ablation in PVP aqueous solution”, *RSC Adv.*, 1 (2011) 847-851.

[21] K. Mitsuo, “Laser-induced fragmentative decomposition of fine CuO powder in acetone as highly productive pathway to Cu and Cu_2O nanoparticles”, *J. Phys. Chem. C*, 115 (2011) 5165–5173.

[22] T. Ghodselahi and M.A. Vesaghi, “Localized surface plasmon resonance of $Cu@Cu_2O$ core-shell nanoparticles: absorption, scattering and luminescence”, *Physica B*, 406 (2011) 2678-2683.

[23] M. Fernández-Arias et al., “Fabrication and deposition of copper and copper oxide nanoparticles by laser ablation in open air”, *Nanomaterials*, 10(2) (2020) 10020300.

[24] T.A. Mezher, A.M. Ali and A.N. Abd, “Characterization and Antimicrobial Activity of Copper Oxide Nanoparticles”, *Iraqi J. Appl. Phys. Lett.*, 4(3) (2021) 19-22.

[25] Asraa M. Hameed and Mohammed A. Hameed, “Spectroscopic characteristics of highly pure metal oxide nanostructures prepared by DC reactive magnetron sputtering technique”, *Emerg. Mater.*, 6 (2022) 627-633.

[26] M. Muniz-Miranda et al., “Characterization of copper nanoparticles obtained by laser ablation in liquids”, *Appl. Phys. A*, 110 (2013) 829-833.

[27] P.K. Dara et al., “Synthesis and biochemical characterization of silver nanoparticles grafted chitosan (Chi-Ag-NPs): In vitro studies on antioxidant and antibacterial applications”, *SN Appl. Sci.*, 2(4) (2020) 1-12.

[28] S. Anwaar et al., “The effect of green synthesized CuO nanoparticles on callogenesis and regeneration of Oryza sativa L”, *Front. Plant Sci.*, 7 (2016) 1330.

[29] A.A. kamil et al., “Synthesis and study of the optical and structural properties of Au and Ag nanoparticles by pulsed laser ablation (PLAL) technique”, *Dige. J. Nanomater. Biostruct.*, 16(4) (2021) 1219-1226.

[30] R. Maisterrena-Epstein et al., “Nanosecond laser ablation of bulk Al, Bronze, and Cu: ablation rate saturation and laser-induced oxidation”, *Superficies y vacío*, 20(3) (2007) 1-5.

[31] S. Jillani et al., “Synthesis, characterization and biological studies of copper oxide nanostructures”, *Mater. Res. Exp.*, 5(4) (2018) 045006.

[32] K. Nesrin and A. Karadağ, “Microwave Assisted Green Synthesis of Ag, Ag_2O, and Ag_2O_3 Nanoparticles”, *J. Turkish Chem. Soc. Sec. A: Chem.*, 8(2) (2021) 585-592.

[33] G.W. Yang, “Laser ablation in liquids: applications in the synthesis of nanocrystals”, *Prog. Mater. Sci.*, 52 (2007) 648-698.

[34] G. Marzun et al., “Role of dissolved and molecular oxygen on Cu and PtCu alloy particle structure during laser ablation synthesis in liquids”, *Chem. Phys. Chem.*, 18 (2017) 1-11.

[35] V. Amendola and M. Meneghetti, “Laser ablation synthesis in solution and size manipulation of noble metal nanoparticles”, *Phys. Chem. C*, 11 (2009) 3805-3821.

[36] S.T. Ellingham, T.J. Thompson and M. Islam, “Scanning Electron Microscopy–Energy-Dispersive X-Ray (SEM/EDX): A Rapid Diagnostic Tool to Aid the Identification of Burnt Bone and Contested Cremains”, *J. Foren. Sci.*, 63(2) (2018) 504-510.

[37] M.A. Gondal et al., “Effects of oxidizing medium on the composition, morphology and optical properties of copper oxide nanoparticles produced by pulsed laser ablation”, *Appl. Surf. Sci.*, 286 (2013) 149-155.

[38] D. Medina Cruz et al., “Citric juice-mediated synthesis of tellurium nanoparticles with antimicrobial and anticancer properties”, *Green Chem.*, 21 (2019) 1982-1998.

[39] I. Jahan et al., “Microwave-irradiated green synthesis of metallic silver and copper nanoparticles using fresh ginger (*Zingiber officinale*) rhizome extract and evaluation of their antibacterial potentials and cytotoxicity”, *Inorg. Nano-Metal Chem.*, 51 (2021) 722-732.

[40] N.N. Greenwood and E.J.F. Ross, **“Index of Vibrational Spectra of Inorganic and Organometallic Compounds”**, vol. II, Butterworth Group (London, 1963), p. 457.

[41] N.N. Greenwood and E.J.F. Ross, **“Index of Vibrational Spectra of Inorganic and Organometallic Compounds**”, vol. III, Butterworth Group (London, 1966), p. 800, 1078.

[42] S. Moniri et al., “Synthesis and optical characterization of copper nanoparticles prepared by laser ablation”, *Bull. Mater. Sci.*, 40 (2017) 37-43.

[43] S. Ţălu et al., “Microstructure and tribological properties of FeNPs@aC:H films by micromorphology analysis and fractal geometry”, *Ind. Eng. Chem. Res.*, 54(33) (2015) 8212-8218.

[44] M. Boutinguiza et al., “Production of nanoparticles from natural hydroxylapatite by laser ablation”, *Nanoscale Res. Lett.*, 6 (2011) 1-5.

[45] B.P. Chouke et al., “Green fabrication of zinc oxide nanospheres by Aspidopterys cordata for

effective antioxidant and antibacterial activity", *Adv. Mater. Lett.*, 10(5) (2019) 355-360.

[46] J.A. Tanna et al., "Copper nanoparticles catalysed an efficient one-pot multicomponents synthesis of chromenes derivatives and its antibacterial activity", *J. Exp. Nanosci.*, 11(11) (2016) 884-900.

[47] F. Erci et al., "Synthesis of biologically active copper oxide nanoparticles as promising novel antibacterial-antibiofilm agents", *Prepar. Biochem. Biotechnol.*, 50 (2020) 538-548.

[48] S. Wu et al., "Green synthesis of copper nanoparticles using *Cissus vitiginea* and its antioxidant and antibacterial activity against urinary tract infection pathogens", *Artif. Cells Nanomed. Biotechnol.*, 48 (2020) 1153-1158.

[49] S.C. Mali et al., "Green synthesis of copper nanoparticles using *Celastrus paniculatus Willd.* leaf extract and their photocatalytic and antifungal properties", *Biotechnol. Rep.*, 27 (2020) e00518.

[50] J.S. Ali et al., "Antimicrobial, antioxidative, and cytotoxic properties of *Monotheca buxifolia* assisted synthesized metal and metal oxide nanoparticles", *Inorg. Nano-Metal Chem.*, 50 (2020) 770-782.

IRAQI JOURNAL OF APPLIED PHYSICS
Vol. 19, No. 4B, November 2023, pp. 121-126

Investigation of Sensitivity of Silver-doped Tin Oxide Nanostructures to Nitrogen Dioxide Gas

Muhannad Sami Jalil [1]
Ahmed T. Hassan [2]
Yaqoob M. Jawad [3]

[1] *Basic Science Branch,*
College of Dentistry,
Mustansiriyah University,
Baghdad, IRAQ
[2] *Ministry of Education,*
General Directorate for Education,
Baghdad, IRAQ
[3] *Department of Physics,*
College of Science,
University of Diyala,
Diyala, IRAQ

Undoped SnO_2 nanoparticles as well as doped with different weight concentrations of silver dopants (1, 3 and 5 wt.%) were synthesized by a simple hydro-thermal method. The x-ray diffraction (XRD) measurements showed that the Ag-doped SnO_2 are polycrystalline with the appearance of tetragonal rutile phase with dominated (111) plane. Surface topography measurements throughout field-emission scanning electron microscopy (FE-SEM) show the formation of Ag-doped SnO_2 nanoparticles in the form of clusters enlarged with increasing doping concentration. The average particle size of these clusters ranged from 77 to 200 nm after introducing Ag dopants. Optical and photoluminescence measurements show a decrease in the energy gap with increasing Ag dopant weight concentration in SnO_2 structure. The sensitivity of Ag-doped SnO_2 films to NO_2 gas has increased up to 66% when exposed to gas concentration of 50 ppm at 100 °C operation temperature.

Keywords: Tin dioxide; Hydrothermal method; Chemiresistor; Gas sensors
Received: 07 July 2023; **Revised:** 19 August 2023; **Accepted:** 26 August 2023

1. Introduction

Recently, doped semiconductor nanomaterials semiconductor metal oxides have attracted a great deal of attention as a result of its wide variety of the potential applications. With the fast-growing and steady field of nanotechnology and nanoscience, Doped semiconductor nanomaterials materials have become the promising gas sensing materials as a result of their low density, small size, and high specific surface area, which are beneficial for the use of gas sensing [1-3]. Amongst these semiconductor metal oxides, is the SnO_2, which is a naturally n-type with a wide band gap of 3.6 eV considered as a significant material for various applications because of its non-toxicity, low cost, abundance in the nature, suitability and great chemical stability [4,5].

However, enhancing the chemiresistant properties of SnO_2 for higher sensing efficiency is remain a challenge because of the ineffective interaction of the charge carriers on its surface with gas molecules [6-8]. Recently, enormous effort given to this particular limitation. It is found that by surface modification of these metal oxide either by enhancing their physical properties such as morphology particle size, and structure, or by doping SnO_2 with some metal ion, noble metal, and semi-conductor to make a Doped semiconductor nanomaterials material. Combining both modification approaches together will enhance its chemiresistant properties. Silver has been selected as one of the composite elements due to the lattice mismatch with SnO_2 lattice as well as high electron mobility [9-12].

These doped semiconductor nanomaterials were prepared via varies techniques and methods such as electron beam evaporation [13], chemical vapor deposition [14], direct current (DC) gas discharges evaporation method, hydrothermal method [15], plasma enhanced chemical vapor depositions [16], chemical spraying [17], direct-current (DC) and radiofrequency (RF) sputtering methods [18-21]. Among these methods, hydrothermal approach has proven to be reproducible, simple, and economical, besides being suitable for the applications of the large-scale. Furthermore, the hydrothermal approach allows controlling the morphology as well as particle size in a nanometer range.

In this study, NO_2 gas sensor based on Ag-doped SnO_2 semiconducting nanomaterial was prepared by simple hydrothermal method. The weight concertation of Ag dopants in the semiconducting nanomaterial has a great effect on controlling morphology and structure and thereby enhancing the chemiresister properties of such material.

2. Experimental Part:

In the first stage, 0.780 g of ($CO(NH_2)_2$) and 2.454 g of $SnCl_4{\cdot}5H_2O$ have been dissolved in the distilled water 100 ml and stirred for 25 min. The solutions heated to a temperature of 90°C for 5 h for promoting $SnCl_4$ hydrolysis. Then, aqueous $AgNO_3$ solution with different ratio of 1, 3 and 5 wt.% added to the mixture as a dopant source. The resultant mix has been transferred to Teflon-lined stainless-steel autoclave of 30 mL capacity, sealed, and kept at a temperature of 150°C for 6 h before naturally cooling to room temperature. The previous solution was subjected to centrifuge and filtration operations and the resultant powder ultrasonically dispersed in the ethanol for 30 min before being dropped onto glass substrate then dried at a temperature of 80 °C for 40 min. Lastly, the dry films have been calcined at 600 °C for 2 hours in an electric furnace. The phase structures of prepared doped semiconductor nanomaterials that had been characterized by using Miniflex II Rigaku XRD instrument with CuKα1 radiation of 1.54058Å wavelength, 40 kV voltage and 300 mA current. A Hitachi-S4160 FE-SEM instrument was used to introduce the particle size and morphology of the samples. The absorption spectra of the films have been recorded using a Shimadzu UV-1650 spectrophotometer in the spectral range of 300-1100 nm. The photoluminescence (PL) spectra were recorded using a xenon lamp with peak intensity at 325 nm and power of 30 mW. A homemade system was built to measure the NO_2 gas sensitivity and this system is schematically shown in Fig. (1). It consists of a compact cylindrical stainless steel chamber with height of 18 cm and diameter of 18 cm with movable base that is sealed by O-ring. The effective volume of test chamber is 5832 cm^3. This chamber was evacuated down to 10^{-3} mTorr using a P-101195 rotary pump. The concentration of NO_2 gas that enters test chamber can be calculated using Eq. (1) [22].

$$\frac{\text{Target gas volume (ml)}}{\text{Test chambervolume (ml)}} = \frac{\text{Volume(ppm)}}{10^6} \qquad (1)$$

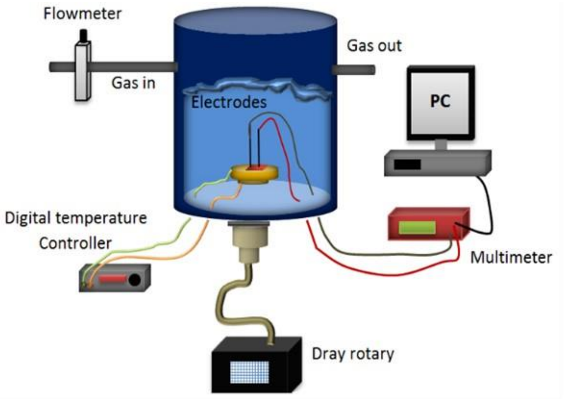

Fig. (1) Scheme of the homemade gas sensitivity system

The Ag-doped SnO_2 film is after that installed on the electrodes which are connected to a Proskit MT1820 multimeter that is interfaced to a computer to measure the electrical resistivity of the Ag-doped film, which is placed on a base and heated using a Chromalox A20, 240V, 400W Ring Heater connected to temperature controller of TCN-4M type.

3. Results and Discussions

To investigate the phase transition and stoichiometry of the prepared Ag-doped SnO_2 semiconducting nanomaterials with different Ag dopant concentrations, the XRD patterns were recorded in the range of diffraction angle 2θ = 20-80° as shown in Fig. (2). The diffraction peaks for the undoped SnO_2 film at 31.17°, 36.35°, 51.0° and 66.44° correspond to the (111), (200), (220) and (222) planes. This indicates formation of SnO_2 nanoparticles with tetragonal lattice that matched with JCPDS card number 43-1038 and 33-1374. It can be observed that by increasing Ag dopant weight concentration (doping level), the dominant reflection peak of (111) is decreased, which indicates that the Ag dopants may have taken interstitial sites not substitutional, which weakens the crystalline structure of SnO_2.

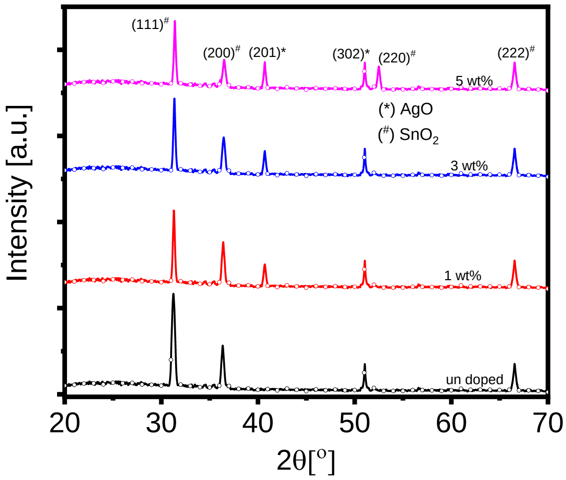

Fig. (2) XRD patterns of the Ag-doped SnO_2 with different weight concentrations of Ag dopants

Furthermore, compared to the peaks of undoped SnO_2 films, the diffraction peaks of Ag appear gradually when Ag weight concentration increases from 1 to 5 wt.% (JCPDS card no. 04-0783), which indicates the introduction of Ag into SnO_2 phase. New peaks at 40.65° and 51.0° corresponding to the (201) and (302) planes of AgO, respectively, can be seen after doping. The intensities of these peaks increased with Ag concentration, which indicates that doping with silver and appearance of the AgO phase reduced the crystallite size and thus increased the gas sensitivity of the Ag-doped SnO_2 nanoparticles. The Debye-Scherrer formula given in Eq. (2) [23] was used to determine the crystallite size for preferred reflection of the (111) plane

$$D = \frac{K\lambda}{\beta\, cos\theta} \qquad (2)$$

where θ is diffraction angle, K is a constant value (0.9), β is the full-width at half maximum (FWHM) in radians, and λ is the wavelength of the x-ray beam (1.5406Å)

The crystallite size decreases from 25 to 19 nm when the weight concentration of Ag dopants increased to 5 wt.%, which could be attributed to the stress that is caused by the difference of the ion size between the Ag and Sn throughout formation of the Ag-doped SnO_2 [24].

The morphology of the prepared doped semiconducting nanomaterials has been investigated by FE-SEM as given in Fig. (3). A uniform, flat, and homogeneous film of undoped SnO_2 nanoparticles with diameters ranging from 20 to 30 nm with small aggregation distributed across the sample's surface as can be seen in Fig. (3a). By increasing Ag weight concentration (Fig. 3b, c and d), the particle size in the clusters has increased to 60-70, 80-100 and 100-200 nm for 1, 3 and 5 wt.%, respectively. The measured crystallite size is matched with that measured via XRD. The increase of surface-to-volume ratio makes it ideal for gas sensing applications [25-26].

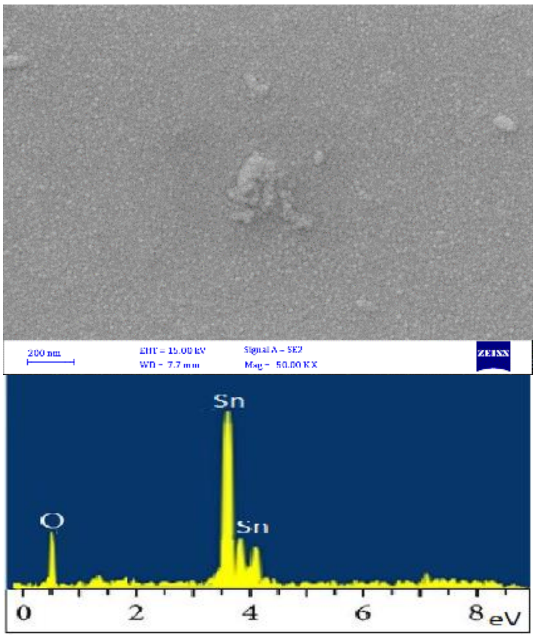

(a)

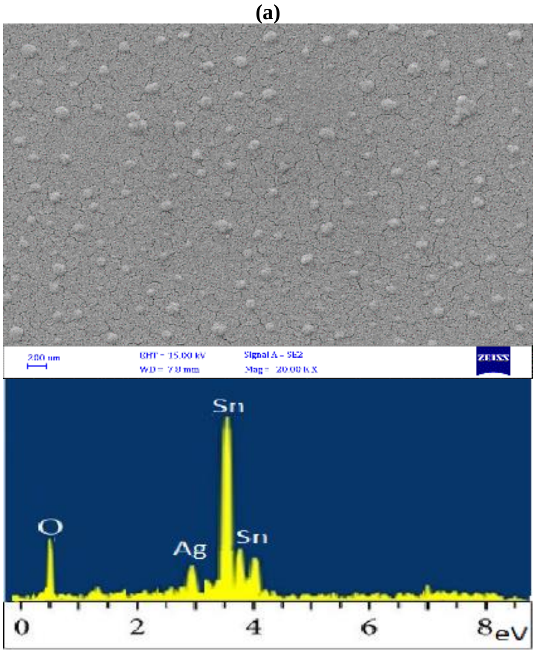

(b)

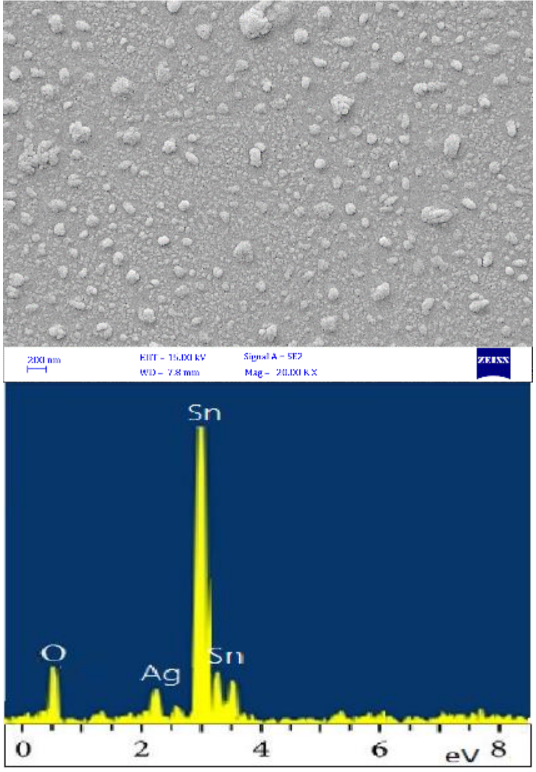

(c)

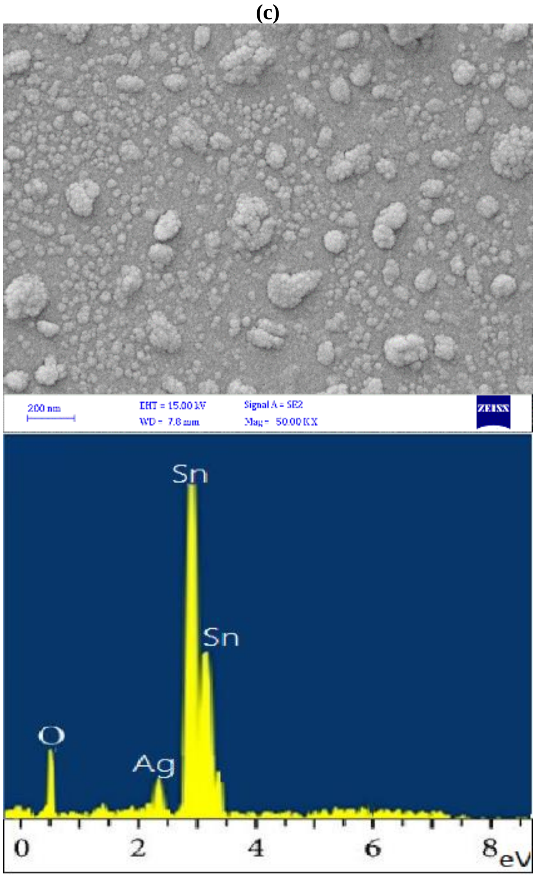

(d)

Fig. (3) FE-SEM images of the Ag-doped SnO_2 nanoparticles with EDS spectra (a) undoped, (b) 1 wt.% Ag, (c) 3 wt.% Ag, and (d) 5 wt.% Ag

The optical absorbance of the prepared doped semiconducting nanomaterials as a function of wavelength (λ) is shown in Fig. (4). The absorbance increases with increasing weight concentration of Ag dopants. Additionally, in comparison to the undoped SnO_2, the edge of the absorption shifts towards lower energies, manifesting the entering of Ag atoms into SnO_2 lattices. This can be attributed to the increase in the number and size of clusters of Ag-doped SnO_2, which makes them centers of absorption or dispersion of the falling spectra. This result is matched with the results of XRD and morphology (figures 1 and 2).

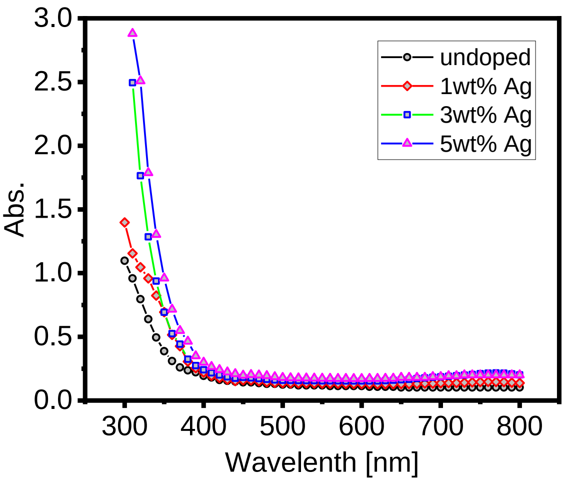

Fig. (4) Absorption spectra of undoped and doped SnO_2 films with different Ag weight concentrations

Further optical characterization of the prepared Ag-doped SnO_2 semiconducting nanomaterials was performed by investigating the photoluminescence (PL) spectra within the spectral range of 300-900nm (Fig. 5). A redshift in PL spectra can be seen when the concentration of Ag increases. For undoped SnO_2 sample, the emission peak at 382 nm (3.251 eV) is shifted to 405 nm (3.066 eV) for the sample doped with 1 wt.% Ag. Increasing the concentration to 3 wt.%, deviation in the PL peak keeps to move toward longer wavelengths of 408 nm (3.044 eV) and 411 nm (3.021 eV) for 5 wt.%. This shift in the PL spectra can be attributed to the nanocrystalline structure by band transition (crystalline with tetragonal structure of the rutile as shown in XRD results) that could be raised from the new localization in forbidden energy gap range [27-28]. The other apparent peak centered at 525 nm is attributed to the recombination of photo-generated charge carriers in shallow traps.

Figure (6) displays the gas sensitivity of Ag-doped SnO_2 semiconducting nanomaterials to NO_2 gas as a function of time exposure to 50 ppm concentration of NO_2 gas at 100 °C operation temperature. As expected, samples have exhibited n-type semiconducting behaviors (increased resistance in the case of being exposed to oxidant gas), and film response increases as the concentration of NO_2 gas inside the chamber is increased. The processes of the oxygen adsorption on the surface of Ag-doped SnO_2 film result in electron extractions from conduction band or donor secondary levels which have been produced via loaded silver, resulting in electron reduction. For the undoped SnO_2 film, the predominant charge carrier increases the area of the depletion and potential barriers to the electron transmission or the depletion area width increases resulting in obvious control of the grain boundary. While increasing the weight concentration of Ag dopants resulting more charge carriers that reducing the depletion area as well as the potential barrier for transmission of electrons [28-29].

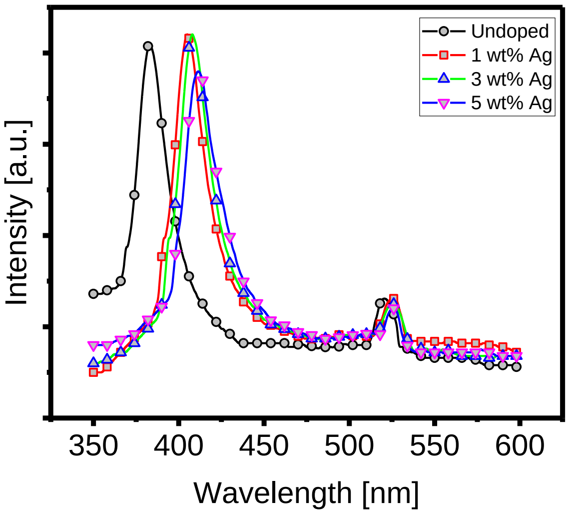

Fig. (5) Photoluminescence spectra of undoped and Ag-doped SnO_2 films with different Ag concentrations

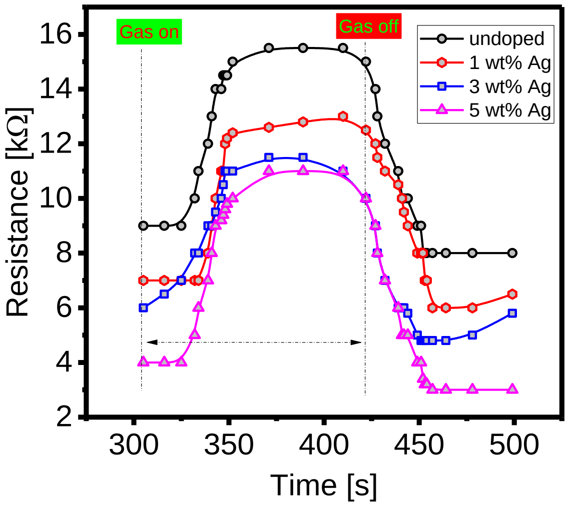

Fig. (6) Response of Ag-doped SnO_2 films to NO_2 gas

Additionally, the formation of small grains after introducing Ag dopants to the composite increased the porosity of Ag-doped SnO_2 film (SEM, Fig. 3) and thereby the neck control principle will be prevailed. Thus, existence of Ag dopants in the composite increased the level of the electrical conductivity and thereby, increased the gas sensitivity of Ag-doped SnO_2 films to the NO_2 gas. Figure (7) shows schematically the reaction of NO_2 gas with Ag-doped SnO_2 semiconducting nanomaterial with two different doping levels (1 and 5 wt.%).

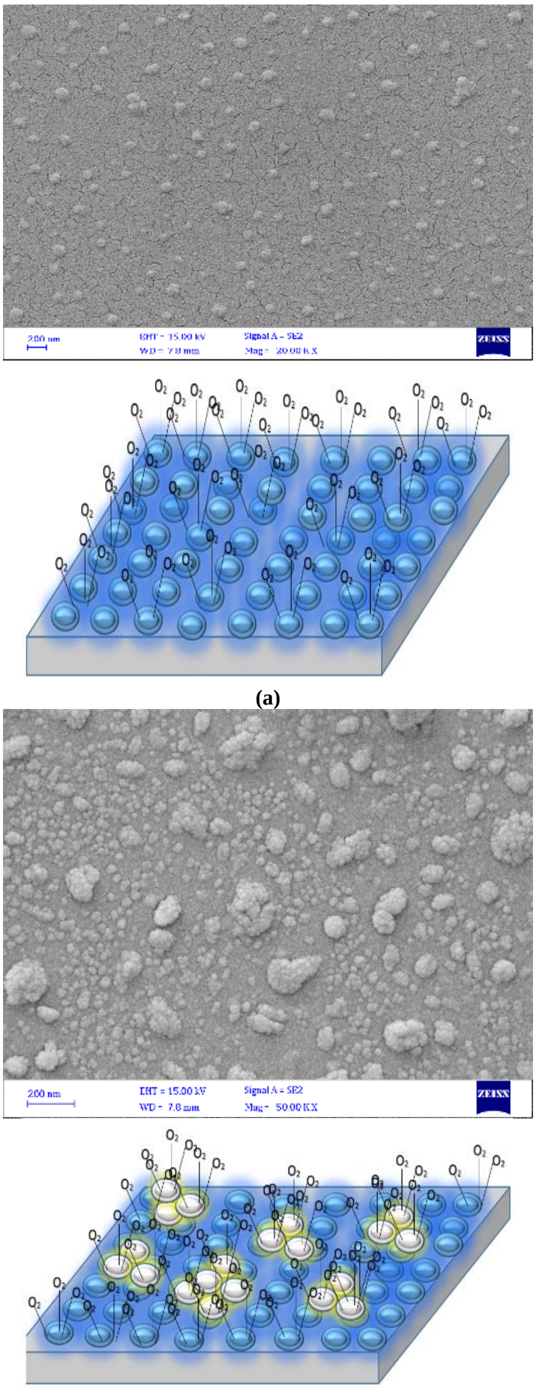

(a)

(b)

Fig. (7) Schemes of NO_2 gas reaction with Ag-doped SnO_2 films with doping level of (a) 1 wt.% and (b) 5 wt.%

Gas sensitivity of n-type semiconducting material to an oxide gas was calculated by Eq. (3) [30-31]. It is equal to 66% for the 5 wt.% Ag-doped SnO_2 film exposed to NO_2 gas with 50 ppm concentration at operation temperature of 100 °C, as

$$S = \frac{R_g - R_a}{R_g} \times 100\% \tag{3}$$

where R_g and R_a represent the electrical resistance of Ag-doped SnO_2 film in presence of air and NO_2 gas, respectively

4. Conclusion

Ag-doped SnO_2 films were prepared using simple hydrothermal method with different percentage weight concentrations of Ag dopants. The Ag dopants may occupy interstitial sites and hence weaken the crystalline structure of SnO_2. The Ag dopants acted as absorption centers for secondary levels within the energy gap. The average particle size ranges in 69-200 nm as the Ag dopant concentration is increased from 0 up to 5 wt.%. The 5 wt.% Ag-doped SnO_2 gas sensor has exhibited a sensitivity of 66% to 50 ppm NO_2 gas at 100°C due to the small size of grains formed as a result of small size effect.

Acknowledgments

The authors would like to express their thanks to Mustansiriyah University, Baghdad.

References:

[1] H.E. Salah et al., "Sensitivity of Nanostructured Mn-Doped Cobalt Oxide Films for Gas Sensor Application", *Nano Biomed. Eng.*, 12(3) (2020) 205-213.

[2] H. Ohgi et al., "Evolution of nanoscale SnO_2 grains, flakes, and plates into versatile particles and films through crystal growth in aqueous solutions", *Cryst. Growth Des.*, 5(3) (2005) 1079-1083.

[3] H.T. Salloom et al., "Characterization of silver content upon properties of nanostructured nickel oxide thin films", *Digest J. Nanomater. Biostr.*, 15(4) (2020) 1189-1195.

[4] A. Kumar et al., "Facile Synthesis and Structural, Microstructural, and Dielectric Characteristics of SnO_2-CeO_2 Semiconducting", *Binary Nanocomp. ECS Trans.*, 107(1) (2022) 3739.

[5] Z. Zhang et al., "Electrospun nanofibers of ZnO−SnO_2 heterojunction with high photocatalytic activity", *The J. Phys. Chem. C*, 114(17) (2010) 7920-7925.

[6] V. Galstyan et al., "Chemical gas sensors studied at SENSOR Lab" Brescia (Italy): from conventional to energy-efficient and biocompatible composite structures", *Sensors*, 20(3) (2020) 579.

[7] H. Ji, W. Zeng and Y. Li, "Gas sensing mechanisms of metal oxide semiconductors: a focus review", *Nanoscale*, 11(47) (2019) 22664-22684.

[8] S. Liu et al., "Enhancing NO_2 gas sensing performances at room temperature based on reduced graphene oxide-ZnO nanoparticles hybrids", *Sens. Actuat. B: Chem.*, 202 (2014) 272-278.

[9] R.V. Vijayalakshmi, R. Kuppan and P.P. Kumar, "Investigation on the impact of different stabilizing agents on structural, optical properties of Ag/SnO_2 core-shell nanoparticles and its biological applications", *J. Mol. Liq.*, 307 (2020) 112951.

[10] G. Müller and G. Sberveglieri, "Origin of Baseline Drift in Metal Oxide Gas Sensors: Effects of Bulk Equilibration", *Chemosens.*, 10(5) (2022) 171.

[11] J. Chen et al., "Interface structure of Ag/SnO_2 nanocomposite fabricated by reactive synthesis", *J. Mater. Sci. Technol.*, 26(1) (2010) 49-55.

[12] P. Chen et al., "SnO_2-Ag composites with high thermal cycling stability created by Ag infiltration of 3D ink-extruded SnO_2 microlattices", *Appl. Mater. Today*, 21 (2020) 100794.

[13] K. Shamala, L. Murthy and K. Narasimha Rao, "Studies on tin oxide films prepared by electron beam evaporation and spray pyrolysis methods", *Bull. Mater. Sci.*, 27 (2004) 295-301.

[14] S.D. Ponja et al., "Enhanced Bactericidal Activity of Silver Thin Films Deposited via Aerosol-Assisted Chemical Vapor Deposition", *Appl. Mater. Interfaces*, 7(51) (2015) 28616-28623.

[15] J. Lu et al., "Supercritical hydrothermal synthesis and in situ organic modification of indium tin oxide nanoparticles using continuous-flow reaction system", *ACS Appl. Mater. Interfaces*, 4(1) (2012) 351-354.

[16] T.M. Al-Saadi et al., "Study the structural and optical properties of Cr doped SnO_2 nanoparticles synthesized by sol-gel method", *Energy Procedia*, 157 (2019) 457-465.

[17] I.H. Kadhim, H.A. Hassan and F.T. Ibrahim, "Hydrogen gas sensing based on nanocrystalline SnO_2 thin films operating at low temperatures", *Int. J. Hydrogen Energy*, 45(46) (2020) 25599-25607.

[18] F. Fang et al., "Electrical and optical properties of nitrogen doped SnO_2 thin films deposited on flexible substrates by magnetron sputtering", *Mater. Res. Bull.*, 68 (2015) 240-244.

[19] T. Li et al., "Grain size and interface modification via cesium carbonate post-treatment for efficient SnO_2-based planar perovskite solar cells", *ACS Appl. Ener. Mater.*, 4(7) (2021) 7002-7011.

[20] R. Medhi et al., "Antimony-and Zinc-Doped Tin Oxide Shells Coated on Gold Nanoparticles and Gold–Silver Nanoshells Having Tunable Extinctions for Sensing and Photonic Applications", *ACS Appl. Nanomater.*, 3(9) (2020) 8958-8971.

[21] A.K. Singh and V.S. Raykar, "Microwave synthesis of silver nanofluids with polyvinylpyrrolidone (PVP) and their transport properties", *Colloid Polym. Sci.*, 286(14) (2008) 1667-1673.

[22] D. Harvey, **"Analytical Chemistry 2.1"**, textbook, DePauw University (2023) 28-29.

[23] J.R.H. Ross, **"Catalyst Characterization: Fundamentals and Current Applications",** Ch. 5 Contemporary Catalysis, Elsevier (2019), 121-132.

[24] M. Anwar, I. Ghauri and S. Siddiqi, "The study of optical properties of amorphous thin films of mixed oxides In_2O_3—SnO_2 system, deposited by co-evaporation", *Czechoslovak J. Phys.*, 55(8) (2005) 1013-1024,.

[25] Y. He et al., "Effect of Ag doping on SnO_2 sensing for detecting H_2S: A first-principles study", *Vacuum*, 194 (2021) 110587.

[26] S.J. Ikhmayies, "Optical parameters of Nanocrystalline SnO_2:F thin films prepared by the spray pyrolysis method", *JOM*, 71(4) (2019) 1507-1512.

[27] S. Jalili, F. Hajakbari and A. Hojabri, "Effect of silver thickness on structural, optical and morphological properties of nanocrystalline Ag/NiO thin films", *J. Theor. Appl. Phys.*, 12(1) (2018) 15-22.

[28] S. Navale et al., "Effect of Ag Addition on the Gas-Sensing Properties of Nanostructured Resistive-Based Gas Sensors:An Overview", *Sensors (Basel)*, 21(19) (2021) 6454.

[29] K. Sirohi et al., "Hydrothermal synthesis of Cd-doped SnO_2 Nanostructures and their Structural, Morphological and Optical Properties", *Mater. Today: Proc.*, 21 (2020) 1991-1998.

[30] S. Dhara and G. Dutta, **"Metal-Oxide Gas Sensors"**, IntechOpen (2023).

IRAQI JOURNAL OF APPLIED PHYSICS
Vol. 19, No. 4B, November 2023, pp. 127-132

Zainab A. Kadem
Ahmed B. Sharba
Jassim M. Jassim

Department of Laser Physics,
College of Science for Women,
University of Babylon,
Babylon, IRAQ

Fine Control of Refractive Index in Large-Size Magnetic Fluids for Photonics Applications

In this work, the changes in refractive index of relatively large-size samples of magnetic fluids containing Fe_3O_4 nanoparticles were studied under different conditions. The results reveal that, in addition to the intrinsic properties of the liquid, the main factor that controls the refractive index of large-size samples is the induced concentration gradient of the magnetic particles, which depends on the strength, the direction, and the action time of the applied magnetic field. Moreover, the results showed that the presence of Fe_3O_4 can enhance the linear and third-order susceptibilities of liquids ($\chi^{(1)}$ and $\chi^{(3)}$) with values depending on the liquid properties. Both dn/dc and $dn^2/dTdc$ were found to be 8.81×10^{-3} and 8.18×10^{-4} cm^3/mg and 3.15×10^{-4} and 9.45×10^{-5} $K^{-1}.cm^3/mg$ for Fe_3O_4 in methanol and water, respectively. The results of this study can be employed to design photonic devices with precisely controllable refractive indices by using large-size samples of magnetic fluids.

Keywords: Magnetic nanoparticles; Refractive index; Magnetic fluids; Thermal variation
Received: 21 June 2023; **Revised:** 17 August 2023; **Accepted:** 24 August 2023

1. Introduction

The linear refractive index is one of the essential properties of media. It is a key property that determines the type and strength of light interactions with the material. In the case of magnetic fluids, the optical properties have aroused great interest in many studies that aim at elucidating the physical mechanisms underlying these properties. Understanding the mechanisms of magneto-optical coupling is essential to advance our knowledge about magnetic materials and improve their potential applications [1-3]. The magneto-optical effect describes the way light interacts with magnetic materials. When light enters a magnetic material, such as magnetic liquids, the interactions between the light and the material can modify the properties of the light, such as the polarization state, spectrum, phase, and intensity [4].

Magnetic fluids consist of colloidal fluids containing nano-sized magnetic particles dispersed in the liquid [5]. They exhibit magneto-optical effects, which were first investigated by Philip et al. in 2008 [6,7]. Magnetic fluids have entered many pioneering applications, such as tunable optical filters [8], optical gratings [9], magneto-optical wavelength filters [10], and optical switches [11].

In magnetic fluids, the refractive index can be sensitive to several factors, including the size, shape, chemical composition, and magnetic properties of the nanoparticles [12]. For the same magnetic fluid, the refractive index is a function of the medium temperature, the concentration of the nanomaterial, and the wavelength of the incident light [13]. This property is useful even in the absence of an external magnetic field [14]. One of the results of applying an external magnetic field to a magnetic fluid is that the magnetic particles are oriented parallel to the magnetic field forming parallel chains [15]. This alignment has been proved to cause changes in the optical refractive index of the fluid [16]. This property can be used to precisely and quickly adjust the refractive index of the magnetic fluids to be invested in many exciting applications [17]. Devices whose properties can be manipulated by changing the refractive index have become important due to their tunability and flexibility [18].

The refractive index of magnetic fluids and its applications have been extensively studied by many researchers to define the mechanisms and the range of adjustment by using external magnetic fields [19]. In these studies, magnetic fluids have been used in the form of thin layers containing a very small amount of fluid [20]. The main idea in these applications is to control the magnitude of the refractive index at specific wavelengths by changing the arrangement of the magnetic particles in the liquid. This tuning is achieved by controlling the strength and direction of an external magnetic field. In these studies, due to the use of small sizes samples, the effect of the external magnetic field is limited to rearranging the nanoparticles [21]. In other words, the particles are not physically moved from one place to another. Hence no local concentration changes are created within the sample [22].

In this work, the dependence of the linear refractive index on temperature, the nanoparticles concentration, and the external magnetic field was studied for relatively large-size samples of Fe_3O_4 nanoparticles suspended in water and methanol.

2. Experimental part

The magnetic Fe_3O_4 nanomaterial was chemically prepared by the co-precipitation method [23,24]. Samples with different concentrations were prepared in water and methanol by dilution. The samples were exposed to ultrasound waves at 40 W for 5 minutes to disintegrate any agglomerated nanoparticles. Absorption spectra within 190-900 nm were measured using a CECIL CE7200 UV-Visible spectrophotometer. Transmission electron microscopy (TEM) measurement was performed for investigating the shape and the size distribution of the particles by using Zeiss-EM10C TEM with 100 kV operating voltage.

As for the detection of the linear refractive index, the experimental setup shown in Fig. (1) was used. In this setup, the deflection of a helium-neon laser (632.8 nm) was used as to sense the changes in the refractive index of the sample. The sample is placed in a 10 mm thick quartz cell. Another laser at 405 nm was used to ensure that the beam-exit surface of the cell is perfectly parallel to the screen. In addition, a laser at 810 nm was used to raise the temperature of the sample when needed. The temperature inside the sample was measured with an accuracy of 0.1 K by using an electronic thermometer installed inside the sample on the side far from the path of the 810 nm laser beam. For uniform heat distribution in the sample, a circulating element was installed next to the thermometer, as shown in Fig. (1).

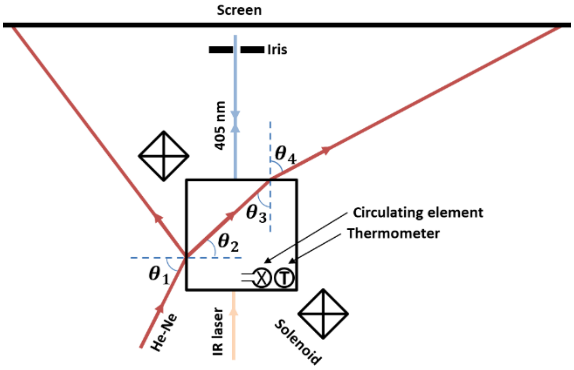

Fig. (1) Scheme of the linear refractive index measurement setup

With reference to Fig. (1), after some simple algebra, the refractive index can be calculated from:

$$n_s = n_o\sqrt{sin^2(\theta_4) + sin^2(\theta_1)} \qquad (1)$$

where, n_s is the linear refractive index of the sample, and n_o is the refractive index of air.

The reflected and refracted He-Ne beams were used to calculate the incident and exit angles (θ_1 and θ_4), respectively, with an accuracy of 9.425×10^{-4} rad. The overall accuracy of calculating the refractive index is $\pm 3.5 \times 10^{-5}$. The variation of the refractive index with time was observed by recording the changes in the position of the refracted beam on the screen with a time resolution of about 30 ms.

3. Results and Discussion

The results of the TEM examination show that the Fe_3O_4 nanoparticles used in this work have irregular shapes with sizes ranging from 8 to 50 nm, as shown in Fig. (2). It can be noted from this figure that, despite the absence of a magnetic field, the particles are linked in the form of chains. This can indicate the presence of residual magnetic hysteresis in these particles, which means that they are closer to having ferromagnetic properties. These chains are redirected when an external magnetic field is applied to be parallel to the field lines. However, by using an ultrasound probe, the particles can be distributed uniformly in the sample.

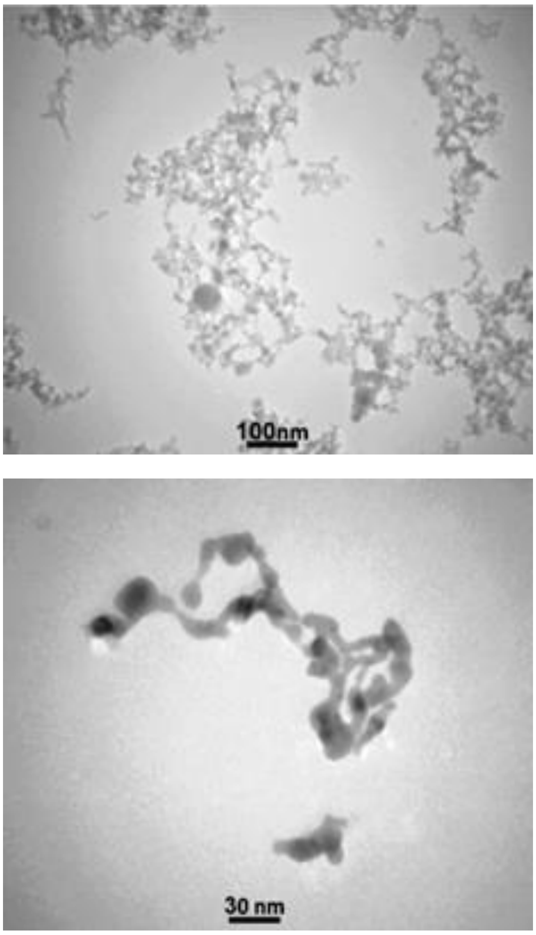

Fig. (2) TEM images for Fe_3O_4 in water

Fe_3O_4 nanoparticles in water and methanol have absorption spectra that fall mostly in the UV region and gradually decrease throughout the visible range and the near-infrared (NIR) region. The highest absorbance is at the wavelength range from 230 to 400 nm, as shown in Fig. (3). It can be seen that the liquid used has a negligible effect on the linear absorption properties of Fe_3O_4 nanoparticles. The spectra are almost identical in both liquids despite their different chemical and physical properties.

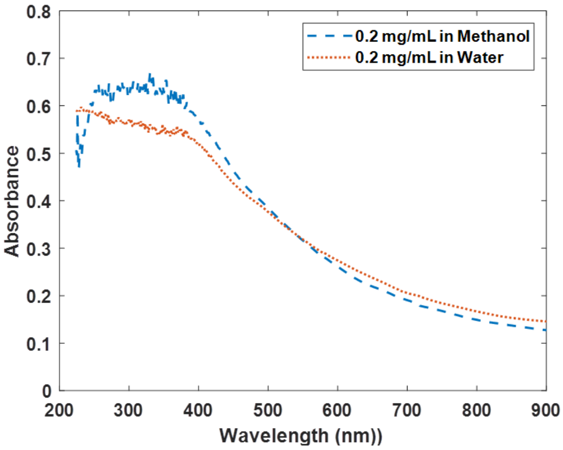

Fig. (3) Linear absorption spectra of Fe_3O_4 nanoparticles

As mentioned previously, Fe_3O_4 particles have been used in many important applications that depend on refractive index tuning. The temperature of the fluids in most of these applications is not controlled. It can change due to the surrounding conditions or due to the absorption of the laser radiation used in the application. To exam the effect of laser radiation (810 nm) on the temperature of liquids containing Fe_3O_4 nanoparticles, hence the refractive index, we used the experimental procedure shown in Fig. (1). In this experiment, the sample volume was about 2 cm^3, and the total surface area was 10 cm^2.

The IR laser beam at 870 mW was directed to pass through the cell, and the changes in temperature and refractive index were recorded as functions of time. Figure (4) shows the temperature changes with time at different concentrations of Fe_3O_4 nanoparticles in water and methanol.

The results show that the temperature of the pure liquids (water and methanol) does not change with time despite the presence of the IR laser. This is due to the weak absorption of the pure liquids at this wavelength. However, the presence of the Fe_3O_4 nanoparticles in the liquids increases the absorption of the laser beam significantly in a way depending on the concentration of the nanomaterial. The laser energy absorbed by the nanoparticles leaks into the liquid in the form of heat, which leads to a rapid increase in the temperature of the medium, as shown in Fig. (4).

The rate of temperature increase depends on a combination including the power of the laser used, the size of the sample, the concentration of the nanomaterial, and the thermal properties of the liquid. This means that applications that use thin films of magnetic material will suffer much greater temperature changes than those shown in Fig. (4). In addition, because we are using a large size sample, the maximum concentration used of nanomaterial is much lower than that used in thin film applications. This means that the effect of the laser beam on these films will be much greater than its effect on the large samples used in this work. Therefore, carful control of the temperature is critically required in such applications.

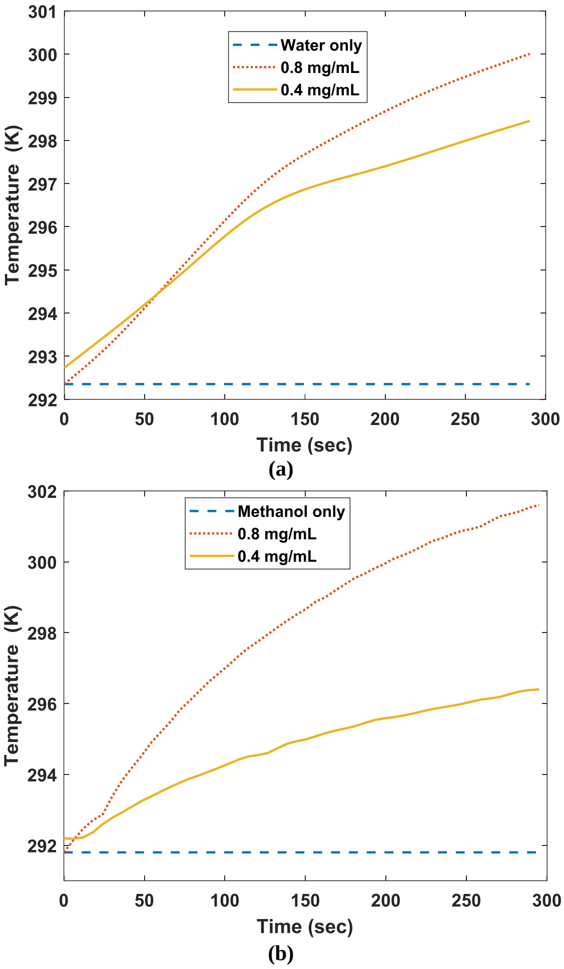

Fig. (4) The change of temperature of (a) water and (b) methanol containing Fe_3O_4 nanoparticles at different concentrations

As the temperature of the sample increases, the refractive index changes in the same manner. Figure (5) shows the change in the refractive index with time for the samples shown in Fig. (4). It can be seen from Fig. (5) that the refractive index changes with time due to the temperature change. The change in methanol is much greater than that in water at the same concentration of nanomaterial. This is due to the different thermo-optical coefficients of methanol and water. Figure (6) shows a comparison between the values of the normalized refractive indices of methanol and water samples containing the same concentration of Fe_3O_4 nanoparticles.

In addition, the results of this work showed that, at the same temperature, the refractive index of liquids containing magnetic nanoparticles is a function of the concentration of these particles. By measuring the refractive index of Fe_3O_4 suspended in water and methanol at different concentrations and different temperatures, the rate of change of the refractive index with temperature and concentration was calculated. In addition, the dependence of the thermal variation of the refractive index (*dn/dT*) the concentration of the magnetic material i.e. ($dn^2/dTdc$), was calculated. The results of these measurements are listed in table (1).

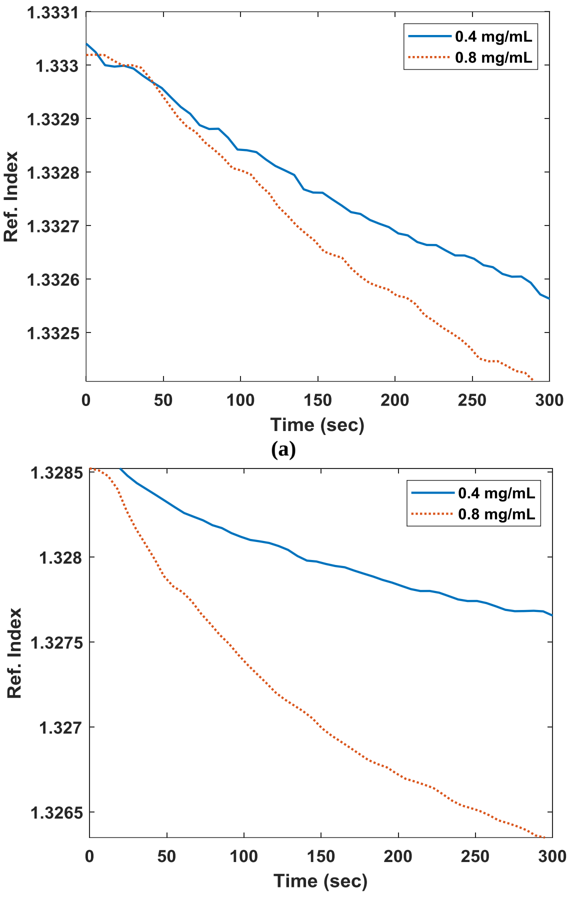

(a)

(b)

Fig. (5) The change of refractive index of (a) water and (b) methanol containing Fe_3O_4 nanoparticles at different concentrations

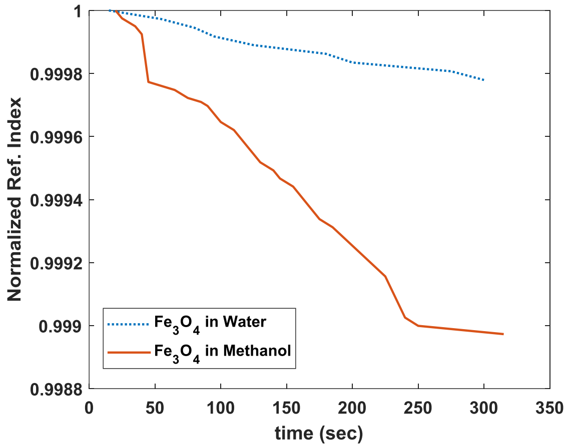

Fig. (6) A comparison between the values of the normalized refractive indices of methanol and water samples containing the same concentration of Fe_3O_4 nanoparticles

Table (1) The refractive properties of Fe_3O_4 nanoparticles in water and methanol

	(*dn/dT*) (K^{-1})	**(*dn/dc*) $(mg/cm^3)^{-1}$**	**($dn^2/dTdc$) $(K.mg/cm^3)^{-1}$**
Fe_3O_4 in water	-1.18×10^{-4}	8.18×10^{-4}	9.45×10^{-5}
Fe_3O_4 in methanol	-4.11×10^{-4}	8.81×10^{-3}	3.15×10^{-4}

The parameter (*dn/dT*) for most liquids is negative due to the change in the density of the liquid and the dependence of the refractive index on the density. (*dn/dT*) values calculated in this work are in very good agreement with the (*dn/dT*) values measured for pure water and methanol [25,26].

The non-zero values of (*dn/dc*) indicate that the addition of nanomaterial to the liquid can change the value of the linear susceptibility of the liquid ($\chi^{(1)}$). The positive values of (*dn/dc*) indicate an enhancement in the induced linear polarization of the liquid. In addition, the value of (*dn/dc*) of methanol is about ten times greater than its value of water, i.e., the same concentration of Fe_3O_4 can induce different levels of effect in the linear response of the host. This can be due to the difference in the physical and chemical properties of the medium in terms of the gathering of liquid molecules around the nanoparticles and the extent to which the properties of the liquid are affected by the impurity. Moreover, the different magnetic properties of water and methanol can lead to large differences in the level of response to the presence of magnetic particles.

Furthermore, the nonzero values of ($dn^2/dTdc$) indicate that the presence of Fe_3O_4 nanoparticles affects the value of the third-order susceptibility of the medium ($\chi^{(3)}$). This effect is not constant but depends on the type of liquid. The positive values of ($dn^2/dTdc$) imply that the absolute value of *dn/dT* decreases as the concentration of nanoparticles increases. This means that the absolute value of the thermally-induced nonlinear refractive index of the medium decreases with the increase of the concentration. This decrease can be due to the changes in the thermal conductivity and specific heat capacity of the liquid induced by the nanoparticles. This level of changes cannot be noticed when performing direct nonlinear measurements because they will be hidden under the huge increase of the medium nonlinearity induced by the increasing linear absorbance of the nanoparticles.

The results of this work can be employed positively in applications using large size samples containing magnetic nanoparticles. In relatively large-size samples, the concentration of magnetic particles in any point of the sample can be easily controlled by using an external magnetic field. In other words, local changes in concentration can be created by physically moving the nanoparticles to a specific direction in the sample. Therefore, the value of the refractive index and the temperature of the medium can be controlled in a specific location inside the sample with high accuracy. Figure (7) shows two trajectories of thermal-induced refractive index changes of samples containing Fe_3O_4 nanoparticles in the presence and absence of an 82 mT external magnetic field. The heating was obtained by an IR laser at 810 nm passing through the sample cell.

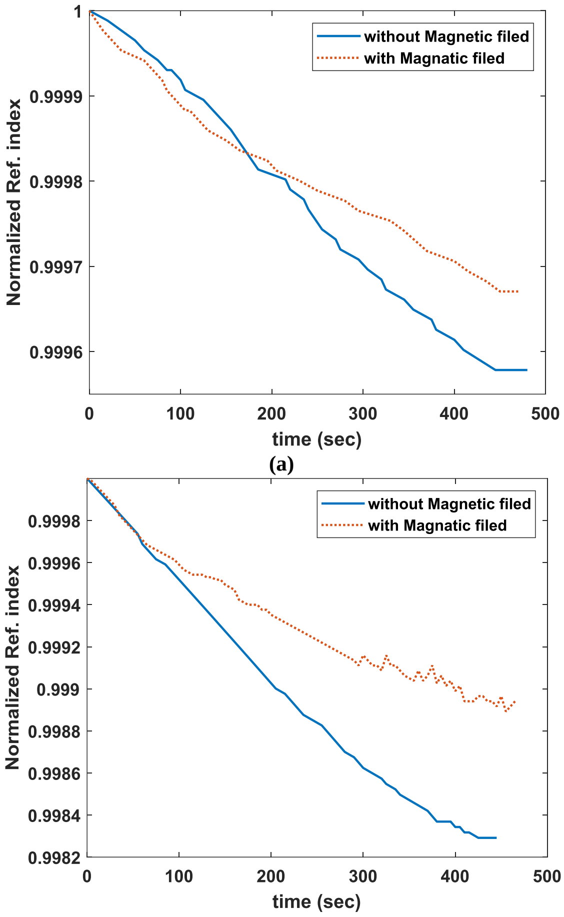

(a)

(b)

Fig. (7) The change of normalized refractive index of (a) water and (b) methanol containing Fe_3O_4 with and without the presence of an external magnetic field

The results shown in Fig. (7) are in a region where the concentration of Fe_3O_4 particles decreases due to the movement of the particles toward the magnetic field. The decrease in the concentration leads to reduce the absorption of laser radiation; thus, lower temperature changes are induced. This change can be reversed to the direction of increasing the concentration by flipping the magnet to the opposite side. Accordingly, this experiment shows the possibility of controlling the refractive index of relatively large-size samples for different applications.

It is worth mentioning that all the magnetic-induced changes in the refractive index detected in this work are due to the change in the local concentration of the nanoparticles. In other words, no direct magnetic effect is observed on the refractive index. In addition, within the concentration range of this study (0-0.8 mg/cm^3), the refractive index is a linear function of the concentration of the magnetic nanoparticles. However, this linearity is not guaranteed at high concentrations. Exploring the properties of high concentrations samples is not possible in the case of thick samples due to the low optical transmittance.

4. Conclusion

The results of this study indicate that magnetic fluids have self-effects that can manipulate their refractive index via temperature changes. These effects depend on the size of the sample, the thermal properties of the liquid, and the concentration of the nanoparticles. In addition, the results indicate that the refractive index of these fluids is a positive function of the concentration of the magnetic nanoparticles. This function strongly depends on the intrinsic properties of the liquid. Moreover, in large-size samples, no direct effects of the magnetic field have been detected on the refractive index. The results of this work reveal the ability of precisely controlling the refractive index of large-size samples of magnetic fluids via inducing local concentration changes.

References

[1] S.-Y. Yang et al., “Magnetically-modulated refractive index of magnetic fluid films”, *Appl. Phys. Lett.*, 81(26) (2002) 4931-4933.

[2] R.A.H. Hassan and F.T. Ibrahim, “Preparation and Characterization of Ni-doped TiO_2 Nanostructures for Surface Cleaning Applications”, Iraqi J. Appl. Phys., 17(1) (2021) 3-8.

[3] O.A. Hammadi, M.K. Khalaf and F.J. Kadhim, “Fabrication of UV Photodetector from Nickel Oxide Nanoparticles Deposited on Silicon Substrate by Closed-Field Unbalanced Dual Magnetron Sputtering Techniques”, Opt. Quantum Electron., 47(12) (2015) 3805-3813.

[4] M. Faraday, “I. Experimental researches in electricity.—Nineteenth series”, *Phil. Trans. Royal Soc. London*, 136 (1846) 1-20.

[5] I. Nkurikiyimfura, Y. Wang and Z. Pan, “Heat transfer enhancement by magnetic Nano fluids—a review”, *Renew. Sustain. Ener. Rev.*, 21 (2013) 548-561.

[6] J. Philip, J.M. Laskar and B. Raj, “Magnetic field induced extinction of light in a suspension of Fe_3O_4 nanoparticles”, *Appl. Phys. Lett.*, 92(22) (2008) 221911.

[7] J.M. Laskar, J. Philip and B. Raj, “Light scattering in a magnetically polarizable nanoparticle suspension”, *Phys. Rev. E*, 78(3) (2008) 031404.

[8] J. Philip and J.M. Laskar, “Optical properties and applications of ferrofluids - a review”, *J. Nano Fluids*, 1(1) (2012) 3-20.

[9] S. Pu et al., “Tunable magnetic fluid grating by applying a magnetic field”, *Appl. Phys. Lett.*, 87(2) (2005) 021901.

[10] T. Liu et al., “Tunable magneto-optical wavelength filter of long-period fiber grating with magnetic fluids”, *Appl. Phys. Lett.*, 91(12) (2007) 121116.

[11] H.-E. Horng et al., “Tunable optical switch using magnetic fluids”, *Appl. Phys. Lett.*, 85(23) (2004) 5592-5594.

[12] J. Gao, H. Gu and B. Xu, “Multifunctional magnetic nanoparticles: design, synthesis, and biomedical applications”, *Accou. Chem. Res.*, 42(8) (2009) 1097-1107.

[13] C.H. Fan and J.P. Longtin, “Laser-based measurement of liquid temperature or concentration at a solid–liquid interface”, *Exp. Therm. Fluid Sci.*, 23(1-2) (2000) 1-9.

[14] M.M. Bilal et al., “Magnetic fluid-based photonic crystal fiber for temperature sensing”, *Opt. Eng.*, 58(7) (2019) 072008-072008.

[15] S. Malynych and I. Moroz, “Time dependent magnetically induced variations in optical transmission of magnetite nanoparticle aqueous suspension”, *Open Phys.*, 10(1) (2012) 159-165.

[16] Y. Zhao et al., “Novel optical devices based on the tunable refractive index of magnetic fluid and their characteristics”, *J. Magn. Magn. Mater.*, 323(23) (2011) 2987-2996.

[17] V. Bashtovoy and B.M. Berkovsky, **“Magnetic Fluids and Applications Handbook”**, Begell House (Danbury, 1996).

[18] A.M. Vengsarkar et al., “Long-period fiber gratings as band-rejection filters”, *J. Lightwave Technol.*, 14(1) (1996) 58-65.

[19] Noor Alhuda H. Hashim and Firas J. Kadhim, “Structural and Optical Characteristics of Co_3O_4 Nanostructures Prepared by DC Reactive Magnetron Sputtering”, Iraqi J. Appl. Phys., 18(4) (2022) 31-36.

[20] O.A. Hammadi and N.E. Naji, “Fabrication and Characterization of Polycrystalline Nickel Cobaltite Nanostructures Prepared by Plasma Sputtering as Gas Sensor”, Phot. Sen., 8(1) (2018) 43-47.

[21] M.A. Hameed, S.H. Faisal, R.H. Turki, “Characterization of Multilayer Highly-Pure Metal Oxide Structures Prepared by DC Reactive Magnetron Sputtering Technique”, Iraqi J. Appl. Phys., 16(4) (2020) 25-30

[22] Noor Alhuda H. Hashim, Firas J. Kadhim and Zinah S. Abdulsattar, “Characterization of Electrochromism and Photoelectrochromism of N-Doped TiO_2 and Co_3O_4 Thin Films Prepared by DC Reactive Magnetron Sputtering: Comparative Study”, Iraqi J. Appl. Phys., 19(1) (2023) 5-12.

[23] T. Ahn et al., “Formation pathways of magnetite nanoparticles by coprecipitation method”, *The J. Phys. Chem. C,* 116(10) (2012) 6069-6076.

[24] M.S. Al-Samak and J.M. Jassim, “Dye-Doped Fe_3O_4 Nanoparticles for Magnetically Controlling Random Laser Parameters at Visible Wavelengths: Literature Review and Experiment”, *Indonesian J. Sci. Technol.,* 7(3) (2022) 497-510.

[25] J.M. Jassim and N.S. Khudhair, “Study the effective a temperature and concentration on refractive index of water by using Michelson interferometer”, *Int. J. Sci. Eng. Res*., 3 (2015) 27-30.

[26] Y. Kohanzadeh, K.W. Ma and J.R. Whinnery, “Measurement of refractive index change with temperature using thermal self-phase modulation”, *Appl. Opt.*, 12(7) (1973) 1584-1587.

IRAQI JOURNAL OF APPLIED PHYSICS
Vol. 19, No. 4B, November 2023, pp. 133-138

Asala R. Lafta
Mohammed D. Noori

Department of Physics,
College of Science,
University of Thi-Qar,
Nasiriyah, Thi-Qar, IRAQ

Thermoelectric Performance of Metallophthalocyanine Molecular Junctions with CIP and CPP Configurations

Normally, most of the previous studies focused on studying the quantum transport properties of metallophthalocyanines (MPcs) with the plane of the skeleton aligned parallel to the direction of charge transport, where we can say the current in plane (CIP). Here we will compare the electrical and thermoelectric properties of CIP MPcs with the structure of the current perpendicular to the plane (CPP). Our results show that the transport from CIP to CPP metallophthalocyanine (MPc, M=Fe, Co, and Cu) configurations leads to a decrease in both electrical and thermal conductivity. Moreover, a big change in the magnitude and sign of thermopower S As a result, the CPP MPc configurations show low ZT values around Fermi energy. According to this result, the CIP MPcs are considered the preferred candidate for high thermoelectric applications compared with the CPP.

Keywords: Metallophthalocyanine; Thermoelectricity; Thermal conductivity; Electrical conductance
Received: 09 August 2023; **Revised:** 21 August 2023; **Accepted:** 28 August 2023

1. Introduction

The thermal electronic field is receiving increasing interest from materials scientists and engineers as a result of the constant rise in thermal stresses placed on the structures of devices and materials. Research into thermoelectric qualities, the identification of materials with high thermal efficiency, and the production of electricity from waste heat has attracted a lot of attention [1–3]. The Seebeck effect, which was introduced in the early nineteenth century, is where the fundamental idea of thermoelectricity originates [4]. The dimensionless thermoelectric value that determines the refractory material's effectiveness is a figure of merit ZT, which is calculated by ($ZT= S^2GT/K$), where S is the Seebeck coefficient, G is the electrical conductance, T is the temperature, and k is the thermal conductivity [5-8].

Utilizing organic materials is becoming more popular as a way to avoid the many drawbacks of inorganic materials, such as their toxicity, inability to save energy, and high cost. Additionally, by taking into account the nanostructure properties of inorganic materials, thermoelectric properties can be adjusted [9, 10]. As a result, it is particularly interesting to take advantage of the properties of molecules linked to nanogap electrodes, which serve as a type of nanodevice, at room temperature. So far, numerous theoretical and experimental investigations have been conducted to create and regulate electronic molecules [11-18]. They have been adjusted for potential uses in molecule wires and other nano-electronic circuits [19]. Electrodes [20, 21], quantum dots [22, 23]. Due to its exceptional high chemical and thermal stabilities as well as excellent geometrical structure, phthalocyanine (Pc) has received a lot of interest [24, 25]. The electrical, structural, magnetic, chemical, and transport properties of phthalocyanines can be adjusted by adding a metallic ion to the center. These substances, referred to as metallophthalocyanines (MPc), have been taken into consideration for a variety of applications, including organic thin film transistors [26], chemical detectors [27], and photovoltaic and optoelectronic devices [1,28].

The molecular device we study in this work is illustrated schematically in Fig. (1). The geometry of each MPc nanoconstriction junctions was relaxed to a force tolerance of 20 meV/Å using the SIESTA implementation of density functional theory (DFT), with a double-ζ polarized basis set (DZP) and generalized gradient functional approximation (GGA-PBE) for the exchange and correlation functionals, which is applicable to arbitrary geometries.

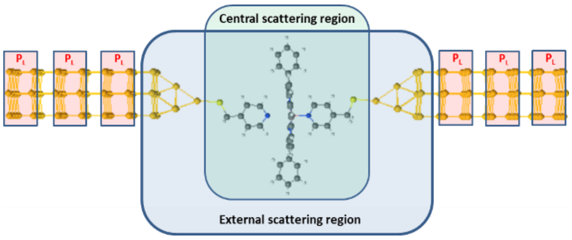

Fig. (1) The lead, external scattering region and central scattering region in our structure

A real-space grid was defined with an equivalent energy cutoff of 150 Ry. So far, in most of the previous studies [29-٣٠], the quantum transport properties have been done on MPc structures with the plane of the skeleton aligned parallel to the direction of charge transport, where we can say the current in plane (CIP), as shown in figures (1a) and (1b). In what follows, we will compare the electrical and thermoelectric properties of CIP MPcs with the structure of the current perpendicular to the plane (CPP) (Fig. 1c).

In this work, we report a joint theoretical study of CIP conductance [33] with our new study to investigate the characteristics of CPP MPc configurations for M=Fe, Co, and Cu. Most of studies that deal with metallo-molecules focus on the transition metals that end with d-orbital. Here we used different transition central metals with even/odd number of electrons in the d-orbital (Fe^{26}, Co^{27}, and Cu^{29}).

2. Method

At the beginning, all the structures of CIP and CPP MPc molecular geometry that shown in Fig. (1) was optimized before building the junction model. Then, the geometry of each structure that consists of two gold electrodes and MPc molecules was optimized again as a one system.

A generalized functional gradient was used to determine the correlation of functional exchange for “the SIESTA (GGA)” [3٢], and Gollum code [3٣] was used to study the zero-bias electronic “transport T(E)”, and the whole structure of (gold-MPc-gold) was Hamiltonian explained using the SIESTA software [3٤].

To calculate thermoelectronic properties of the molecules in the junction from the converged DFT calculation, the underlying mean-field Hamiltonian (H) was combined with quantum transport code Gollum to calculate the transmission coefficient T(E) for electrons of energy E passing from the source to the drain. In the Fig. (1), we have shown the lead, external scattering region and central scattering region in our structure.

After we obtain the mean-field Hamiltonian H then combined it with the quantum transport code, GOLLUM to calculate the transmission coefficient $T_{el}(E)$. The electrical conductance G was computed by using Landauer formula. We compute the thermopower S over a wide range of Fermi energies by using equation

$$S = -\frac{1}{eT}\frac{L_1}{L_0} \qquad (1)$$

where T is the temperature, e is electron charge and L_n can be calculated as

$$L_n = \int_{-\infty}^{\infty} (E - E_F)^n \, T(E) \left(\frac{\partial f(E,T)}{\partial E}\right) dE \qquad (2)$$

where $f(E,T)$ is the Fermi-Dirac probability distribution function

So the key quantity is transmission coefficient T(E) when we obtain T(E) then we can computed L_n which means compute electrical conductance G, thermopower S, and thermal conductivity K.

After obtained the transmission coefficient T(E) the Landauer formula is used to get the electrical conductance G. Then we compute Seebeck coefficient S, Finally we used $ZT=S^2GT/K$ to get ZT.

3. Results and Discussion

Figure (2) shows the optimum structures of CIP MPcs in cis configuration (Fig. 2a,) and trans configuration (Fig. 2b) and (Fig. 2c) illustrate CPP MPcs. In what follows we will compare the electrical and thermoelectric properties of these MPc configurations for M=Fe, Co, and Cu. For all structures of Fig. (2).

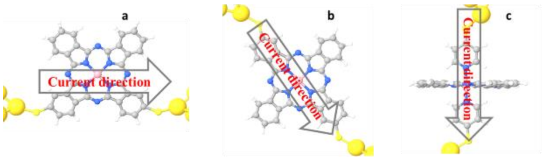

CIP- cis Metallophthalocyanine CIP- trans Metallophthalocyanine CPP Metallophthalocyanine

Fig. (2) Structure of metallophthalocyanine (MPc) molecule sandwiched between two gold electrodes in three different configurations (a)CIP-cis, (b)CIP-trans, and (c) CPP

Figure (3) shows the electronic transmission which is clearly shows the change in the spintronic state when we moved from cis, to trans CIP MPCs (planar structures), or even to CPP MPcs (axial structures). As mentioned in the introduction, the electronic transport properties of cis, and trans CIP MPcs have been studied theoretically in the [3١]. Contrary to CIP MPcs where all cases (CIP-cis, and CIP-trans) show spintronic properties, in CPP MPcs only iron MPcs shows non spintronic properties where both the spin up (black dotted line) and the spin down (red line) transmission coefficient carves are identical. This can be attitude to the change of energy level diagram between planar structure (CIP) and axial octahedral structure (CPP) cases.

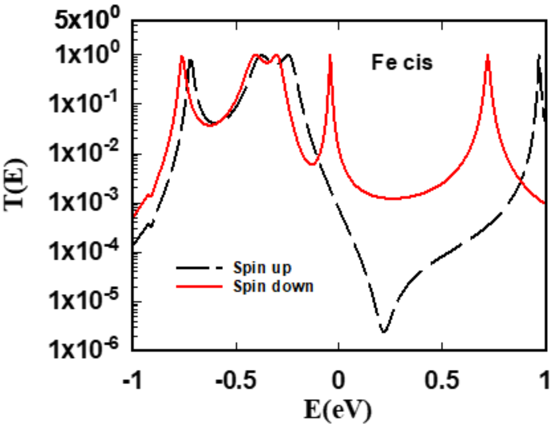

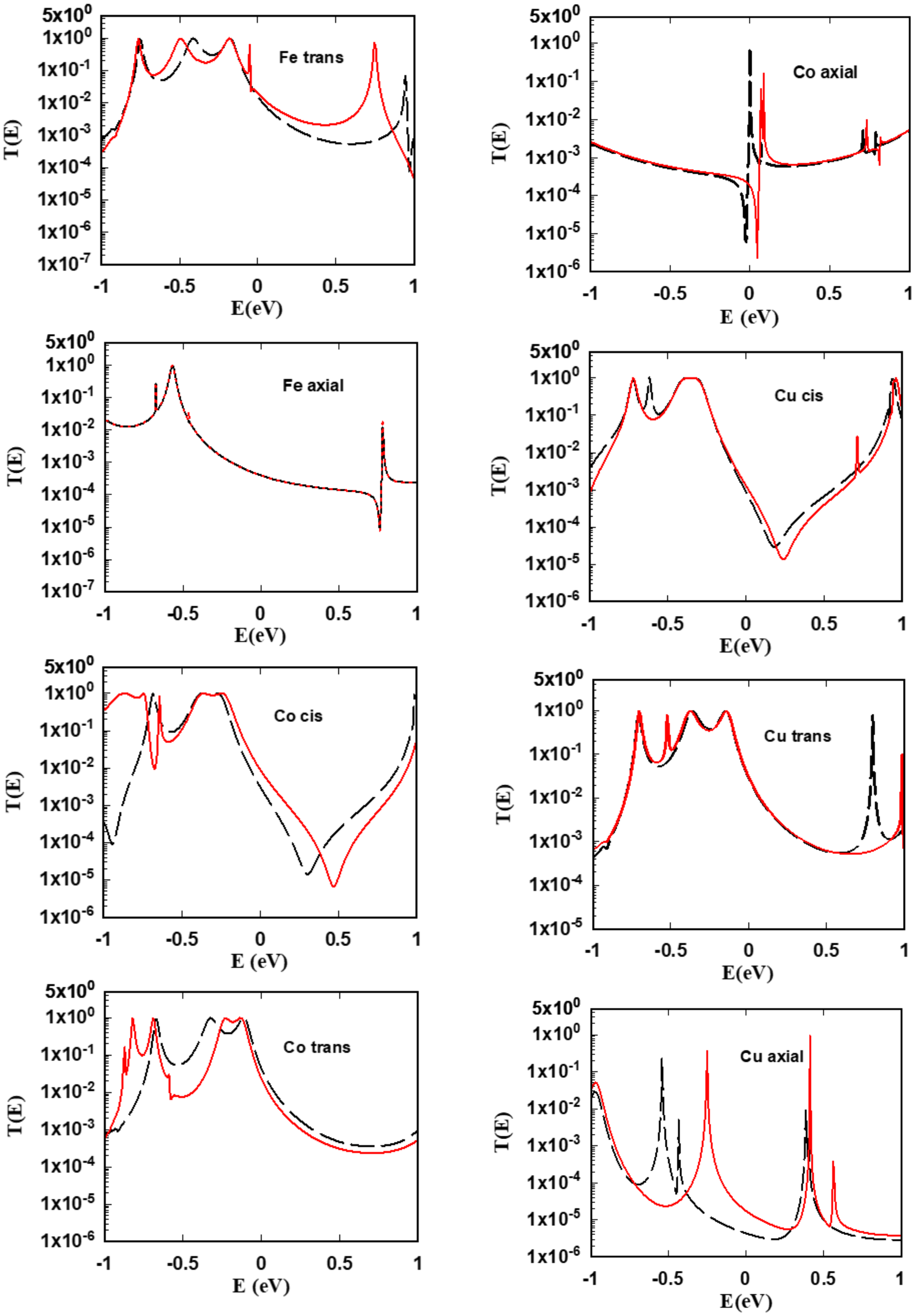

Fig. (3) Electron transmission coefficient of MPc CIP-cis, and CIP-trans and CPP (axial) configurations

Figure (4) shows the corresponding room temperature electrical conductance as a function of energy. Figure (4c) shows that the electrical conductance for all cases (M=Fe, Co, and Cu) in the CIP MPcs configurations have almost higher values than the CPP MPc configurations around Fermi energy E=0 eV.

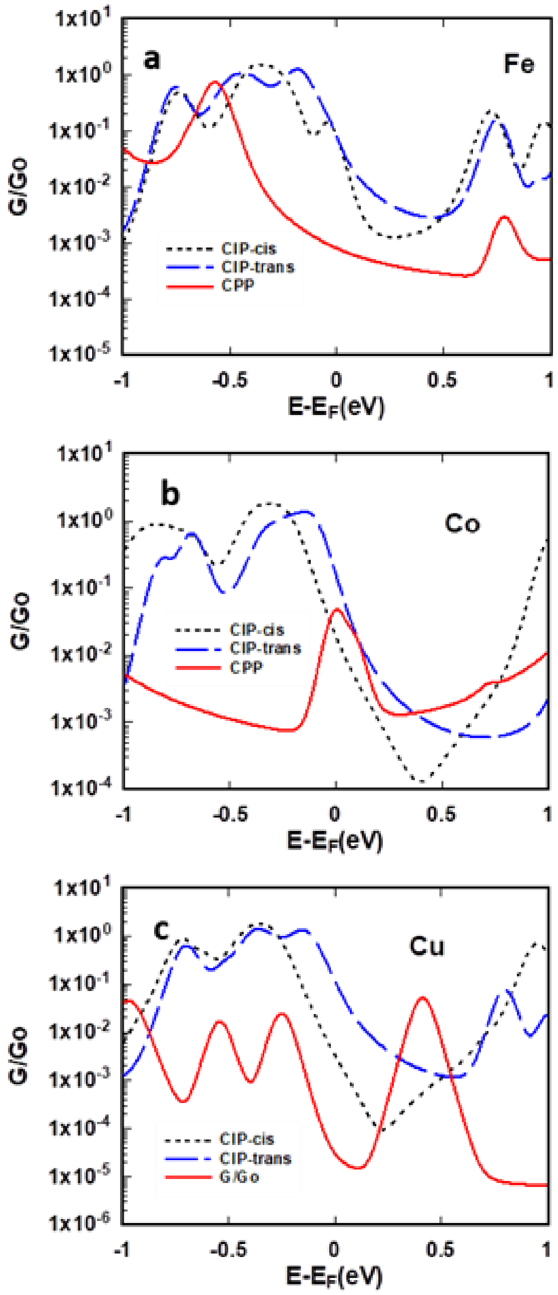

Fig. (4) Room temperature electrical conductance of MPc CIP-cis, and CIP-trans and CPP (axial) configurations

Figure (5) shows the thermal conductivity versus energy. It clear from Fig. (5a-c) that there is a huge decrease in thermal conductivity when we moved from CIP MPc to CPP MPc configurations for all cases (M=Fe, Co, and Cu).

To investigate the thermoelectric properties of all configurations, we have obtained the Seebeck coefficient (S) as shown in Fig. (6) as a function of energy. Figure (6a-c) state that both the magnitude and sign of (S) are sensitive to configuration of the junction in other words S can be tended by moved from CIP –cis to CIP-trans or even to CPP MPc. Figure (7) shows the figure of merit (ZT) as a function to energy. Figure (7a-c) states that the ZT values for all cases (M=Fe, Co, and Cu) in the CIP MPcs have lower values than the CPP MPcs especially in small window around Fermi energy E=0 eV.

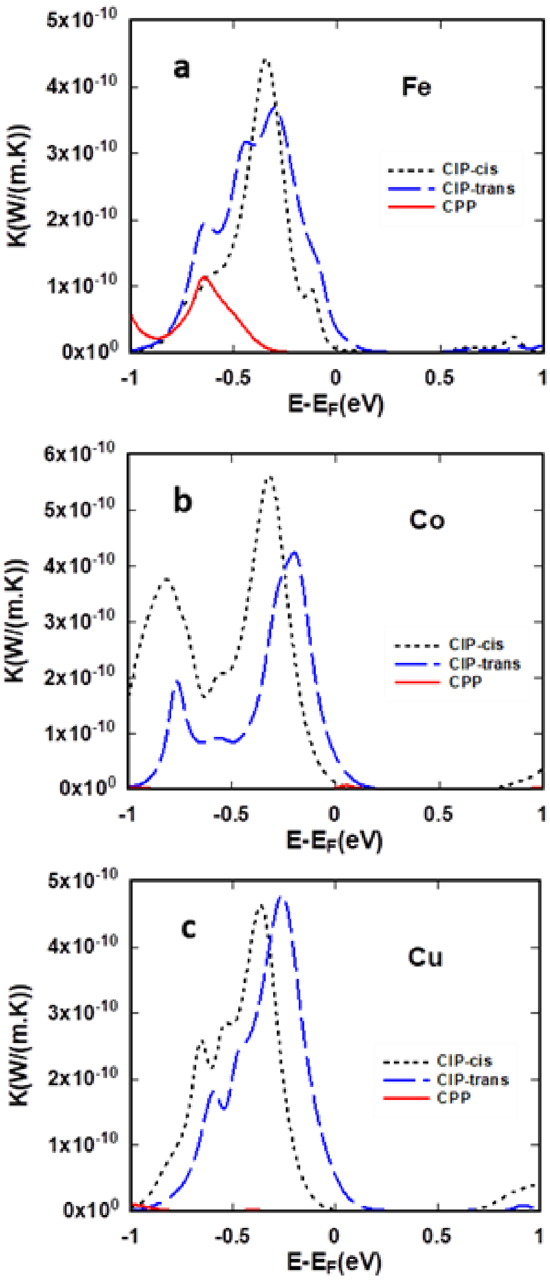

Fig. (5) Thermal conductivity of MPc CIP-cis, and CIP-trans and CPP (axial) configurations

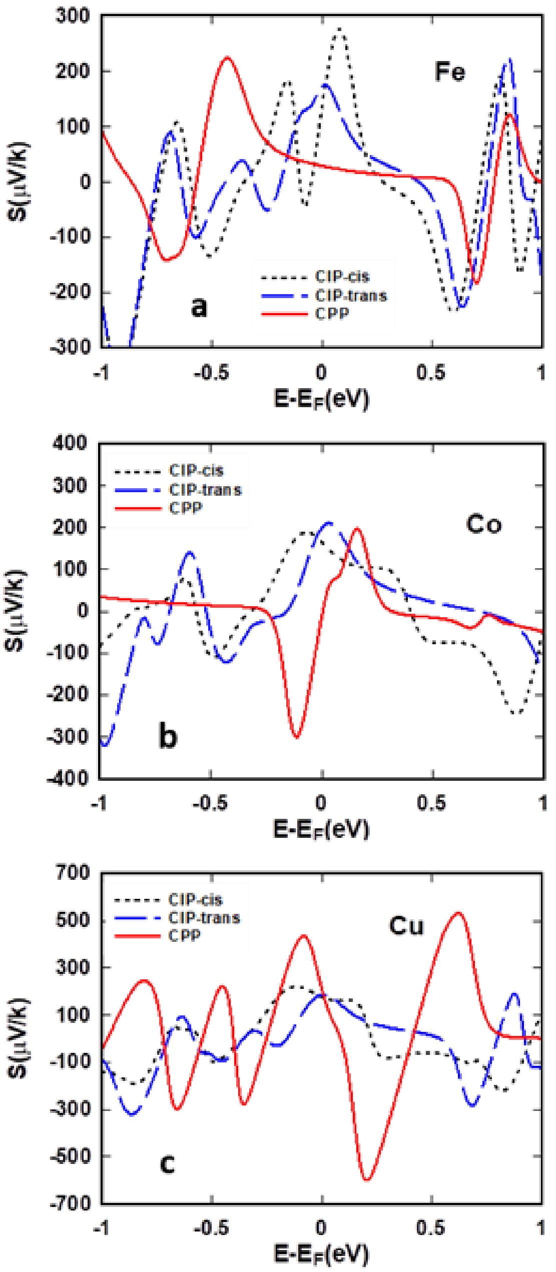

Fig. (6) Seebeck coefficient (S) curves of MPc CIP-cis, and CIP-trans and CPP (axial) configurations

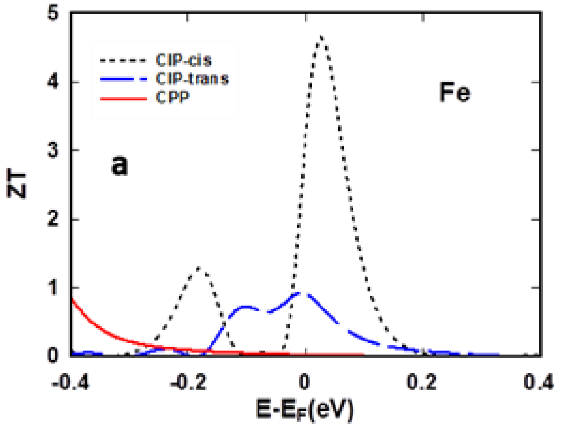

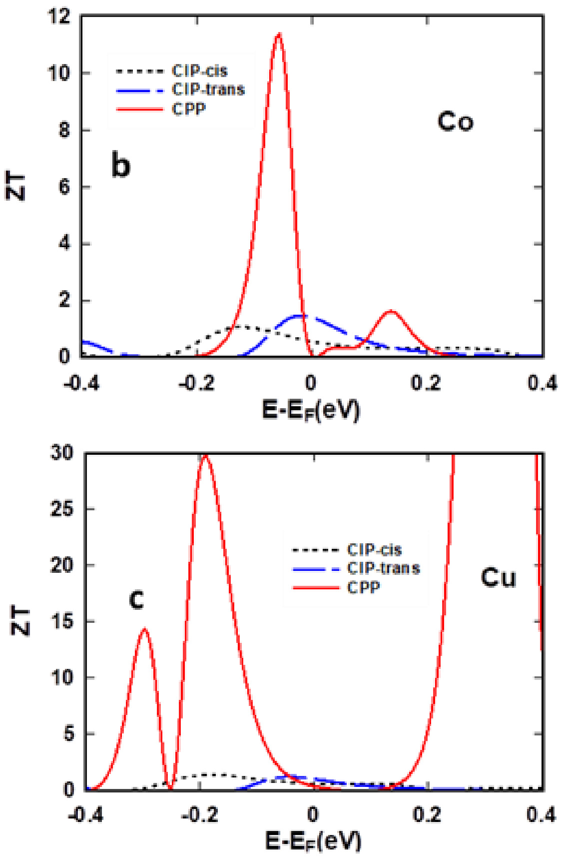

Fig. (7) Room temperature figure of merit ZT of MPc CIP-cis, and CIP-trans and CPP (axial) configurations to (a) Fe and (b) Co and (c) Cu

4. Conclusions

Here, we have investigated the electric and thermoelectric properties of MPc with two different molecular structures (CIP and CPP). The results showed that the transport from CIP MPc to CPP MPc leads to reduce both electrical and thermal conductivities. As a result, the CPP MPc configurations show low ZT values around Fermi energy. According to these results, CIP MPc configurations are identified as the favored candidate for high thermoelectric single-molecule devices.

Acknowledgement

Authors express heartfelt gratitude to the Department of Physics, College of Science at University of Thi Qar for supporting our research project. This research is part of the master graduation requirements.

References

[1] M.D. Noori et al., “The effect of anchor group on the phonon thermal conductance of single molecule junctions”, *Appl. Sci.*, 11 (2021) 1066.

[2] M.D. Noori and A.A. Al-Jobory, “Tuning the Thermoelectric Properties of Ferrocene Molecular Junctions”, *IOP Conf. Ser.: Mater. Sci. Eng.*, 454(3) (2018) 012143.

[3] L. Chen, R. Liu and X. Shi, “Organic thermoelectric materials”, Ch. 6, in **Thermoelectric Materials and Devices**, Elsevier (2021) 183-219.

[4] W. Zhou et al., “Seebeck-driven transverse thermoelectric generation”, *Nat. Mater.*, 20(4) (2021) 463-467.

[5] L. Al-Badry, “Theoretical Treatment for Electron Transport throughout Molecular Wire Bridge”, *Univ. Thi-Qar J. Sci.*, 4 (2014) 128-132.

[6] A.A. Al-mebir et al., “Tuning the Electrical and Thermoelectric Properties of Phthalocyanine and Metallo-Phthalocyanine Molecular Junction”, *J. Phys.: Conf. Ser.*, 1999 (2021) 012036.

[7] R.H. Sakban et al., “Radical Enhancement Electric and Thermoelectric Efficiency of Graphene Nano constrictions”, *Solid State Technol.*, 63(1) (2020) 1788-1793.

[8] T.A. Hussein and M.D. Noori, “Investigation Electrical and Thermoelectrical properties of Ferrocene in staggered and eclipsed conformations”, *J. Phys.: Conf. Ser.*, 1973 (2021) 012055.

[9] K. Yanagi et al., “Tuning of the thermoelectric properties of one-dimensional material networks by electric double layer techniques using ionic liquids”, *Nano Lett.*, 14(11) (2014) 6437-6442.

[10] B. Poudel et al., “High-thermoelectric performance of nanostructured bismuth antimony telluride bulk alloys”, *Science*, 320(5876) (2008) 634-638.

[11] M. Noori et al., “Stable-radicals increase the conductance and Seebeck coefficient of graphene nanoconstrictions”, *Nanoscale*, 10(40) (2018) 19220-19223.

[12] E. Leary et al., “Bias-driven conductance increase with length in porphyrin tapes”, *J. Amer. Chem. Soc.*, 140(40) (2018) 12877-12883.

[13] M.D. Noori, “Quantum Theory of Electron Transport through Photo-Synthetic Porphyrins”, Doctoral thesis, Lancaster University (UK, 2017) p. 133.

[14] A.A. Al-Jobory et al., “Tuning electrical conductance of molecular junctions via multipath Ru-based metal complex wire”, *Indian J. Phy.*, 94(8) (2020) 1189-1194.

[15] A.A. Al-Jobory and M.D. Noori, “Electrical and thermal properties of $GaAs_{1-x}P_x$ 2D-nanostructures”, *Euro. Phys. J.*, 73 (2019) 1-4.

[16] R.C. Johnson, “A simple approach to crystal field theory”, *J. Chem. Edu.*, 42(3) (1965) 147.

[17] Q. Zhou et al., “Electronic Structure of Metallophthalocyanines, MPc (M= Fe, Co, Ni, Cu, Zn, Mg) and Fluorinated MPc”, *J. Phys. Chem. A*, 125(19) (2021) 4055-4061.

[18] E. Leary et al., “Detecting mechanochemical atropisomerization within an STM break junction”, *J. Amer. Chem. Soc.*, 140(2) (2018) 710-718.

[19] M. Kiguchi, **“Single- Molecule Electronics: An Introduction to Synthesis, Measurement and Theory”**, Kiguchi, M. (ed.), Springer (Singapore, 2016) 87-116.

[20] S.-H. Ke et al., “Models of electrodes and contacts in molecular electronics”, *J. Chem. Phys.*, 123(11) (2005) 114701.

[21] G. Schull et al., “Atomic-scale engineering of electrodes for single-molecule contacts”, *Nat. Nanotechnol.*, 6(1) (2011) 23-27.

[22] A.A.K. Al-mebir and S.A. Al-Saidi, “Tuning Optoelectronic Properties of Double Quantum Dot Structure Using Tight-Binding Model for Photo-Electric Applications”, *NeuroQuantol.*, 19(3) (2021) 1.

[23] S.A. Al-Saidi and A.A.K. Al-mebir, “Asymmetric Double Quantum Dot Structure as Nanoscale Diode”, *Univ. Thi-Qar J. Sci.*, 13(4) (2018) 1-17.

[24] N.B. McKeown, **“Phthalocyanine Materials: Synthesis, Structure and Function”**, Cambridge University Press, Cambridge (UK, 1998), Ch. 1, 7, p. 1, 3, 144.

[25] I.M. Denekamp et al., “A simple synthesis of symmetric phthalocyanines and their respective perfluoro and transition- metal complexes”, *Appl. Organomet. Chem.*, 33(5) (2019) e4872.

[26] N.T. Boileau et al., “Metal phthalocyanine organic thin-film transistors: Changes in electrical performance and stability in response to temperature and environment”, *RSC Adv.*, 9(37) (2019) 21478-21485.

[27] M. Chaabene et al., “New zinc phthalocyanine derivatives for nitrogen dioxide sensors: A theoretical optoelectronic investigation”, *J. Mol. Graph. Model.*, 88 (2019) 174-182.

[28] Z.U. Islam et al., “Fabrication and photovoltaic properties of organic solar cell based on zinc phthalocyanine”, *Energies*, 13(4) (2020) 962.

[29] C. Fang et al., “Intermolecular coupling enhanced thermopower in single-molecule diketopyrrolopyrrole junctions”, *Nat. Sci. Open*, 2(1) (2023) 20220039.

[30] M. Noori et al., “High-performance thermoelectricity in edge-over-edge zinc-porphyrin molecular wires”, *Nanoscale*, 9(16) (2017) 5299-5304.

[31] A.R. Lafta, “High Thermoelectric Performance of Metallophthalocyanine Molecular Junctions with cis and trans Configuration”, *Eurasian J. Phys. Chem. Math.*, 16 (2023) 46-53.

[32] J.P. Perdew et al., “Generalized gradient approximation made simple”, *Phys. Rev. Lett.*, 77(18) (1996) 3865-3868.

[33] J. Ferrer et al., “GOLLUM: a next-generation simulation tool for electron, thermal and spin transport”, *New J. Phys.*, 16(9) (2014) 093029.

[34] J.M. Soler et al., “The SIESTA method for ab initio order-N materials simulation”, *J. Phys.: Cond. Matter*, 14(11) (2002) 2745.

IRAQI JOURNAL OF APPLIED PHYSICS
Vol. 19, No. 4B, November 2023, pp. 139-144

Raghad H. Ahmed [1]
Seham A. Hashem [1]
Entidhar M. Zghair [2]

[1] *Department of Technical Electronic, Technical Instructors Training Institute, Middle Technical University, Baghdad, IRAQ*
[2] *Department of Technical Electrical, Technical Instructors Training Institute, Middle Technical University, Baghdad, IRAQ*

Nonlinear Control Back Stepping Controllers for Max Power Point Tracking in Photovoltaic Systems under Variable Environmental Situations

The proposed solution is a nonlinear back stepping controller that employs a DC-DC buck converter to extract the optimal amount of energy from a PV array. Using data collected from the characteristic curves of the PV array, the controller formulates a regression model to serve as a voltage standard for measuring MPP changes. The system's stability is ensured used Lyapunov's roles for stability. The test outcomes demonstrate that the suggested controller can efficiently and swiftly track the MPP. To further validate the results, in this study, we evaluate the control method against the standard perturbation and observation (P&O) method when the environment changes quickly. In general, the nonlinear back stepping controller proposed provides an efficient solution for MPPT in PV systems. With variable power sources, maximum power point tracking (MPPT), or sometimes simply power point tracking (PPT), is a method used to maximize energy extraction when circumstances change. In addition to the more well-known PV solar systems, the technique may be used to thermophotovoltaics, optical power transmission, wind turbines, and photovoltaic (PV) solar systems..

Keywords: Max power point tracking; Photovoltaics; Back stepping; Buck converter
Received: 13 August 2023; **Revised:** 26 August 2023; **Accepted:** 02 September 2023

1. Introduction

To stop the damage to the environment that comes from people's reliance on fossil fuels, we need renewable energy sources, especially solar energy. Photovoltaic (PV) cells, which turn solar energy into electricity because they have a lot of energy potential, are a good way to turn solar energy into electrical energy. But PV cells have nonlinear power characteristics that change depending on things like temperature and light, which makes it hard to get the most power out of them. The amount vary of solar energy that a PV cell turns into useful power is called its optimization of transfer, and different ways have been found to get the most power out of PV cells in order that they could work at their most efficient. The optimum power point of a PV array is the working point at which it can produce the most power, and the voltage at which the PV module could generate the most power is known as the highest power voltage [1]. Since the greatest strength point changes built on the environment, a way to keep track of it is needed. Overall, the paragraph emphasizes the need for efficient techniques to derive maximum power from PV cells as a means to surmount the limitations of their nonlinear power characteristics and operate them at peak efficiency [2], as illustrated in Fig. (1) [3]. The maximum power at the greatest radiance Level is shown in Fig. (1). The output power decreases as irradiance decreases [3].

A nonlinear back stepping controller may be used for optimal energy point monitoring in a photovoltaic (PV) system. Variations in environmental situations, factors which include solar radiation and temperature affect the quantity of energy produced by photovoltaic systems. To meet the growing energy demand, the photovoltaic system must work at its highest power point (MPP), which varies depending on the demand and environmental factors.

Different techniques have been proposed in the literature for achieving optimal power point monitoring [4,5]. Perturb and Observe (P&O) This is among the greatest widely used methods for maintaining optimum efficiency in photovoltaic cells [6]. in this method, a small perturbation is implemented to the running point of the PV module, and the resulting power change is observed [7]. The direction of the perturbation is then adjusted to move towards the maximum power point [٨].

The regression plane is a statistical model that uses multiple input variables (in this case, irradiance and temperature) to predict an output variable (the peak power voltage) [٩]. By fitting the sample values to a curve plane, we can estimate maximum electricity voltage for a given combination of irradiance and temperature, even if we do not have data for that specific point [١٠].

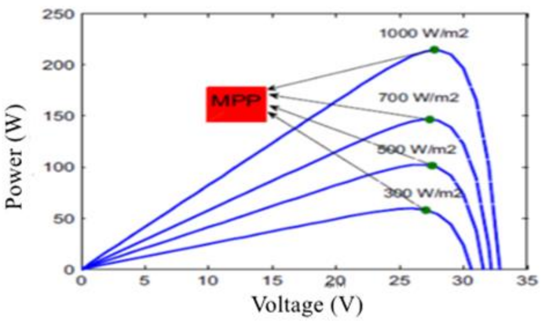

Fig. (1) Photovoltaic module power and voltage characteristics curves [3]

The PV symptom profiles are produced by altering the temperature from 5 to 70°C at a consistent 800 W/m^2 irradiance. Similarly, by altering irradiance levels from 200 to 1200 W/m^2 at a steady temperature of 20°C, more data points were achieved [1١],. The data usual attained from these property curves is utilized to produce a regression graph that allow the necessary peak power voltage V_{PVR}. Figure (2) depicts the derived regression plane [12], which is described using the following formula:

$$V_{PVR} = 322 - 1\ 31\ T - 0\ 00037 I \qquad (1)$$

where T is the temperature and I is the irradiance

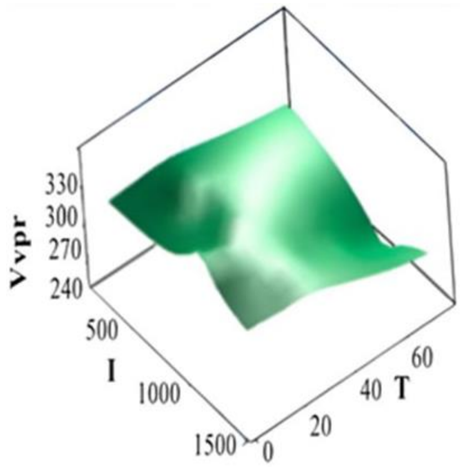

Fig. (2) Surface graph of VPVR against T in the I regression model [12]

2. 2.Material and Methods

Buck is a type of DC-DC transformer that is often called a step-down converter because the voltage it puts out is lower than the voltage it takes in. The circuit diagram for this device is depicted in Fig. (3). In this article, the Buck converter is assumed for continuous conduction mode to operate (CCM). Mode 1 and Mode 2 are double operational modes for the Buck converter [13,14]. During mode 1, the switch S of the Buck converter is on while its diode D is off. We can derive equations that characterize the actions of the Buck converter in this mode of operation by applying Kirchhoff's voltage and current rules [15].

$$i_{C1} = i_{PV} - i_L, \quad V_L = v_{C1} - v_{C2}, \quad i_{C2} = i_L - \frac{v_{C2}}{R}. \qquad (2)$$

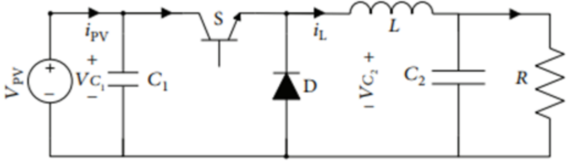

Fig. (3) Buck conversion

When operating in style 2, Change S is not conducting while Diode D is forward biased and therefore conducting. Practise Kirchoff's voltage and current laws to analyse the circuit and ascertain the behaviour of the components [16]. The current flowing through the circuit can be determined by summing the currents at each node, while the voltage across each component can be determined by accounting for the voltage drops and rises across each component in the circuit [17,18]. Using these principles, we can calculate the current and voltage values in the circuit and predict the behavior of the system in mode 2.

$$\mathrm{i}_{C1} = \mathrm{i}_{PV}, \quad \mathrm{v}_L = \mathrm{v}_{C2}, \quad \mathrm{i}_{C2} = \mathrm{i}_L - \frac{\mathrm{v}_{C2}}{\mathrm{R}}. \qquad (3)$$

Using the inductor's volt-second stability as well as the capacitor's energy stability yields equations for analyzing circuits and understanding their behavior. Balancing volt-seconds in an inductor with capacitor charge determines frequency response and is crucial for designing and optimizing circuits. Knowing these principles is essential for working with electronic circuits. We can write:

$$\frac{d_{vC1}}{d_t} = \frac{i_{PV}}{C_1} - \frac{i_L}{C_1}u, \quad \frac{d_{i_L}}{d_t} = \frac{v_{C1}}{L}u - \frac{v_{C2}}{L}, \quad \frac{dv_{C2}}{d_t} = \frac{i_L}{C_2} - \frac{v_{C2}}{RC_2}. \qquad (4)$$

After optimizing the design over one switching duration and supposing that x_1, x_2, x_3, and μ represent an average values of v_{C1}, i_L, v_{C2}, as well as u, severally, Those expressions may be recorded as:

$$x_1 = \langle v_{C1} \rangle, \quad x_2 = \langle i_L \rangle, \quad x_3 = \langle v_{C2} \rangle, \quad \mu = \langle u \rangle \qquad (5)$$

measure the time derived of Eq. (5), with Eq. (4), become

$$x_1^* = \frac{i_{pv}}{c_1} - \frac{x_2}{c_2}\mu, \quad x_2^* = \frac{x_1}{L}\mu - \frac{x_3}{L}, \qquad (6)$$

$$x_3^* = \frac{x_2}{c_2} - \frac{x_3}{R\ c_2}$$

Using the back stepping method, a nonlinear controller effectively follows the relation made by the regression plane. The controller figures out how much power to send to the buck converter switch based on what comes in. So that there isn't any confusion during controller derivation, the reference made in Section 2 is called x_{1ref} and is called the PVR voltage reference [19]. Suppose e1 is disparity among the real and necessary output voltage of the PV array.

$$e_1 = x_1 - x_{1ref} \qquad (7)$$

The objective is to zero out the error signal e_1. The derivative of Eq. (7) in terms of time yields

$$e_1^* = x_1^* - x_{1ref}^* \qquad (8)$$

Inserting Eq. (6) in Eq. (8) gives

$$e_1^* = \frac{i_{pv}}{C_1} - \frac{x_2}{C_1}\mu - x_{1ref}^* \qquad (9)$$

Consider V_1 to stay a positive, certain Lyapunov potential work for testing the regression of e_1 to 0.

$$v_1 = \frac{1}{2}e_1^2 \qquad (10)$$

For asymptotic constancy, the Lyapunov role's derivative necessity be negatively certain. Using the time derivative of Eq. (10)

$$V_1^* = e_1 e_1^* \qquad (11)$$

Using Eq. (9), we get

$$V_1^* = e_1\left(\frac{i_{pv}}{C_1} - \frac{x_2}{C_1}\mu - x_{1ref}^*\right) \qquad (12)$$

For V_1^* to be negative definite, let

$$\frac{i_{pv}}{C_1} - \frac{x_2}{C_1}\mu - x_{1ref}^* = -K_1 e_1 \qquad (13)$$

So that V_1^* becomes

$$V_1^* = -K_1 e_1^2 \qquad (14)$$

Rewriting Eq. (13) as

$$x_2 = \frac{C_1}{\mu}\left(K_1 e_1 + \frac{i_{pv}}{C_1} - x_{1ref}^*\right) \qquad (15)$$

Let Eq. (15) remain the situation current for inductor, assumed through

$$\beta = \frac{C_1}{\mu}\left(K_1 e_1 + \frac{i_{pv}}{C_1} - x_{1ref}^*\right) \qquad (16)$$

Let us describe the mistake e_2 to path x_2 to β

$$e_2 = x_2 - \beta \qquad (17)$$

Rewriting Eq. (17) as

$$x_2 = e_2 + \beta \qquad (18)$$

Putting Eq. (18) in Eq. (9) gives

$$e_1^* = \frac{i_{pv}}{C_1} - \frac{e_2+\beta}{C_1}\mu - x_{1ref}^* \qquad (19)$$

Adding from Eq. (16) to Eq. (19). Following simplification, we obtain

$$e_1^* = -K_1 e_1 - \frac{e_2}{C_1}\mu \qquad (20)$$

Hence, equation (21) becomes

$$V_1^* = e_1 e_1^* = e_1\left(-K_1 e_1 - \frac{e_2}{C_1}\mu\right) \qquad (21)$$

$$V_1^* = -K_1 e_1^2 - \frac{e_1 e_2}{C_1}\mu \qquad (22)$$

In the expression (22), the first term is negative and certain, while the second term is uncertain. Using the derivatives of equations (16) and (17) to simplify the expressions

$$e_2^* = x_2^* - \beta^* \qquad (23)$$

and

$$\beta^* = \frac{C_1}{\mu}\left(K_1 e_1^* + \frac{i_{pv}^*}{C_1} - x_{1ref}^{**}\right) - \frac{\mu^*}{\mu^2}C_1\left(K_1 e_1 + \frac{i_{pv}}{C_1} - x_{1ref}^*\right) \qquad (24)$$

Simplifying using Eq. (16) and Eq. (20)

$$\beta^* = \frac{C_1}{\mu}\left(K_1\left(-K_1 e_1 \frac{e_2}{C_1}\mu\right) + \frac{i_{pv}}{C_1} - x_{1ref}^{**}\right) - \frac{\mu^*}{\mu}\beta \qquad (25)$$

Inserting Eq. (25) in Eq. (23), e_2^* becomes

$$e^* = x_2^* - \frac{C_1}{\mu}\left(-K_1^2 e_1 - \frac{K_1 e_2}{C_1}\mu\right) - \frac{C_1}{\mu}\left(\frac{i_{pv}^*}{C_1} - x_{1ref}^{**}\right) + \frac{\mu^*}{u}\beta \qquad (26)$$

The combined Lyapunov's role VC is now definite like follows to make sure that both e_1 and e_2 converge to zero:

$$V_C = V_1 + \frac{1}{2}e_2^2 \qquad (27)$$

According to the Lyapunov constancy standards, together the e1 and e_2 errors will converge to 0 if the time derived of VC is the definitive negative. In other words, it will make sure that x_1 will get closer and closer to x_{1ref}, which will let our arrangement reach MPP. Using the time derived of Eq. (27) to yield Eq. (1)

$$V_C^* = V_1^* + e_2 e_2^* = -K_1 e_1^2 - \frac{e_1 e_2}{C_1}\mu + e_2 e_2^* \qquad (28)$$

or

$$V_C^* = -K_1 e_1^2 + e_2\left(e_2^* - \frac{e_1}{C_1}\mu\right) \qquad (29)$$

For V_C^* negative

$$e_2^* - \frac{e_1}{C_1}\mu = -K_2 e_2 \qquad (30)$$

and a positive constant K_2 is used. To the extent that V_c^*

$$V_C^* = -K_1 e_1^2 - K_2 e_2^2 \qquad (31)$$

Using equations (6), (26), and (30), we get

$$-K_2 e_2 = \frac{x_1}{L}\mu + \frac{x_3}{L} + \frac{K_1^2 C_1 e_1}{\mu} + K_1 e_2 - \frac{i_{pv}}{\mu} + \frac{C_1 x_{1ref}^2}{\mu} + \frac{\mu^*}{\mu}\beta - \frac{e_1}{C_1}\mu \qquad (32)$$

Solving Eq. (32) for μ^*

$$\mu^* = \frac{\mu}{\beta}\left(-K_2 e_2 - \frac{x_1}{L}\mu + \frac{x_3}{L} - \frac{K_1^2 C_1 e_1}{\mu}\right)\frac{\mu}{\beta}\left(-K_1 e_2 + \frac{i_{pv}}{\mu} - \frac{C_1 x_{1ref}^*}{\mu} + \frac{e_1}{C_1}\mu\right) \qquad (33)$$

where $0 < \mu < 1$ besides $\beta \neq 0$. Utilizing μ got through participating Eq. (33), V_c^* will become negative determine, demonstrating the system's asymptotic constancy, that is plain from Eq. (31) as $V_c^* \leq 0$. Besides, the conjunction of e1 to 0 or PV array enter voltage to V_{PVR} is similarly certified.

3. Results and Discussion

This work employs the PV array's parameters, which are detailed in table (1). Additionally, the converter and controller factors are presented in table (2).

To validate the efficacy of the suggested controller, MATLAB/SIMULINK simulations were performed. There are two subsections in the section discussing these simulations. The first subparagraph provides a critical evaluation of the performance of the suggested controller below abrupt variations in irradiance and temperature. In the final sectionThe suggested controller is contrasted. to the P&O method.

(i) In order to check the suggested controller's performance in a demanding situation, a test was conducted under varying irradiance. The experiment began with an initial irradiance of 200 W/m^2, which was suddenly altered to 800 W/m^2 after 0.1 s. After 0.2 s, the irradiance was further increased to 1200 W/m^2, while putting the temperature of the PV component constant at 20°C. The regression plane was utilized to effectively generate the tracking peak power voltage, which was then monitored by the controller. This successful tracking of the voltage can be observed in Fig. (4). Likewise, figure (5) illustrates the resulting difference in generated power due to the sudden change in irradiance. The PV part reached peak power in 0.002 s, besides nearly minimal wave.

Table (1) PV Array Parameters

Parameters	Value
Parallel connected strings	1
PV module per string	7
Short circuit current	5.6
Open circuit current	350
Maximum power per module	137.8
Number of cells per module	60
Current at MPP	5.3
Voltage at MPP	260

Table (2) Controller and Conversion Parameters

Parameter	Value
K_1	6
K_2	24.000
Input capacitor, C_1	36 UF
Inductor, L	5 mH
Output capacter,C_2	36 UF
Load resistor, R	8 ohms
Switching frequency, f_s	90 kHz

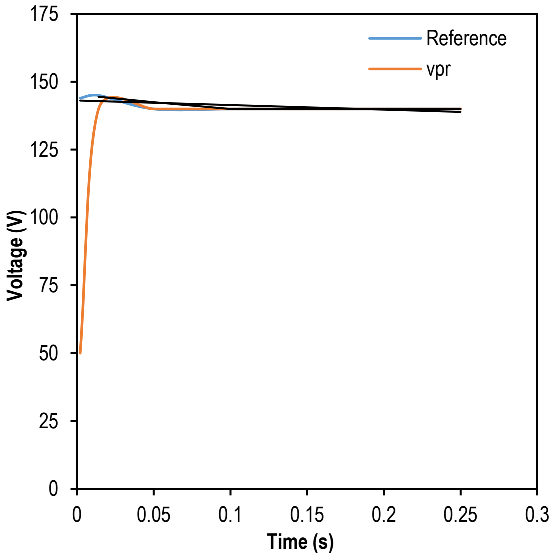

Fig. (4) Voltage monitoring of PV modules

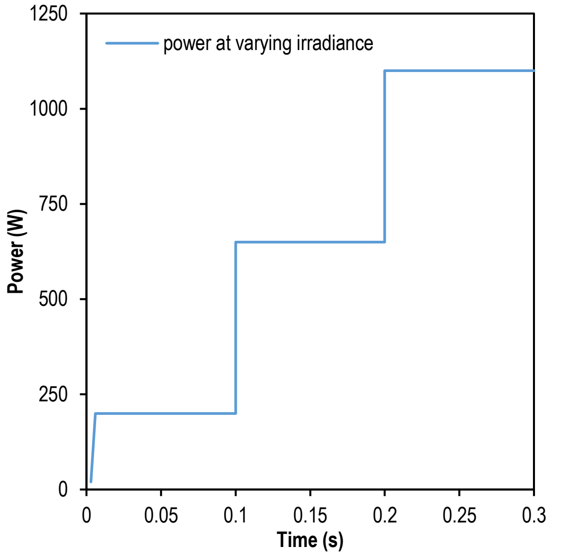

Fig. (5) Various levels of irradiance can generate different amounts of energy

(ii) To assess the effectiveness of the suggested controller further, a series of temperature tests were conducted. After a brief interval of 0.1 s, the temperature was increased from 20 to 40°C. Following 0.2 s, The temperature climbed. abruptly to 55 °C while the irradiance remained constant at 1200 W/m^2. Thus, the system's efficacy was evaluated exclusively under varying temperature conditions. Figure (6) demonstrates that the suggested controller effectively tracked the reference voltage. Moreover, the controller was able to increase power by attaining MPP in fewer than 0.001 s, demonstrating its durability. Figure (7) depicts the generated power under varying temperatures.

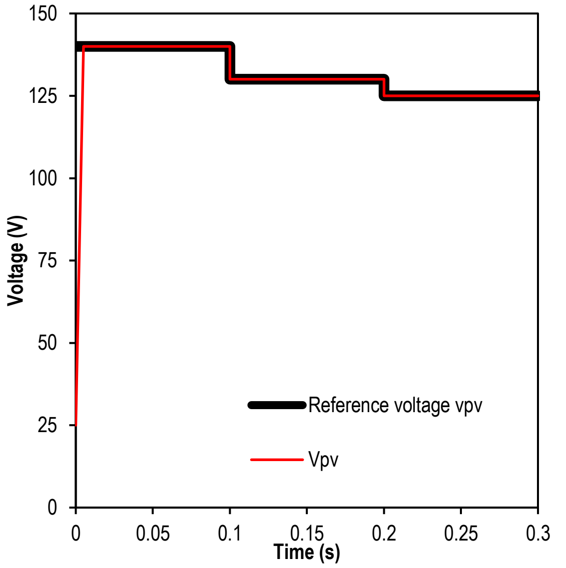

Fig. (6) Monitoring the voltage of PV

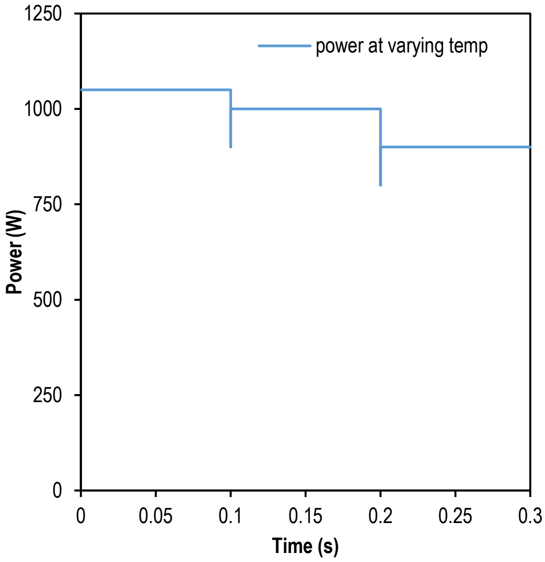

Fig. (7) Power generated at different

(iii) Two experiments were conducted to compare the achievement of the suggested controller to that of the conventional P&O algorithm. The first experiment involved varying irradiance while maintaining the same, and the second experiment involved changing temperature while maintaining constant radiance. Both evaluations were conducted under the same conditions as the previous investigations. In both experiments, the results demonstrated that proposed control system outperformed the P&O algorithm. Figure (8) depicts the power produced by different irradiance, demonstrating the controller's superiority. In addition to its robustness, the controller's ability to maintain negligible disturbances was also observed. Utilizing the proposed controller enhanced the system's performance significantly.

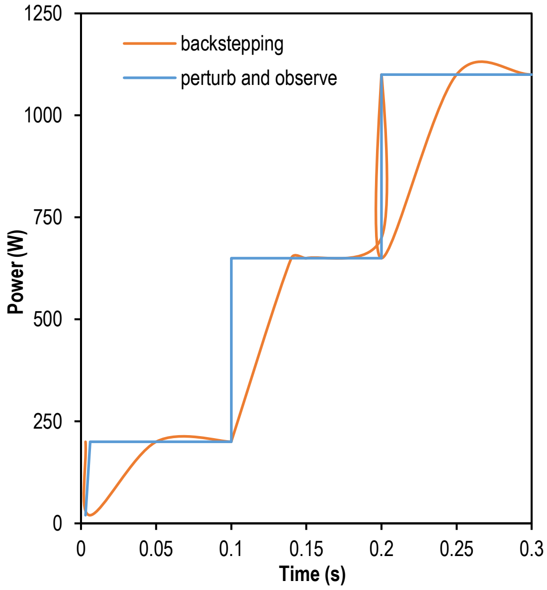

Fig. (8) Comparison of power under varying irradiance

Figure (9) illustrates the electricity generated under various conditions of temperature, further validating the superiority designed control system over P&O. When initial conditions were held constant, the P&O algorithm also required significantly time to do attain the MPP.

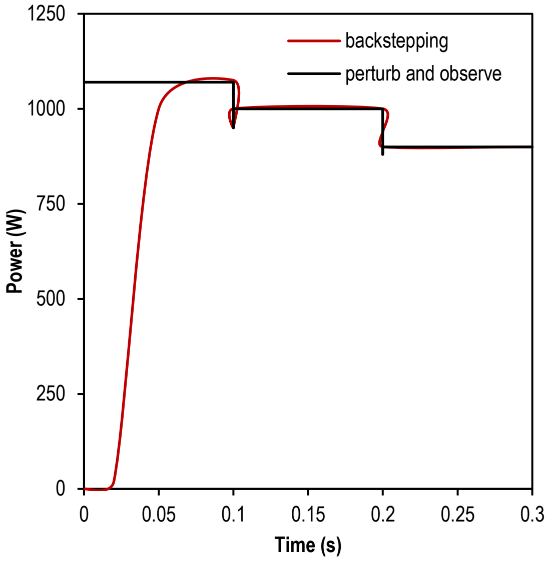

Fig. (9) Comparison of power as the Temperature varies

4. Conclusion

This article describes a nonlinear back stepping controller for MPPT using buck converters. The controller tracks a reference generated by a regression plane to extract maximum power. The proposed controller exhibited global asymptotic stability and outperformed the conventional P&O. However, due to the deterioration of PV arrays, the regression plane requires maintenance. Further work can include experimental implementation of the converter and improving the robustness of bio-inspired algorithms to replace the regression plane.

References

[1] M. Morcos, et al., “MPPT of photovoltaic systems using sensorless current-based model predictive control”, *IEEE Trans. Ind. Appl.*, 53(2) (2016) 1157-1167.

[2] F. Dincer, “The analysis on wind energy electricity generation status, potential and policies in the world”, *Renew. Sustain. Ener. Rev.*, 15(9) (2011) 5135-5142.

[3] M. Kamran et al., “Solar photovoltaic grid parity: a review of issues, challenges and status of different PV markets”, *Int. J. Renew. Ener. Res.*, 9(1) (2019) 244-260.

[4] B. Parida, S. Iniyan and R. Goic, “A review of solar photovoltaic technologies”, *Renew. Sustain. Ener. Rev.*, 15(3) (2011) 1625-1636.

[5] P. Sindhuja and V. Usha Reddy, “Enhancement of grid connected PV inverter using optimal maximum power point tracking algorithm with estimation of climatic parameter”, *Int. Conf. on Inven. Syst. Control (ICISC)*, IEEE (2017).

[6] N. Femia et al., “Predictive & adaptive MPPT perturb and observe method”, *IEEE Trans. Aerosp. Electron. Syst.*, 43(3) (2007) 934-950.

[7] I.V. Banu, R. Beniugă and M. Istrate, “Comparative analysis of the perturb-and-observe and incremental conductance MPPT methods”, *8th Int. Symp. on Adv. Topics in Electr. Eng. (ATEE)*, IEEE (2013).

[8] M.A. Elgendy, B. Zahawi and D.J. Atkinson, “Assessment of perturb and observe MPPT algorithm implementation techniques for PV pumping applications”, *IEEE Trans. Sustain. Ener.*, 3(1) (2011) 21-33.

[9] J. Chauhan et al., “Comparison of MPPT algorithms for DC-DC converters based photovoltaic systems”, *Int. Conf. on Ener. Efficient Technol. Sustain.*, IEEE (2013).

[10] L. Corradini et al., “Continuous-Time Averaged Modeling of DC-DC Converters”, in *Digital Control of High-Frequency Switched-Mode Power Converters*, IEEE (2015) 13-50.

[11] T. Laagoubi, M. Bouzi and M. Benchagra, “Analysis and comparison of MPPT nonlinear controllers for PV system”, *3rd Int. Renew. Sustain. Ener. Conf. (IRSEC)*, IEEE (2015).

[12] F. Dincer, “The analysis on photovoltaic electricity generation status, potential and policies of the leading countries in solar energy”, *Renew. Sustain. Ener. Rev.*, 15(1) (2011) 713-720.

[13] R.H. Ahmed, A.A. Abdulrazzaq and M.T. Yunis, “The implementation (hybrid unit power supply) of a portable plant power by employ (solar cell and fuel cell) using deep learning technology for neural networks”, *AIP Conf. Proc.*, 2404(1) (2021) 020001.

[14] L. An and D.D.-C. Lu, “Design of a single-switch DC-DC converter for PV-battery powered pump system”, *1st Int. Fut. Ener. Electron. Conf. (IFEEC)*, IEEE (2013).

[15] R.H. Ahmed and A.A. Abdulrazzaq, “Reduced pole to pole voltage deviations through stopping MMC blockading loss of terminals below DC faults”, *IOP Conf. Series: Mater. Sci. Eng.*, 881(1) (2020) 1-10.

[16] A.M. Atallah, A.Y. Abdelaziz and R.S. Jumaah, “Implementation of perturb and observe MPPT of PV system with direct control method using buck and buck-boost converters”, *Emerg. Trends in Electr. Electron. Instrum. Eng.: An Int. J.*, 1(1) (2014) 31-44.

[17] A. Zeghoudi et al., “Determination of Electromagnetic disturbances in a buck chopper”, *Australian J. Electr. Electron. Eng.*, 19(2) (2022) 149-157.

[18] A.D. Martin and J.R. Vazquez, “MPPT algorithms comparison in PV systems: P&O, PI, neuro-fuzzy and backstepping controls”, *IEEE Int. Conf. on Ind. Technol. (ICIT)*, IEEE (2015).

[19] M. Arsalan et al., “MPPT for photovoltaic system using nonlinear backstepping controller with integral action”, *Solar Energy*, 170 (2018) 192-200.

IRAQI JOURNAL OF APPLIED PHYSICS
Vol. 19, No. 4B, November 2023, pp. 145-150

Houra'a K. Hussein
Kawkab D. Salim

Department of Physics,
College of Education for
Pure Sciences,
Tikrit University,
Tikrit, IRAQ

Thickness-Dependent Optical and Topographical Characteristics of Ferric Oxide Thin Films prepared by Spray Pyrolysis

Thin films of ferric oxide (Fe_2O_3) have been prepared and deposited on glass substrates by chemical spray pyrolysis technique. The molar concentration of the sprayed solution was 0.1 M and the glass substrates were heated to a 350°C before deposition. The absorption and transmission spectra were recorded in the spectral region 300-1100nm. They have shown that the film thickness determines the spectroscopic characteristics. Furthermore, these films have exhibited energy gap ranging between 2.38 and 2.62 eV. Moreover, the images of the atomic force microscopy (AFM) have shown that average diameter of the particles in the deposited films decreased when the film thickness is decreased too.

Keywords: Ferric oxide; Optical properties; Thin films; Spray pyrolysis
Received: 10 July 2023; **Revised:** 24 August 2023; **Accepted:** 31 August 2023

1. Introduction

Semiconducting oxides are important for many practical applications and increasing the possibility of manufacturing advanced electronic devices [1-4]. In the recent decades, the research works on thin films prepared from semiconducting metal oxides have received wide and increasing attention due to the fact that they are the basic elements used in most electrical, electronic and photovoltaic devices and applications [5-7]. Integrated circuits, detectors, optical filters, reflective mirrors, rectifiers, magnetic memory devices, and computers are also making use of such metal oxide thin films [8-14]. The importance of thin films lies in the fact that their structural, optical and electrical properties can be changed depending on their preparation techniques and conditions, such as varying the types of substrates (glass, silicon and quartz) on which these films are deposited, changing the type of material to be oxidized, varying the deposition temperature, etc. [15-17]. The iron or ferric oxide (Fe_2O_3) is one of the promising semiconducting oxides. It has an optical energy gap of about 2 eV [18,19]. In addition, it is low in cost, non-toxic [20], completely stable, resistant to photocorrosion, and has high resistance at room temperature [21-24]. This material is found in nature in three forms, magnetite (Fe_2O_4), maghemite (ɤ-Fe_2O_3), and hematite (α-Fe_2O_3) [25]. These oxides are prepared as thin films by many physical and chemical methods and techniques, such as sol-gel [26], chemical spray pyrolysis (CSP) [27], electro-bath deposition [28], electrodeposition [29], and Successive Ionic Layer Adsorption and Reaction (SILAR) method [30]. Large-scale films can be successfully deposited on glass substrates by CSP for different industrial applications [31,32].

In this research, the optical and topographical characteristics of pure iron (ferric) oxide (Fe_2O_3) prepared by chemical spray pyrolysis (CSP) were determined and studied. This method is competitive with other methods of thin film deposition due to its advantages, including obtaining high deposition rates and easy to control the film thickness. However, preparing thin films of good quality is only possible by raising the temperatures of the substrates on which these films are deposited.

2. Experimental Part

The precursor material used to produce Fe_2O_3 was $FeCl_3.6H_2O$ supplied by THOMAS BAKER company. This material is supplied as a brown solid pieces with a molecular weight of 270.30 g/mol. To calculate the mass of $FeCl_3.6H_2O$, a sensitive electronic balance with a sensitivity of 10^{-4} g was used. In order to prepare the solution at room temperature, 1.3515 g of $FeCl_3.6H_2O$ was dissolved in 50 mL of distilled water using a magnetic stirrer for 15 min. To determine the weight to be dissolved, the following relationship was used [33]:

$$M = \frac{M_t}{M_{wt}} \times \frac{1000}{V} \qquad (1)$$

where M is the molar concentration (0.1M), M_t is the mass of $FeCl_3.6H_2O$, M_{wt} is the molecular weight of $FeCl_3.6H_2O$, V is the volume of distilled water (50mL)

The solution was then deposited on heated glass substrates to produce ferric oxide thin films. It was found that the best conditions for preparing homogeneous thin films those are free of holes and cohesive with the substrate, spraying time should be 5 s, stopping time after each spray should be 20s, and the vertical distance from atomizer nozzle to the substrates should be 25±1cm. The thickness (t) of the thin film was measured by the optical interferometry using the following equation [34]:

$$t = \frac{\Delta x}{x} . \frac{\lambda}{2} \quad (2)$$

where Δx is the dark fringe width, x is the bright fringe width, and λ is the wavelength

The optical characteristics of thin ferric oxide (Fe_2O_3) thin films were recorded using a Shimadzu two-beam UV-Visible1650 spectrophotometer. The topography of the prepared films was introduced using a Nanosurf NaioAFM-2022 atomic force microscope (AFM).

3. Results and Discussion

The absorption and transmission spectra of the prepared films were recorded as functions of the wavelength in the spectral region 300-1100 nm. These films show high absorbance at wavelengths shorter than 400nm. Then, the absorbance begins to decrease until it reaches the minimum value at 1100 nm, as shown in Fig. (1) making these thin films suitable for solar cell applications. Coinciding to Beer-lambert's law, the absorbance typically increases with increasing film thickness.

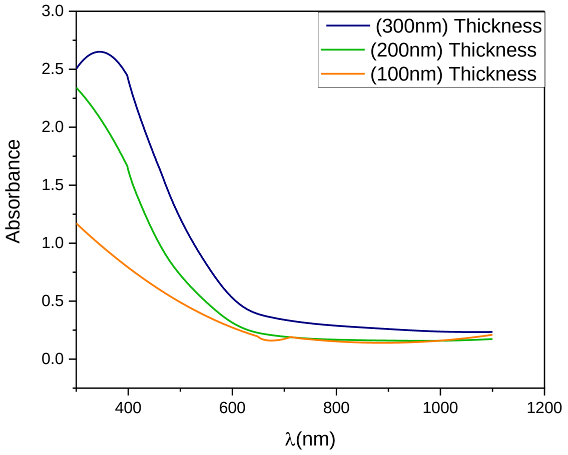

Fig. (1) Variation of absorbance with wavelength for pure Fe_2O_3 thin films with three different values of film thickness

The transmission spectra behave differently from the absorption spectra, where the transmittance increases with wavelength, as illustrated in Fig. (2). For the film thickness of 100 nm, the transmittance is very low at wavelengths shorter than 400 nm and starting to increase in the visible region and maximized at wavelengths longer than 800 nm. Such behavior of ferric oxide (Fe_2O_3) thin films makes them suitable as active material as well as optical windows for solar cells. For larger values of film thickness (200 and 300 nm), the transmittance is lowered due to the increase in crystallite size, which leads to reduce the density of charge carriers.

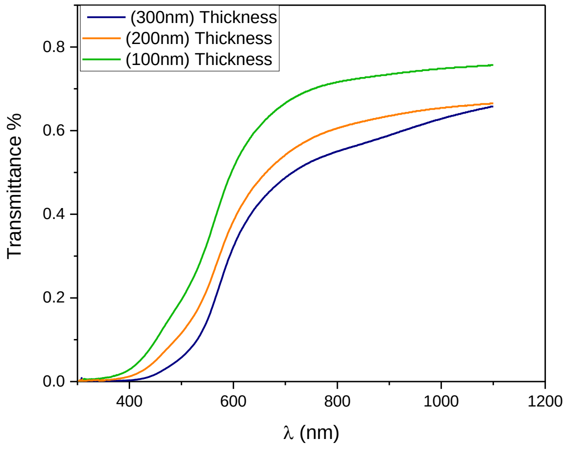

Fig. (2) Variation of transmittance with wavelength for pure Fe_2O_3 thin films with three different values of film thickness

The absorption coefficient (α) of the prepared thin films shows similar behavior to that of the absorbance with wavelength, as shown in Fig. (3). However, the effect of film thickness is much clearer than that on absorbance.

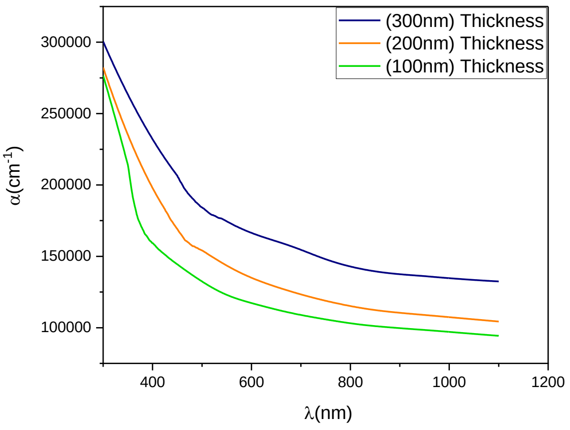

Fig. (3) The relationship between the absorption coefficient and the photon energy of Fe_2O_3 thin film

The optical energy gap represents the minimum energy required for the transfer of an electron from the top of the valance band to the bottom of the conduction band of Fe_2O_3 thin films. It was calculated according to the Tauc's plot illustrated in Fig. (4). It shows the relationship between $(\alpha h\nu)^2$ and photon energy ($h\nu$). The values of energy gap are 2.66, 2.55, and 2.38 eV for films thickness of 100, 200, and 300 nm, respectively. The result reveals an increase in the energy gap as the thickness decreases. This is due to the appearance of irregular defects within the energy gap, which in turn leads to a decrease the value of optical energy gap [35,36].

Figure (5) clarifies the variation of the extinction coefficient as a function of the wavelength as well film thickness. It was found that the extinction coefficient gradually increases with increasing wavelength. In addition, the extinction coefficient behaves in almost the same way as the absorption coefficient, where it increases with the increase in film thickness.

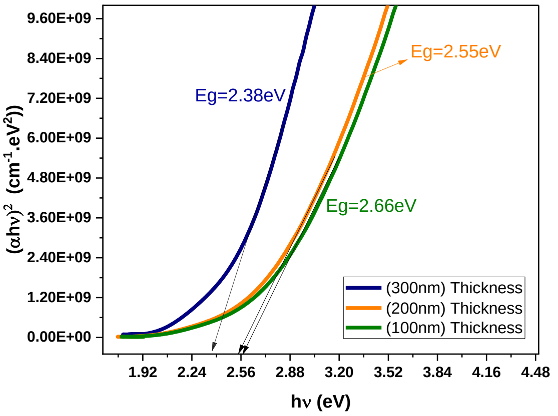

Fig. (4) Variation of $(\alpha h\nu)^2$ as a function of photon energy ($h\nu$) for the prepared Fe_2O_3 thin films

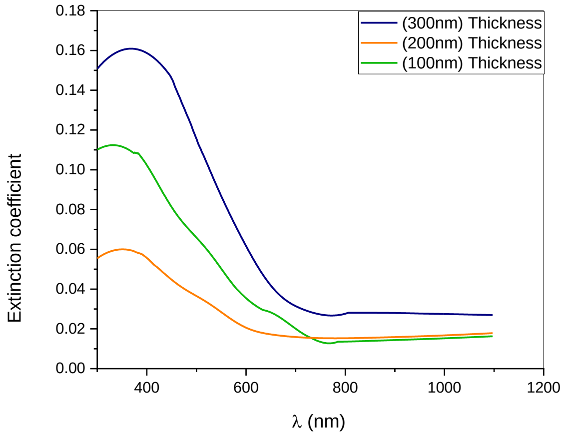

Fig. (5) Variation of extinction coefficient as a function of wavelength for the prepared Fe_2O_3 thin films

The atomic force microscopy (AFM) was used to study the surface topography of the prepared film samples deposited on glass substrates with different thicknesses (100, 200, and 300nm). Table (1) shows that when the films thickness increased, the surface roughness decreased from 23.47 to 22.7 and 8.156 nm, respectively.

Table (1) Values of surface roughness, RMS roughness and granular size calculated from AFM measurements

Sample	D_{av} (nm)	Surface Roughness (nm)	R.M.S. (nm)
Fe_2O_3 (100nm)	١١٠,٤	٢٣,٤٧٠	٢٨,٢٧
Fe_2O_3 (200nm)	٦٧,٩٠	٢٢,٧00	١٠,٠٤
Fe_2O_3 (300nm)	٤٣,٦6	٨,١٥٦	١٠,٣٨

In addition, when the film thickness is changed, the RMS roughness value decreased from 28.27 to 10.18 nm. The AFM images revealed the presence of valleys on the surface of thin film with 100nm thickness. Then, these valleys disappeared when the film thickness became 200 and 300 nm. This is probably due to the increase in the number of particles that fill these valleys. So, smoother films were produced [36-38].

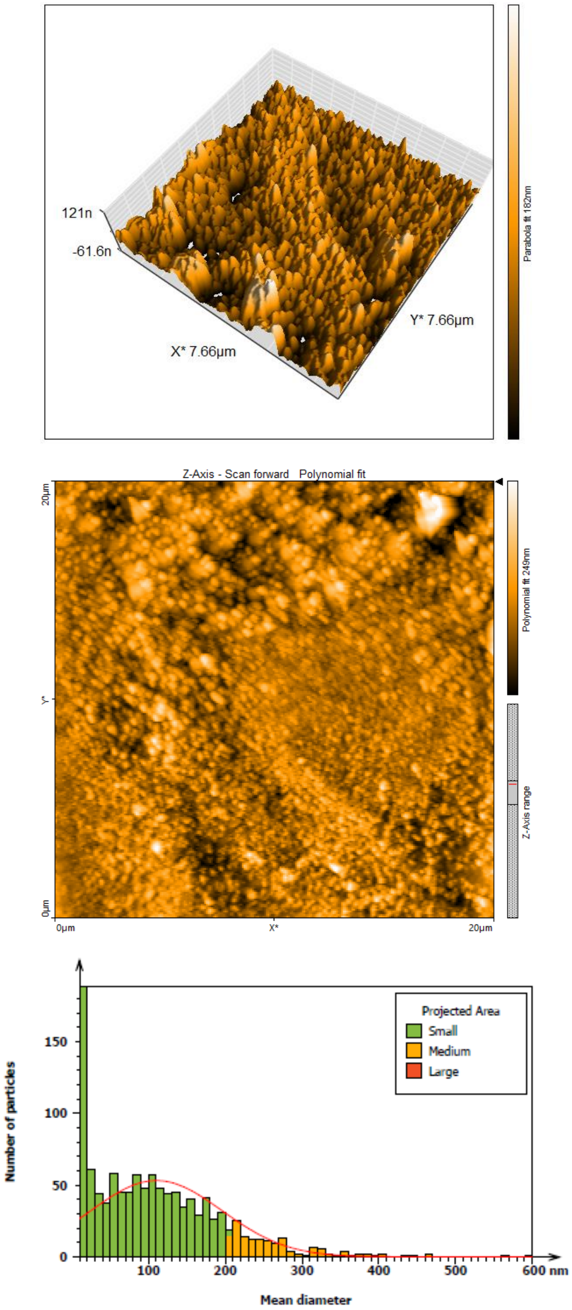

(a) Fe_2O_3 thin film of 100nm thickness

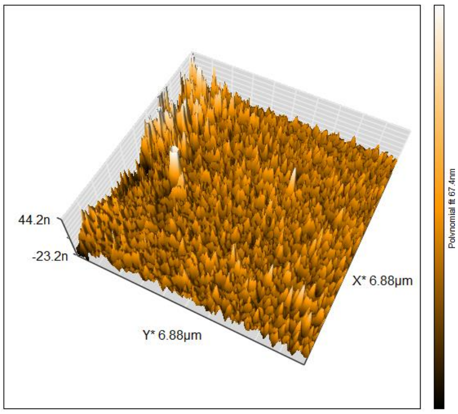

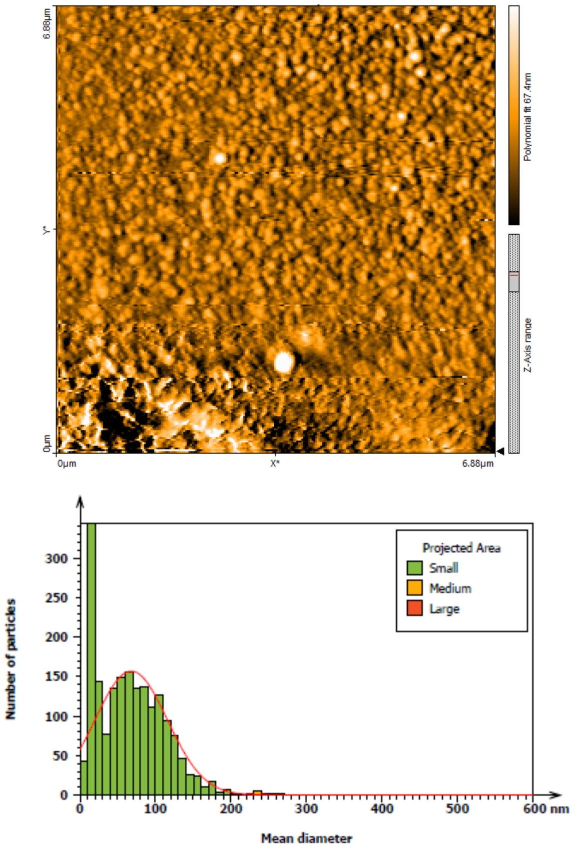

(b) Fe_2O_3thin film of 200nm thickness

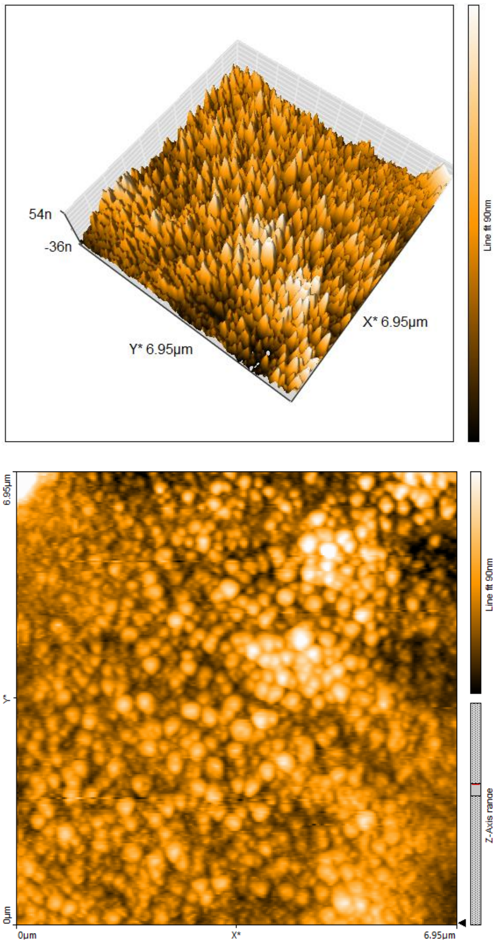

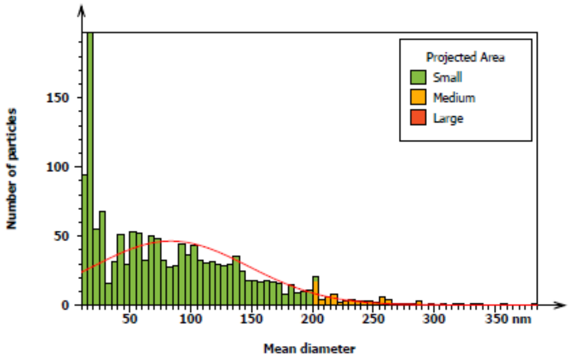

(c) Fe_2O_3 thin film of 300nm thickness

Fig. (6) 2D and 3D AFM images with particle size distribution of Fe_2O_3 thin films prepared in this work

Conclusion

The effects of film thickness on the absorption and transmission spectra as well as on the surface roughness of the ferric oxide thin films prepared by the chemical spray pyrolysis method were studied. The optical characteristics are reasonably sensitive to the variation in film thickness. The optical energy band gap was found to decrease with increasing film thickness. As the film thickness was increased by 200%, the energy and gap was decreased by 10.5%, which may represent good tool to control the properties of the semiconducting material by determining the thickness. The surface roughness of the prepared thin films was found to depend on film thickness as it decreases by 65% when the film thickness is increased by 200%. Such control is very necessary in the optical, electrical and electronic applications of thin films and their devices.

References

[1] Z.R. Dai et al., “Novel Nanostructures of functional oxides synthesized by thermal evaporation”, *Adv. Funct. Mater.*, 13 (2003) 9-24.

[2] V.H. Singh et al., “Influence of SiO_2, MgO, and Fe_2O_3 metallic nano cutting fluids of AA6061 in MQL environment”, *Mater. Today: Proc.*, 69(Pt 3) (2022) 1103-1109.

[3] A. Lassoued et al., “Synthesis, photoluminescence and Magnetic properties of iron oxide (α-Fe_2O_3) nanoparticles through precipitation or hydrothermal methods”, *Phys. E: Low-dim. Syst. Nanostruct.*, 101 (2018) 212-219.

[4] S.M. Reda, “Synthesis of ZnO and Fe_2O_3 nanoparticles by sol–gel method and their application in dye-sensitized solar cells”, *Mater. Sci. Semicond. Process.*, 13(5-6) (2010) 417-425.

[5] M.A. Mahadik et al., “Photoelectrocatalytic activity of ferric oxide nanocatalyst: A synergestic effect of thickness”, *Ceram. Int.*, 40(7A) (2014) 9463-9471.

[6] N.M.S. Kaawash et al., “High-performance and ultra-sensitive ultraviolet photodetector based on surface passivated α-Fe_2O_3 thin film”, *Mater. Chem. Phys.*, 300 (2023) 127546.

[7] A. Badawi et al., “The influence of La/Mg co-doping on the structure, linear and nonlinear optical properties of Fe_2O_3 nanoparticles for environmentally friendly applications”, *Opt. Mater.*, 142 (2023) 113912.
[8] R.D. Suryavanshi and K.Y. Rajpure, “Spray deposited Fe_2O_3 and stratified Fe_2O_3/ZnO novel photoelectrode for photoelectrocatalytic degradation of benzoic acid under solar light illumination”, *J. Photochem. Photobiol. A: Chem.*, 357 (2018) 72-80.
[9] R.D. Suryavanshi et al., “Photoelectrocatalytic activity of spray deposited Fe_2O_3/ZnO photoelectrode for degradation of salicylic acid and methyl orange dye under solar radiation”, *Mater. Sci. Eng. B*, 248 (2019) 114386.
[10] L. De Los Santos Valladares et al., “Characterization and magnetic properties of hollow α-Fe_2O_3 microspheres obtained by sol gel and spray roasting methods”, *J. Sci. Adv. Mater. Dev.*, 4(3) (2019) 483-491.
[11] S. Choudhary, A. Bisht and S. Mohapatra, “Microwave-assisted synthesis of α-Fe_2O_3/$ZnFe_2O_4$/ZnO ternary hybrid nanostructures for photocatalytic applications”, *Ceram. Int.*, 47(3) (2021) 3833-3841.
[12] M.M. Rahman et al., “Fabrication of a methanol chemical sensor based on hydrothermally prepared α-Fe_2O_3 codoped SnO_2 nanocubes”, *Talanta*, 95 (2012) 18-24.
[13] T. Sen et al., “Polyaniline/γ-Fe_2O_3 nanocomposite for room temperature LPG sensing”, *Sens. Actuat. B: Chem.*, 190 (2014) 120-126.
[14] G. Kaur et al., “Nano-hetero-structured thin films, ZnO/Ag-(α)Fe_2O_3, with n/n junction, as efficient photoanode for renewable hydrogen generation via photoelectrochemical water splitting”, *Renew. Ener.*, 164 (2021) 156-170.
[15] S.K. Pawar and S.H. Pawar, “Studies on deposition of Fe_2O_3 films by spray pyrolysis method”, *Mater. Res. Bull.*, 18(2) (1983) 211-215.
[16] E. Celik et al., “Preparation and characterization of Fe_2O_3–TiO_2 thin films on glass substrate for photocatalytic applications”, *Mater. Sci. Eng. B*, 129(1-3) (2006) 193-199.
[17] R.N. Goyal, D. Kaur and A.K. Pandey, “Growth and characterization of iron oxide nanocrystalline thin films via low-cost ultrasonic spray pyrolysis”, *Mater. Chem. Phys.*, 116(2-3) (2009) 638-644.
[18] R. Ben Ayed, M. Ajili and N.K. Turki, “Physical properties and Rietveld analysis of Fe_2O_3 thin films prepared by spray pyrolysis: Effect of precursor concentration”, *Phys. B: Cond. Matter*, 563 (2019) 30-35.
[19] A.S.N. Murth and K.S. Reddy, “Photoelectrochemical behaviour of undoped ferric oxide (α-Fe_2O_3) electrodes prepared by spray pyrolysis”, *Mater. Res. Bull.*, 19(2) (1984) 241-246.
[20] T.L. Indgren, H. Wang and N. Beermann, “Aqueous photoelectron chemistry of hematite nanorod array”, *Sol. Ener. Mater. Sol. Cells*, 71 (2002) 231-243.
[21] A. Watanabe and H. Kozuka, “Photoanodic Properties of Sol-Gel- Derived Fe_2O_3 Thin Film Containing Dispersed Gold and Silver Particles”, *J. Phys. Chem. B*, 107 (2003) 12713-12720.
[22] B.J. Lokhande, R.C. Ambare and S.R. Bharadwaj, “Thermal optimization and supercapacitive application of electrodeposited Fe_2O_3 thin films”, *Measurement*, 47 (2014) 427-432.
[23] B.G. Ghule et al., “Self-assembled α-Fe_2O_3-GO nanocomposites: Studies on physical, magnetic and ammonia sensing properties”, *Mater. Chem. Phys.*, 278 (2022) 125617.
[24] H.-J. Ye, Y.-R. Hsu and Y.-T. Nien, “Microstructure and electrical characterizations of CuO/Fe_2O_3 ceramics sintered by CO_2 laser beams”, *Mater. Chem. Phys.*, 297 (2023) 127417.
[25] D.E. Fouad et al., “Improved size, morphology and crystallinity of hematite (α-Fe_2O_3) nanoparticles synthesized via the precipitation route using ferric sulfate precursor”, *Resul. Phys.*, 12 (2019) 1253-1261.
[26] L. Huo et al., “Sol–gel route to pseudocubic shaped α-Fe_2O_3 alcohol sensor: preparation and characterization”, *Sens. Actuat. B: Chem.*, 107(2) (2005) 915-920.
[27] B.R. Ayed et al., “Physical Properties Investigation and Gas Sensing Mechanism of Al:Fe_2O_3 Thin Films Deposited by Spray Pyrolysis”, *Superlat. Micortruct.*, 129 (2019) 91-104.
[28] C. Cao et al., “Improving Photoelectrochemical Performance by Building Fe_2O_3 Heterostructure on TiO_2 Nanorod Arrays”, *Mater. Res. Bull.*, 70 (2015) 155-162.
[29] P.M. Kulal et al., “Chemical Synthesis of Fe_2O_3 Thin Film for Supercapacitor Application”, *J. Alloys Compounds*, 509 (2011) 2567-2571.
[30] O. Erken, “Effect of cycle numbers on the structural, linear and nonlinear optical properties in Fe2O3 thin films deposited by SILAR method”, *Curr. Appl. Phys.*, 34 (2022) 7-18.
[31] Y.J. Onfre et al., “Highly Selective Ozone Gas Sensor Based on Nanorcystalline $Zn_{0.95}Co_{0.05}O$ Thin Film Obtained via Spray Pyrolysis Technique”, *Appl. Surf. Sci.*, 478 (2019) 347-354.
[32] S.R. Ardekani et al., “A Comprehensive Review on Ultrasonic Spray Pyrolysis Technique; Mechanism, Main Parameters and Applications in Condensed Matter”, *J. Anal. Appl. Pyrol.*, 141 (2019) 104631.
[33] C.E. Housecroft and A.G. Sharpe, **“Inorganic Chemistry”**, 2nd ed., Pearson Education, Ltd. (UK, 2005), p. 165.
[34] H.M. Shabana, “Determination of film thickness and refractive index by interferometry”, *Polym. Test.*, 23(6) (2004) 695-702.
[35] C. Han et al., “Phase transition behavior in Fe_2O_3 nanofibers”, *Appl. Surf. Sci.*, 507 (2020) 145179.

[36] B. Ouertani et al., “Effect of the ruthenium incorporation on iron oxide phases synthesis, Fe_2O_3 and Fe_3O_4, at low annealing temperature”, *Mater. Chem. Phys.*, 242 (2020) 122272.

[37] A. Peeva et al., “Rare-Earth Implanted Y_2O_3 Thin Films”, *Appl. Surf. Sci.*, 253 (2007) 8167-8168.

[38] N.I. Muhamad Fauzi et al., “Nanostructured Chitosan/Maghemite Composites Thin Film for Optical Detection of Mercury Ion by Surface Plasmon Resonance Investigation”, *mdpi Polymer*, 12(7) (2020) 1497.

[39] A.A. Majeed and R.T. Rasheed, “Preparation, Characterization and Mimetic Activities of Fe_2O_3 and Fe_3O_4 Nanoparticles as Catalase and Peroxidase”, *J. Appl. Sci. Nanotechnol.*, 2(2) (2022) 166-181.

IRAQI JOURNAL OF APPLIED PHYSICS
Vol. 19, No. 4B, November 2023, pp. 151-156

Heba H. Ali
Mazin A. Alalousi

Department of Physics,
College of Science,
University of Anbar,
Ramadi, IRAQ

Initial Characterization of the Prepared Au-Decorated TiO_2:Fullerene Films Using Electrospray Method

This study aims to enhance the properties of fullerene composite films and investigate the impact of incorporating TiO_2 on their structural, topographic, and optical characteristics. A hybrid method was employed to prepare these composite films by combining laser ablation to produce the colloidal of carbon, titanium dioxide and gold, then using the electro-spraying technique to produce TiO_2:fullerene films and then decorate them with gold nanoparticles. Addition of TiO_2 and decoration by gold have led to variations in the structural phases and a decrease in both crystallite and particle sizes. Similar effects were observed for band gap energy and Urbach energy.

Keyword: Titanium dioxide; Fullerene; Electro-spray; Wasted batteries; Laser ablation
Received: 31 July 2023; **Revised:** 28 August 2023; **Accepted:** 04 September 2023

1. Introduction

Carbon-based nanomaterials, such as graphene, fullerenes, carbon nanotubes, and carbon dots, have been extensively studied [1]. One of fullerenes is C_{60} also known as buckminsterfullerene or simply fullerene, is a carbon-based nanomaterial with consisting of 60 carbon atoms arranged in a hollow sphere [2]. Due to its unique a unique structural, electronic, and optical properties [3], involves many applications including photo-optical, supercapacitors, biomedical [4], drug delivery [1] applications. Addition to transistors and solar cells [5]. Titanium oxide (TiO_2) in one-dimensional (1D) nanostructure has a large surface/volume, a volume of the pore, and a mean-free-path length of electrons comparable with the two directions perpendicular to the long axis of the particles [5-9]. Therefore, TiO_2 with these properties is attractive and promising to the high-activity TiO_2-based photocatalyst [10-13]. Despite the relatively large gap in TiO_2 (more than a volt), the presence of C_{60} provides a smooth transfer of electrons in the presence of ultraviolet radiation, as it is in the presence of the non-local P structure that acts as a good acceptor for photocatalyzed electrons. In the C_{60}/TiO_2 system, the conduction band of TiO_2 is higher compared to that of $C_{60}/C_{60}^{\cdot-}$ (vs. NHE), so photoelectrons can transfer from TiO_2 nanoparticles to C_{60} in the presence of UV light [14]. Moreover, the amalgamation of TiO_2 and C_{60} results in heightened absorption attributed to an increase in surface electric charge. This, in combination with the heightened Schottky barrier between the deposited noble metal and the electron catalyst, serves to facilitate the capture of electrons by the noble metal. Consequently, it impedes the recombination of electron-hole pairs and amplifies the interaction for interfacial charge transfer. In this perspective, TiO_2 and gold decoration are expected to improve the optical properties of fullerenes towards photocatalysis [15]. Figure (1) explains the electronic reaction between C_{60} and TiO_2.

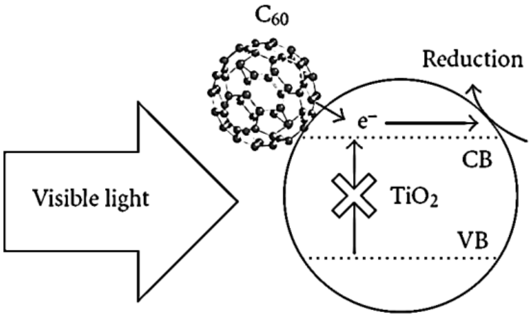

Fig. (1) A diagram of the photoelectron transfer model of TiO_2-C_{60} composite by visible light effect [18]

The photocatalytic activity enhancement of C_{60} and some compounds by C_{60} were discussed by many studies, such as Yu et al. [14], who have synthesized fullerene-modified TiO_2 nanocomposites and studied the enhancement of photocatalytic activity of the C_{60}/TiO_2 nanocomposites. Dai et al. [16] have improved the photocatalytic of the modifying $PbMoO_4$ by C_{60}. Tahir et al. [17] have fabricated fullerene-WO_3 composite systems for the photocatalytic. Also, Shahzad et al. [18] have fabricated heterojunction composites from WO_3/fullerene/Ni_3B/$Ni(OH)_2$ structures. Peng [19] has reported a theoretical study on the ability of using a Monolayer Fullerene Networks (MLFN) as photocatalyst for water treatment. In 2022, Fadhil et al. have studied the photocatalytic behaviour of C_{60}-TiO_2-ZnO, C_{60}-ZnO, C_{60}-TiO_2 nanocomposites. Liping et al. [20] have enhanced it by creating C_{60}@NU-901. Likewise, Munawar et al. [21] have fabricated a dual-functional La_2O_3–C_{60}

nanocomposite as an effective photocatalyst and supercapacitors electrode.

In this study, the structural, morphological, and optical properties, of Au-decorated TiO_2:fullerene films were investigated as a proposed photocatalyst.

2. Materials and Method

Carbon pellet extracted from battery electrodes were prepared by pressing carbon powders by means of a hydraulic press [22]. The same applies to TiO_2 powder to fabricate a TiO_2 pellet, which was placed in 50 ml of deionized water (DW), then bombarded with 3000 shots from pulsed Nd:YAG laser of 1064 nm wavelength and 100 mJ energy. The duration, width, and intensity of laser at the spot of shot were 6 Hz, 10 nm, and 4 $J.cm^{-2}$, respectively, and the distance between the surface target and the laser source was 12 cm. Then, carbon/TiO_2 colloidal was prepared by irradiating the carbon pellet in colloidal TiO_2 in 10, 30, and 50 vol.% of 50 ml of DW using the same laser parameters as well as the same number of laser shots. Finally, for decoration, the prepared films were sprayed by gold nanoparticles (AuNPs) colloidal, which was prepared with the same previous condition, but 1000 laser shots.

Carbon colloidal of 50 ml was sprayed on quartz and Au-coated glass substrates at 300±25 °C by electrospray technique with dc electrical bias potential of 5 kV, flow rate about 1 ml/min, ON/OFF spraying time of 10 and 30s, respectively. Figure (2) shows the schematic of the electrospray device used in this work.

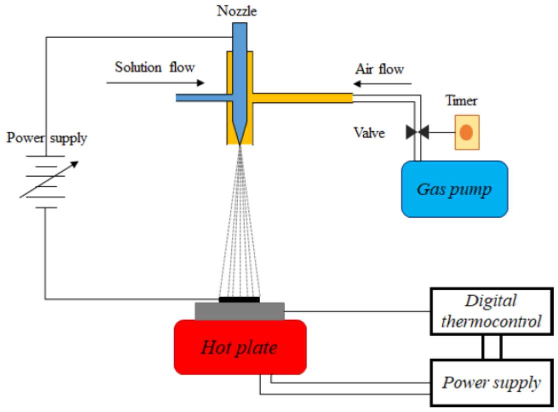

Fig. (2) Schematic of the electrospray device used in this work

The structural properties of the prepared films were performed on x-ray diffractometer (XRD) using CuKα radiation and accelerated voltage of 40 kV. The crystallite size had been estimated based on the Williamson-Hall relation [23]

$$D_{hkl} = \left(\frac{A\lambda}{cos\theta . \beta_{hkl}}\right) + (4\varepsilon \sin\theta) \qquad (1)$$

where D (nm) is the crystallite size, A is a dimensionless shape factor (0.89), λ is the wavelength of the x-ray beam (nm), β_{hkl} is the full-width at half maximum (FWHM) of the diffraction peaks, ε is the strain, and θ (rad) is the diffraction angle

The quantitate phase measurements were achieved using the reference intensity ratio (RIR) method [22]. A field-emission scanning electron microscope (FE-SEM, INSPECT-550) was used to introduce the surface morphology of the prepared films. The optical properties of the prepared films were investigated using a PG-T-80 UV-Visible spectrophotometer in the spectral range 200-900 nm.

3. Result and Discussion

The XRD patterns of the prepared films have been analyzed based on ICSD 98-060-2518, ICSD 98-005-6668, ICSD 98-009-5370, ICSD 98-007-5506, ICSD 98-000-9161, ICDD 98-005-6902, and ICSD 98-005-6909 cards for C_{60}, C_{60}–Polymeric, C_{70}, TiO_2 (Rutile), $C_{14}H_{10}$ (Ravatite), and $C_{20}H_{36}$ (Dinite). The thumbnail at the top of Fig. (3) represents the real XRD pattern of pure fullerene, in which the amorphous phase is hidden. Figure (3) shows XRD patterns of the prepared fullerenes films. XRD pattern of the prepared carbon films appears to be polycrystalline of C_{60} in (211), (311), (146), (352), and (651), where the dominant phase was (311) at 20.77° with crystallite size of about 80.76 nm, in conjunction with two structures: C_{60}-polymer (333), (170), and (600), and both (420) and (307) for C_{70}. It is clear that the addition of TiO_2 has led to significant changes in the structures, as shown in diffraction patterns. There is instability in the dominant phase site with variation of TiO_2 ratio and structures with the adding of TiO_2 [24]. At TiO_2 of 10 vol.%, the C_{60}-polymer ratio increased significantly with emergence of $C_{14}H_{10}$ phase (102). This structure is possibly a result of the dissociation of one of the fullerene molecules because of the high temperature and pressure in the plasma bubble generated by the laser in the presence of hydrogen resulting from the instantaneous dissociation of water with the same reason. The dominant phase is (600) which related to C_{70} with crystallite size of about 69 nm with a decrease in the quantity ratio to C_{60} as shown in table (1). With TiO_2 of 30 vol.%, it was observed that the polymerization continued to dominate the structure and the dominating phase returned to C_{60} (221) at 20.81° with crystallite size of about 31.68 nm and an increase of both RIR of C_{60}–Polymeric and C_{70} and vanishing of $C_{14}H_{10}$ phase. It is interesting that when the percentage of TiO_2 was increased to 50 vol.%, a phase emersion of Bis(cyclopentadienyl)bis(m-methoxybenzoato) titanium(IV) $Ti_4C_{104}O_{24}$ was observed. This result confirms the reaction of the Ti^+ ion with carbon atoms and O^- ion. The dominate phase was related C_{70} (141) at 21.60° in conjunction a drastic drop in RIR and an increase for C_{60} and C_{70}, respectively. Moreover, no peaks were seen for AuNPs due to their small amount.

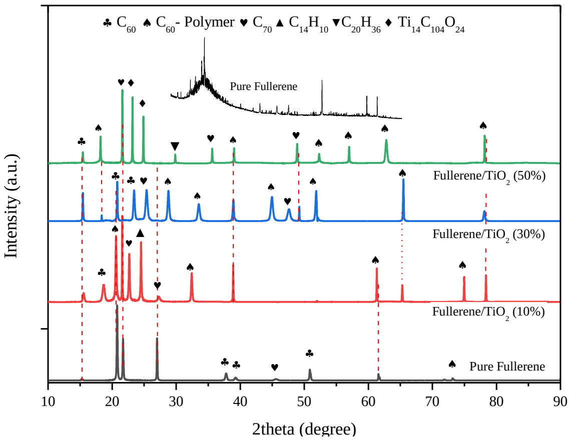

Fig. (3) XRD patterns of the prepared fullerenes and Au-decorated TiO_2:fullerene films

Table (1) Influence of TiO_2 addition on the RIR of the prepared Au-decorated TiO_2: fullerene films

Ratio of TiO_2 (vol.%)	C_{60} (%)	C_{60}–Polymeric (%)	C_{70} (%)
0	48.4700	5.51	46.02
10	6.7400	22.42	35.54
30	13.8800	70.64	15.48
50	2.9315	31.68	30.32

Figure (4) represents images of the prepared fullerenes and Au-decorated TiO_2:fullerene films. Fullerene films showed a variety of different shapes of nanoparticles, it is remarkable that there is a type of separation between the different particles, especially the rods. These nanorods can be C_{60}-polymeric with an average diameter of 39 nm, as shown in Fig. (4a). The separation between the particles and the inhomogeneity of the distribution can be attributed to the segregation of impurity phenomena as a result of the difference in the surface energy of the different particles [25]. Figure (4b) shows a better distinction for polymeric C_{60} with a change in the form of the formed particles that appear like disks longitudinally stacked (about 80 nm of thickness) tablets interspersed with spherical particles (about 34 nm of size) as they approach the assembly line. Increasing of TiO_2 ratio to 30 and 50 vol.% has led to appearance of material as heterogeneous aggregates with undifferentiated components as shown in figures (4c) and (4d). For clarity, the thumbnail images have been processed at a lower magnification to show the general distribution pattern of the deposited films. It appears that there is an evolution of the texture, where becomes more regular (as a fiber structure) with increasing TiO_2 ratio and begins to lose its agglomerated state in the form of fibrils when increasing to 50 vol.%. The cross section images of films showed a change in the deposited thickness of films to be 1172±664, 1373±217, 579±238.8, and 540±199.8 nm for 0, 10, 30, and 50 vol.% of TiO_2 ratio, respectively, as shown in Fig. (4e, f, g, and h).

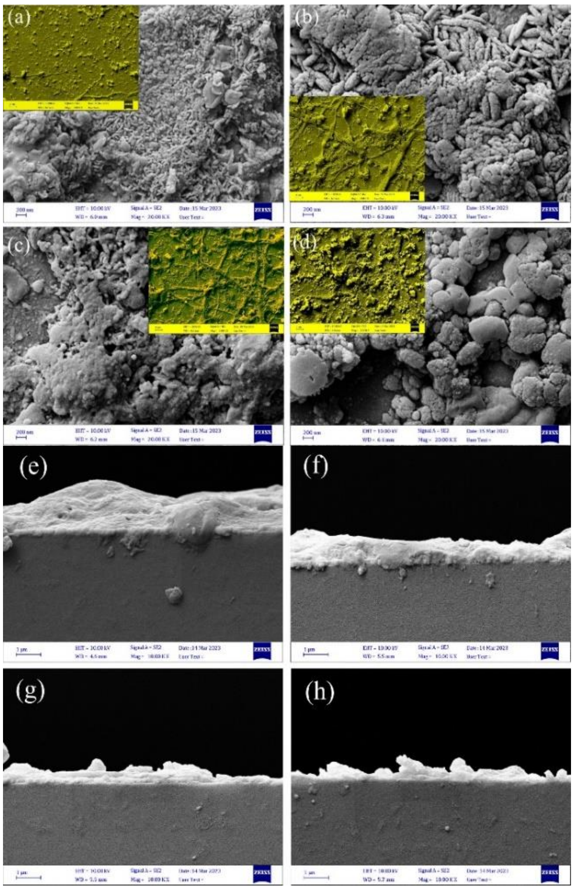

Fig. (4) FE-SEM images of the prepared Au-decorated TiO_2:fullerene films (a, b, c, and d) for the surface, (e, f, g, and h) for thickness

Figure (5) illustrates the behavior of the optical absorption of the prepared films. Fullerene displays a very interesting, complex and characteristic absorption spectrum with UV light because it has 30 weakly conjugated double bonds. Fullerene shows two intense bands at about 210 and 275 nm. The other absorption band of fullerene appearing in the UV region is located at about 330 nm. In the visible region, the spectrum of fullerene is dominated by a band at about 404 nm and by a broad and relatively weak groups of band between 430 and 670 nm with subfeatures at 500, 530, 570, 600, and 628 nm [26-29]. Clearly, at 210 nm, there is relatively high absorption with decreasing and shift by adding of TiO_2, blue shift for 30 and 50 vol.% and red for 10 vol.%, while at 385 nm for 0 vol.% TiO_2, which is related to a peak of 410 nm (as previous studies mentioned [9]), the spectrum suffered from a blue shift due to containing other structural phases as shown in the XRD pattern in Fig. (3). Concurrently, adding TiO_2 has led this peak to expand and merge with the previous one for both 10 and 50 vol.%, while its prominence is clear at 30 vol.%, which may be related to the increase of C_{60}-polymeric. There was also a clear decrease in the absorbance of films with a 30 vol.% TiO_2 ratio. The XRD pattern of fullerene:TiO_2 (30 vol.%) showed the absence of any structures outside the fullerene structures, which led to the abundance of TiO_2 without linkage that caused dominance of the optical TiO_2 behavior in addition to heavy attendance of C_{60}-polymeric [18]. Although the peaks of 500 and 530 nm (which is believed to be a contribution from the localized surface plasmon resonance (LRSP) of AuNPs) did not appear in the reference films as they became transparent when adding TiO_2 at all ratios with a clear convexity in the spectrum within the 550 nm regions down. This appearance can be confirmed as it represents the plasmon peak of AuNPs added as a decoration.

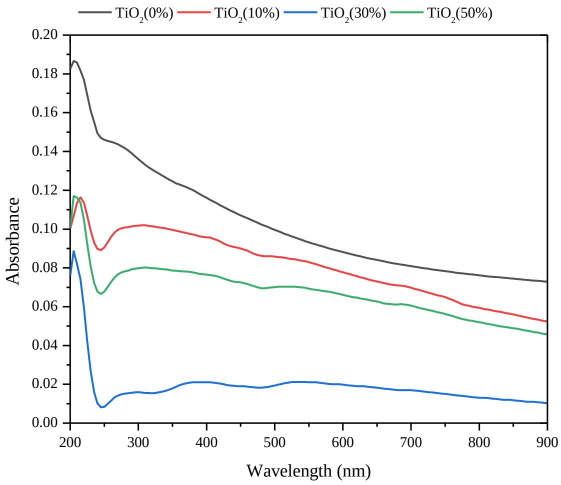

Fig. (5) Absorption spectra of the prepared Au-decorated TiO_2:fullerene films with different ratios of TiO_2

The bandgap energy (E_g) can be estimated by the Tauc's equation as [28]

$$\alpha h\upsilon = A(h\upsilon - Eg)^n \qquad (2)$$

where $h\upsilon$ is the photon enery, α is the absorption coefficient, A is a constant, and n has the values of 1/2 and 2/3 for direct and indirect transitions, respectively

The plots of $(\alpha h\upsilon)^{1/2}$ versus $h\upsilon$ are depicted in Fig. (6) for all samples. Increasing TiO_2 ratio has clearly influenced the values of bandgap of the prepared Au-decorated TiO_2:fullerene films, as the bandgap was decreased with increasing TiO_2 ratio. Although, the energy gaps of C_{60} and C_{70} obtained from this study are large when compared to the typical values (1.86 and 1.57 eV). The lack of complete purity of the prepared films (containing amorphous phases) as proven by the analysis of the XRD patterns (Fig. 3), will lead to a large difference in the values of the energy gap and the mechanisms used by the material in the optoelectronic transitions, as exploded in table (2).

Table (2) Summary of influence of TiO_2 addition on the bandgap and Urbach energies of the prepared Au-decorated TiO_2:fullerene films

Ratio of TiO_2 (vol. %)	E_g (eV)	E_u (eV)	Crystallite Size (nm)	Lattice Strain [%]
0	2.15	3.60	80.74	0.265
10	1.87	1.36	69.02	0.298
30	1.63	1.42	31.68	0.213
50	1.62	1.42	96.69	1.845

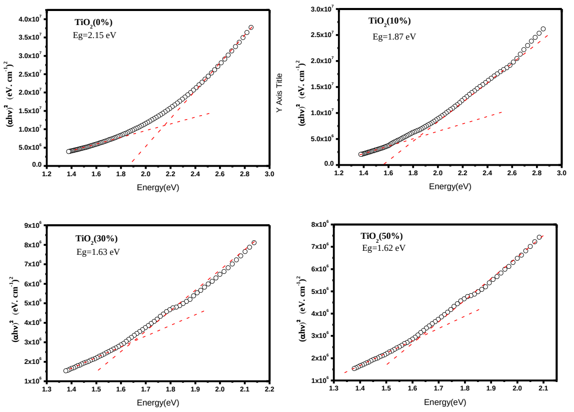

Fig. (6) The optical bandgap of the prepared Au-decorated TiO_2:fullerene films with different TiO_2 ratios

Urbach energy (E_u) related to both band tails of the localized states with the microstructural lattice disorders, and the crystal defects, can be estimated by the follwoing [29]

$$\alpha = \alpha_o exp\left(\frac{h\upsilon}{E_u}\right) \qquad (3)$$

Figure (7) is a graphical representation of Eq. (3) for the prepared films with varying TiO_2 ratio, where E_u or the disturbance can be estimated by calculating the reverse slope of the linearly fitted line. However, E_u decreases with increasing TiO_2 ratio but keeps constant with 30 and 50 vol.%. Smaller strain decreases the structural disorder since it will influence the built-in electric field at the grain boundary and hence will consequently inhibit a disturbance of the density of the states [29,30]. Referring to the calculations derived from the analysis of the XRD patterns, it is noted that there is a correlation between the values of the Urbach energy and the strain values for the ratios of 0, 10, and 30 vol.%.

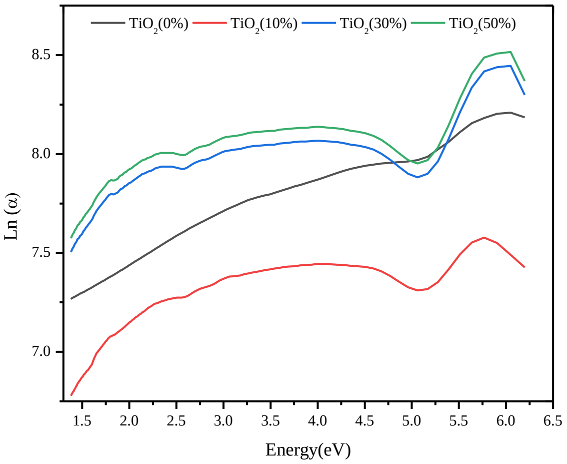

Fig. (7) Urbach energies of the prepared Au-decorated TiO_2:fullerene films as functions of energy

4. Conclusion

Au-decorated TiO_2:fullerene films were successfully prepared to produce fullerene and TiO_2:fullerene composites. The wasted batteries were used as a source for the pure carbon. In general, structural, morphological, and optical properties were affected by the variations in TiO_2 ratio in the prepared composites mainly on the crystalline phases, surface formation, and optical properties. These results encourage the selection of dry battery electrodes as a raw source for fullerenes and the Au-decorated TiO_2:fullerene films in several applications, such as photodetectors, gaseous and biosensors based on photocatalytic activity of such films.

References

[1] E. Özkan et al., "Sensor application of doped C_{60} fullerenes in detection of 1-(3-trifluoromethylphenyl)piperazine as an alternative to ecstasy", *Main Gr. Met. Chem.*, 42 (2019) 23-27.

[2] D.A. Heredia et al., "Fullerene C_{60} derivatives as antimicrobial photodynamic agents", *J. Photochem. Photobiol. C Photochem. Rev.*, 51 (2022) 100471.

[3] C. Ji et al., "Recent Developments of Carbon Dots in Biosensing: A Review", *ACS Sensors*, 5 (2020) 2724-2741.

[4] Y.Z.C. Ji, R.M. Leblanc and Z. Peng, "Recent Developments of Carbon Dots in Biosensing: A Review", *ACS Sensors*, 5 (2020) 2724-2741.

[5] S.H. Faisal and M.A. Hameed, “Heterojunction Solar Cell Based on Highly-Pure Nanopowders Prepared by DC Reactive Magnetron Sputtering”, *Iraqi J. Appl. Phys.*, 16(3) (2020) 27-32.

[6] R.H. Turki and M.A. Hameed, “Spectral and Electrical Characteristics of Nanostructured NiO/TiO_2 Heterojunction Fabricated by DC Reactive Magnetron Sputtering”, *Iraqi J. Appl. Phys.*, 16(3) (2020) 39-42.

[7] M.A. Hameed, S.H. Faisal, R.H. Turki, “Characterization of Multilayer Highly-Pure Metal Oxide Structures Prepared by DC Reactive Magnetron Sputtering Technique”, *Iraqi J. Appl. Phys.*, 16(4) (2020) 25-30

[8] O.A. Hammadi, “Effects of Extraction Parameters on Particle Size of Titanium Dioxide Nanopowders Prepared by Physical Vapor Deposition Technique”, *Plasmonics*, 15 (2020).

[9] F.J. Al-Maliki et al., “Enhanced photocatalytic activity of Ag-doped TiO_2 nanoparticles synthesized by DC Reactive Magnetron Co-Sputtering Technique”, *Opt. Quantum Electron.*, 52 (2020) 188.

[10] E.A. Al-Oubidy and F.J. Al-Maliki, “Effect of Gas Mixing Ratio on Energy Band Gap of Mixed-Phase Titanium Dioxide Nanostructures Prepared by Reactive Magnetron Sputtering Technique”, *Iraqi J. Appl. Phys.*, 14(4) (2018) 19-23.

[11] F.J. Al-Maliki and E.A. Al-Oubidy, “Effect of gas mixing ratio on structural characteristics of titanium dioxide nanostructures synthesized by DC reactive magnetron sputtering”, *Physica B: Cond. Matter*, 555 (2019) 18-20

[12] O.A. Hammadi, F.J. Kadhim and E.A. Al-Oubidy, “Photocatalytic Activity of Nitrogen-Doped Titanium Dioxide Nanostructures Synthesized by DC Reactive Magnetron Sputtering Technique”, *Nonl. Opt. Quantum Opt.*, 51(1-2) (2019) 67-78.

[13] E.A. Al-Oubidy and F.J. Al-Maliki, “Photocatalytic activity of anatase titanium dioxide nanostructures prepared by reactive magnetron sputtering technique”, *Opt. Quantum Electron.*, 51(1-2) (2019) 23.

[14] D. Thakur et al., "Self-stability of un-encapsulated polycrystalline $MAPbI_3$ solar cells via the formation of chemical bonds between C60 molecules and MA cations", *Sol. Ener. Mater. Sol. Cells*, 235 (2022) 111454.

[15] J. Yu et al., "Enhanced photocatalytic activity of bimodal mesoporous titania powders by C_{60} modification", *Dalt. Trans.*, 40 (2011) 6635-44.

[16] Y.Z. Long et al., "Effect of C_{60} on the photocatalytic activity of TiO_2 nanorods", *J. Phys. Chem. C*, 113 (2009) 13899-13905.

[17] K. Dai et al., "Enhancing the photocatalytic activity of lead molybdate by modifying with fullerene", *J. Mol. Catal. A Chem.*, 374-375 (2013) 111-117.

[18] M.B. Tahir et al., "Role of fullerene to improve the WO_3 performance for photocatalytic applications and hydrogen evolution", *Int. J. Energy Res.*, 42 (2018) 4783-4789.

[19] K. Shahzad, M.B. Tahir and M. Sagir, "Engineering the performance of heterogeneous WO_3/fullerene@Ni_3B/$Ni(OH)_2$ Photocatalysts for Hydrogen Generation", *Int. J. Hydrog. Ener.*, 44 (2019) 21738-21745.

[20] B. Peng, "Monolayer Fullerene Networks as Photocatalysts for Overall Water Splitting", *J. Am. Chem. Soc.*, 144 (2022) 19921-19931.

[21] L. Liu et al., Enhancing Built-in Electric Fields for Efficient Photocatalytic Hydrogen Evolution by Encapsulating C_{60} Fullerene into Zirconium- Based Metal-Organic Frameworks, *Angew. Chemie.*, 135 (2023) e202217897.

[22] T. Munawar et al., "Fabrication of fullerene-supported La_2O_3–C_{60} nanocomposites: dual-functional materials for photocatalysis and supercapacitor electrodes", *Phys. Chem. Chem. Phys.*, 25 (2023) 7010-7027.

[23] B.M.A. Alani and M.A. Alalousi, "Structural, Morphological, and Spectroscopical Properties of Fullerenes (C_{60}) Thin Film Prepared via Electrospray Deposition", *IOP J. Phys.: Conf. Ser.*, 1829 (2021) 012018.

[24] F.J. Al-Maliki, O.A. Hammadi and E.A. Al-Oubidy, “Optimization of Rutile/Anatase Ratio in Titanium Dioxide Nanostructures prepared by DC Magnetron Sputtering Technique”, *Iraqi*

J. Sci., 60(special issue) (2019) 91-98.

[25] S. Ilyas et al., "X-ray diffraction analysis of nanocomposite Fe_3O_4/activated carbon by Williamson–Hall and size-strain plot methods", *Nano-Struct. Nano-Obj.*, 20 (2019) 100396.

[26] M.A. Alalousi et al., "Sensing Enhancement of Gold Nanoparticles Doped-TiO_2 Thin Films as H_2S Gas Sensor", *Nano Hybrids Compos.*, 35 (2022) 1-10.

[27] F. Cataldo, S. Iglesias-Groth and A. Manchado, "On the molar extinction coefficient and integrated molar absorptivity of the infrared absorption spectra of C_{60} and C_{70} fullerenes", *Fuller. Nanotubes Carbon Nanostruct.*, 20 (2012) 191-199.

[28] K.I. Katsumata, N. Matsushita and K. Okada, "Preparation of TiO_2-fullerene composites and their photocatalytic activity under visible light", *Int. J. Photoener.*, 2012 (2012) 9.

[29] D. Patil et al., "Facile synthesis of stable Cu and CuO particles for 4-nitrophenol reduction, methylene blue photodegradation and antibacterial activity", *J. Hazard. Mater. Adv.*, 4 (2021) 100032.

[30] P. Norouzzadeh et al., "Investigation of structural, morphological and optical characteristics of Mn substituted Al-doped ZnO NPs: A Urbach energy and Kramers-Kronig study", *Optik*, 204 (2020) 164227.

IRAQI JOURNAL OF APPLIED PHYSICS
Vol. 19, No. 4B, November 2023, pp. 157-161

Lisa M. Ghazi
Rasha H. Ahmed

Department of Physics,
College of Education
For Pure Sciences,
University of Tikrit,
Tikrit, IRAQ

Structural, Morphological and Mechanical Characteristics of Ni_{55}-Cu_{45} Alloy Prepared by Powder Technology

In this study, powder technology was utilized to synthesize Ni_{55}-Cu_{45} alloy. The effect of sintering process on the characteristics of the synthesized alloy. Sintering process was carried out at 950 °C for two hours. This heat treatment process had reasonable effect on cubic structure of the alloy as the particle size was decreased after sintering as confirmed by the x-ray diffraction (XRD) patterns. Results of atomic force microscopy (AFM) have supported the XRD results by showing a reduction in particle size following sintering process. On the other hand, the values of average and root-mean-square surface roughness have been increased after sintering. The optical microscopy has revealed that the alloy's surface was homogenized and the cracks formed during the synthesis process were disappeared after sintering, which increased its hardness.

Keywords: Powder technology; Heat treatment; Vickers hardness; Metal alloys
Received: 10 July 2023; **Revised:** 27 August 2023; **Accepted:** 03 September 2023

1. Introduction

Alloys generally consist of a complete or partial union of two or more chemical elements with each other, and they have a metallic luster, are malleable for malleability and withdrawal, and conduct heat and electricity [1-3]. The alloys that have practical importance are the metal alloys, which are often distinguished over the metals included in their composition, such as durability, hardness, corrosion resistance, and also a high melting point. Alloys have wide applications in all fields of industry [4-9].

Chemical composition, purity, and particle size are some of the most crucial features that set powders apart since they affect the hardness and compressibility of the material [10-13]. In powder technology, the size of the powder is crucial because it impacts the majority of the qualities [14-19].

The sintering process, which is a heat treatment that involves changes in the size and shape of the pores that are also related to crystal growth, or geometric changes in the materials, can turn powders into solid, dense bodies [20-23]. These changes depend on the properties of the sintering material and the conditions of the sintering process [24,25].

In this research, the nickel-copper alloy has been addressed, and this alloy is considered one of the most important copper alloys, so that copper is dissolved from nickel in all proportions used, as nickel works to increase the durability of the alloy in addition to that it increases its resistance to corrosion. The alloy has good ductility and is usually suitable for most production methods. It can be formed by hot or cold rolling. It is considered one of the most important heat treatable alloys.

2. Experimental part

The basic materials used in this study are copper (Cu), from Avonchem Co. (UK) with a percentage of 45% and a purity of 99.9%, and nickel (Ni), from Buchs Fluka AG Co. (Germany) with a percentage of 55% and a purity of 99.95%. These two materials are manually mixed and blended together using a container, specifically an agate mortar and pestle. Once the mixing and grinding process is concluded, the formation of a homogeneous powder is resulted. The ingot is fabricated by a cold pressing technology. This involves the unidirectional compression of the mixed powder within a solid steel mold. The press is meticulously positioned within the piston to ensure stability and prevent any displacement of the mold components, thereby avoiding the occurrence of elastic rebound [26,27]. Subsequently, a pressure of 8 tons is applied for a duration of 5 minutes to achieve a highly robust and cohesive ingot. However, it should be noted that the ingot is not yet in its final state after the completion of the pressing process. During examination, the material exhibits a limited resistance known as ‘green resistance’. Additionally, it necessitates careful handling during transportation and is prone to crumbling when subjected to external influences. The sintering process is conducted on the specimen using a CARBOLITE electric furnace at a temperature of 950 °C for two hours.

The x-ray diffraction (XRD) analysis is conducted using the ICDD method by a Shimadzu 6000 X-ray diffractometer. The atomic force microscopy (AFM) is performed employing the Nanosurf Naio AFM 2022 instrument. The optical microscopy is carried out using an OLYMPUS microscope. The mechanical tests involve the determination of Vickers hardness using MEKTON THV–501E instrument.

3. Results and Discussion

The XRD patterns was studied to find out the crystal structures of the constituent elements of the prepared alloy (55%Ni-45%Cu). The results showed that the crystal structure of each of the nickel and copper is a cubic system, as the nickel appeared at diffraction angles of 44.49°, 51.97° and 76.59° corresponding to Miller planes of (111), (200) and (220), respectively, and axial lengths $a=b=c=3.5157$ according to the JCPDS card 01-070-0989. For copper, peaks are seen at 43.317°, 50.44°, and 74.12° corresponding to Miller planes of (111), (200) and (220) and axial lengths $a=b=c=3.615$, as in table (1), and no new phase appeared. Superimposition between nickel and copper indicates that the prepared alloy is characterized by porosity and voids between the particles of the material due to adding copper, because copper is characterized by a hardness less than nickel. Figure (1) shows the results of XRD of this alloy before sintering.

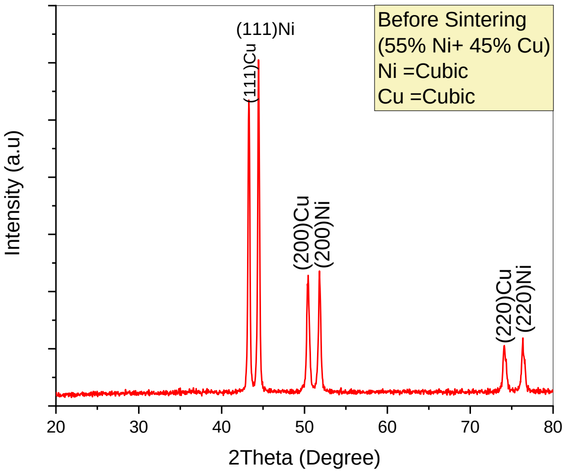

Fig. (1) The XRD pattern before sintering

Figure (2) shows the XRD pattern of the alloy after sintering and the intensity appears regularly and homogeneously, which indicates that the heat treatment was completely accurate because it was not affected by oxidation, and no unwanted phases or side phases appeared, but rather the material appeared with purity, which is the appearance of the two materials and with varying intensity depending on the addition ratios. This means that there is crystalline growth of molecules of the prepared compound [28-30].

Due to the close ratios between the two elements in the alloy, as well as the alloy's crystalline structure, which gives the alloy excellent mechanical properties, such as high resistance to corrosion and stress corrosion, it was discovered by analyzing the results that the average and root-mean-square roughness values are increased after the sintering process, as confirmed by figures (3) and (4). The metal structure, in addition to the sintering method, is one of the main factors that lead to change results after the sintering process. As a result, the quality and intensity of sintering affects the mechanical properties of the alloy, and the composition of the final layer may also affect its properties, including its roughness. The correlation and homogeneity between the two components of the alloy before and after heat treatment at 950°C for two hours on the manufactured alloy is shown in table (3) and via microscopic photographs.

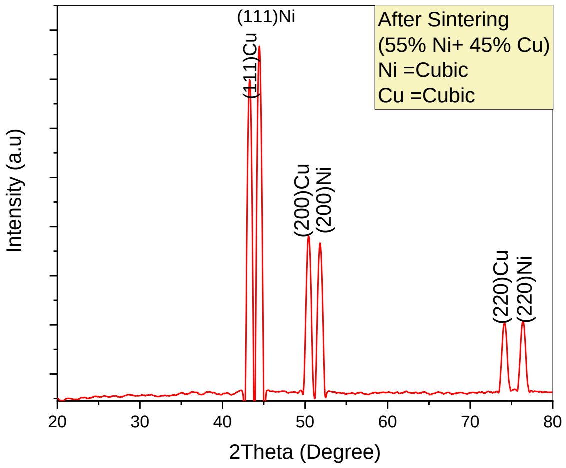

Fig. (2) The XRD pattern after sintering

Table (3) Results of average (R_{ave}) and root-mean-square ($R_{r.m.s}$) roughness of 55%Ni-45%Cu alloy before and after sintering

	Average Roughness R_{ave} (nm)	Roughness $R_{r.m.s}$ (nm)	Average Dimeter (nm)
Before Sintering	39.33	55.61	201.20
After Sintering	46.34	57.75	186.48

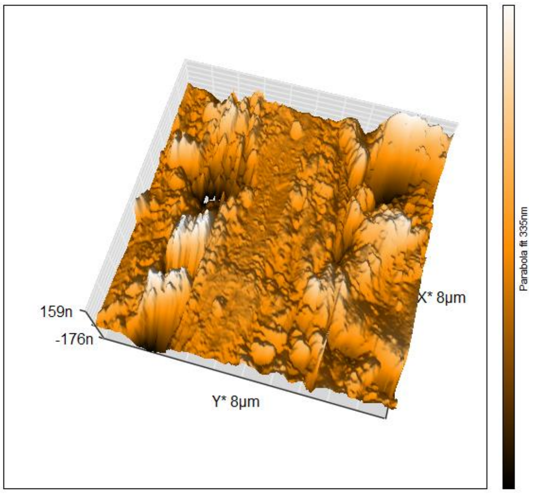

Fig. (3) AFM image of the manufactured alloy before sintering

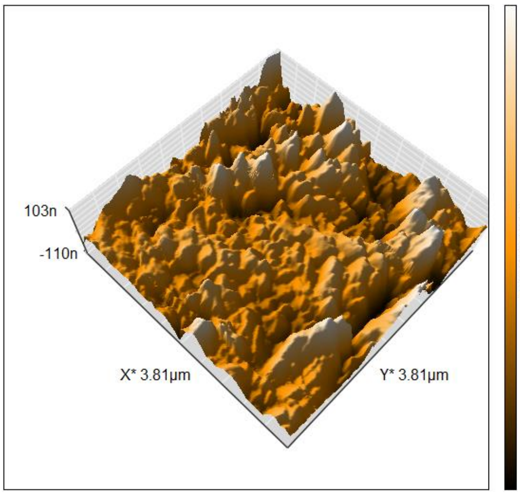

Fig. (4) AFM image of the manufactured alloy after sintering

Figure (5) shows the optical microscope image of the microstructure of the ingot before sintering process, and figure (6) shows the image of the microstructure after sintering process at 950°C for two hours and with a magnification of x80. It is noted throughout these images that there is a uniform and homogeneous distribution of the phases and there is a diffusion process clear and coherent. Also, there is a good bond between the two elements (nickel and copper).

Fig. (5) Optical microscope image of the ingot before the sintering

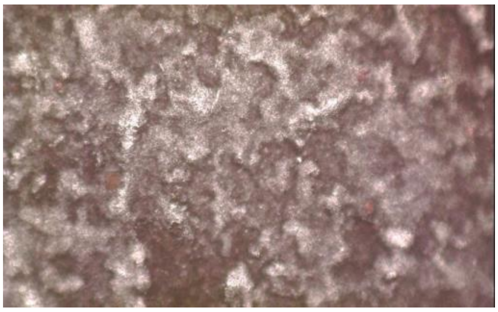

Fig. (6) Optical microscope image of the ingot after the sintering

Vickers hardness test is one of the most important mechanical properties and is defined as the initial surface distance obtained by the material [31]. The hardness of the ingot has been verified by using the Vickers method throughout the stitching tool. It is in the form of a pyramid with a quadruple base and under pressure (load) applied to the amount of 500g for a period of 5s. By examining the results, it was found that the hardness increased after the sintering process compared to the hardness value before the sintering process. This is due to recrystallization, grain growth, and stress relief (compression process residues) in the covering layer due to sintering at a high temperature (950°C) for two hours. Compression is a complex process, and this reaction can be divided into two phases compared to solid minerals, the first phase appears as an accumulation of free powder particles in the early stages of the densification or compression process, while the second phase appears as a porous body later in the process of compression and heat treatment [32,33]. Table (4) shows the results of the Vickers hardness values for the alloy before and after the sintering process.

Table (4) Vickers hardness of the manufactured alloy before and after the sintering process

Alloy Proportions	Vickers hardness before sintering (g/cm^3)	Vickers hardness after sintering (g/cm^3)
55%Ni-45%Cu	38.8	180.5

4. Conclusions

In concluding remarks, the heat treatment had altered the examined properties of the Ni_{55}-Cu_{45} alloy. The particle size decreases after sintering, but for the prevalent levels, the particle size determined by AFM is larger than that determined by XRD because AFM measures the size of the grains on the surface of the ingot, whereas XRD determines its size inside the ingot. The hardness plays a role in demonstrating this because it rose following the sintering process, which demonstrates the inverse relationship between the hardness and particle size. The optical microscopy revealed the removal of the divisions and cracks. The characteristics of the Ni_{55}-Cu_{45} alloy were successfully altered by sintering at 950°C for two hours.

References

[1] R.D. Jananin et al., “Effect of composition on the stacking fault energy of copper-nickel alloys using molecular dynamics simulations”, *Mater. Today: Proc.*, 39(Pt 4) (2021) 1796-1800.

[2] E.M.S. Salih, H.A.H. Al-Jubori and R.J. Abbas, “Finding an alternative to nickel used in an alloy (copper-nickel) in electric power plants”, *Mater. Today: Proc.*, 61(Pt 3) (2022) 700-705.

[3] T. Deng and H. Liu, “A study of mechanical characteristics and microstructural evolution of copper-nickel alloy sheet undergoing ultrasonic vibration assisted uniaxial tension”, *Mater. Sci. Eng. A*, 885 (2023) 145608.

[4] Mahmoud Naji, Mining Science (Damascus University, 1990/1991).

[5] B. Yin et al., “Experimental and density functional studies on the corrosion behavior of the copper-nickel-tin alloy”, *Chem. Phys. Lett.*, 509(4-6) (2011) 192-197.

[6] Y. An et al., “Effect of laser remelting on copper‑nickel alloy coating prepared by extreme high-speed laser cladding”, *J. Manufact. Process.*, 95 (2023) 497-507.

[7] L. Cassayre et al., “Electrochemical oxidation of binary copper–nickel alloys in cryolite melts”, *Corr. Sci.*, 49(9) (2007) 3610-3625.

[8] I. Oh et al., “Enhanced stability and electrocatalytic activity of graphene on copper-nickel alloys for hydrogen production from wastewater”, *mdpi Carbon*, 161 (2020) 665-673.

[9] G. Ferk et al., “The synthesis and characterization of nickel–copper alloy nanoparticles with a narrow size distribution using sol–gel synthesis”, *Mater. Lett.*, 124 (2014) 39-42.

[10] J. Rozsypal et al., “Use of interelectrode material transfer of nickel and copper‑nickel alloy to carbon fibers to assemble miniature glucose sensors”, *J. Electroanal. Chem.*, 816 (2018) 45-53.

[11] E. García-Martínez et al., “Low initial lubrication procedure in the machining of copper-nickel 70/30 ASTM B122 alloy”, *J. Manufact. Process.*, 62 (2021) 623-631.

[12] M.G. Pavloic et al., “The Effect of Particle Structure on Apparent Density of Electrolytic Copper Powder”, *J. Serbian Chem. Soc.*, 66(11) (2001) 923-933.

[13] M. Kumar, D.I. Jeong and D.H. Yoon, “Copper nickel alloy nanorods textured nanoparticles for oxygen evolution reaction”, *Electrochim. Acta*, 333 (2020) 135545.

[14] S. Li et al., “Cost-efficient copper-nickel alloy for active cooling applications”, *Int. J. Heat Mass Transfer*, 195 (2022) 123181.

[15] Y. Miao et al., “Material properties of gradient copper-nickel alloy fabricated by wire arc additive manufacturing based on bypass-current PAW”, *J. Manufact. Process.*, 83 (2022) 637-649.

[16] P. Rojas et al., “Effect of the Powder Metallurgy Manufacture Process on the Electrochemical Behaviour of Copper, Nickel and Copper-Nickel Alloys in Hydrochloric Acid”, *Int. J. Electrochem. Sci.*, 11(6) (2016) 4701-4711.

[17] D. Riman et al., “Glucose sensing on graphite screen-printed electrode modified by sparking of copper nickel alloys”, *Talanta*, 165 (2017) 466-473.

[18] B.-Z. Li et al., “Insight to corrosion mechanism of 90/10 copper-nickel alloys under different sea depths”, *Mater. Lett.*, 303 (2021) 130513.

[19] H. Wei et al., “Dendritic core-shell copper-nickel alloy@metal oxide for efficient non-enzymatic glucose detection”, *Sens. Actuat. B: Chem.*, 337 (2021) 129687.

[20] C. Bai et al., “A rapid two-step method for fabrication of superhydrophobic-superoleophobic nickel/copper alloy coating with self-cleaning and anticorrosion properties”, *Coll. Surf. A: Physicochem. Eng. Asp.*, 651 (2022) 129635.

[21] I.C. Ukaga et al., “The inhibitive performance of 2,3-pyrazine dicarboxylic acid and synergistic impact of KI during acid corrosion of 70/30 and 90/10 copper–nickel alloys”, *Mater. Chem. Phys.*, 296 (2023) 127313.

[22] N. Mary et al., “Electrochemical behaviour of copper–nickel alloys as immobilisation matrices for the storage of fission products in CO_2-enriched synthetic groundwater”, *Electrochim. Acta*, 98 (2013) 11-19.

[23] S. Al-Saadi et al., “Graphene coating on a nickel-copper alloy (Monel 400) for microbial corrosion resistance: Electrochemical and surface characterizations”, *Corr. Sci.*, 182 (2021) 109299.

[24] M.Y. Lee et al., “Artificial Stone Slab Production Using Waste Glass, Stone Fragments and Vacuum Vibratory Compaction”, *J. Cement Concr. Compos.*, 30(7) (2008) 583-587.

[25] R. Rajesh et al., “Copper nickel alloys made using direct metal laser sintering method for assessing corrosion resistance properties”, *Mater. Today: Proc.*, 49(Pt 3) (2022) 703-713.

[26] Y.P. Jin and M. Hu, “Densification of Graphite/Copper Compound Powder”, *2nd Int. Conf. on Mech. Automat. Control Eng. Electr. Electron. Eng., IEEE* (2011) 1131-1135.

[27] C.P. Samal, “Microstructure and Mechanical Property study of Cu-graphite Metal Matrix composite Prepared by Powder Metallurgy Route”, MSc thesis, National Institute of Technology Rourkela Orissa, India (2012).

[28] S.Y Darweesh, I.K Jassim and A.S. Mahmood, “Characterization Of Cerment Composite Coating Al_2O_3-Ni System”, *IOP J. Phys.: Conf. Ser.*, 1294 (2019) 022011.

[29] S. Hu et al., “Influence of hydrostatic pressure on the corrosion behavior of 90/10 copper-nickel alloy tube under alternating dry and wet condition”, *Corr. Sci.*, 146 (2019) 202-212.

[30] Y. Liu et al., “Metal-organic framework derived carbon-supported bimetallic copper-nickel alloy electrocatalysts for highly selective nitrate reduction to ammonia”, *J. Coll. Interface Sci.*, 614 (2022) 405-414.

[31] K. Wada, J. Yamabe and H. Matsunaga, “Mechanism of hydrogen-induced hardening in pure nickel and in a copper–nickel alloy analyzed by micro Vickers hardness testing”, *Mater. Sci. Eng. A*, 805 (2021) 140580.

[32] R.N. Ahmed and C.S. Ramesh, “Tribological Properties of Cast Copper-SiC-Graphite Hybrid Composites”, *Int. Symp. of Res. Stud. on Mater. Sci. Eng. (ISRS)*, Chennai, India (2004) 1-15.

[33] J.S. Colton, **“Manufacturing Processes and Engineering Metal Powder Processing”**, ver. 1, Colton © *GIT* (2009) 2-28.

Table (1) calculations of XRD parameters before sintering

Content %	2Theta (Degree)	FWHM (Deg)	d_{hkl} Exp (°A)	C.S (nm)	d_{hkl} Std (°A)	Hkl	Phase	System	Card No
55%Ni-45%Cu	43.317	0.5512	2.052	137.3211	2.087	(111)	Cu	Cubic	01-085-1326
	44.494	0.66374	2.015	155.2048	2.03	(111)	Ni	Cubic	03-065-2865
	50.449	0.684	1.772	144.4313	1.807	(200)	Cu	Cubic	01-085-1326
	51.847	0.81065	1.605	192.3348	1.76	(200)	Ni	Cubic	00-001-1292
	74.126	0.65	1.246	152.342	1.278	(220)	Cu	Cubic	01-085-1326
	76.378	0.8282	1.185	199.431	1.245	(220)	Ni	Cubic	00-001-1292

Table (2) calculations of XRD parameters after sintering

Content %	2Theta (Degree)	FWHM (Deg)	d_{hkl} Exp (°A)	C.S (nm)	d_{hkl} Std (°A)	Hkl	Phase	System	Card No
55%Ni-45%Cu	43.317	0.7272	2.03	129.3211	2.087	(111)	Cu	Cubic	01-085-1326
	44.494	0.83974	1.993	147.2048	2.03	(111)	Ni	Cubic	03-065-2865
	50.449	0.86	1.75	136.4313	1.807	(200)	Cu	Cubic	01-085-1326
	51.847	0.98665	1.583	184.3348	1.76	(200)	Ni	Cubic	00-001-1292
	74.126	0.826	1.224	144.342	1.278	(220)	Cu	Cubic	01-085-1326
	76.378	1.0042	1.163	191.431	1.245	(220)	Ni	Cubic	00-001-1292

IRAQI JOURNAL OF APPLIED PHYSICS
Vol. 19, No. 4B, November 2023, p. 162

Iraqi Journal of Applied Physics (IJAP)
Performance Indicators on Scopus Database

By
Oday A. Hammadi
Editor-In-Chief, IJAP

In July 20121, IJAP was indexed in Scopus and all articles published with IJAP since January 2021 up to now have appeared on Scopus database. In 5th September 2023, as the last update of Scopus database was released, the articles published with IJAP during January 2019 to December 2020 have been indexed too. Therefore, the archive of IJAP is available now since 2019. Accordingly, the CiteScore of IJAP has increased from 0.2 in May 2023 to 0.5 in September 2023 due to the inclusion of citations of IJAP articles before July 2021.

IJAP is progressing relatively slowly, but this progress is based on stable policies and coherent scientific, technical and administrative foundations since 2005. Consequently, we expect that there will be advanced steps forward during the next year 2024, with greater scientific sobriety, wider global exposure, and faster access to researchers inside Iraq and abroad.

Below are the most recent performance indicators of IJAP on Scopus database.

Source details

Iraqi Journal of Applied Physics
Scopus coverage years: from 2019 to Present
Publisher: Iraqi Society for Alternative and Renewable Energy Sources and Techniques
ISSN: 1813-2065 E-ISSN: 2309-1673
Subject area: Chemistry: Physical and Theoretical Chemistry; Physics and Astronomy: General Physics and Astronomy; Materials Science: Electronic, Optical and Magnetic Materials
Source type: Journal

CiteScore 2022
0.2

SJR 2022
0.186

SNIP 2022
0.045

CiteScore 2022
0.2 = 8 Citations 2019 - 2022 / 45 Documents 2019 - 2022
Calculated on 05 May, 2023

CiteScoreTracker 2023
0.5 = 53 Citations to date / 100 Documents to date
Last updated on 05 September, 2023 • Updated monthly

CiteScore rank 2022

119 document results

Select year range to analyze: 2019 to 2023

Year	Documents
2023	38
2022	24
2021	22
2020	18
2019	17

IRAQI JOURNAL OF APPLIED PHYSICS
Vol. 19, No. 4B, November 2023, pp. 163-166

Naba H. Al-Ahbabi [1]
Nadim K. Hassan [2]

Department of Physics,
College of Education
For Pure Science,
University of Tikrit,
Tikrit, IRAQ

Characterization of Nickel-doped PVA Gas Sensors Fabricated by Electrospinning Method

In this work, gas sensor was prepared from polyvinyl alcohol (PVA) polymer fibers doped with nickel nanoparticles using the electrospinning method. It was found from the x-ray diffraction (XRD) patterns that the structural properties of the undoped and doped films were unstructured and the crystallite size decreases with increasing doping level in presences of nickel nanoparticles. The results of gas sensing experiments showed high sensitivity of the PVA nanofiber films doped with nickel nanoparticles, fast response time (14.4s) and fast recovery time (53.1s) at operation temperature of 150°C. Throughout the study of the electrical properties (Hall effect), it was found that the prepared PVA polymer films are p-type, and when they are doped with 2% nickel, they change their conductivity to n-type, and then return to be p-type when doped with 3% nickel.

Keywords: Gas sensors; Polyvinyl alcohol (PVA); Electrospinning; Nickel dopant
Received: 24 June 2023; **Revised:** 17 August 2023; **Accepted:** 24 August 2023

1. Introduction

Gas sensing technologies play a crucial role in various fields, including environmental sensing and monitoring, industrial safety and diagnostics, and healthcare applications [1,2]. Electrospinning, a versatile fabrication technique, has emerged as a promising method to develop gas sensors with enhanced performance characteristics [3-5].

There has been an increasing demand for gas sensors that are not only highly sensitive and selective but are also operable at room temperature, eliminating the need for energy-intensive heating elements [6-9]. Polyvinyl alcohol (PVA) has attracted significant interest in the field of gas sensing due to its excellent film-forming properties, chemical stability, and simplicity of operation [10-12].

Incorporating metal nanoparticles into PVA matrices has shown great potential in improving the sensing properties of these materials [13-15]. Among the various metal nanoparticles, nickel (Ni) stands out as a suitable candidate owing to its high electrical conductivity, ferromagnetism, and remarkable gas-sensing attributes [16-18].

The electrospinning process allows homogeneous dispersion of nanoparticles inside polyvinyl alcohol (PVA), which ensures a good nanostructure and effective gas interaction [19]. When manufacturing gas sensors, scientists began to modify some of their characteristics to obtain a distinct response, for example, nickel doped with cobalt is used with polyvinyl alcohol to make a gas sensor with unique characteristics and a high ability to respond to harmful and polluting gases, which contributes greatly to the protection of public health [20-23].

In this work, undoped polymer films (PVA) as well as films doped with nickel were prepared and their electrical, structural and gas sensing characteristics were studied.

2. Experimental work

In order to prepare solutions to be spun, the polyvinyl alcohol (PVA) polymer is dissolved in distilled water. To obtain 10% wt., 6 g of PVA is added to 60 ml distilled water. The undoped PVA solution is mixed using a magnetic stirrer for 6 hours at a temperature of 50 °C. To prepare nickel dopant solution with concentration of 0.05 M, 0.131 g of nickel is added to 10 ml distilled water as a solvent. Then the solution was placed on a magnetic stirrer at room temperature for two hours. After that, the nickel solution is added with different ratios (1, 2, 3 ml) separately to 9, 8, 7 ml of undoped PVA solution, respectively, and then, these solutions are mixed on a magnetic stirrer for 3 hours at room temperature to obtain homogeneous solutions used in the deposition of nanofibers.

3. Results and Discussion

The results of the x-ray diffraction (XRD), shown in Fig. (1), indicate that polyvinyl alcohol (PVA) has an amorphous structure due to the weak vibration peaks of the polymer and the increased bending of the (O-H) chain, which is related to the polymer (PVA). This is similar to what was found by reference [24]. When the doping level with nickel is (2,3)%, we notice the emergence of peaks belonging to the nickel (Ni) element at the planes (111), (200) and (220). It is noted that there is a change in the intensity and the positions of the diffraction angles, which indicates that the polyvinyl alcohol (PVA) has a non-crystalline structure [25,26].

From table (1), the crystallite size, full-width at half maximum (FWHM) and inter-planar distance (d) were calculated, and it was found that the average crystallite size ranged in 50.8-76.6 nm.

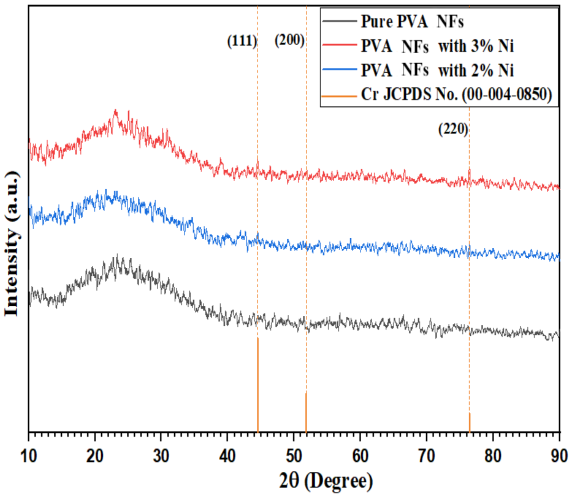

Fig. (1) The XRD patterns of Ni-doped PVA samples at doping ratio of (2,3)%

The results of the gas sensor showed that increasing the operation temperature leads to an improvement in the sensitivity of the prepared films, as shown in Fig. (2), which explains the relationship between the response time and the recovery time for Ni-doped PVA deposited on glass substrates at (2,3) doping level with different number of pulses at operation temperature of 200°C. The fastest response was recorded after 14.4 s at operation temperature of 150 °C while the recovery time was 53.1 s. As the response time gets faster, electrons move easily to the conduction band, so that the resistance of the film decreases and the increasing adsorption of oxygen by the surface leads to the extraction of conduction electrons from the near surface area. This forms a surface layer that depletes the electrons, especially when increasing the doping level with nickel.

The electrical properties of the films are greatly affected by the deposition conditions and crystalline structure [27]. The electrical properties were studied using the Hall effect method. As given in table (3), the results showed that the polymer material (PVA) is p-type and when the concentration of nickel dopants is increased to 2%, the concentration of negative charge carriers of increases too and the material becomes n-type due to the decrease in the voltage barrier, which generates secondary energy levels between valence and conduction bands [28].

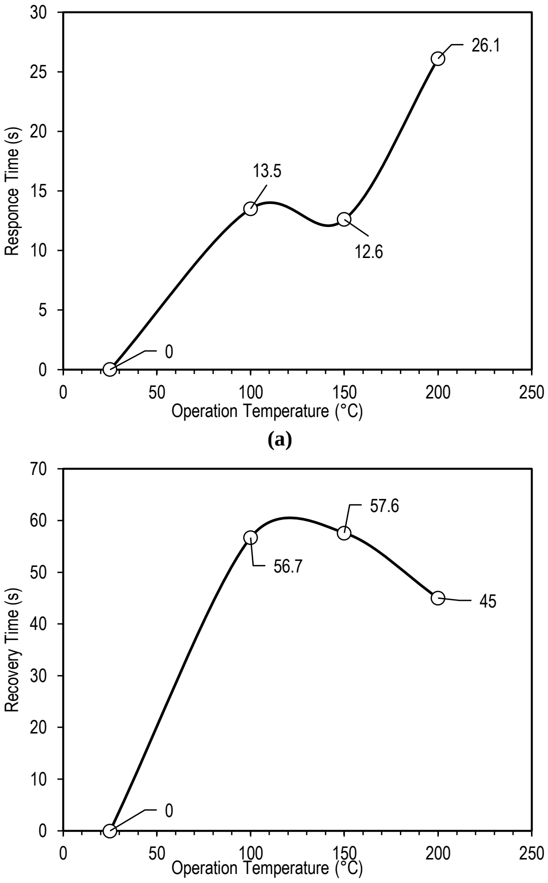

(a)

(b)

Fig. (2) variation of response time (a) and recovery time (b) with operation temperature for undoped (PVA) and Ni-doped at doping levels of (2,3)%

Table (2) Parameters of the prepared gas sensor at different temperatures

Temperature	t_{gas} (on)	t_{gas} (off)	$t_{gas\ recover}$	Response Time (s)	Recovery time (s)
25				0	0
100	21	42	100	18.9	52.2
150	25	41	100	14.4	53.1

4. Conclusion

The x-ray diffraction pattern shows that the undoped films of the polymer (PVA) and doped with nickel are amorphous and that the crystal size decreases with increasing nickel doping. The presence of nickel nanoparticles in the doping films. The results showed high sensitivity to gas sensor for films of a mixture (PVA NFs / Ni NPs) with various gases. From the study of electrical properties (Hall effect), it was found that the films prepared for polymer (PVA) are p-type which change to n-type when doping with 2% nickel and return to p-type with 3% nickel doping.

References

[1] M.S.H. Ador et al., “Review of new developments in different types of sensors over the past 15 years”, Reference Module in **Materials Science and Materials Engineering**, Elsevier (2023), ISBN 9780128035818.

[2] X.F. Wang, B. Ding and J.Y. Yu, **"Functional nanofibers in sensor applications"**, editor(s): Qufu Wei, in Woodhead Publishing Series in Textiles, Functional Nanofibers and their Applications, Woodhead Publishing (2012) 209-235.

[3] Q. Gao et al., "Electrospun fiber-based flexible electronics: Fiber fabrication, device platform, functionality integration and applications", *Prog. Mater. Sci.*, 137 (2023) 101139.

[4] D.A. Oriero et al., "Electrospun biocatalytic hybrid silica–PVA-tyrosinase fiber mats for electrochemical detection of phenols", *Microchem. J.*, 118 (2015) 166-175.

[5] E.A. Kamoun et al., "Recent advances in PVA-polysaccharide based hydrogels and electrospun nanofibers in biomedical applications: A review", *Int. J. Biol. Macromol.*, 187 (2021) 755-768.

[6] S. Arumuganathar and J.N. Reddy, "Polyvinyl alcohol (PVA) NFss: A review on high-temperature characteristics and the influence of NFs surface modification", *J. Mater. Sci.*, 53(10) (2018) 7311-7336.

[7] T. Yoshimura et al., "Development of energy intensive multifunction cavitation technology and its application to the surface modification of the Ni-based columnar crystal superalloy CM186LC", *Heliyon*, 7(12) (2021) e08572.

[8] R. Mehrabi et al., "Thermo-mechanical assessment of heated bridge deck under internal cyclic thermal loading from various heating elements: pipe, cable, rebar", *Cold Reg. Sci. Technol.*, 194 (2022) 103466.

[9] W. Zhu et al., "Impacts on the embodied carbon emissions in China's building sector and its related energy-intensive industries from energy-saving technologies perspective: A dynamic CGE analysis", *Ener. Build.*, 287 (2023) 112926.

[10] O.S. Kwon et al., "Novel flexible chemical gas sensor based on poly(3,4-ethylenedioxythiophene) nanotube membrane", *Talanta*, 82(4) (2010) 1338-1343.

[11] R. Rajan et al., **"Functionalized Nanofiber-based Anticorrosive Coatings"**, Ch. 11, editor(s): K. Deshmukh et al., Functionalized Nanofibers, Elsevier (2023) 307-328.

[12] B.D. Cullity and S.E. Stock, **"Elements of X-ray Diffraction"**, Prentice Hall (NJ, 2001) 388.

[13] B. Manjunath et al., "Electrochemical sensing of carcinogenic p-dimethylamino antipyrine using sensor comprised of eco-friendly MoS_2 nanosheets encapsulated by PVA capped Mn doped ZnS nanoparticle", *Inorg. Chem. Commun.*, 151 (2023) 110617.

[14] M.A. El-Morsy et al., "Optical, and electrical conductivity properties of ZnO and TiO_2 nanoparticles scattered in PEO-PVA for electrical devices", *Results in Physics*, 50 (2023) 106592.

[15] D. Khanna et al., "Microwave processed metal nanoparticles/MoO_3-PVA photoactive nanocomposites for energy applications", *Mater. Sci. Eng. B*, 297 (2023) 116822.

[16] R. Rajeev et al., "Recent advances in bimetallic based nanostructures: Synthesis and electrochemical sensing applications", *Microchem. J.*, 163 (2021) 105910.

[17] Z. Yang, C. Wang and X. Lu, **"Nanofiber Materials"**, Ch. 3, editor(s): B. Ding, X. Wang, J. Yu, in Micro and Nano Technologies, Electrospinning: Nanofabrication and Applications, William Andrew Publishing (2019) 53-92.

[18] M.A. Kanjwal and A. Al Ghaferi, "Hybrid nanofibers opportunities and frontiers – A review", *J. Environ. Chem. Eng.*, 10(6) (2022) 108850.

[19] L. Dai et al., "Electrospinning fabrication and gas sensing properties of PVA/NiO mix nano NFss", *J. Mater. Sci.: Mater. In Electron.*, 29(19) (2018) 16850-16858.

[20] J. Wang, D. Wang and X. Han, "Gas sensors based on metal oxide semiconductors", *Sensors*, 19(12) (2019) 2726.

[21] R.B. Kamble and V.L. Mathe, "Nanocrystalline nickel ferrite thick film as an efficient gas sensor at room temperature", *Sens. Actuat. B Chem.*, 131(1) (2008) 205-209.

[22] D.M. Fernandes et al., "Thermal and photochemical effects on the structure, morphology, thermal and optical properties of PVA/$Ni_{0.04}Zn_{0.96}O$ and PVA/$Fe_{0.03}Zn_{0.97}O$ nanocomposite films", *Polym. Degrad. Stabil.*, 98(9) (2013) 1862-1868.

[23] A. Naeimi et al., "Enhanced electrocatalytic performance of Pt nanoparticles immobilized on novel electrospun PVA@Ni/NiO/Cu complex bio-nanofiber/chitosan based on Calotropis procera plant for methanol electro-oxidation", *Int. J. Hydro. Ener.*, 46(36) (2021) 18949-18963.

[24] C.-C. Yang, "Preparation of the PVA/HAP composite polymer membrane for alkaline DMFC application", *Desalination*, 233 (2008) 137-146.

[25] K.E. Strawhecker and E. Manias, "Structure and Properties of Polyvinyl alcohol)/Na^+ Montmorillonite Nanocomposites", *Chem. Mater.*, 12(10) (2000) 2943-2949.

[26] E.K.M. Tawfik, "Radiation effect on characterization and physical properties of polymer nanocomposites", MSc thesis, Zagazig University (Egypt, 2013).

[27] S. Joishy et al., "Influence of solution molarity on structure, surface morphology, non-linear optical and electric properties of CdO thin films prepared by spray pyrolysis technique", *Mater. Res. Exp.*, 6(10) (2019) 106447.

[28] M.A. Fakhri, "Effect of Substrate Temperature on Optical and Structural Properties of Indium Oxide Thin Films Prepared by Reactive PLD Method", *Eng. Technol. J.*, 32(5A) (2014) 1323-1330.

Table (1) The XRD parameters for (PVA) doped with nickel (Ni) and with doping rates (2,3)%

Ni-doped PVA fibers Sample	2θ (deg.)	FWHM (deg.)	$d_{exp.}$ (Å)	D (nm)	$D_{avg.}$ (nm)	2θ (deg.)	$d_{sta.}$ (Å)	hkl	Card No.	Structure
2% Ni	44.5307	0.1762	2.03469	50.885	66.94	44.508	2.034	111	00-004-0850	Cubic
	51.8497	0.1258	1.76338	73.337		51.847	1.762	200		
	76.3700	0.1378	1.24706	76.605		76.372	1.246	220		
3% Ni	44.6085	0.1378	2.03132	65.082	65.55	44.508	2.034	111	00-004-0850	Cubic
	64.6771	0.1720	1.44002	57.096		51.847	1.762	200		
	82.3500	0.1480	1.17003	74.483		76.372	1.246	220		

Table (3) Values of carrier concentration, sheet concentration, electrical resistivity (ρ), Hall coefficient, and mobility of undoped and Ni-doped (PVA) polymer with ratios of (2,3)%

Sample	Carrier Concentration (1/cm^3) x10^{12}	Sheet Concentration (1/cm^2) x10^7	ρ (Ω.cm) x10^4	Conductivity Type	Hall Coefficient (cm^3/C) x10^6	Mobility (cm^2/V.s) x10^2
PVA (undoped)	2.067	2.067	2.216	p-type	3.020	1.36
PVA (8%) with 2% Ni NPs	-2.134	-2.134	١.245	n-type	-2.926	2.350
PVA (7%) with 3% Ni NPs	0.7071	0.7071	0.8787	p-type	8.828	10.05

IRAQI JOURNAL OF APPLIED PHYSICS
Vol. 19, No. 4B, November 2023, pp. 167-170

Lara S. Khalil
Mazin A. Alalousi

Department of Physics,
College of Science,
University of Anbar,
Ramadi, IRAQ

Preparation and Characterization of Fullerene/AuNPs Composite Films

This study aims to prepare fullerene/gold nanoparticles composite by electrospray and investigate the influence of the gold nanoparticles concentration of 0.412, 1.944, and 3.575 ppm on the film structural, morphological, and Raman properties. XRD patterns demonstrated initial changes in the structural phases, where the increasing of AuNPs concentration led to decrease of C_{60} phases and increase of both C_{60}-polymaric and C_{70} phases. Moreover, the field emission electron microscope images evident a variation in size distribution, formation, and phase patterns with the AuNPs concentration. Raman spectra demonstrated the formation of fullerenes C_{60}, C_{60} polymer, and C_{70} with appearance of the characteristic vibrational modes of these fullerenes $H_g^{(1)}$, $F_{2g}^{(1)}$, and $A_g^{(2)}$.

Keywords: Fullerene; Laser ablation; Wasted batteries; Raman spectroscopy
Received: 06 August 2023; **Revised:** 28 August 2023; **Accepted:** 30 August 2023

1. Introduction

Fullerenes are distinguished by their highly symmetrical cage-like spherical shape, which aroused much interest for this reason [1]. Additionally, these structures have infinitesimal sizes and adopt various shapes within a fully or partially enclosed carbon net. These structures consist of carbon atoms connected by single or double bonds, often forming rings comprising 5 to 7 atoms. Their closed structure can be represented by the formula C_n, where n corresponds to the number of carbon atoms involved. Notably, graphene serves as the fundamental building block for all raw materials that give rise to fullerenes [2]. Due to their unique chemical and physical properties such as their affinity with carbonic compounds, noble metals, other materials, controlled optical gaps, and electronic structure were nominated for entry into several applications [3]. Recently, new trends for fullerenes in biomedical uses have emerged [4-6], pharmacology, and photocatalysis applications [7]. Therefore, made the reactivity of fullerenes is an area of immense interest in the synthetic organic chemistry field [8]. Despite the importance of entering this type of carbon in many applications and causing breakthroughs in some industries, there are many challenges, including challenges in its manufacture and production, as the quantities of fullerene produced were not sufficient to be used in many applications in addition to its high cost [9-11]. There are four our main routes for the fullerenes synthesis; laser irradiation of carbon, laser irradiation of poly aromatic hydrocarbon, electrical arc graphene heating, and resistive arc graphene heating [12]. Recently, Alani and Alalousi succeeded in producing carbon particles colloidal through the utilization of an Nd-YAG laser. These particles were then electrostatically sprayed to directly obtain fullerene films [13]. One of the methods used in the previous C60 configuration Carbon types, especially C60 and C70, are characterized by Raman spectroscopy by calculating their vibrational patterns depending on the form of their unified bonds, which are carbon-carbon (C-C) bonds [1].

Gold and silver nanoparticles are considered to have a great effect in improving the surface, which aims to enhance the Raman spectra, where the surface plasmon resonance absorption of gold nanoparticles on the surface contributes to strengthening and strengthening that very surface. This technique is called Surface-Enhanced Raman Scattering (SERS) because these particles are the mineral has a distinctive nanostructure that contributes to the detection of particles [14,15].

This study aims to prepare and study the effect of gold nanoparticles (AuNPs) concentration on the structural, morphological, and Raman spectroscopic of the prepared fullerene/ AuNPs films based on dry batteries.

2. Experimental Part

A colloidal carbon solution was prepared according to previous study [13]. A carbon target was placed in a beaker containing 50 mL of deionized water and irradiated by a pulsed Nd:YAG laser with (λ=1064 nm, 100 mJ of energy, 6 Hz of pulses rate, and 6000 pulses). The distance between the surface of pellet and the laser lens was 12 cm. Then, the gold colloidal was prepared in the same laser parameters with (0.412, 1.944, and 3.575) ppm of concentration, respectively. The color of the water began to change to a light purple color. As well, mixtures of carbon/AuNPs colloidal were prepared by irradiating of target into AuNPs colloidal (50 ml) with 1000, 2000, and 3000 pulses. To fabricate fullerene and fullerene/AuNPs films, each colloidal was sprayed separately after filtration on quartz using an electrospray device. The nozzle biased positively while the substrates biased negatively with DC 5 KV as a bias potential, additional to 250±25°C of substrates temperature.

Characterization: Structural properties were chartered by analysis of X-ray diffraction (XRD) patterns (x-ray CuKα radiation and accelerated voltage of 40 kV). Williamson-Hall relation was [13] applied to estimate the crystalline size

$$D_{hkl} = \left(\frac{A\lambda}{cos\theta . \beta_{hkl}}\right) + (4\varepsilon \sin\theta) \qquad (1)$$

FE-SEM images achieved via field emission scanning electron microscope (FE-SEM, INSPECT-550) have been used to evaluate the morphological properties of the prepared film surfaces, addition to the energy dispersive x-ray (EDX) microanalysis to estimate elemental analysis associated with the prepared films, as well Raman spectra were achieved to detect their vibrational and rotational.

3. Results and discussion

XRD patterns have been analyzed based on ICSD 98-060-2518, ICSD 98-007-5506, ICSD 98-009-5370, and ICSD 98-005-6668 cards. Pure carbon films showed a polycrystalline structure with the dominance of C_{60} phases at 2θ of approximately 15.29°, 20.77°, 37.77°, 39.25°, and 50.8663°. The dominant phase was observed at about 20.77° (311) with crystallite size found at about 80.76 nm. Likewise, the presence of two main phases, C_{70} and C_{60}- Polymer but with lower attributions as shown in Fig. (1).

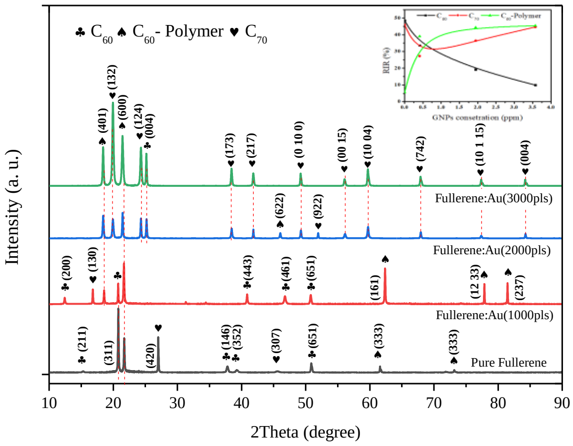

Fig. (1) XRD patterns of Fullerene-Au films

Notably, the introduction of AuNPs indicates their influence on the distribution of diffraction phases, which led to the dominant phase shift (600) at 2θ = 21.65° (C_{70}) with crystallite size about 68 nm when AuNPs prepared with concentration of 0.412 ppm, In the meantime, the dominant phase (600) shifted by approximately 0.202°, and the lattice stress decreased by around 0.207. These changes are likely a result of the crystalline potentials influenced by the increased concentration of the C_{60}-polymer phase when the AuNPs concentration was raised to 1.944 ppm. In contrast, the dominant phase shifted to (132) at 19.9° (C_{70}), which can be attributed to the AuNPs concentration reaching 3.575 ppm. As for the quantitative intensity calculated using the (RIR) method, it was observed that the C_{60}-polymer exhibited a clear increase with the rising concentration of AuNPs as shown in thumbnail chart in Fig. (1), indicating their role as nucleation centers. Table (1) demonstrates the dominant phases of the fullerene and fullerene/AuNPs films XRD patterns.

Figure (2) represents FE-SEM images that mainly give morphological information about the surface of the prepared fullerenes and AuNPs-fullerene composite films with 0, 0.412, 1.944, and 3.575 ppm.

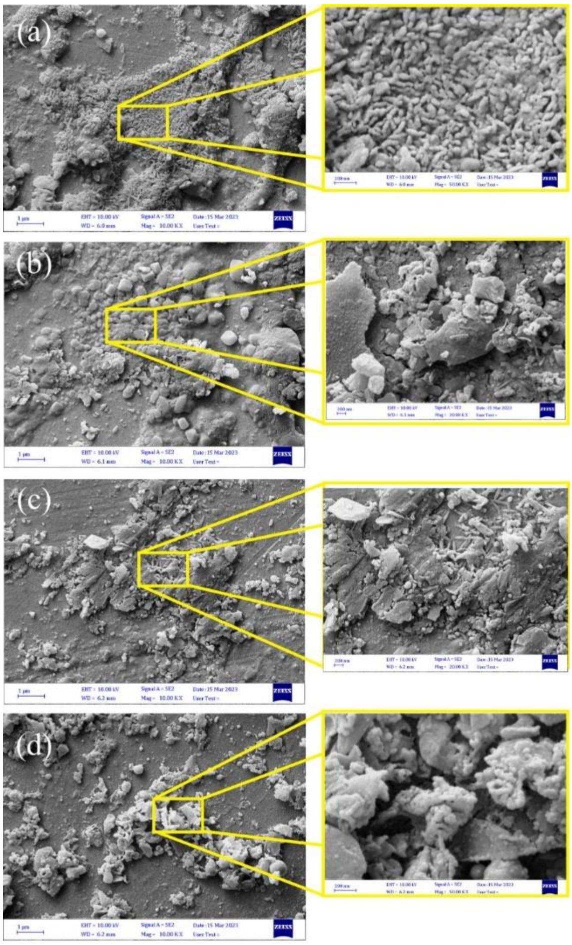

Fig. (2) FE-SEM images of the prepared fullerenes and AuNPs-fullerene composite films with 0.412, 1.944, and 3.575 ppm

Notably, a distinct separation can be observed among the various particles, particularly nanorods (that are believed to be C_{60}-polymeric can be known as nanowhiskers (C_{60}FNWs) [16]) with an average diameter of approximately 39 nm, as depicted in Fig. (2a). The particle separation and the non-uniformity of their distribution can be attributed to the phenomenon of impurity segregation due to variations in the surface energy of these different particles [17]. The addition of AuNPs have led to a clear change in the phases of the composition of the prepared films, where the addition of gold with a concentration of 0.412 and 1.944 ppm led to a variety of formations consisting of a shell-like formation consisting of aggregated spherical particles with average size about 11 nm. In addition, find rods with an average diameter of about 51 nm, which are thought to go back either to gold or as an accidental product with carbon nanotubes. With regard to the visible cracks in the ground, they are believed to be caused by the effect of both substrate temperature and surface energy. This is due to the film formation mechanism, where it is likely to be a surface density of the product from the effect of uneven heat distribution due to differing thickness of membrane areas and heterogeneous surface energy. The increase in the concentration of AuNPs to 3.575 ppm led to the emergence of the so-called segregation of impurity phenomena, formations similar to cauliflower flower as shown in Fig. (2c).

One of the active techniques to characterization of the carbon structures is Raman spectroscopy [18]. At high symmetry of fullerenes (C_{60} and C_{70}) has numerous vibrational modes, where are ten modes for C_{60} and 53 modes for C_{70} [19]. $A_g^{(2)}$, $H_g^{(1)}$, $H_g^{(7)}$, and $Hg^{(8)}$ are the apparent mean vibrational modes in C_{60} spectra [1]. In fact, $Ag^{(2)}$ mode, which is non-degenerate and the strongest among the Raman-active $Ag^{(2)}$) modes in addition to $Hg^{(8)}$ of C_{60}, has frequently been utilized to characterize C_{60} solids, these two modes and $Hg^{(7)}$ that related to pentagon shear [20], while some theoretical studies exceed this limit [21]. The $Ag^{(2)}$ mode peak position of accurately reflects the physical state of C_{60} molecules [16].

However, in Fig. (3), the Raman spectra of fullerene and fullerene/AuNPs films can be seen. The spectra included peaks for different modes with varying shifts and intensities according to the concentration of gold compared to what was reported previously in numerous of literature because of these films containing structural phases as observed in the X-ray diffraction patterns. All spectra showed the strong appearance of the peaks that represent $H_g^{(1)}$ mode [22], starting at the wavenumber 288 cm^{-1}, which is observed to shift to the right and increase in intensity with increasing gold concentration. This change in location and intensity is attributed to the effect of the crystal field resulting from the polymerization of C_{60} and the increase in chains length that occurs during the formation of nanopeapod [23]. In the meanwhile, $F_{2g}^{(1)}$ represented at wavenumber of 644 cm^{-1} which associated with internal active Raman mode of C_{60} molecule I_h polarization, that suffered of downshifting due to varying in the rotation factor [24]. The weak peak at 897 cm^{-1} is a non-Raman active mode, but it shows oscillation in position, intensity, and broadening (FWHM) as the concentration of AuNPs increases., where upshift to 910, 920.6, then downshift to 908 cm^{-1} with increasing of AuNPs concentration. Furthermore, the pentagonal pinch mode associated with the $Ag^{(2)}$ mode for both C^{60} and C^{70} is strongly visible at 1449 cm^{-1}, which suffers intensity increases with the volume fraction for C^{70} increasing. This peak is important in determining the molecular structure of fullerenes as it relates to the vibration of the five-ring present in fullerenes [8,25,26]. The graphite may be contributed several weak peaks at 1930, 2145, 3009, 3282, 4015, 4272 cm^{-1}, including the characterized peak 2079 cm^{-1}, which is related to 2D (or as originally known G'), the distortion and deflection that this peak suffers from results from disturbances in the vibration mode as a result of the field potential factors of the surrounding crystals [27].

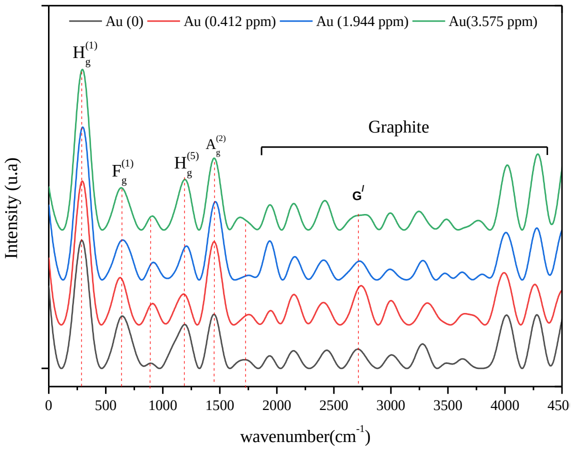

Fig. (3) Raman spectra of the prepared fullerenes and AuNPs-fullerene composite films with 0.412, 1.944, and 3.575 ppm

4. Conclusions

Graphite parts of wasted batteries can be utilized as precursors to prepare the fullerenes materials. These materials were effectively created in the form of thick films utilizing pulsed laser ablation and electrospray techniques successfully, containing C_{60}, C_{70}, and C_{60}-polymer structures. Concentration of AuNPs in fullerene/AuNPs influenced the structural properties of the prepared films, which led to the transit of most C_{60} structure to C_{70}, and C_{60}-polymer structures with increasing of AuNPs concentration. This applies to both morphological characteristics and enhanced Raman spectra.

References

[1] D. Jing and Z. Pan, "Molecular vibrational modes of C_{60} and C_{70} via finite element method", *Eur. J. Mech. A: Solids*, 28 (2009) 948–954.

[2] N. Ota, "Graphene Molecule Compared With Fullerene C_{60} As Circumstellar Carbon Dust Of Planetary Nebula", *ArXiv Astrophys.*, 1904 (2019) 1-9.

[3] C. Ji et al., "Recent Developments of Carbon Dots in Biosensing: A Review", *ACS Sensors*, 5

(2020) 2724–2741.

[4] A.B. Gaur et al., "Biomedical Applications of Carbon Nanomaterials: Fullerenes, Quantum Dots, Nanotubes, Nanofibers, and Graphene", *Materials (Basel)*, 14 (2021) 5978.

[5] N. Mulqueen, K. Sneed and Y. Pathak, "Recent Trends in Fullerenes Biomedical Applications", *Nov. Res. Sci.*, 10 (2022) 000748.

[6] A. Kausar, "Potential of Polymer/Fullerene Nanocomposites for Anticorrosion Applications in the Biomedical Field", *J. Compos. Sci.*, 6 (2022) 1-13.

[7] M.S. Nadeem et al., "Synergistic photocatalytic properties of fullerene (C_{60}) anchored V/Cu dual-doped NiO nanocomposites for water disinfection", *Mater. Sci. Eng. B*, 297 (2023) 116705.

[8] J.B. Kimbrell et al., "Analysis of mixtures of C_{60} and C_{70} by Raman spectrometry", *Nanosci. Meth.*, 3 (2014) 40–46.

[9] J. Sanchís et al., "Transformation of C60 fullerene aggregates suspended and weathered under realistic environmental conditions", *Carbon*, 128 (2018) 54–62.

[10] A.I. Kharlamov, M.E. Bondarenko and N.V. Kirillova, "New method for synthesis of fullerenes and fullerene hydrides from Benzene", *Russian J. Appl. Chem.*, 85 (2012) 233–238.

[11] L.T. Scott, "Methods for the chemical synthesis of fullerenes", *Angew. Chemie - Int. Ed.*, 43 (2004) 4994–5007.

[12] A. Nimibofa et al., "Fullerenes: Synthesis and Applications", *J. Mater. Sci. Res.*, 7 (2018) 22.

[13] B.M.A. Alani and M.A. Alalousi, "Structural, Morphological, and Spectroscopical Properties of Fullerenes (C_{60}) Thin Film Prepared via Electrospray Deposition", *J. Phys. Conf. Ser.*, 1829 (2021).

[14] H. Chu et al., "Decoration of gold nanoparticles on surface-grown single-walled carbon nanotubes for detection of every nanotube by surface-enhanced raman spectroscopy", *J. Am. Chem. Soc.*, 131 (2009) 14310–14316.

[15] D. Roy, S. Kanojia and K. Mukhopadhyay, "Analysis of carbon-based nanomaterials using Raman spectroscopy : principles and case studies", *Bull. Mater. Sci.*, 44 (2021) 1-9.

[16] T. Konno et al., "Precise Raman measurements of C_{60} fullerene nanowhiskers synthesized using the liquid-liquid interfacial precipitation method", *Trans. Mater. Res. Soc. Japan.*, 41 (2016) 289–295.

[17] M.A. Alalousi et al., "Sensing Enhancement of Gold Nanoparticles Doped-TiO_2 Thin Films as H_2S Gas Sensor", *Nano Hybr. Compos.*, 35, (2022) 1–10.

[18] M. Han et al., "PEI-functionalized carbon nanotube thin film sensor for CO_2 gas detection at room temperature", *mdpi Micromach.*, 12(9) (2021) 1053.

[19] H. Chadli, F. Fergani and A. Rahmani, "Structural and Vibrational Properties of C_{60} and C_{70} Fullerenes Encapsulating Carbon Nanotubes", in N. Kamanina (Ed.), **Fullerenes Relat. Mater. Appl.**, IntechOpen (2018) pp. 109-127.

[20] A. Dorner-Reisel et al., "Effect of fullerene C_{60} thermal and tribomechanical loading on Raman signals", *Diam. Relat. Mater.*, 126 (2022) 109036.

[21] N. Khinevich et al., "Surface enhanced Raman spectroscopy of fullerene C_{60} drop-deposited on the silvered porous silicon", *J. Phys. Conf. Ser.*, 917 (2017) 8–12.

[22] H. Chadli, A. Rahmani and J.L. Sauvajol, "Raman spectra of C_{60} dimer and C_{60} polymer confined inside a (10,10) single-walled carbon nanotube", *J. Phys. Cond. Matter*, 22 (2010).

[23] S. Samiullah, "Spectroscopic characterization of fullerenes", Luleå University of Technology (2008).

[24] H. Kuzmany et al., "Raman spectroscopy of fullerenes and fullerene-nanotube composites", *Philos. Trans. R. Soc. London. Ser. A Math. Phys. Eng. Sci.*, 362 (2004) 2375–2406.

[25] R. Saito et al., "Raman spectroscopy of graphene and carbon nanotubes", *Adv. Phys.*, 60 (2011) 413–550.

[26] Z.F. Kadhim, E.M. Saeed and H.A.H. Al-jubouri, "Phases of Deposited Carbon Films By Pulsed Laser Deposition - Review", *Int. J. Mech. Prod. Eng. Res. Develop.*, 10 (2020) 5139–5156.

[27] V. Zólyomi, J. Koltai and J. Kürti, "Resonance Raman spectroscopy of graphite and graphene", *phys. stat. sol. Basic Res.*, 248 (2011) 2435–2444.

Table (1) XRD parameters of the dominant phase for fullerene and fullerene/AuNPs films

AuNPs Conc. (ppm)	2θ (deg)	d (Å)	hkl	FHWM (deg)	Intensity	Crystallite Size (nm)	Lattice strain	Fullerene	Crystalline System
0	20.77	4.28	3 1 1	0.13	52.01	80.73	0.265	C_{60}	Cubic
0.412	21.65	4.10	6 0 0	0.155	44	67.67	0.303	C_{70}	Orthorhombic
1.944	21.45	4.14	6 0 0	0.155	27.74	208.55	0.099	C_{70}	Orthorhombic
3.575	19.93	4.45	1 3 2	0.216	67.72	44	0.506	C_{70}	Orthorhombic

IRAQI JOURNAL OF APPLIED PHYSICS
Vol. 19, No. 4B, November 2023, pp. 171-174

Sara M. Ahmed [1]
Asia H. Al-Mashhadani [2]
Hussain S. Akbar [1]

[1] *Department of Physics, College of Education for Pure Sciences, University of Kirkuk, Kirkuk, IRAQ*
[2] *Department of Physics, College of Science, University of Baghdad, Baghdad, IRAQ*

Nano Nigella Sativa Used as Free Radicals Scavenger

In this research, natural nanomaterials such as Nigella sativa were used as scavenging materials for free radicals generated as a result of human exposure to nuclear radiation. Nuclear radiation interacts with cell components in several ways, including ionization and excitation. As a result of these interactions, free radicals such as hydroxide, electrons, and others are generated. These free radicals cause many diseases, especially cancer. To get rid of these disease-causing free radicals, anti-oxidizing substances must be used that have the effectiveness to get rid of these free radicals. For this purpose, samples of very small sizes, approximately 21 nanometers, were prepared from Nigella sativa using simple methods and added to the phantom, a live cell substitute, and irradiated with deionized water. Free radicals were calculated before and after the irradiation of the phantom. Free radicals were screened using chemical materials such as 2,2-Diphenyl-1-picrylhydrazyl (DPPH) assay by a UV-visible spectrophotometer. Then these nano Nigella sativa were used and given to irradiate mice, and it was found that nano Nigella sativa can get rid of the free radicals formed as a result of exposure of mice to nuclear radiation.

Keywords: Nigella sativa; Nanoparticles; Free radicals scavenger; Gamma rays
Received: 22 August 2023; **Revised:** 01 September 2023; **Accepted:** 08 September 2023

1. Introduction

According to some experts, oxidative stress, which oxygen radicals cause, contributes more to a number of degenerative diseases like diabetes, cancer, atherosclerosis, stomach ulcers, and others [1]. The body of a man develops "hydroxyl radicals and hydrogen peroxide; they are free radicals and Reactive Oxygen Species (ROS)" as a result of nutrition disorder treatment, exposure to external stress, and other factors. Pollutants and ionizing radiation, for instance, can harm the body's physiological processes and cell functions. The body's structure includes enzymes and antioxidant defenses that remove ROS. But regrettably, increasing reactive oxygen levels or decreasing the effectiveness of antioxidant defense mechanisms to detoxify might contribute to an increase in oxidative stress and injury or even death for live cells [2-4]. Antioxidants protect the body from harmful effects caused by unpredictable and uncontrollable ROS; they are naturally present in plants and improve a person's health by consuming a variety of plant foods [4,5]. Antioxidants are a group of compounds that have conservative effects on cells. As a result, they will protect the body from damage caused by unpredictably and uncontrollably derived ROS. Despite the fact that much research has looked into the leaves, roots, and seeds of whole plants as potential sources of beneficial phytochemicals, a number of naturally occurring antioxidant molecules in plants have already been identified as free radical and oxygen scavengers. There has been an increase in interest recently. Dramatically moving away from synthetic antioxidants that have been restricted because of their adverse effects, like carcinogenicity, and replacing them with naturally occurring antioxidants [6]. Nanometals like gold and silver have been used in numerous studies as antioxidants to scavenge free radicals [7,8].

Nigella sativa is a botanical species known for its possession of potent and non-hazardous bioactive constituents. Nigella, also known as Nigella sativa, is an herbaceous plant that is classified as an annual and belongs to the family Ranunculaceae. Mature seeds are utilized for both culinary and medicinal applications. The seeds are utilized as a condiment for vegetables, lentils, and many forms of baked goods [9]. Nigella seeds are utilized for their carminative and diuretic properties, as well as their potential to aid in the regulation of delayed menses and breastfeeding. Additionally, the oil derived from these seeds has been found to possess protective effects against histamine-induced bronchospasm, cough, and bronchial asthma [10]. Other study was done to study the influences, preventive and diuretic, of Nigella sativa seeds oil on calcium oxalate (CaOx) urolithiasis induced in wistar male rats. Methodology seeds of Nigella sativa were analyzed for the evaluation of the concentration of oxalate and calcium [11]. The fixed oil derived from nigella seeds is abundant in linoleic, oleic, and palmitic acids [12]. Numerous researchers have conducted studies on the essential oil derived from nigella seeds, wherein they have successfully isolated and discovered active ingredients that have advantageous therapeutic properties [13]. The oil has been derived through the process of extracting the raw or roasted seeds by means of pressing. The utilization of the pressed cake by-product has been inefficient due to its inability to be directly employed as animal feed. As a result, previous researchers have looked into a number of nigella seed cake applications [9].

The aim of the present work is to study the ability of Nano Nigella sativa to scavenge the free radicals which is produced in water due to exposure to gamma ray.

2. Preparation of Nano Nigella Sativa Extract

The Nigella sativa seeds were ground and milled into a fine powder using a mortar. A quantity of four grams of nigella sativa powder was combined with 100 milliliters of distilled water (D.W.) solvent. The mixture was then agitated for a duration of 60 minutes at a temperature of 45 °C. Subsequently, the mixture was subjected to distillation using filter paper, resulting in the production of a hydrous extract. To investigate the surface roughness and topography of deposited thin films, atomic force microscopy (AFM) micrographs were acquired utilizing digital instrumentation. The determination of the morphology and size of the produced nigella sativa was conducted using AFM. The mean diameter of Nigella sativa was observed to be 21 nm. Figures (1) and (2) display the AFM pictures alongside the corresponding histograms illustrating the distribution of particle sizes. The particles exhibit nanoscale dimensions and possess a mostly spherical morphology.

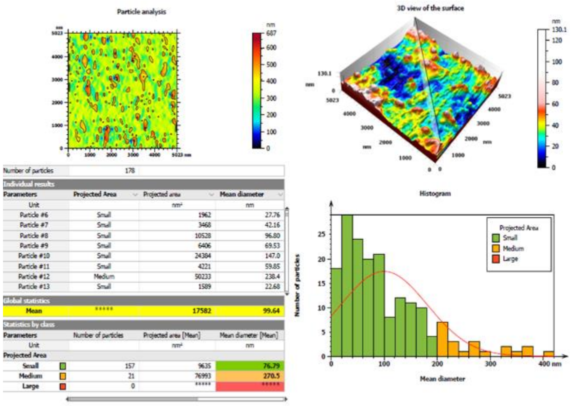

Number of particles	178		
Individual results			
Parameters	**Projected Area**	**Projected area**	**Mean diameter**
Unit		nm²	nm
Particle #6	Small	1962	27.76
Particle #7	Small	3468	42.16
Particle #8	Small	10528	96.80
Particle #9	Small	6406	69.53
Particle #10	Small	24384	147.0
Particle #11	Small	4221	59.85
Particle #12	Medium	50233	238.4
Particle #13	Small	1589	22.68
Global statistics			
Mean	*****	17582	99.64
Statistics by class			
Parameters	Number of particles	Projected area [Mean]	Mean diameter [Mean]
Unit		nm²	nm
Projected Area			
Small 🟩	157	9635	76.79
Medium 🟧	21	76993	270.5
Large 🟥	0	*****	*****

Fig. (1) The AFM images of the nano Nigella sativa particles prepared in this work

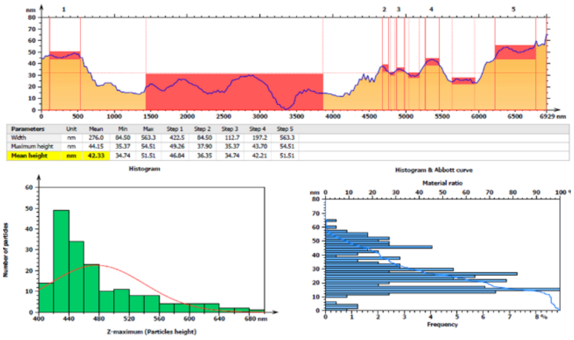

Parameters	Unit	Mean	Min	Max	Step 1	Step 2	Step 3	Step 4	Step 5
Width	nm	276.0	84.50	563.3	422.5	84.50	112.7	197.2	563.3
Maximum height	nm	44.15	35.37	54.51	49.26	37.90	35.37	43.70	54.51
Mean height	**nm**	**42.33**	34.74	51.51	46.84	36.35	34.74	42.21	51.51

Fig. (2) The AFM histograms of the particle size distribution for nano Nigella sativa

3. Results and Discussion

The antioxidant activities of Nano nigella sativa extracts have been evaluated using several oxidation tests, including DPPH radical scavenging. Ascorbic acid was employed as a reference for comparison, along with 2,2-azinobis-(3-ethylbenzothiazoline)-6-sulfonic acid (ABTS) and total antioxidant capacity (TAC) [14,15].

One potential constraint or drawback that should be considered is the limitation. The antioxidant potency of Nigella sativa was evaluated primarily by comparison with ascorbic acid by preparing extracts with varying concentrations. In this study, a concentration of 400 mg/ml was prepared by diluting 0.004/10 ml with other concentrations using the formula [16]

$$C_1V_1 = C_2V_2 \qquad (1)$$

Here, C_1 represents the initial higher concentration in molarity, V_1 denotes the volume prior to dilution in liters, C_2 represents the desired lower concentration in molarity, and V_2 represents the final gross volume after dilution in liters

These diluted solutions were subsequently added to each tube. The synthesis of Standard Blank was conducted using the same methodology, excluding the inclusion of nano Nigella sativa. A positive control was employed in the experiment, consisting of a solution of ascorbic acid with a concentration of 12.5 mg/ml and an absorbance value of 1.23. The inhibition scavenging activity at room temperature was assessed using the formula [16]

$$\% \text{ Inhibition } (I\%) = [(AC-AS)/AC] \times 100 \qquad (2)$$

In this equation, AC represents the absorbance of ascorbic acid as a control, and AS represents the absorbance of the samples with varying concentrations. It is shown that there is a positive correlation between absorbance and total antioxidant activity, indicating that an increase in absorbance is associated with an increase in total antioxidant activity. From the present search, it is illustrated that the antioxidant activity of the Nano Nigella sativa with a standard ascorbic acid was shown in Fig. (3) and table (1). The concentrations used in this work are 0.00030, 0.00035 0.00040, 0.00045 and 0.00050 mg/ml.

Table (1) The absorbance percentage, and the inhibition of free radicals the total antioxidant activity, for different concentration of nano Nigella sativa

Samples Irradiated (H-NPs) Concentration (mg/ml)	Absorption After Irradiated 0.314	Inhibition %
0.00030	0.256	18.4%
0.00035	0.220	29.9%
0.00040	0.189	39.8%
0.00045	0.180	40.7%
0.00050	0.180	40.7%

The Nano nigella sativa was used to protect the mouse skin from nuclear radiation, where the mouse was given a dose of the nanomaterial orally, knowing that this dose is sufficient to scavenge free radicals with phantom. Then two groups of mice were exposed to gamma rays, part of these mice were provided with nanomaterials and the other part were not given nanomaterials.

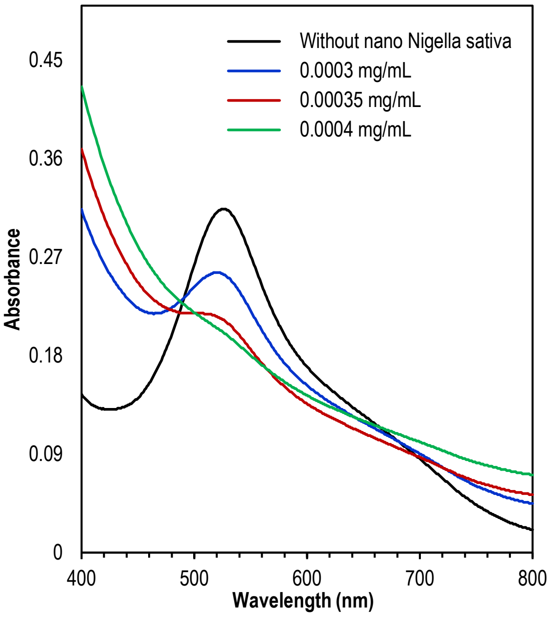

Fig. (3) Values of DPPH absorption and inhibition% for samples added with various concentrations of nano Nigella sativa after irradiation where "black" line is the absorbance curve for irradiated phantom without nano Nigella sativa, "blue" line is for irradiated phantom after added 0.00030 mg/ml from nano Nigella sativa, "red" line is for irradiated phantom after added 0.00035 mg/ml from Nano nigella sativa and "green" line is for irradiated phantom after added 0.00040 mg/ml from nano Nigella sativa

Control mice and mice exposed to radiation that were not given a dose of nanomaterials, as well as mice fed with nanomaterials were dissected as shown in figures (4) and (5). It was observed that the mice that were not fed with the Nano nigella sativa develop cancerous tumors while the mice fed with nanomaterials did not develop any disease as shown in Fig. (6).

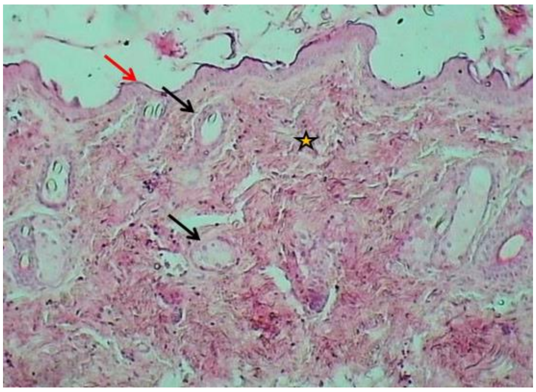

Fig. (4) Section of skin (control) shows: normal epidermis (Red arrow), hair follicles (Black arrow) & normal dermal fibrous tissue (Asterisk). H&E stain (100x)

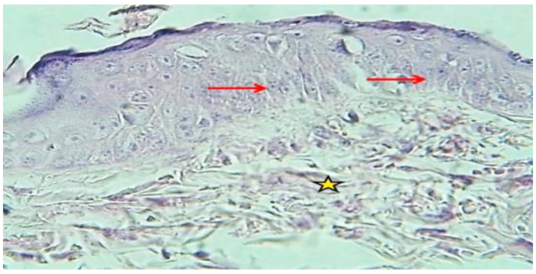

Fig. (5) Section of skin shows epidermal thickening associated with cellular swelling of keratocytes without necrosis, (red arrows) with inflammatory cells infiltration in the cutaneous fibrous tissue. H&E stain (400x)

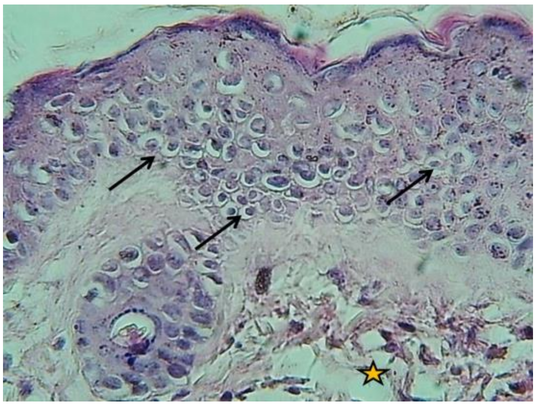

Fig. (6) Section of skin (Before) protect at 0.4x10^{-4}) shows: mild epidermal thickening associated with mild cellular swelling of keratocytes (arrow), with normal hair follicles & normal dermal fibrous tissue (Asterisk). H&E stain (400x)

4. Conclusions

This work provides evidence of the robust antioxidant characteristics of Nano nigella sativa in comparison to ascorbic acid, attributed to its substantial phenolic acid content and effective scavenging capabilities. These substances have the ability to effectively mitigate and prevent the generation of harmful free radicals, thereby curbing the creation of toxic waste within the human body. Furthermore, they offer several beneficial impacts on our everyday existence. The Nano nigella sativa results for free radicals scavenger are best than other natural particles [17,18].

References

[1] W. Gulam and H. Ahsan, "Reactive oxygen species: role in the development of cancer and various chronic conditions", *J. Carcinogen.*, 5 (2006) 14.

[2] M. Asori and A. Hedayati-Omran, "Antioxidant and Free Radical Scavenging Activities of Curcumin", *Asian J. Chem.*, 23 (2011) 3713.

[3] S. Fulda, "Modulation of Apoptosis by Natural Products for Cancer Therapy", *Planta Medica*, 76(11) (2010)1075-1079.

[4] T. Ozben, "Oxidative Stress and Apoptosis: Impact on Cancer Therapy", *J. Pharmaceut. Sci.*, 96(9) (2007) 2181-2196.

[5] A. Pourali, M. Afrouziyeh and S. Moghaddaszadeh-ahrabi, “Extraction of phenolic compounds and quantification of the total phenol of grape pomace”, *Euro. J. Exp. Biol.*, 4(1) (2014) 174-176.

[6] S. Cuzzocrea et al., “Antioxidant therapy: A new pharmacological approach in shock, inflammation, and ischemia/reperfusion injury”, *Pharmacol. Rev*., 53 (2001) 135.

[7] T. Ak and İ. Gülçin, “Antioxidant and radical scavenging properties of curcumin”, *Chemico-Biol. Interact.*, 174(1) (2008) 27-37.

[8] O.S. Ashour, A.H. Al-Mashhadani and R.M. Yas, “Studying the free radical scavenging activity using low concentration of nanogold particle”, *IOP J. Phys.: Conf. Ser.*, 1279(1) (2019) 012066.

[9] M. Akram Khan, “Chemical composition and medicinal properties of Nigella sativa Linn”, *Inflam. Pharmacol.*, 7 (1999) 15-35.

[10] M.B. Atta and K. Imaizumi, “Antioxidant activity of nigella”, *J. Jpn. Oil Chem. Soc*., 47 (1998) 475-480.

[11] A. Benhelima et al., “Nephroprotective and diuretic effect of Nigella sativa L seeds oil on lithiasic wistar rats”, *African J. Trad. Complem. Alter. Med.*, 13(6) (2016) 204-214.

[12] M.A. Salem, “Effect of some heat treatment on nigella seeds characteristics. 1-Some physical and chemical properties of nigella seed oil”, *J. Agric. Res. Tanta Univ*., 27 (2001) 471-486.

[13] E.S.M. Abdel-Aal and R.S. Attia, “Characterization of black cumin (Nigella sativa) seeds. 2- Proteins”. *Alexandria Sci. Exch.*, 4 (1993) 483-496.

[14] M.S. Karawya et al., “Essential oil and lipids of Nigella sativa seeds and their biological activity”, *Zagazig J. Pharm. Sci*., 3(2) (1994) 49-57.

[15] S. Pavel, B. Klejdus and V. Kubáň, “Determination of total content of phenolic compounds and their antioxidant activity in vegetables - evaluation of spectrophotometric methods”, *J. Agricul. Food Chem.*, 54(3) (2006) 607-616.

[16] G.D. Christian, P.K. Dasgupta and K.A. Schug, **“Analytical Chemistry”**, 7th ed., Wiley (2014) Ch. 7, p. 225.

[17] N.Z. Habeeb, A.H. Al-Mashhadani and A.M. Ali, “Antioxidant Activity and Radical Scavenging Properties of Nano Natural Material”, *AIP Conf. Proc.*, 2414 (2023) 030017.

[18] N.Z. Habeeb, A.H. Al-Mashhadani and A.M. Ali, “Natural antioxidant by scavenging free radicals activities using nano turmeric”, *AIP Conf. Proc.*, 2372 (2021) 130018.

IRAQI JOURNAL OF
APPLIED PHYSICS
EDITORIAL BOARD

COPYRIGHT RELEASE FORM
IRAQI JOURNAL OF APPLIED PHYSICS (IJAP)

We, the undersigned, the author/authors of the article titled
………
………
………
………
………
………
………

that is submitted to the Iraqi Journal of Applied Physics (IJAP) for publication, declare that we have neither taken part or full text from any published work by others, nor presented or published it elsewhere in any other journal. We also declare transferring copyrights and conduct of this article to the Iraqi Journal of Applied Physics (IJAP) after accepting it for publication.

The authors will keep the following rights:

1. Possession of the article such as patent rights.
2. Free of charge use of the article or part of it in any future work by the authors such as books and lecture notes after informing IJAP editorial board.
3. Republishing the article for any personal purposes of the authors after taking journal permission.

To be signed by all authors:

Signature:………………………………………………………..date: …………………………………………
Printed name: ……………………………………………………………………………………………………

Signature:………………………………………………………..date: …………………………………………
Printed name: ……………………………………………………………………………………………………

Signature:………………………………………………………..date: …………………………………………
Printed name: ……………………………………………………………………………………………………

Correspondence author:……………………..………………………………………………………………...
………
Address:………………………………………………...…………………………………………………
………
Telephone:…………………….……………………..email: …………………………………………………

Note: Complete and sign this form and mail it to the below address with your finally revised manuscript

The Iraqi Journal of Applied Physics
P. O. Box 88052, Baghdad 12631, IRAQ
www.iraqiphysicsjournal.com
Email: info@iraqiphysicsjournal.com
Email: editor_ijap@yahoo.co.uk
Email: ijap.editor@gmail.com

IRAQI JOURNAL OF APPLIED PHYSICS

Volume (19) Issue (4B) November 2023

CONTENTS